BEILSTEIN JOURNAL OF ORGANIC CHEMISTRY

Non-central chirality in organic chemistry

Edited by Ken Tanaka and Naohiko Yoshikai

Imprint

Beilstein Journal of Organic Chemistry
www.bjoc.org
ISSN 1860-5397
Email: journals-support@beilstein-institut.de

The *Beilstein Journal of Organic Chemistry* is published by the Beilstein-Institut zur Förderung der Chemischen Wissenschaften.

Beilstein-Institut zur Förderung der
Chemischen Wissenschaften
Trakehner Straße 7–9
60487 Frankfurt am Main
Germany
www.beilstein-institut.de

BEILSTEIN JOURNAL OF ORGANIC CHEMISTRY

Pd-Catalyzed asymmetric allylic amination with isatin using a P,olefin-type chiral ligand with C–N bond axial chirality

Natsume Akimoto[1], Kaho Takaya[1], Yoshio Kasashima[2], Kohei Watanabe[3],
Yasushi Yoshida[1,4,5,6] and Takashi Mino[*1,4,5]

Full Research Paper

Open Access

Address:
[1]Graduate School of Engineering, Chiba University, 1-33 Yayoi-cho, Inage-ku, Chiba 263-8522, Japan, [2]Education Center, Chiba Institute of Technology, 2-2-1 Shibazono, Narashino, Chiba 275-0023, Japan, [3]Faculty of Education, Chiba University, 1-33 Yayoi-cho, Inage-ku, Chiba 263-8522, Japan, [4]Molecular Chirality Research Center, Chiba University, 1-33 Yayoi-cho, Inage-ku, Chiba 263-8522, Japan, [5]Soft Molecular Activation Research Center, Chiba University, 1-33 Yayoi-cho, Inage-ku, Chiba 263-8522, Japan and [6]Institute for Advanced Academic Research (IAAR), Chiba University, 1-33 Yayoi-cho, Inage-ku, Chiba 263-8522, Japan

Email:
Takashi Mino[*] - tmino@faculty.chiba-u.jp

[*] Corresponding author

Keywords:
asymmetric allylic amination; axial chirality; isatin; palladium catalysis; P,olefin-type chiral ligand

Beilstein J. Org. Chem. **2025,** *21,* 1018–1023.
https://doi.org/10.3762/bjoc.21.83

Received: 10 April 2025
Accepted: 13 May 2025
Published: 23 May 2025

This article is part of the thematic issue "Non-central chirality in organic chemistry".

Associate Editor: N. Yoshikai

Abstract

In this study, we implemented the P,olefin-type chiral ligand (a*R*)-(−)-**6**, which contains a cyclohexyl group and a cinnamoyl group on the nitrogen atom, in the Pd-catalyzed asymmetric allylic amination of allylic esters with isatin derivatives **11** as nucleophiles. The reaction proceeds efficiently, yielding the products (*S*)-**13** with good-to-high enantioselectivity. A scale-up reaction was also successfully conducted at a 1 mmol scale. Additionally, when malononitrile was added to the resulting product (*S*)-**13a** in the presence of $FeCl_3$ as the catalyst, the corresponding malononitrile derivative (*S*)-**16** was obtained without any loss in optical purity.

Introduction

Isatin is a well-known natural indole derivative. Due to the broad biological activities of its derivatives, extensive research has been conducted on their synthesis. Furthermore, the isatin framework is a versatile starting material for various transformations, including multicomponent reactions and the synthesis of spirocyclic compounds [1-3]. The nucleophilicity of isatin at the nitrogen atom allows it to participate in reactions such as alkylation [4], arylation [5], and *aza*-Michael addition [6-8]. However, the products obtained from these reactions are primarily achiral or racemic, and only a few studies have reported the use of isatin as a nucleophile in asymmetric reactions [9-11]. On the other hand, it has been revealed that compounds in which the carbon bonded to the nitrogen atom of newly constructed *N*-substituted isatin becomes a chiral center exhibit pharmacological properties in medicinal chemistry. For example, racemic compound **1** (Figure 1) was evaluated for its cytotoxicity against human breast cancer cells (MCF7) in comparison to the standard doxorubicin and exhibited excellent activity against the MCF7 cell line [12]. The optically active compound **2** also showed activity against Huh7.5-FGR-JC1-Rluc2A cells, which carry HCV gt 2a [13].

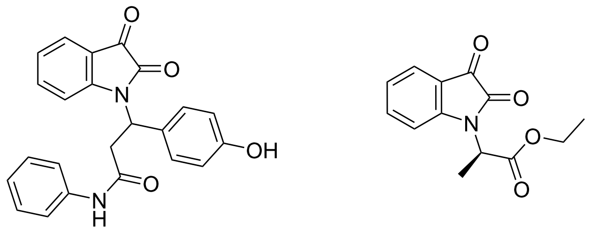
1 **2**

Figure 1: Compound **1** and **2**.

Therefore, developing asymmetric reactions that simultaneously form a carbon–nitrogen bond and construct a chiral center is of great importance. Although a relatively large number of asymmetric allylic amination reactions using palladium catalysts with amines as nucleophiles have been reported [14-25], there have been only a few reports on the *N*-substitution of isatin using asymmetric methods. Recently, Wolf's group reported a transition-metal-catalyzed (Pd-catalyzed) asymmetric allylic amination of allyl esters using isatin as a nucleophile. In this reaction, bisphosphine-type ligands such as BINAP and SEGPHOS derivatives, as well as P,N-type ligands like oxazoline-type ligands, were utilized as chiral ligands [26]. On the other hand, several groups have recently reported new chiral ligands with axial chirality for Pd-catalyzed asymmetric allylic substitution reactions. For example, the Zhou group reported a P,olefin-type chiral ligand **3** with C–C bond axial chirality for this reaction (Figure 2) [27]. Additionally, we have recently reported chiral ligands with C–N bond axial chirality, such as *N*-alkyl-*N*-cinnamyl-type chiral ligands **4** [28,29] and **5** [30], and a P,olefin-type chiral ligand **6** [31] with a cinnamoyl group instead of a cinnamyl group. In particular, the chiral ligand **6** is effective in the Pd-catalyzed asymmetric allylic substitution reaction of allylic esters with indoles. Here, we describe the Pd-catalyzed asymmetric allylic amination of allylic esters with isatin as a nucleophile using chiral ligand **6** and its derivative **7**. Compared to chiral ligand **6**, which has a secondary alkyl group (cyclohexyl) as a substituent on the nitrogen and has already been reported, compound **7** has a primary alkyl group (*n*-propyl). This difference reduces steric hindrance and lowers the rotational barrier around the carbon–nitrogen bond, increasing the likelihood of racemization.

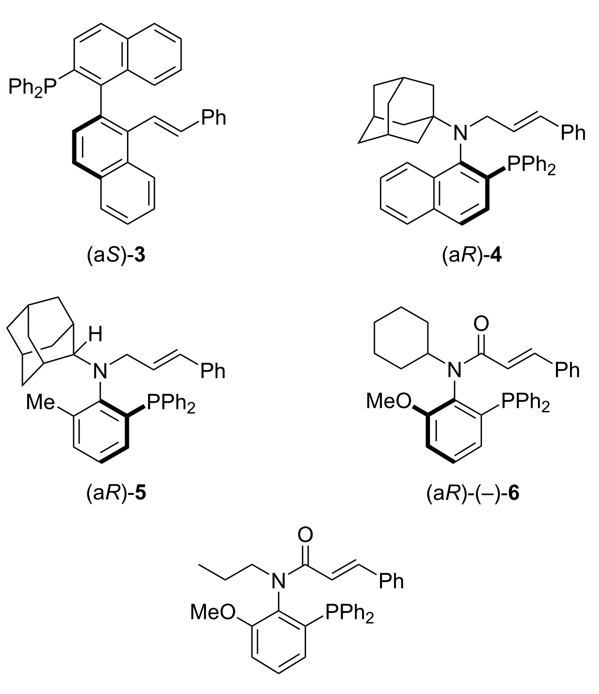
(a*S*)-**3** (a*R*)-**4** (a*R*)-**5** (a*R*)-(–)-**6** **7**

Figure 2: Chiral ligands **3**–**7**.

Results and Discussion

N-Propyl-*N*-cinnamoylamide **7** was prepared from phosphine oxide **8** [32] via an $\mathrm{S_N}$Ar reaction with nucleophilic lithium amide from *n*-propylamine, the reduction of phosphine oxide **9** by trichlorosilane/triethylamine, and the *N*-acylation of **10** with cinnamoyl chloride in three steps (Scheme 1). We also analyzed amide compound **7** by HPLC analysis using a chiral stationary phase column with a CD detector and found that the C(aryl)–N(amide) bond axial chirality exists in amide compound **7**. We attempted the optical resolution of racemic compound (±)-**7** and obtained (+)-**7** and (−)-**7** using a semi-preparative chiral HPLC on 50 milligram scales. We also investigated the racemization process associated with the axial chirality of compound **7** (see Supporting Information File 1). The racemization barrier ($\Delta G^{\ddagger}_{\mathrm{rac}}$) of (−)-**7** in *n*-dodecane was determined to be 25.0 kcal/mol at 25 °C, as calculated using the Arrhenius and Eyring equations [33-35]. Therefore, the half-life of racemization of ligand (−)-**7** at 25 °C in *n*-dodecane is approximately 1.3 days, which is faster compared to ligand **6**, which has a half-life of about 3.7 days [31].

We next investigated the ability of optically active amides (a*R*)-(−)-**6** and (−)-**7** as chiral ligands for the Pd-catalyzed asym-

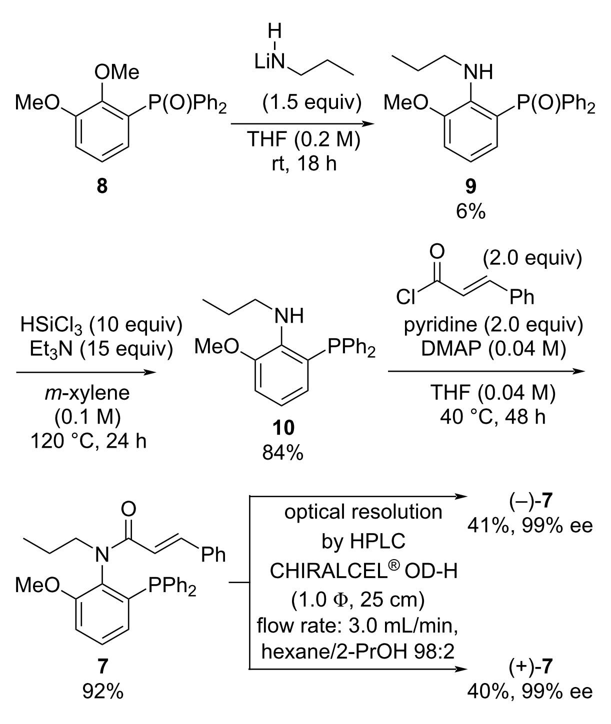

Scheme 1: Preparation and optical resolution of **7**.

metric allylic amination of allylic acetate, such as a 1,3-diphenyl-2-propenyl acetate (**12**) with isatin (**11a**). We began the investigation under conditions using 5 mol % of $[Pd(C_3H_5)Cl]_2$ (Pd = 10 mol %) and 12 mol % of chiral ligands (Table 1).

The reaction with (a*R*)-(−)-**6** as the chiral ligand and K_2CO_3 as the base in $CHCl_3$ gave the desired product (*S*)-**13a** in 72% yield with 87% ee (Table 1, entry 1). In contrast, the reaction with (−)-**7** afforded (*S*)-**13a** in significantly lower yield, albeit with an enantioselectivity similar to that of the reaction with **6** (Table 1, entry 2). This result clarifies that (−)-**7**, with a racemization half-life of only approximately 1.3 days, also has a chiral induction ability. However, improvement is required in terms of the reactivity of the catalytic reaction. Subsequently, we investigated the effect of the base using (a*R*)-(−)-**6** by testing various bases. The reaction in the presence of Na_2CO_3 delivered the product in 99% yield, although the enantioselectivity slightly decreased compared to the reaction using K_2CO_3 (see Table 1, entry 1 vs entry 3). The use of Cs_2CO_3 resulted in a significant drop in the yield (Table 1, entry 4), whereas NaOAc improved the yield but slightly lowered the enantioselectivity (Table 1, entry 5). Other potassium salts such as K_3PO_4 led to a low yield

Table 1: Optimization of conditions for the Pd-catalyzed asymmetric allylic amination of acetate **12** with isatin (**11a**).[a]

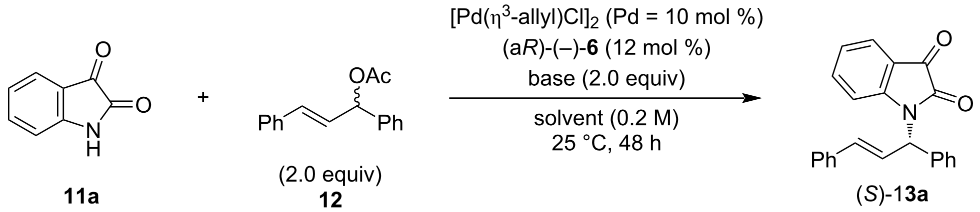

Entry	Base	Solvent	Yield (%)[b]	ee (%)[c]
1	K_2CO_3	$CHCl_3$	72	87
2[d]	K_2CO_3	$CHCl_3$	3	84
3	Na_2CO_3	$CHCl_3$	99	85
4	Cs_2CO_3	$CHCl_3$	19	86
5	NaOAc	$CHCl_3$	89	86
6	K_3PO_4	$CHCl_3$	12	86
7	Na_3PO_4	$CHCl_3$	60	88
8	Na_3PO_4	CH_2Cl_2	88	92
9	Na_3PO_4	CH_3CN	75	93
10	Na_3PO_4	THF	74	93
11	Na_3PO_4	DMF	trace	–
12	Na_3PO_4	$PhCF_3$	84	95
13[e]	Na_3PO_4	$PhCF_3$	50	86
14[f]	Na_3PO_4	$PhCF_3$	80	94

[a]The reaction was carried out at 0.1 mmol scale. [b]Isolated yield. [c]Determined by chiral HPLC analysis using a chiral column. Absolute configuration was assigned by comparison of HPLC analysis with reported data [26]. [d]This reaction was carried out using (–)-**7** instead of (a*R*)-(–)-**6** as a chiral ligand. [e]This reaction was carried out using 1,3-diphenylallyl pivalate (**14**) instead of acetate **12**. [f]This reaction was carried out at a 1.0 mmol scale.

of the product (Table 1, entry 6). Meanwhile, when Na_3PO_4 was tested, the yield decreased, but the enantioselectivity improved to 88% ee (Table 1, entry 7). With Na_3PO_4 as the optimum base, which showed the highest enantioselectivity, we conducted a solvent screening. The reaction in CH_2Cl_2 resulted in better yield and enantioselectivity than in $CHCl_3$ (Table 1, entry 8). The coordinating solvents, CH_3CN and THF, further improved the enantioselectivity to 93% ee (Table 1, entries 9 and 10). In contrast, the reaction barely proceeded when DMF was used (Table 1, entry 11). The reaction in $PhCF_3$ afforded the target product in a good yield with the highest enantioselectivity compared to other solvents (Table 1, entry 12). Furthermore, when (*E*)-1,3-diphenyl-2-propenyl pivalate (**14**) was tested as the allyl ester, the desired product (*S*)-**13a** was obtained with a yield of 50% and an enantioselectivity of 86% ee (Table 1, entry 13). Additionally, the scale-up reaction using 1 mmol of isatin (**11a**) as the nucleophile under the optimal conditions (Table 1, entry 12) afforded the desired product (*S*)-**13a** with nearly the same yield and enantioselectivity as the 0.1 mmol scale reaction (entry 14).

Next, we investigated the substrate scope of the palladium-catalyzed asymmetric allylic amination of 1,3-diphenyl-2-propenyl acetate (**12**) with isatin derivatives **11** as nucleophiles under the optimized conditions using (a*R*)-(−)-**6** as the ligand and Na_3PO_4 as the base in $PhCF_3$ as the solvent (Scheme 2). An isatin derivative bearing a chloro group at the 4-position afforded the desired product (*S*)-**13b** with good yield and enantioselectivity. Similarly, an isatin derivative with a methyl group as an electron-donating group at the 5-position gave (*S*)-**13c** in good yield, although with slightly decreased enantioselectivity. The introduction of the chloro group at the same position led to a moderate yield for (*S*)-**13d**, while the enantioselectivity remained high. In contrast, the reaction with the isatin derivative bearing a nitro group at the 5-position did not proceed, and (*S*)-**13e** was not produced. Likewise, no reaction occurred with

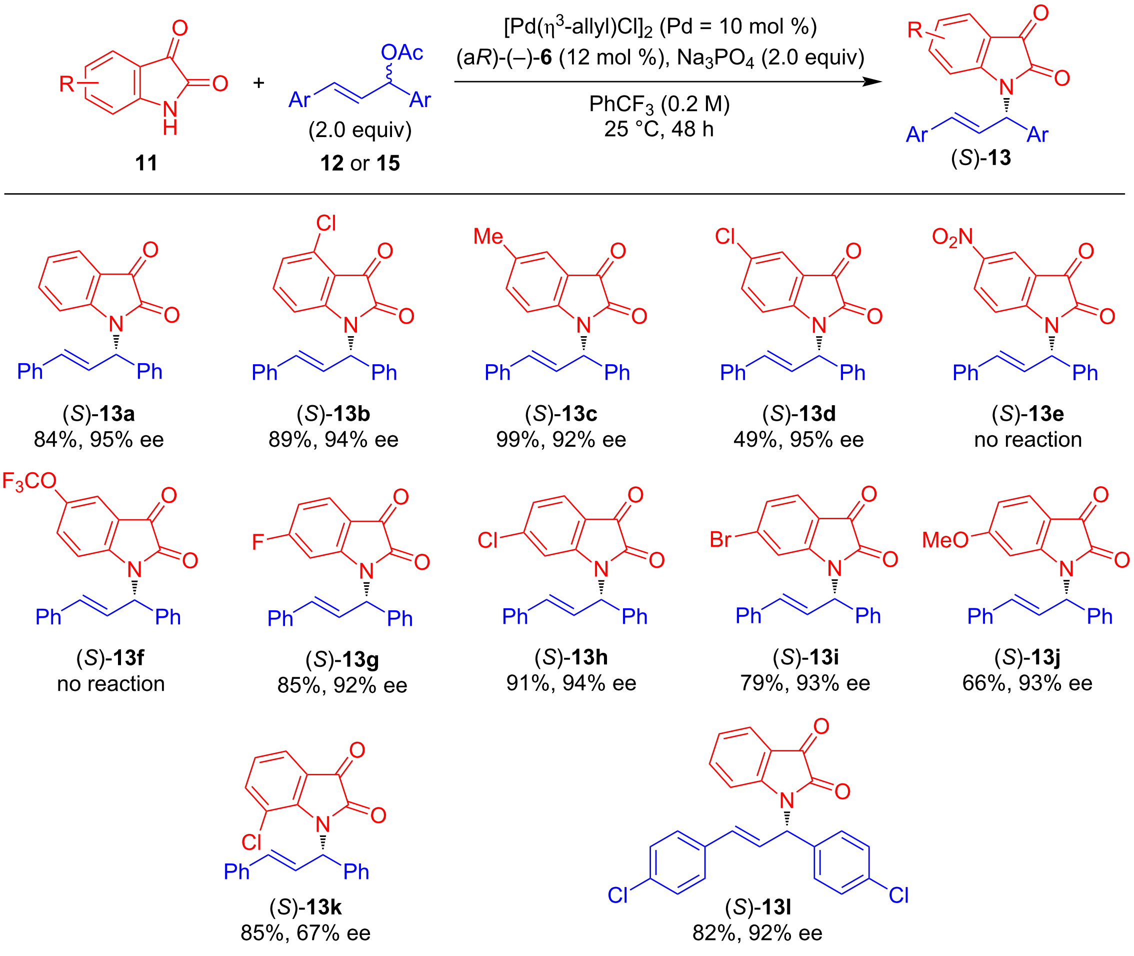

Scheme 2: Pd-catalyzed asymmetric allylic amination of acetate **12** (Ar = Ph) or **15** (Ar = *p*-ClC_6H_4) with isatin derivatives **11** using (a*R*)-(–)-**6** as a chiral ligand: The reaction was carried out at 0.1 mmol scale; yields refer to isolated yields.

a trifluoromethoxy-substituted derivative, resulting in no formation of (*S*)-**13f**. Reactions using isatin derivatives bearing halogen substituents at the 6-position proceeded efficiently, affording (*S*)-**13g–i** in good yields with high enantioselectivities. Conversely, the isatin derivative bearing a methoxy group at the 6-position led to a decreased yield for (*S*)-**13j**, though the enantioselectivity remained high. Additionally, we tested the reaction using an isatin derivative with a chloro group at the 7-position and obtained (*S*)-**13k** in good yield with moderate enantioselectivity. Furthermore, when (*E*)-1,3-di(*p*-chlorophenyl)-2-propenyl acetate (**15**) was utilized as an allylic acetate, the desired product (*S*)-**13l** was obtained in high yield with excellent enantioselectivity. We confirmed that the product **13** from the Pd-catalyzed asymmetric allylic amination of allyl esters with isatin using (a*R*)-(−)-**6** possesses an *S*-configuration. This stereochemical outcome follows the same reaction mechanism as the Pd-catalyzed asymmetric allylic substitution of allyl esters with indoles using (a*R*)-(−)-**6** [31]. To explore further applications of this product, we treated (*S*)-**13a** (94% ee) with malononitrile in the presence of $FeCl_3$ as a catalyst [36] and obtained the corresponding malononitrile derivative (*S*)-**16** without any loss of optical purity (Scheme 3).

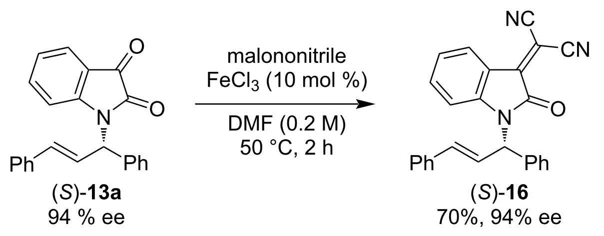

Scheme 3: Transformation of the reaction product (*S*)-**13a**: The reaction was carried out at 0.1 mmol scale and the yield refers to the isolated yield.

Conclusion

In this study, *N*-propyl-*N*-cinnamoylamide **7** was synthesized in three steps from phosphine oxide **8**. Chiral HPLC analysis confirmed its axial chirality at the C(aryl)–N(amide) bond. The optical resolution of (±)-**7** yielded (+)-**7** and (−)-**7**. The racemization barrier of (−)-**7** in *n*-dodecane was determined to be 25.0 kcal/mol at 25 °C, with a half-life of approximately 1.3 days. The chiral amides (a*R*)-(−)-**6** and (−)-**7** were evaluated as ligands in Pd-catalyzed asymmetric allylic amination, and while (−)-**7** exhibited promising enantioselectivity, its yield was lower than (a*R*)-(−)-**6**. Further optimization of reaction conditions led to improved yields and enantioselectivities up to 95% ee. Moreover, the reaction was successfully scaled up to 1 mmol. The substrate scope was investigated using various isatin derivatives, yielding high enantioselectivities (up to 95% ee) for most, except for those bearing certain electron-withdrawing groups. Additionally, we demonstrated the further conversion of (*S*)-**13a** into the malononitrile derivative (*S*)-**16** without loss of optical purity.

Supporting Information

Data of thermal racemization of **7**, DFT calculations for investigating racemization mechanism of **7**, general methods and materials, experimental procedures and characterization data, ^{1}H, ^{13}C and ^{31}P NMR spectra for **9** and **10**, ^{1}H, ^{13}C and ^{31}P NMR spectra and HPLC charts for (±)-**7**, (+)-**7** and (–)-**7**, ^{1}H and ^{13}C NMR spectra and HPLC charts for (*S*)-**13a**–**k** (except (*S*)-**13e**) and (*S*)-**16**.

Supporting Information File 1

Experimental section and compounds characterization.
[https://www.beilstein-journals.org/bjoc/content/supplementary/1860-5397-21-83-S1.pdf]

Funding

This work was supported by a Grant-in-Aid for Scientific Research (C) (No. JP22K05107) to TM and for Wakate (No. JP23K13741) to KW from Japan Society for the Promotion of Science (JSPS).

Author Contributions

Natsume Akimoto: investigation. Kaho Takaya: investigation. Yoshio Kasashima: investigation. Kohei Watanabe: investigation. Yasushi Yoshida: investigation. Takashi Mino: conceptualization; supervision.

ORCID® iDs

Yoshio Kasashima - https://orcid.org/0000-0002-6224-4495
Kohei Watanabe - https://orcid.org/0000-0002-3146-5439
Yasushi Yoshida - https://orcid.org/0000-0002-3498-3696
Takashi Mino - https://orcid.org/0000-0003-1588-1202

Data Availability Statement

All data that supports the findings of this study is available in the published article and/or the supporting information of this article.

References

1. Ye, N.; Chen, H.; Wold, E. A.; Shi, P.-Y.; Zhou, J. *ACS Infect. Dis.* **2016,** *2,* 382–392. doi:10.1021/acsinfecdis.6b00041
2. Santos, M. M. M. *Tetrahedron* **2014,** *70,* 9735–9757. doi:10.1016/j.tet.2014.08.005
3. Williams, R. M.; Cox, R. J. *Acc. Chem. Res.* **2003,** *36,* 127–139. doi:10.1021/ar020229e
4. Shmidt, M. S.; Reverdito, A. M.; Kremenchuzky, L.; Perillo, I. A.; Blanco, M. M. *Molecules* **2008,** *13,* 831–840. doi:10.3390/molecules13040831

5. Coppola, G. M. *J. Heterocycl. Chem.* **1987,** *24,* 1249–1251. doi:10.1002/jhet.5570240503
6. Imanzadeh, G.; Soltanizadeh, Z.; Khodayari, A.; Zamanloo, M.; Mansoori, Y.; Salehzadeh, J. *Chin. J. Chem.* **2012,** *30,* 891–899. doi:10.1002/cjoc.201100351
7. Imanzadeh, G. H.; Mollaei Tavana, M.; Zamanloo, M. R.; Mansoori, Y. *Chin. J. Chem.* **2009,** *27,* 389–396. doi:10.1002/cjoc.200990064
8. Cheng, Y.; Li, Z. *J. Heterocycl. Chem.* **2020,** *57,* 3574–3583. doi:10.1002/jhet.4075
9. Žari, S.; Metsala, A.; Kudrjashova, M.; Kaabel, S.; Järving, I.; Kanger, T. *Synthesis* **2015,** *47,* 875–886. doi:10.1055/s-0034-1379956
10. Žari, S.; Kudrjashova, M.; Pehk, T.; Lopp, M.; Kanger, T. *Org. Lett.* **2014,** *16,* 1740–1743. doi:10.1021/ol500421k
11. Yang, W.; Du, D.-M. *Chem. Commun.* **2013,** *49,* 8842–8844. doi:10.1039/c3cc44930k
12. Deepthi, K. L.; Subhashini, N. J. P.; Maneshwar, T. *Asian J. Chem.* **2022,** *34,* 1097–1104. doi:10.14233/ajchem.2022.23561
13. Andreev, I. A.; Manvar, D.; Barreca, M. L.; Belov, D. S.; Basu, A.; Sweeney, N. L.; Ratmanova, N. K.; Lukyanenko, E. R.; Manfroni, G.; Cecchetti, V.; Frick, D. N.; Altieri, A.; Kaushik-Basu, N.; Kurkin, A. V. *Eur. J. Med. Chem.* **2015,** *96,* 250–258. doi:10.1016/j.ejmech.2015.04.022
14. Zhang, X.; Zhang, J.-Q.; Sun, Z.-H.; Shan, H.-M.; Su, J.-C.; Ma, X.-P.; Su, G.-F.; Xu, L.-P.; Mo, D.-L. *Angew. Chem., Int. Ed.* **2025,** *64,* e202420390. doi:10.1002/anie.202420390
15. Li, J.-J.; Zeng, X.-X.; Kuang, X.; Shen, H.-C.; Wang, P.; Yu, J.-Q. *J. Am. Chem. Soc.* **2025,** *147,* 6594–6603. doi:10.1021/jacs.4c15491
16. Chen, Z.; Liu, J.; Ou, W.; Kato, T.; Wang, Z.; Chen, Y.; Liu, Y.; Maruoka, K. *J. Org. Chem.* **2024,** *89,* 12800–12811. doi:10.1021/acs.joc.4c01334
17. Gavrilov, K. N.; Chuchelkin, I. V.; Trunina, V. M.; Gavrilov, B. K.; Firsin, I. D.; Rud, E. S.; Tafeenko, V. A.; Bermesheva, E. V. *Russ. Chem. Bull.* **2024,** *73,* 574–579. doi:10.1007/s11172-024-4167-0
18. Gavrilov, K. N.; Chuchelkin, I. V.; Gavrilov, V. K.; Firsin, I. D.; Trunina, V. M.; Shiryaev, A. A.; Shkirdova, A. O.; Bermesheva, E. V.; Tafeenko, V. A.; Chernyshev, V. V.; Zimarev, V. S.; Goulioukina, N. S. *Org. Biomol. Chem.* **2024,** *22,* 6362–6369. doi:10.1039/d4ob00840e
19. Gavrilov, K. N.; Chuchelkin, I. V.; Firsin, I. D.; Trunina, V. M.; Gavrilov, V. K.; Zheglov, S. V.; Fedorov, D. A.; Tafeenko, V. A.; Zamilatskov, I. A.; Zimarev, V. S.; Goulioukina, N. S. *Org. Biomol. Chem.* **2024,** *22,* 538–549. doi:10.1039/d3ob01891a
20. Liu, M.; Zhang, X.; Bao, R.; Xiao, F.; Cen, S.; Zhang, Z. *Org. Lett.* **2023,** *25,* 5946–5950. doi:10.1021/acs.orglett.3c01972
21. Gavrilov, K. N.; Chuchelkin, I. V.; Shiryaev, A. A.; Firsin, I. D.; Trunina, V. M.; Gavrilov, V. K.; Bityak, Y. P.; Fedorov, D. A.; Zimarev, V. S.; Goulioukina, N. S. *Mendeleev Commun.* **2023,** *33,* 776–778. doi:10.1016/j.mencom.2023.10.012
22. Feng, B.; Fang, P.-W.; Lan, G.-M.; Peng, L.-Y.; Liang, L.-F.; You, G.-Y. *Org. Biomol. Chem.* **2022,** *20,* 7415–7418. doi:10.1039/d2ob01249a
23. Gavrilov, K. N.; Chuchelkin, I. V.; Gavrilov, V. K.; Zheglov, S. V.; Firsin, I. D.; Trunina, V. M.; Zamilatskov, I. A.; Tyurin, V. S.; Tafeenko, V. A.; Chernyshev, V. V.; Zimarev, V. S.; Goulioukina, N. S. *New J. Chem.* **2022,** *46,* 1751–1762. doi:10.1039/d1nj05143a
24. Gavrilov, K. N.; Chuchelkin, I. V.; Trunina, V. M.; Firsin, I. D.; Bityak, Y. P.; Fedorov, D. A.; Zimarev, V. S.; Goulioukina, N. S. *Russ. J. Gen. Chem.* **2022,** *92,* 2612–2619. doi:10.1134/s1070363222120088
25. Firsin, I. D.; Chuchelkin, I. V.; Gavrilov, V. K.; Trunina, V. M.; Zimarev, V. S.; Zheglov, S. V.; Gavrilov, K. N.; Goulioukina, N. S. *Phosphorus, Sulfur Silicon Relat. Elem.* **2022,** *197,* 518–519. doi:10.1080/10426507.2021.1989691
26. Lynch, C. C.; Balaraman, K.; Wolf, C. *Org. Lett.* **2020,** *22,* 3180–3184. doi:10.1021/acs.orglett.0c00936
27. Liu, Z.-S.; Hua, Y.; Gao, Q.; Ma, Y.; Tang, H.; Shang, Y.; Cheng, H.-G.; Zhou, Q. *Nat. Catal.* **2020,** *3,* 727–733. doi:10.1038/s41929-020-0494-1
28. Mino, T.; Youda, J.; Ebisawa, T.; Shima, Y.; Nishikawa, K.; Yoshida, Y.; Sakamoto, M. *J. Oleo Sci.* **2018,** *67,* 1189–1199. doi:10.5650/jos.ess17260
29. Mino, T.; Nishikawa, K.; Asano, M.; Shima, Y.; Ebisawa, T.; Yoshida, Y.; Sakamoto, M. *Org. Biomol. Chem.* **2016,** *14,* 7509–7519. doi:10.1039/c6ob01354f
30. Mino, T.; Yamaguchi, D.; Masuda, C.; Youda, J.; Ebisawa, T.; Yoshida, Y.; Sakamoto, M. *Org. Biomol. Chem.* **2019,** *17,* 1455–1465. doi:10.1039/c9ob00075e
31. Mino, T.; Takaya, K.; Koki, K.; Akimoto, N.; Yoshida, Y.; Kasashima, Y.; Sakamoto, M. *Org. Biomol. Chem.* **2023,** *21,* 2775–2778. doi:10.1039/d3ob00224a
32. Mino, T.; Tanaka, Y.; Sakamoto, M.; Fujita, T. *Tetrahedron: Asymmetry* **2001,** *12,* 2435–2440. doi:10.1016/s0957-4166(01)00426-8
33. Cooke, A. S.; Harris, M. M. *J. Chem. Soc. C* **1967,** 988–992. doi:10.1039/j39670000988
34. Cagle, F. W., Jr.; Eyring, H. *J. Am. Chem. Soc.* **1951,** *73,* 5628–5630. doi:10.1021/ja01156a038
35. Eyring, H. *Chem. Rev.* **1935,** *17,* 65–77. doi:10.1021/cr60056a006
36. Huang, L.-S.; Lai, Y.-H.; Yang, C.; Xu, D.-Z. *Appl. Organomet. Chem.* **2019,** *33,* e4910. doi:10.1002/aoc.4910

License and Terms

The definitive version of this article is the electronic one which can be found at:
https://doi.org/10.3762/bjoc.21.83

BEILSTEIN JOURNAL OF ORGANIC CHEMISTRY

Advances in nitrogen-containing helicenes: synthesis, chiroptical properties, and optoelectronic applications

Meng Qiu, Jing Du, Nai-Te Yao, Xin-Yue Wang and Han-Yuan Gong*

Review

Open Access

Address:
College of Chemistry, Beijing Normal University, Xinjiekouwaidajie 19,
Beijing, 100875, China

Email:
Han-Yuan Gong* - hanyuangong@bnu.edu.cn

* Corresponding author

Keywords:
azahelicene; chiroptical properties; circularly polarized luminescence (CPL); heteroatom containing; optoelectronic applications

Beilstein J. Org. Chem. **2025,** *21,* 1422–1453.
https://doi.org/10.3762/bjoc.21.106

Received: 28 April 2025
Accepted: 26 June 2025
Published: 11 July 2025

This article is part of the thematic issue "Non-central chirality in organic chemistry".

Associate Editor: N. Yoshikai

Abstract

Helicenes, a class of non-planar polycyclic aromatic hydrocarbons composed of *ortho*-fused aromatic rings forming helical architectures, have attracted considerable attention due to their intrinsic chirality and tunable optoelectronic properties. Among them, nitrogen-doped helicenes (azahelicenes) and their heteroatom-co-doped counterparts – such as B/N-, O/N-, S/N-, and Se/N-doped helicenes – have emerged as highly versatile scaffolds for chiral optoelectronic applications. The incorporation of nitrogen enables precise modulation of electronic structures, redox characteristics, and intermolecular interactions, thereby enhancing performance in circularly polarized luminescence (CPL), thermally activated delayed fluorescence (TADF), and chiral sensing. Notably, recent developments have yielded π-extended, structurally robust, and stimuli-responsive azahelicenes exhibiting record-high dissymmetry factors ($|g_{\mathrm{abs}}|$ and $|g_{\mathrm{lum}}|$), elevated CPL brightness (B_{CPL}), and efficient integration into CPL-OLEDs and redox-switchable emitters. Boron–nitrogen co-doping strategies, in particular, have facilitated the development of materials with ultra-narrowband emissions, near-unity photoluminescence quantum yields, and electroluminescence dissymmetry factors ($|g_{\mathrm{EL}}|$) exceeding 10^{-3}. Likewise, heteroatom co-doping with oxygen, sulfur, or selenium enables spectral tuning across the visible to near-infrared range, improved photostability, and dual-state emissive behavior. In parallel, significant progress in synthetic methodologies – including enantioselective catalysis, electrochemical cyclizations, and multicomponent reaction systems – has granted access to increasingly complex helicene frameworks with well-defined chirality. This review systematically summarizes recent advancements in the synthesis, structural engineering, and chiroptical performance of nitrogen-doped helicenes and their heteroatom-doped derivatives, emphasizing their potential as next-generation chiral optoelectronic materials and outlining future directions toward multifunctional integration and quantum technological applications.

Introduction

Helicenes, a class of non-planar polycyclic aromatic hydrocarbons characterized by *ortho*-fused aromatic rings forming a helical framework, have attracted significant attention due to their inherent chirality, unique optoelectronic properties, and wide-ranging applications in asymmetric catalysis [1,2], molecular recognition [3], and organic electronics [4,5]. In recent years, the incorporation of heteroatoms – particularly nitrogen – into the helicene backbone, giving rise to so-called "azahelicenes", has emerged as a powerful strategy to modulate electronic structures, enhance solubility, and expand functional diversity [6]. Substituting carbon atoms with electron-deficient nitrogen atoms introduces new opportunities to fine-tune redox potentials, charge-transport behavior, and intermolecular interactions [7]. These modifications have proven especially valuable in applications such as organic light-emitting diodes (OLEDs) [8], circularly polarized luminescence (CPL) [9], and chiral photocatalysis [10]. In the past decade, heteroatom-containing helicenes have attracted increasing attention due to their tunable optoelectronic properties and potential applications in chiral optoelectronics. Several comprehensive reviews have examined specific classes of these molecules. Crassous and co-workers provided a detailed overview of heterohelicenes up to 2019, focusing on their structural diversity and functional applications [11]. Nowak-Król and colleagues reviewed boron-doped helicenes, emphasizing their roles in chiral materials design [12], while Maeda and Ema explored the circularly polarized luminescence (CPL) properties of azahelicenes [13]. However, despite these valuable contributions, a dedicated and up-to-date overview of nitrogen-doped helicenes – particularly those incorporating additional heteroatoms within the helical π-conjugated framework – remains lacking.

This review addresses this gap by systematically summarizing recent advances (from the past five years) in the synthesis, structural modification, and chiroptical properties of nitrogen-doped helicenes. Particular attention is given to multi-heteroatom systems co-doped with elements such as boron, oxygen, sulfur, and selenium, highlighting their influence on CPL performance and structure–property relationships. We classify the nitrogen-doped helicenes into only N-containing helicenes, B,N-containing helicenes, and X,N-containing helicenes (X = O, S or Se). In each section, structurally similar compounds are categorized into groups to facilitate comparison. Then, the others are discussed in chronological order based on their reported publication dates, with attribution to the respective research groups. Notably, helicenes bearing nitrogen atoms located outside the conjugated system are excluded from this discussion to maintain a consistent focus on electronically integrated heteroatom-doped architectures.

Review

N-Containing helicenes

Among nitrogen-containing helicenes, HBC-fused azahelicenes represent a particularly significant subclass due to their extended π-conjugation and potential for enhanced chiroptical properties. Over the past few years, multiple research groups have investigated their synthesis, structural characteristics, and optoelectronic behavior. Notably, in 2021, Jux and co-workers reported a series of superhelicenes that combine helical and planar π-systems. However, the structural characterization of compound **1** (Table 1) was impeded by its inherent instability, limiting further analysis [14]. In 2024, Liu's group developed a series of nonalternant nanographenes **2a–c** featuring a nitrogen-embedded cyclopenta[*ef*]heptalene core [15]. These compounds exhibit λ_{abs} at 363, 452, and 580 nm, and PLQYs of 0.05, 0.33, and 0.32, respectively. While compounds **2a** and **2b** display broad emission near 505 nm, **2c** shows dual-emission peaks at 588 and 634 nm with an ultranarrow FWHM of 22 nm. Notably, **2b** and **2c** demonstrate strong chiroptical activity with $|g_{abs}|$ values of 6.7×10^{-3} and 1.0×10^{-2}, $|g_{lum}|$ of 2.4×10^{-3} and 7.0×10^{-3}, and B_{CPL} values of 9.1 and 95.2 $M^{-1}\ cm^{-1}$, respectively. Shortly thereafter, Gong's group further expanded the π-system by constructing a tris-hexabenzo[7]helicene **3** with a carbazole core, which emits at 595/628 nm (PLQY = 0.40), displays $|g_{abs}| = 2.98 \times 10^{-3}$, and achieves a B_{CPL} of 32.5 $M^{-1}\ cm^{-1}$ [16]. In 2025, Babu's group synthesized two regioisomeric π-extended azahelicenes, **4a** and **4b**, which differ in the position of attachment to the carbazole core [17]. Compared to **4a**, compound **4b** exhibits bathochromic shifts of 12 nm in absorption and 45 nm in emission, as well as a higher Φ_F (0.75 vs 0.68). Both isomers display TADF at room temperature and phosphorescence at 77 K. Notably, **4a** demonstrates a long-lived red afterglow persisting for up to 30 seconds. In contrast, **4b** exhibits superior chiroptical properties, with $|g_{abs}|$ and $|g_{lum}|$ values of 3.91×10^{-3} and 1.12×10^{-3}, respectively, and an impressive B_{CPL} of 45.77 $M^{-1}\ cm^{-1}$ (Table 1).

In 2021, several research groups reported structurally diverse heterohelicene systems exhibiting distinctive chiroptical and photophysical properties, highlighting the expanding potential of these molecules in chiral optoelectronics. Yorimitsu's group developed a series of dihetero[8]helicenes through a systematic asymmetric synthesis. Among these, diaza[8]helicene **5** exhibited pronounced chiroptical activity, with absorption and emission maxima (λ_{abs} = 399 nm, λ_{em} = 405 nm), a fluorescence quantum yield (Φ_F) of 0.13, and high dissymmetry factors ($|g_{abs}| = 1.9 \times 10^{-2}$, $|g_{abs}| = 9.5 \times 10^{-3}$ at 403 nm) [18] (Table 2). Miura and co-workers employed Pd(II)/Ag(I)-catalyzed cyclizations to construct azahelicenes, with compound **6** exhibiting enhanced chiroptical performance and protonation-

Table 1: Structures and optical properties of compounds **1**, **2a–c**, **3**, and **4a**,**b**.[a]

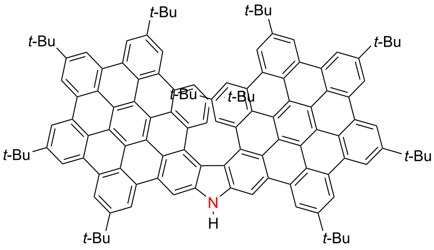

1

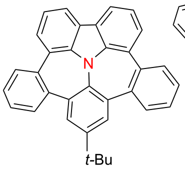

2a

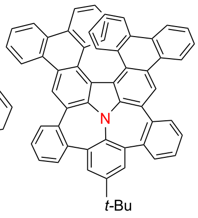

2b

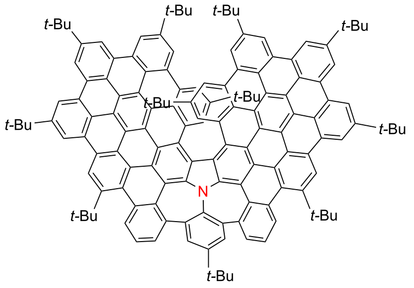

2c

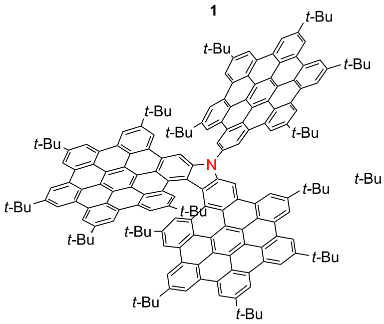

3

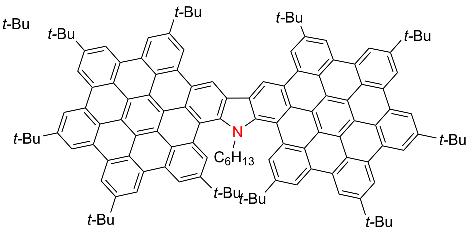

4a

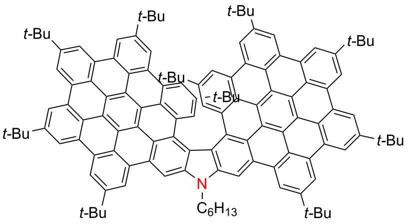

4b

compound	$\lambda_{abs(max)}$ [nm]	λ_{em} [nm]	Φ_F	$\lvert g_{abs}\rvert$	$\lvert g_{lum}\rvert$	B_{CPL} [M^{-1} cm^{-1}]
2a	363	508	0.05	–	–	–
2b	452	503	0.33	6.7×10^{-3}	2.4×10^{-3}	9.1
2c	580	588, 634	0.32	1.0×10^{-2}	7.0×10^{-3}	95.2
3	525	595, 628	0.40	2.98×10^{-3}	4.3×10^{-4}	32.5
4a	497	497, 531, 570	0.677	–	–	–
4b	522	542, 581, 630	0.754	3.91×10^{-3}	1.12×10^{-3}	45.77

[a] Compound **1** is unstable and characterized only by mass spectrometry.

induced CPL amplification [19]. Meanwhile, Audisio's team developed heterohelicenes via regioselective [3 + 2]-cycloadditions, with compound **7** displaying pH-responsive CPL sign inversion ($|g_{lum}| = +1.1 \times 10^{-3}$ at 430 nm, -1.2×10^{-3} at 585 nm) attributed to reversible intramolecular charge transfer [20]. In parallel, several groups explored the functional versatility of heterohelicenes in device-oriented and sensing applications. Crassous's group synthesized bipyridine-embedded helicenes via the Mallory reaction, enabling coordination with Ru(II) to form NIR-emissive complexes that exhibit redox-responsive chiroptical switching, notably with complex **8** showing reversible electronic circular dichroism (ECD) upon oxidation [21]. Liao and co-workers introduced a narrowband CP-TADF emitter **9**, characterized by a narrow emission bandwidth (FWHM = 36 nm), $|g_{lum}| = 1.1 \times 10^{-3}$, $|g_{EL}| = 1.5 \times 10^{-3}$, and an external quantum efficiency (EQE) of 0.14 – demonstrating promise for CPL-OLED applications [22]. Wanichacheva's team reported urazole-functionalized aza[5]helicene **10**, exhibiting selective Fe(III) sensing, marked solvatochromism, and a large Stokes shift (85 nm) with emission at 530 nm in DMSO [23] (Table 2). Collectively, these studies underscore the structural versatility and functional tunability of heterohelicenes, establishing them as robust platforms for advanced chiral optoelectronic materials. Their diverse response to external stimuli, modular synthetic accessibility, and strong CPL performance render them ideal candidates for applications in molecular sensing, stimuli-responsive switches, and next-generation CPL-active devices.

In 2021, Ema's group reported the synthesis of carbazole-based azahelicenes **11a–e** via intramolecular Scholl reactions [24] (Table 3). All compounds exhibited strong absorption in the UV–vis region (250–450 nm) and fluorescence emission between 400–550 nm. Among these, compound **11c**, a saddle-shaped dibenzodiaza[8]circulene, was particularly noteworthy as the first example of its kind synthesized in solution and structurally confirmed via single-crystal X-ray diffraction. It demon-

Table 2: Structures and optical properties of compounds **5**–**10**.

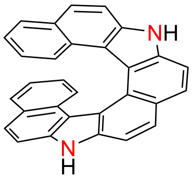

5

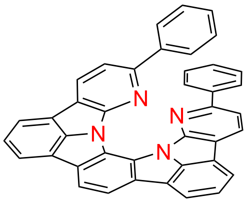

6

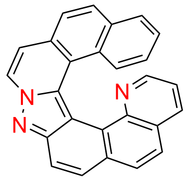

7

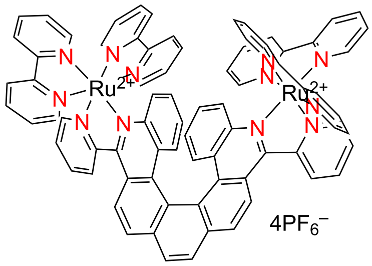

8

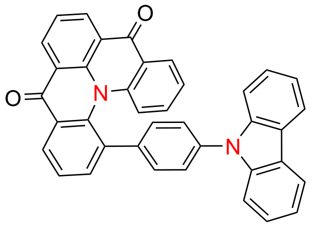

9

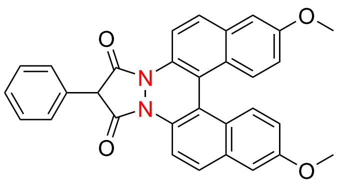

10

compound	$\lambda_{abs(max)}$ [nm]	λ_{em} [nm]	Φ_F	$\lvert g_{abs}\rvert$	$\lvert g_{lum}\rvert$
5	399	405, 430, 460	0.13	1.9×10^{-2}	9.5×10^{-3}
6	405	420, 439	0.14	1.1×10^{-2}	4.4×10^{-3}
7	430	436, 460, 500	0.10	–	1.1×10^{-3}
8 (*M*,*Λ*,*Λ*)	522	788	0.10	–	–
(*P*,*Λ*,*Λ*)	512	786	0.25	–	–
9	440	467	0.47[a]	–	1.1×10^{-3}
10	400	485	–	–	–

[a] As detected in film.

strated the highest CPL performance among the series, with a $|g_{lum}|$ value of 3.5×10^{-3} and a photoluminescence quantum yield (PLQY) of 0.31, indicating its potential as a chiral emissive material. Building upon this foundation, the same group in 2024 developed a series of structurally refined aza[7]helicenes (compounds **12a** and **12b**) under modified Scholl reaction conditions [25]. These products were obtained as optically active diastereomers, which were successfully separated using silica gel chromatography. Additionally, two cyclic dimers, designated as compounds **12c** and **12d**, were isolated, exhibiting strong absorption bands at 493 and 474 nm, high PLQYs of 0.61 and 0.54, and notable CPL activity ($|g_{lum}| = 0.74 \times 10^{-3}$ and 1.3×10^{-3}, respectively), with corresponding brightness values (B_{CPL}) reaching 19 and 31 M^{-1} cm^{-1} (Table 3). Importantly, both dimers displayed selective fluoride ion recognition through hydrogen bonding, with (*M*,*M*)-**12c** exhibiting a high binding constant ($K_a = 2 \times 10^5$ M^{-1}). The resulting [**12c·F**$^-$] and [**12d·F**$^-$] complexes exhibited red-shifted circular dichroism (CD), fluorescence, and CPL spectra, underscoring the capability of helicene-based frameworks for anion-responsive chiroptical modulation. These findings highlight how precise structural design and supramolecular engineering can facilitate the development of high-performance, stimuli-responsive chiral luminophores.

In 2022, Zhang and co-workers reported a nitrogen-embedded quintuple [7]helicene **13**, constructed by hybridizing helicene and azacorannulene π-systems [26] (Table 4). Compound **13** exhibited distinct absorption bands at 408, 611, and 715 nm, with strong near-infrared (NIR) fluorescence centered at 770 nm and a PLQY value of 0.28. Upon coordination with tris(4-bromophenyl)aminium hexachloroantimonate (BAHA), a new absorption band emerged around 900 nm, extending to 1300 nm, indicative of charge-transfer processes. The enantiomers of **13** displayed mirror-image CD signals and showed excellent dispersibility in polar solvents, highlighting their potential for NIR bio-imaging applications. In parallel, Církva's group synthesized a series of aza[*n*]helicenes **14a**–**d** via photocyclodehydrochlorination [27]. These compounds exhibited dual fluorescence bands, with emission red-shifting progressively with increasing helical length. Protonation further induced red-shifted emission, with compound **14d**-H$^+$ emitting at

Table 3: Structures and optical properties of **11a–e** and **12a–d**.

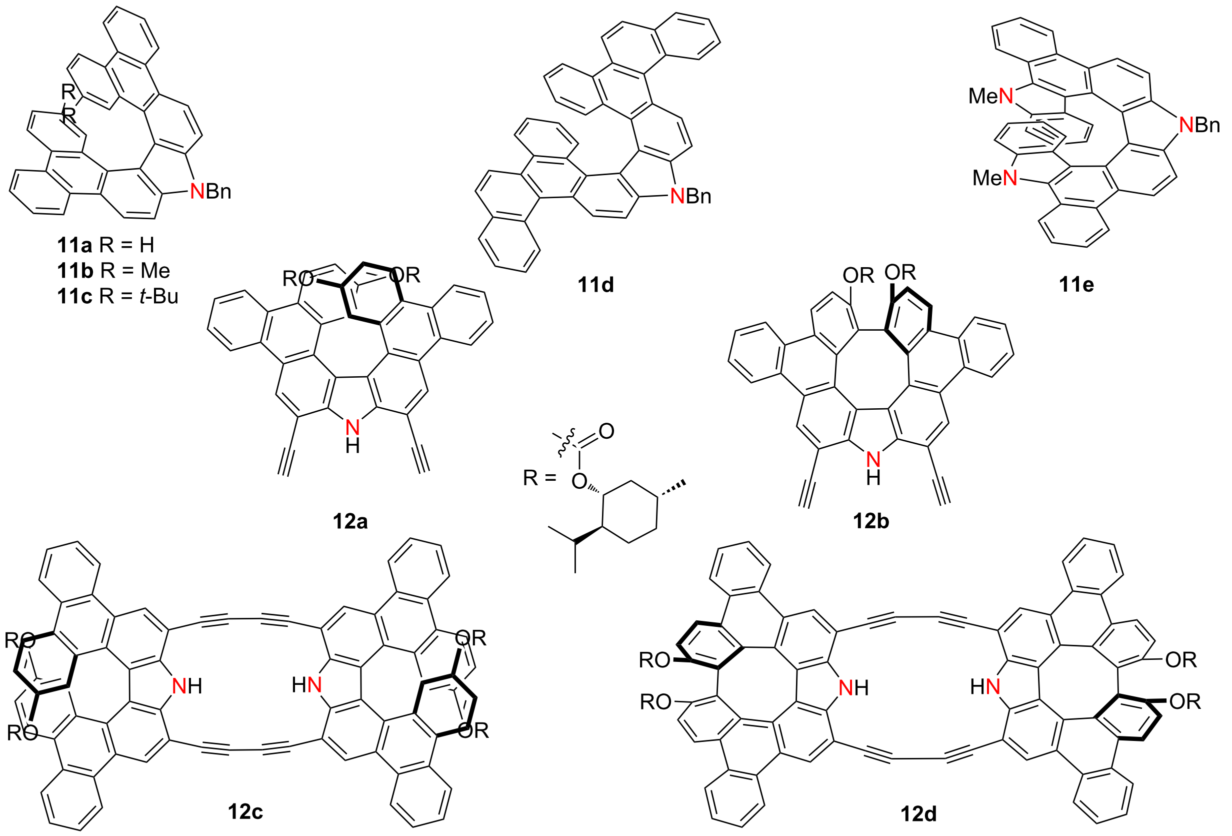

compound	$\lambda_{abs(max)}$ [nm]	λ_{em} [nm]	Φ_F	$\lvert g_{abs}\rvert$	$\lvert g_{lum}\rvert$	B_{CPL} [M^{-1} cm^{-1}]
11a	418	432, 454	0.28	4.9×10^{-3}	3.2×10^{-3}	–
11b	419	432, 455	0.27	5.9×10^{-3}	3.4×10^{-3}	–
11c	419	432, 456	0.31	5.4×10^{-3}	3.5×10^{-3}	–
11d	422	458, 480	0.10	3.2×10^{-3}	3.9×10^{-4}	–
11e	412	456	0.24	4.5×10^{-4}	2.9×10^{-4}	–
12a	436	447, 474	0.45	4.8×10^{-3}	2.6×10^{-3}	6.7
12b	423	431, 456	0.32	3.8×10^{-3}	2.2×10^{-3}	2.8
12c	494	502, 536	0.64	2.4×10^{-3}	6.5×10^{-4}	19
12d	475	485, 514	0.54	2.7×10^{-3}	1.4×10^{-3}	31

542 nm. However, PLQYs decreased significantly from 0.078 to 0.006 with longer helicenes. The CD spectra of **14c** and **14d** were found to resemble their carbohelicene analogues, underscoring the structural fidelity and chiroptical retention upon nitrogen incorporation. Qian's group developed a series of azahelicenes **15a–d** through Bischler–Napieralski cyclization [28]. Notably, compound **15b** displayed a high interconversion barrier of 36.0 kcal mol^{-1}, enabling enantiomeric resolution. All compounds exhibited visible-range fluorescence (400–500 nm) and structured UV–vis absorption spectra. Importantly, **15b** showed acid/base-switchable UV and CD spectra, suggesting potential for use in responsive optoelectronic systems. Hu's group reported an X-shaped double [7]helicene **16** functionalized with four triazole units, which demonstrated absorption at 368 and 516 nm, strong emission at 553 nm, a high PLQY of 0.96, $|g_{abs}|$ of 1.1×10^{-2}, $|g_{lum}|$ of 9.1×10^{-4}, and B_{CPL} of 30.1 M^{-1} cm^{-1} – surpassing the performance of its all-carbon and thiadiazole counterparts [29]. In a related study, Hu's team synthesized double aza[5]helicenes **17a** and **17b**, among which compound **17b** exhibited red-shifted emission (538–632 nm in $CHCl_3$) and the largest Stokes shift (192 nm), attributed to extended conjugation and sulfur incorporation [30] (Table 4). These findings collectively underscore how structural modulation and heteroatom doping can tailor the optical, chiroptical,

Table 4: Structures and optical properties of **13**, **14a–d**, **15a–d**, **16**, and **17a**,**b**.

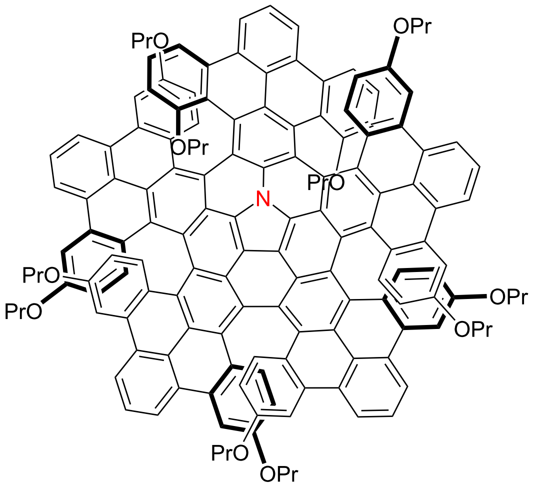

13

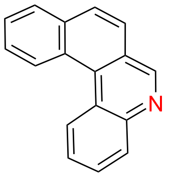

14a

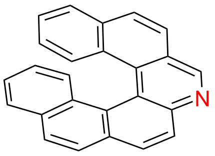

14c

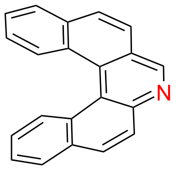

14b

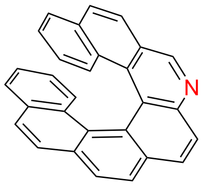

14d

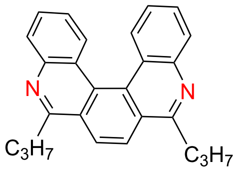

15a

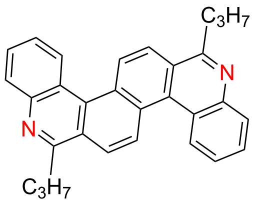

15c

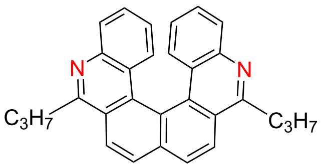

15b

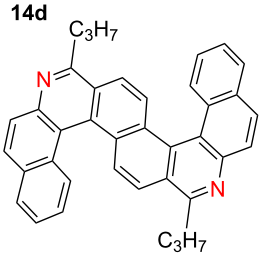

15d

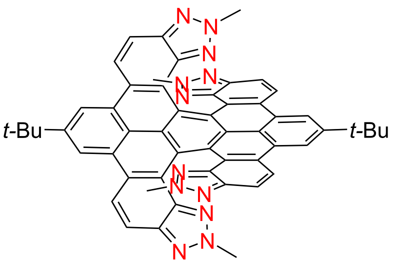

16

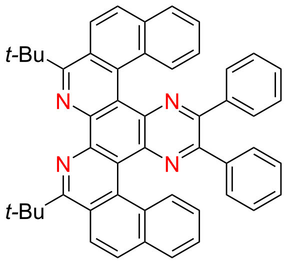

17a

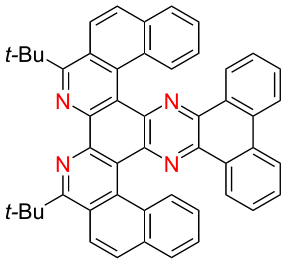

17b

compound	$\lambda_{abs(max)}$ [nm]	λ_{em} [nm]	Φ_F	$\lvert g_{abs} \rvert$	$\lvert g_{lum} \rvert$	B_{CPL} [M^{-1} cm^{-1}]
13	715	770	0.28	–	–	–
14a	313	380, 399	0.077	–	–	–
14b	302	410, 431	0.120	–	–	–
14c	311	421, 443	0.067	–	–	–
14d	337	443, 467	0.029	–	–	–
15a	398	408, 430	–	–	–	–
15b	404	408, 434	–	–	–	–
15c	407	413, 437	–	–	–	–
15d	424	434, 456	–	–	–	–
16	516	553	0.96	1.1×10^{-2}	9.1×10^{-4}	30.1
17a	328	458	0.010	–	–	–
17b	440	632	0.014	–	–	–

and stimuli-responsive behavior of azahelicenes, providing strategic design avenues for next-generation chiral optoelectronic materials.

In 2023, Langer's group synthesized a series of double aza[4,6]helicenes **18a–l** featuring diverse peripheral substituents through a one-pot, multistep synthetic protocol [31]

(Table 5). Selected compounds such as **18b**, **18c**, **18d** and **18l** exhibit similar λ_{abs} around 410 nm and emit fluorescence centered near 530 nm, demonstrating consistent optical profiles despite structural variation. In a parallel effort, Yang's group developed an efficient, enantioselective synthetic approach toward azahelicenes via a chiral phosphoric acid-catalyzed multicomponent Povarov reaction or oxidative aromatization [32]. Among the synthesized compounds, compound **19** displayed dual absorption bands at 260 and 325 nm and emission peaks at 420 and 440 nm, which red-shifted to approximately 500 nm upon trifluoroacetic acid treatment. Both the neutral and protonated forms of **19** exhibited mirror-image CD and CPL spectra, with high $|g_{lum}|$ values of 1.4×10^{-3} and 1.3×10^{-3}, respectively, underscoring their potential for responsive chiral optoelectronic applications. Concurrently, Liu [33] and Ishigaki's [34] groups independently reported a class of highly twisted nitrogen-doped heptalene derivatives (e.g., compound **20a**), which exhibit consistent absorption at 315 nm and blue fluorescence centered near 450 nm, regardless of the substituents. These compounds display redox and electronic behaviors reminiscent of nitrogen-doped azulenes, featuring strong absorption dissymmetry factors ($|g_{abs}|$) at 345 nm – 1.2×10^{-2} for compound **20a**, 1.0×10^{-2} for **20d**, and 1.3×10^{-2} for **20e** (Table 5). Notably, the radical cation form of compound **20e** (**20e**$^{\bullet+}$) exhibits pronounced CD signals extending into the near-infrared region, suggesting potential for redox-responsive chiral photonic systems.

In 2023, Chen's group reported three nitrogen–nitrogen (NN)-embedded azahelicenes **21a–c**, among which compound **21c**, a structurally defined antiaromatic double aza[7]helicene – exhibited distinctive long-wavelength optical and chiroptical properties [35] (Table 6). In the solid state, **21c** emitted in the far-red region at 641 nm ($\Phi_F = 0.10$) and demonstrated CPL with $|g_{lum}| = 2.04 \times 10^{-4}$. In solution, **21c** showed a strong absorption band at 560 nm and a high Φ_F value of 0.86 at 583 nm, yielding a B_{CPL} value of 13.2 M^{-1} cm^{-1}. Notably, compound **21c** undergoes reversible redox interconversion to its radical

Table 5: Structures and optical properties of **18a–l**,**19**, and **20a–e**.

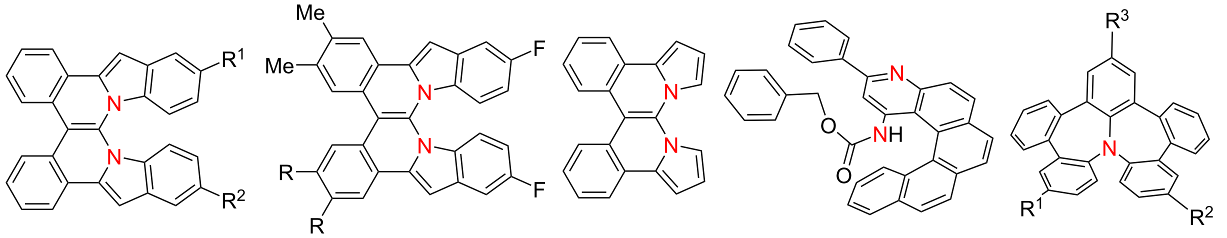

18a $R^1 = R^2 = F$
18b $R^1 = R^2 = H$
18c $R^1 = R^2 = CN$
18d $R^1 = R^2 = OMe$
18e $R^1 = R^2 = Cl$
18f $R^1 = F$, $R^2 = CN$
18g $R^1 = F$, $R^2 = OMe$
18h $R^1 = F$, $R^2 = H$
18i $R^1 = OMe$, $R^2 = CN$

18j R = H
18k R = Me

18l

19

20a $R^1 = R^2 = R^3 = H$
20b $R^1 = R^2 = H$, $R^3 = Cl$
20c $R^1 = R^2 = H$, $R^3 = t$-Bu
20d $R^1 = Br$, $R^2 = R^3 = H$
20e $R^1 = R^2 = Br$, $R^3 = H$

compound	$\lambda_{abs(max)}$ [nm]	λ_{em} [nm]	Φ_F	$\lvert g_{abs}\rvert$	$\lvert g_{lum}\rvert$
18b	411	530	0.15	–	–
18c	409	520	0.16	–	–
18d	419	525	0.17	–	–
18i	413	525	0.14	–	–
19	325	420, 440	–	–	1.4×10^{-3}
20a	315[a], 320[b]	447	–	1.2×10^{-2}	–
20b	315	459	–	–	–
20c	315	446	–	–	–
20d	320	–	–	1.0×10^{-2}	–
20e	321	–	–	1.3×10^{-2}	–

[a]Based on reports from Liu's group; [b]based on reports from Ishigaki's group.

Table 6: Structures and optical properties of **21a–c** and **22**.

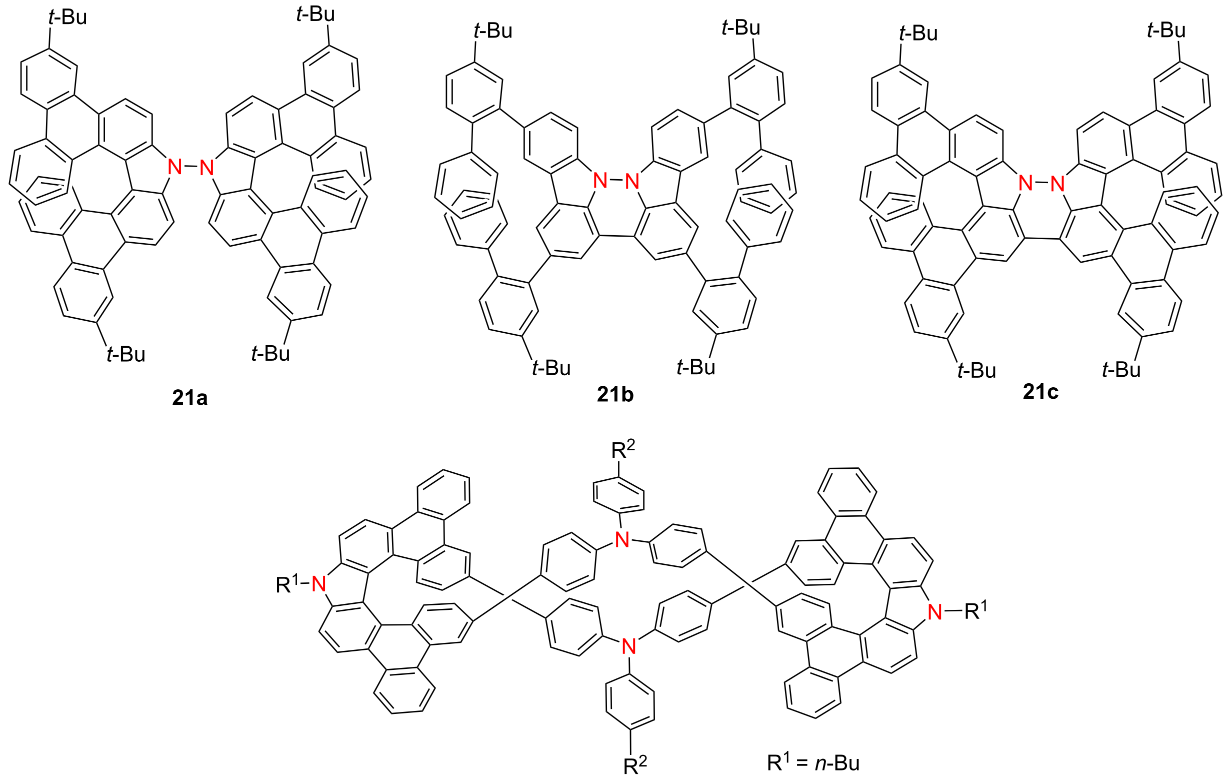

21a **21b** **21c**

22

R^1 = n-Bu
R^2 = t-Bu

compound	$\lambda_{abs(max)}$ [nm]	λ_{em} [nm]	Φ_F	$\lvert g_{abs}\rvert$	$\lvert g_{lum}\rvert$	B_{CPL} [M^{-1} cm^{-1}]
21a	408	423	0.26	9.78×10^{-4}	–	–
21a in film	≈410	449	0.15	–	–	–
21b	495	521	0.77	–	–	–
21b in film	≈500	548	0.63	–	–	–
21c	560	583	0.86	4.76×10^{-4}	2.22×10^{-4}	13.2
21c in film	≈570	641	0.10	–	2.04×10^{-4}	–
22	438	480	0.99	2.50×10^{-3}	5.00×10^{-3}	100.2

cation **21c**$^{\bullet+}$ and dicationic **21c**$^{2+}$ states via chemical oxidation, enabling controllable switching between antiaromatic and aromatic configurations. These results provide a compelling strategy for engineering redox-switchable chiral luminophores. In 2024, the same research group expanded on this redox-responsive platform by constructing a polycationic open-shell cyclophane **22**, comprising carbazole-embedded aza[7]helicene subunits [36]. Compound **22** displays intense fluorescence (Φ_F = 0.99), exceptionally high B_{CPL} as 100.2 M^{-1} cm^{-1}, and marked chiroptical activity ($|g_{abs}|$ = 2.50×10^{-3} at 435 nm; $|g_{lum}|$ = 5.00×10^{-3} at 460 nm) (Table 6). Upon mild oxidation, neutral **22** undergoes stepwise conversion into highly charged, multispin open-shell species **22**$^{2+2\bullet}$ and **22**$^{4+4\bullet}$, preserving strong chiroptical signals. This study presents a novel approach to constructing stable, redox-switchable chiral luminophores based on extended azahelicene architectures, offering broad potential for molecular electronics and spintronic devices.

In 2024, Qiu's group synthesized π-extended diaza[7]helicenes **23a–f** incorporating dual heptagonal rings [37]. Compound **23a** exhibits dynamic chirality, aggregation-induced emission (AIE), and intense CPL ($|g_{lum}|$ = 1.7×10^{-2}), whereas compound **23f**, with lateral π-extension, shows enhanced thermal stability and green emission at 517 nm (Table 7). Kuehne and co-workers reported two radical aza[7]helicenes, **24a** and **24b**, exhibiting distinct photophysical behaviors [38]. Compound **24b** features a higher PLQY (0.43), while **24a** demonstrates doublet-state CPL ($|g_{lum}|$ = 5.0×10^{-4}), highlighting the

Table 7: Structures and optical properties of **23a–f**, **24a**,**b**, **25a**,**b**, **26a**,**b**, **27a–d**, and **28a–e**.

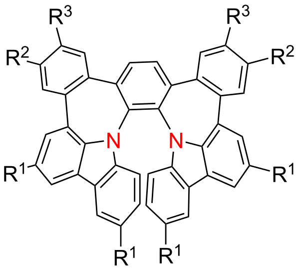

23a $R^1 = R^2 = R^3 = H$
23b $R^1 = R^3 = H$, $R^2 = CF_3$
23c $R^1 = R^2 = H$, $R^3 = CF_3$
23d R^1 = *t*-Bu, $R^2 = R^3 = H$
23e R^1 = *t*-Bu, $R^2 = CF_3$, $R^3 = H$

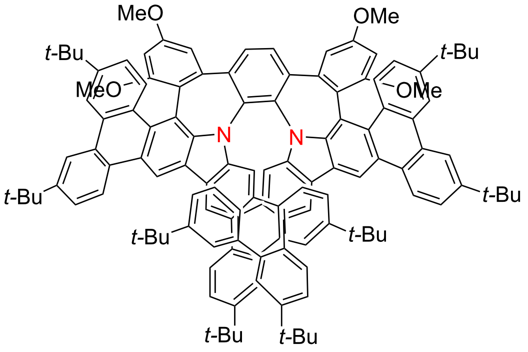

23f

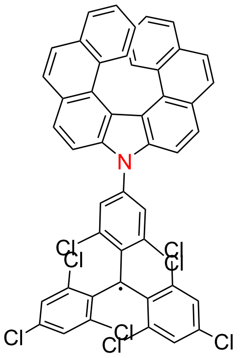

24a

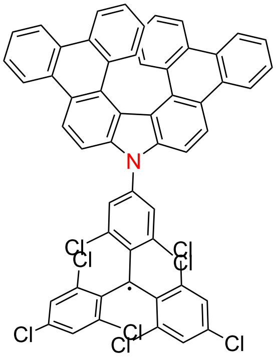

24b

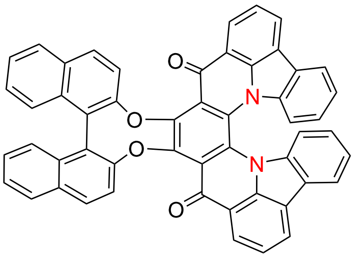

25a (*R*,*M*)
25b (*R*,*P*)

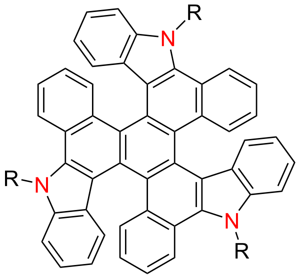

26a R = H
26b R = C_4H_9

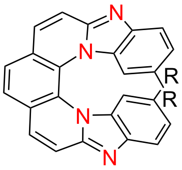

27a R =

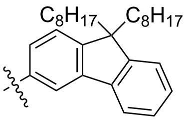

27b R =

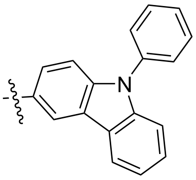

27c R =

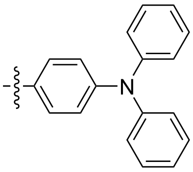

27d R =

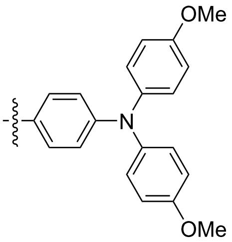

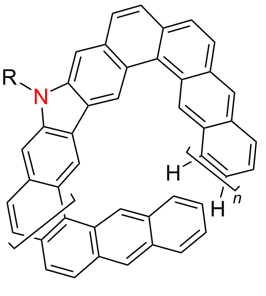

28a *n* = 1
28b *n* = 2
28c *n* = 3
28d *n* = 4
28e *n* = 5

compound	$\lambda_{abs(max)}$ [nm]	λ_{em} [nm]	Φ_F	$\lvert g_{abs} \rvert$	$\lvert g_{lum} \rvert$	B_{CPL} [M^{-1} cm^{-1}]
23a	360	625	–	–	1.7×10^{-2}[a]	–
23f	462	517	–	–	2.0×10^{-3}	–
24a	642	696	0.34	4.4×10^{-4}	5×10^{-4}	0.25
24b	655	712	0.43	1×10^{-4}	–	–
25a	506	525	0.57	1.7×10^{-2}	1.4×10^{-3}	8.94
25b	513	535	0.55	2.2×10^{-2}	8×10^{-4}	4.29
26a	388	506, 530	0.055	1.2×10^{-2}	3.0×10^{-3}	–
26b	393	508, 532	0.058	1.4×10^{-2}	3.2×10^{-3}	–
27a	483	524	0.38	–	–	–
27b	487	539	0.71	–	–	–

Table 7: Structures and optical properties of **23a–f**, **24a**,**b**, **25a**,**b**, **26a**,**b**, **27a–d**, and **28a–e**. (continued)

27c	459	590	0.24	–	–	–
27d	470	611	0.53	–	–	–
28a	414	496, 532	0.152	–	–	–
28b	≈475	511, 543	0.116	4.4×10^{-2}	3×10^{-3}	16
28c	≈475	522, 550	0.089	4.8×10^{-2}	1.4×10^{-2}	61
28d	≈475	530, 554	0.066	4.3×10^{-2}	2.1×10^{-2}	76
28e	≈475	530, 555	0.034	–	–	–

[a] In the aggregated state.

potential of helicene radicals for spintronic applications. Meng's group synthesized carbonyl-nitrogen embedded hetero[7]helicenes **25a** and **25b** bearing axial chirality [39]. Compound **25a** displays excellent optical characteristics with $\Phi_F = 0.57$, $|g_{abs}| = 1.7 \times 10^{-2}$, $|g_{lum}| = 1.4 \times 10^{-3}$, and a B_{CPL} of 8.94 M^{-1} cm^{-1}. Then, Chen's group contributed triple aza[6]helicenes **26a** and **26b** with $|g_{lum}|$ values of approximately 3.0×10^{-3}, offering new architectures for CPL-active helicenes [40]. Singh's group developed fluorophore-conjugated aza[7]helicenes **27a–d**, with **27b** demonstrating pronounced intramolecular charge transfer (ICT), a high Φ_F of 0.71 and an extended fluorescence lifetime (τ) of 15.5 ns [41]. Wu's group synthesized a family of expanded azahelicenes **28a–e**, where increasing helical length leads to red-shifted emission, prolonged lifetime, and attenuated PLQY [42]. Nonetheless, these compounds exhibit outstanding chiroptical performance, with $|g_{abs}|_{max}$ reaching 4.8×10^{-2}, $|g_{lum}|_{max} = 2.1 \times 10^{-2}$, and B_{CPL} values up to 76 M^{-1} cm^{-1}. Collectively, these investigations underscore the efficacy of heteroatom doping, extended π-conjugation, and radical design in advancing azahelicene-based systems. These approaches significantly enhance optical and chiroptical performance, paving the way for high-efficiency chiral optoelectronic and quantum materials.

In 2024, Kivala's group selectively synthesized highly distorted [6]helicenes **29a** and **29b** incorporating azocine units via a regioselective Beckmann rearrangement from oxime precursor **29c** [43] (Table 8). For comparative evaluation, the corresponding lactams **29d** and **29e** and amines **29f** and **29g** were also obtained. Compounds **29a** and **29b** exhibit λ_{abs} centered at 513 nm, while the amines **29f** and **29g** display high Φ_F values of 0.48 and 0.56, respectively. Notably, azocine derivative **29b** exhibits the highest CPL activity among the series, with a $|g_{lum}|$ value of 1.6×10^{-3}. In addition, both **29a** and **29b** demonstrate redox activity, undergoing reversible formation of radical anions, dianions, and radical cations. The radical cation $\mathbf{29b}^{\bullet+}$, in particular, exhibits a broad near-infrared (NIR) absorption band extending to 3000 nm, highlighting its potential for NIR optoelectronic applications. Building on this work, in 2025 the same group reported the synthesis of a stable N-heterotriangulene dimer (compound **30**) bridged by a rigid π-conjugated [5]helicene [44]. This chiral dimer undergoes reversible stepwise oxidation to $\mathbf{30}^{\bullet+}$ and $\mathbf{30}^{2+}$, accompanied by pronounced NIR Cotton effects extending up to 2000 nm. These results provide critical insights into the rational design of redox-switchable, NIR-active chiral molecular systems, underscoring their promise in advanced optoelectronic and spintronic technologies.

In 2024, Tanaka's group synthesized and characterized a series of length-variable aza[*n*]helicenes **31a–f** via a one-pot intramolecular cyclodehydrogenation [45] (Table 9). Notably, compounds **31e** and **31f** represent the first examples of triple-layered heterohelicenes with fully conjugated frameworks. All members of the series demonstrate high solubility, attributed to intermolecular hydrogen bonding with solvent molecules. With increasing helical length, both the λ_{abs} and λ_{em} exhibit progressive bathochromic shifts, while the Φ_F values systematically decline, without clear saturation within the investigated range. Chiroptical measurements of the *N*-butylated aza[*n*]helicenes **31g–j** reveal $|g_{abs}|$ and $|g_{lum}|$ values on the order of 10^{-3}. These findings address long-standing challenges in the synthesis and stabilization of extended heterohelicenes, paving the way for the development of structurally persistent, π-extended chiral materials. In a parallel effort, Tanaka's group synthesized benzannulated double aza[9]helicene **32a** and its alkylated derivatives **32b** and **32c** via a one-pot oxidative fusion strategy [46]. Compared to the parent compound **32a** ($\Phi_F = 0.07$), compounds **32b** and **32c** exhibit significantly enhanced Φ_F (0.35), red-shifted absorption bands, and $|g_{abs}|$ values of 2.4×10^{-3} and 2.3×10^{-3} at 345 nm, respectively. Their corresponding B_{CPL} values reach 16.0 and 19.2 M^{-1} cm^{-1}. Furthermore, terminus-functionalized aza[9]helicenes **33a**, **33b**, and **33c** were prepared to investigate interlayer interactions [47]. Among them, the pyrene-decorated compound **33c** displays red-shifted emission and prolonged fluorescence lifetimes as solvent polarity increases, indicating enhanced excited-state stabilization. Collectively, these studies offer valuable strategies for stabilizing long π-extended helicenes and finely tuning their chiroptical and emissive properties, thereby advancing their application in multifunctional chiral photonic and sensing platforms.

Table 8: Structures and optical properties of **29a–f** and **30**.[a]

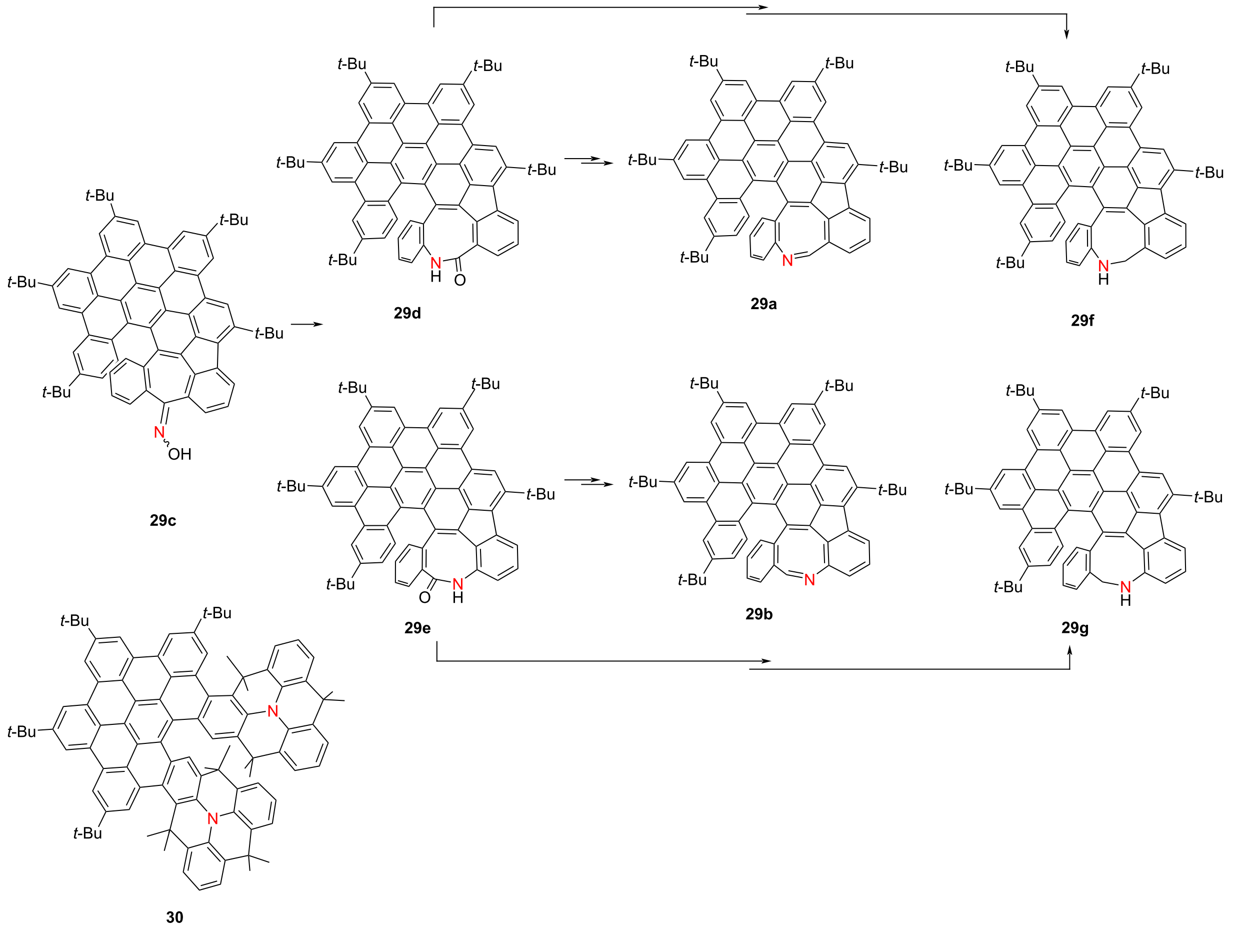

compound	$\lambda_{abs(max)}$ [nm]	λ_{em} [nm]	Φ_F	$\lvert g_{abs}\rvert$	$\lvert g_{lum}\rvert$	B_{CPL} [M^{-1} cm^{-1}]
29a	513	540, 565	0.01	2.5×10^{-3}	–	–
29b	513	552, 582	0.12	1.9×10^{-3}	1.6×10^{-3}	–
29d	510	539, 570	0.52	3.0×10^{-3}	6.0×10^{-4}	–
29e	510	543, 575	0.51	2.1×10^{-3}	2.4×10^{-4}	–
29f	510	536, 570	0.48	2.0×10^{-3}	9.1×10^{-4}	–
29g	547	609, 652	0.56	2.4×10^{-3}	6.0×10^{-4}	–
30	495	534	0.42	1.25×10^{-3}	1.1×10^{-3}	7.00

[a]The optical properties of compound **29c** are not mentioned in the original paper.

In 2025, Gryko's group synthesized a series of heterohelicenes **34a–c**, featuring a 1,4-dihydropyrrolo[3,2-*b*]pyrrole (DHPP) core [48] (Table 10). The compounds exhibit similar absorption and emission profiles. However, compound **34c** stands out due to its pronounced solvatofluorochromism (λ_{em} = 546 nm, Φ_F = 0.42 in DMSO). Among the series, compound **34b** exhibits the highest $|g_{lum}|$ of 7.22×10^{-3}, while compound **34c** shows the greatest B_{CPL} as 29.3 M^{-1} cm^{-1}. These studies underscore the importance of regioisomerism and molecular core design in optimizing the chiroptical and emissive properties of heteroatom-rich nanographenes, advancing their potential in next-generation optoelectronic and chiral photonic devices.

B,N-containing helicenes

Enhancing charge transfer between electron-donating and electron-accepting units, as well as extending π-conjugated frameworks, are widely employed strategies for achieving longer-wavelength emission in optoelectronic materials. Inspired by the electronic configuration of borazine, boron has emerged as a valuable electron-accepting counterpart to electron-donating

Table 9: Structures and optical properties of **31a**–**j**, **32a**–**c**, and **33a**–**c**.

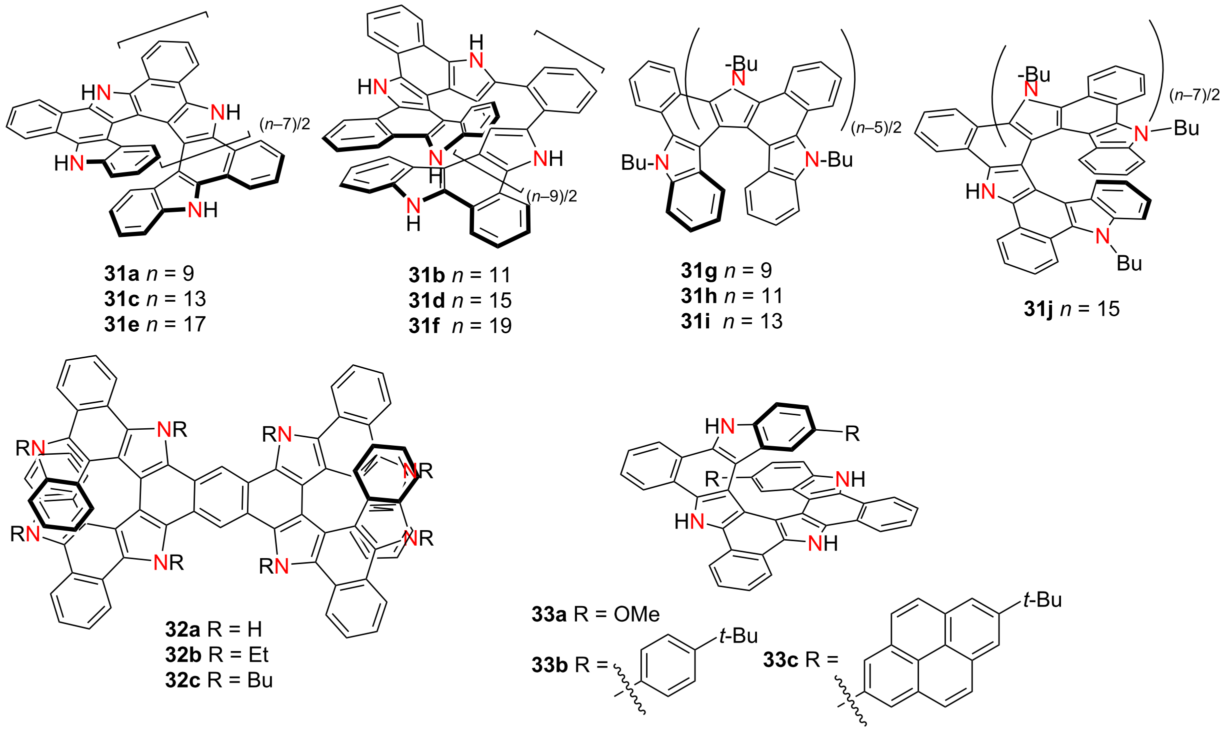

31a $n = 9$
31c $n = 13$
31e $n = 17$

31b $n = 11$
31d $n = 15$
31f $n = 19$

31g $n = 9$
31h $n = 11$
31i $n = 13$

31j $n = 15$

32a R = H
32b R = Et
32c R = Bu

33a R = OMe
33b R =
33c R =

compound	$\lambda_{abs(max)}$ [nm]	λ_{em} [nm]	Φ_F	$\lvert g_{abs}\rvert$	$\lvert g_{lum}\rvert$	B_{CPL} [M^{-1} cm^{-1}]
31a	412	437, 466, 500	0.21	–	–	–
31b	425	452, 479, 514	0.17	–	–	–
31c	438	427, 450, 480	0.11	–	–	–
31d	451	466, 491, 530	0.09	–	–	–
31e	388	483, 511	0.18	–	–	–
31f	310	508	0.08	–	–	–
31g	409	465, 495	0.16	5.6×10^{-3}	4.5×10^{-3}	8.6[a]
31h	314	482, 508	0.16	4.2×10^{-3}	4.2×10^{-3}	–
31i	315	508	0.09	4.2×10^{-3}	1.7×10^{-3}	–
31j	≈385	≈520	0.07	1.7×10^{-3}	5.7×10^{-3}	–
32a	464	496, 529, 570	0.07[b] 0.33[c]	–	–	–
32b	510	521, 555	0.35	2.4×10^{-3}	–	16.0
32c	508	522, 556	0.35	2.3×10^{-3}	–	19.2
33a	415	441, 466, 500	0.19	–	–	–
33b	414	437, 466, 500	0.21	–	–	–
33c	416	441, 466, 500	0.08	–	–	–

[a]According to reference paper [42]; [b]in THF; [c]in DMSO.

nitrogen in conjugated systems, enabling the design of donor–acceptor helicenes with tunable photophysical properties.

In 2020, Ema and co-workers developed a series of chiral carbazole-based BODIPY analogues **35a–f**, derived from helical carbazole-based BF_2 dyes [49] (Table 11). These analogues exhibit red-shifted emission and enhanced CPL compared to their carbazole-based helicene precursors. At λ_{abs} (≈500 nm), the compounds display $|g_{abs}|$ values ranging from 1.1×10^{-3} to 3.1×10^{-3}, Φ_F values of 20–36%, and $|g_{lum}|$ values between 7.0×10^{-4} and 1.9×10^{-3}. In a subsequent study, Ema's group reported an *N*-containing hetero[7]helicene

Table 10: Structures and optical properties of **33a**,**b** and **34a**–**c**.

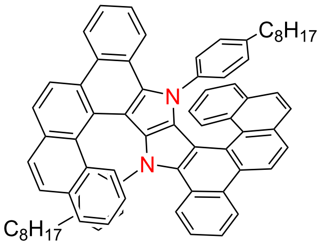

34a

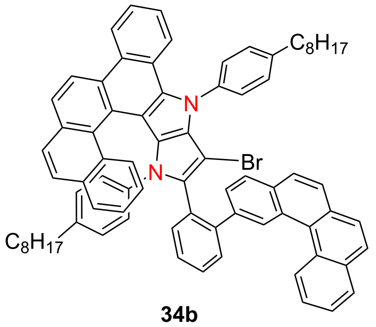

34b

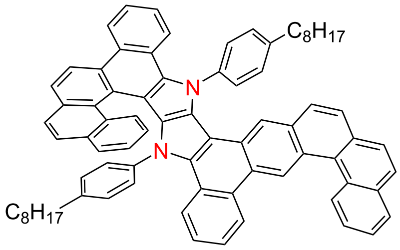

34c

compound	$\lambda_{abs(max)}$ [nm]	λ_{em} [nm]	Φ_F	$\lvert g_{abs}\rvert$	$\lvert g_{lum}\rvert$	B_{CPL} [M^{-1} cm^{-1}]
34a	438	460, 481	0.270	–	1.33×10^{-3}	2.0
34b	446	463, 488	0.045	–	6.11×10^{-3}	4.3
34c	456	483, 505	0.324	–	3.25×10^{-3}	29.3

36a containing a boron–nitrogen coordination site [50]. Its chiroptical properties could be modulated through the addition of tetrabutylammonium (TBA) salts, which transformed the boron center from a trigonal planar to a tetrahedral geometry, thereby enhancing the $\lvert g_{lum}\rvert$ from 4.7×10^{-4} to 1.5×10^{-3} (OAc^-, **36c**) and 1.7×10^{-3} (F^-/OH^-, **36b**/**36d**). Treatment with Ag^+ ions reversed this coordination, restoring the neutral trigonal boron center and its initial optical characteristics. These findings underscore the potential of boron–nitrogen-embedded helicene frameworks as tunable chiral luminophores with reversible CPL modulation, offering promising strategies for the development of advanced molecular optoelectronic devices.

In 2021, Hatakeyama and co-workers developed an expanded B,N-containing heterohelicene **37** via a one-step synthesis employing excess BBr_3 at 180 °C in an autoclave, achieving a 44% yield [51] (Table 12). In a 1 wt % PMMA-dispersed film, compound **37** exhibited ultra-narrowband emission (FWHM = 16 nm) at 484 nm with an 80% PLQY. OLEDs based on **37** demonstrated excellent external quantum efficiency, current efficiency, and power efficiency. Duan and co-workers reported B,N-containing double hetero[7]helicenes **38a**,**b**, which exhibited deep-red fluorescence emission at 662 and 692 nm, respectively, with narrow emission bandwidths (full width at half maximum, FWHM = 38 nm) and exceptional PLQYs of 100% [52]. Remarkably, they achieved maximum EQEs of 28.1% and 27.6%, representing the highest reported values for thermally activated delayed fluorescence (TADF) emitters operating above 650 nm. Shortly thereafter, Wang's group reported a related series of B,N-containing compounds **38a**–**c**, which displayed pronounced chiroptical activity in the visible region [53]. These compounds displayed the highest $\lvert g_{abs}\rvert$ values recorded for helicenes to date – 0.033, 0.031, and 0.026 at 502, 518, and 526 nm, respectively. They also showed near-unity Φ_F values of 100%, 99%, and 90%, with corresponding λ_{em} at 660, 684, and 696 nm, and $\lvert g_{lum}\rvert$ values of 2×10^{-3}. The calculated B_{CPL} reached 28.5, 37.1, and 40.0 M^{-1} cm^{-1}, positioning these helicenes among the most efficient red CPL emitters reported to date (Table 12).

However, such long-wavelength emission poses challenges for achieving optimal color purity in OLED devices. To overcome this limitation, Duan's group subsequently introduced a covalent B–N bond into the helicene framework in 2023, affording compound **39** [54]. This material emits at 617 nm with a FWHM of 38 nm and maintains a near-unity PLQY. Circularly polarized OLEDs (CP-OLEDs) based on **39** exhibit outstanding device performance, achieving a $\lvert g_{EL}\rvert$ of 1.91×10^{-3}, a record-high EQE exceeding 36%, and operational stability with an LT_{95} of approximately 400 h at 10,000 cd m^{-2}. These findings underscore the efficacy of B–N covalent integration in helicene-based frameworks for realizing high-efficiency, spectrally optimized, and robust red CP-OLED emitters.

In 2022, Yang and co-workers reported a W-shaped double hetero[5]helicene **40**, incorporating boron, nitrogen, and sulfur atoms within its framework [55] (Table 13). Compound **40** exhibits exceptional photophysical and electroluminescent performance, including a PLQY value of 100% and a $\lvert g_{lum}\rvert$ value of 2.1×10^{-3}. Circularly polarized organic light-emitting diodes (CP-OLEDs) based on **40** demonstrated a $\lvert g_{EL}\rvert$ of 2.2×10^{-3}, a narrow emission bandwidth (FWHM = 49 nm), and a maximum external quantum efficiency (EQE) of 31.5%, placing it among the highest-performing multiple-resonance-induced thermally

Table 11: Structures and optical properties of **35a–f** and **36a–d**.

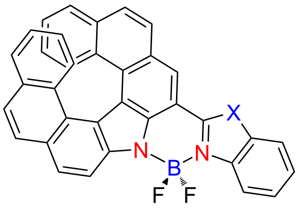

35a X = O
35b X = S

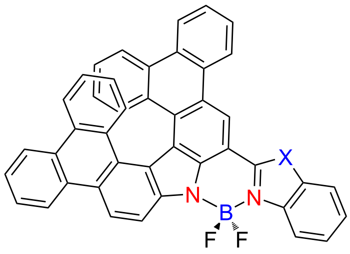

35c X = O
35d X = S

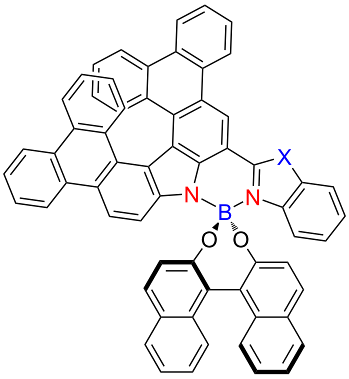

35e X = O
35f X = S

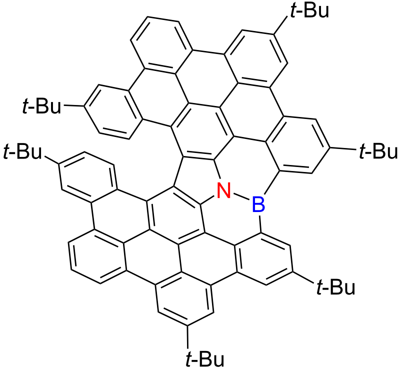

36a

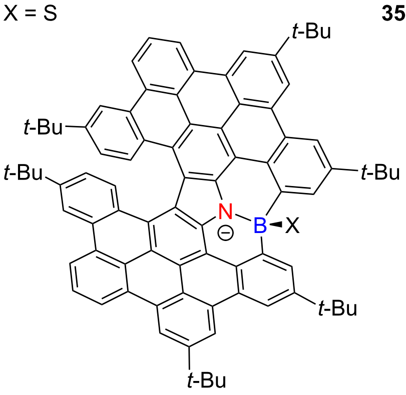

36b X = F
36c X = OAc
36d X = OH

compound		$\lambda_{abs(max)}$ [nm]	$\lambda_{em(max)}$ [nm]	Φ_F	$\lvert g_{abs} \rvert$	$\lvert g_{lum} \rvert$
35a		495	568	0.22	2.7×10^{-3}	1.7×10^{-3}
35b		508	594	0.20	3.1×10^{-3}	1.3×10^{-3}
35c		508	566	0.33	1.2×10^{-3}	8.7×10^{-4}
35d		524	592	0.21	1.1×10^{-3}	7.0×10^{-4}
35e	(*R*,*P*)	508	576	0.30	2.3×10^{-3}	1.5×10^{-3}
	(*R*,*M*)	509	571	0.36	1.5×10^{-3}	1.2×10^{-3}
35f	(*R*,*P*)	530	605	0.20	1.8×10^{-3}	1.2×10^{-3}
	(*R*,*M*)	532	602	0.26	1.5×10^{-3}	8.8×10^{-4}
36a		487	493	–	1.6×10^{-3}	4.7×10^{-4}
36b		502	512	–	3.0×10^{-3}	1.7×10^{-3}
36c		510	526	–	2.9×10^{-3}	1.5×10^{-3}
36d		511	520	–	3.2×10^{-3}	1.7×10^{-3}

activated delayed fluorescence (MR-TADF) emitters to date. In 2023, the same group introduced the first deep-blue chiral MR-TADF emitters based on heterohelicene scaffolds **41a**–**c** [56]. These compounds exhibited sharp emissions at 440–444 nm in solution and 445–449 nm in doped films, with emission bandwidths as narrow as 23 nm and PLQYs reaching up to 95%. Notably, racemic **41b** and **41c** displayed excellent chiroptical properties, with $\lvert g_{\text{lum}} \rvert$ values ranging from 1.4 to 1.5×10^{-3} and B_{CPL} values exceeding 22 M^{-1} cm^{-1}. Compound **41c**, in particular, achieved a $\lvert g_{\text{EL}} \rvert$ of 2.6×10^{-3} and a maximum luminance exceeding 10,000 cd m^{-2}. These findings underscore the significant potential of heteroatom-integrated helicene systems as high-efficiency, CPL-active MR-TADF materials for next-generation OLED technologies, particularly

Table 12: Structures and optical properties of **37**, **38a–c**, and **39**.

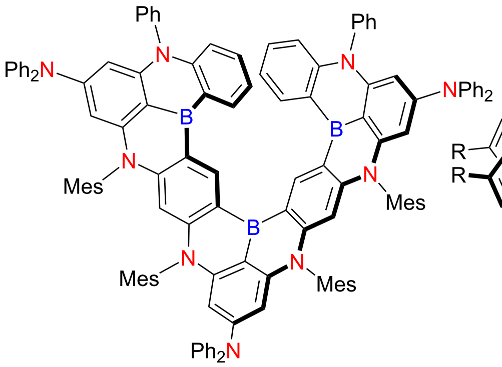

37

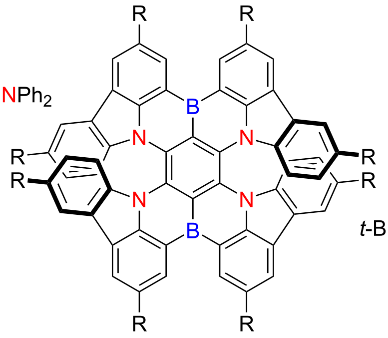

38a R = H
38b R = *t*-Bu
38c R = 4-(*t*-Bu)phenyl

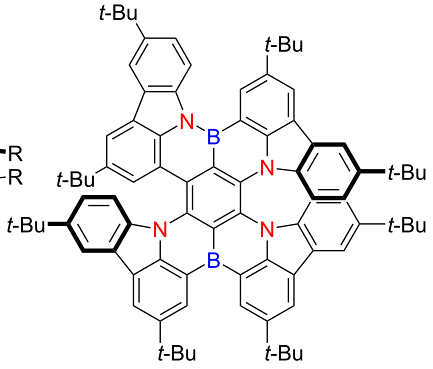

39

compound	$\lambda_{abs(max)}$ [nm]	$\lambda_{em(max)}$ [nm]	Φ_F	$\lvert g_{abs}\rvert$	$\lvert g_{lum}\rvert$
38a	627	660	1.00	3.3×10^{-2}	2.0×10^{-3}
38b	650	684	0.99	3.1×10^{-2}	2.0×10^{-3}
38c	662	696	0.90	2.6×10^{-2}	2.0×10^{-3}
39	590	617	0.96	1.2×10^{-2}	1.4×10^{-3}
film		$\lambda_{abs(max)}$ [nm]	$\lambda_{em(max)}$ [nm]	Φ_F	FWHM [nm]
37 in PMMA		477	484	0.80	16
38a in CBP		–	672	–	48
38b in CBP		–	698	–	49
39 in mCPBC		–	624	0.95	–
device	$\lambda_{EL(max)}$ [nm]	$\lvert g_{EL}\rvert$	FWHM [nm]	CIE coordinate	EQE_{max} [%]
37	480	–	17	(0.09, 0.21)	22.9[a]
38a	664	–	48	(0.72, 0.28)	28.1
38b	686	–	49	(0.72, 0.28)	27.6
39	617	1.9×10^{-3}	48	(0.67, 0.33)	36.6

[a] As detected at 10 cd m^{-2}.

in the development of deep-blue emissive devices with high color purity and device efficiency.

In 2022, Marder and co-workers introduced various boryl substituents at both termini of a series of nitrogen-doped [5]helicenes, yielding helicenoids **42a–h** [57] (Table 14). The Bpin-substituted derivatives **42a–e** exhibited broad emission across the 400–800 nm range, whereas their analogues **42f** and **42g** showed negligible emission, indicating a strong dependence of photophysical behavior on boryl-substituent identity. Compared to their parent azahelicenes, these compounds displayed significantly larger Stokes shifts, highlighting the pronounced electronic effects of boryl incorporation. Notably, when a CF_3 group was introduced as a substituent on the azahelicene core, the resulting boryl-functionalized compound **42c** exhibited an emission maximum at 563 nm in CH_2Cl_2, with a quantum yield of 15%, representing the highest emission efficiency observed among the boron-containing quasi-circulenes.

In 2022, Lu and co-workers developed a series of helical aza-BODIPY analogues **43a–h**, featuring a distinctive B–O–B bridge installed within each molecule [58] (Table 15). These compounds display broad chiroptical responses extending from the ultraviolet to the entire visible spectrum – an uncommon characteristic among helicene-type systems. Among them, the phenyl-substituted aza[7]helicene **43f** exhibits pronounced chiroptical activity, with $\lvert g_{abs}\rvert$ and $\lvert g_{lum}\rvert$ values reaching 3.04×10^{-3} and 1.30×10^{-3}, respectively, and a high B_{CPL} of 11.5 M^{-1} cm^{-1} in the near-infrared region. In contrast, the corresponding aza[5]helicene analogue shows negligible chiral

Table 13: Structure and optical properties of **40** and **41a–c**.

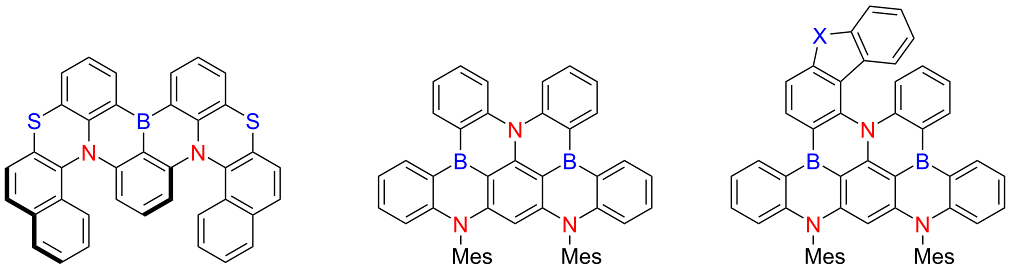

40 **41a** **41b** X = O
41c X = S

compound	$\lambda_{abs(max)}$ [nm]	$\lambda_{em(max)}$ [nm]	Φ_F	$\lvert g_{abs}\rvert$	$\lvert g_{lum}\rvert$
40	483	520	0.98	–	2.1×10^{-3}
41a	424	440	0.82	–	–
41b	422	443	0.91	1.4×10^{-3}	1.4×10^{-3}
41c	427	444	0.95	1.5×10^{-3}	1.5×10^{-3}

film	$\lambda_{abs(max)}$ [nm]	$\lambda_{em(max)}$ [nm]	Φ_F	FWHM [nm]
40 in DMIC-TRZ	–	525	–	48
41a in DOBNA-OAr	–	445	0.82	35
41b in DOBNA-OAr	–	448	0.91	28
41c in DOBNA-OAr	–	449	0.95	28

device	$\lambda_{EL(max)}$ [nm]	$\lvert g_{EL}\rvert$	FWHM [nm]	CIE coordinate	EQE_{max} [%]
40	524	2.2×10^{-3}	49	(0.26, 0.66)	31.5
41a	443	–	26	(0.15, 0.05)	23.4
41b	445	2.2×10^{-4}	24	(0.15, 0.04)	27.5
41c	447	2.6×10^{-4}	24	(0.15, 0.05)	29.3

response, with $|g_{abs}|$ and $|g_{lum}|$ values in the 10^{-5} range. To further enhance chiroptical performance, Lu's group introduced edge-positioned methyl and ethyl substituents into the helical core, affording **44a** and **44b** [59]. Compared with **43c**, they are with significantly improved $|g_{abs}|$ values of 1.51×10^{-3} and 1.69×10^{-3}, respectively. This study underscores the critical importance of molecular design in modulating chiroptical properties and provides valuable insights into the development of helicene-based BODIPY systems for near-infrared CPL applications. In 2024, Shimizu's group reported azabora[6]helicenes **45a** and **45b** [60]. However, their enantiomers could not be isolated due to low racemization barriers. The F- and Ph-coordinated derivatives displayed moderate PLQYs in solution (0.26 and 0.18, respectively), which dropped markedly in the solid state (0.02 and 0.04) owing to aggregation-caused quenching (ACQ).

In 2023, Yang and co-workers reported a pair of $(NBN)_2$-containing double and quadruple helicenes **46a–d** [61] (Table 16). The neutral compounds exhibited high PLQYs of 99% and 65% in solution, and 90% and 55% in PMMA-doped films, respectively, with exceptionally narrow full-width (FWHM values as 24 nm and 22 nm). Stepwise titration experiments with fluoride ions induced a change in the coordination number of the boron centers from three to four, forming corresponding anionic species. This coordination triggered red-shifted absorption and CPL responses while maintaining excellent PLQYs – 99% and 90% in solution, and 80% and 77% in PMMA-doped films, respectively.

In 2024, Wang's group developed a B,N-embedded hetero[8]helicene **47**, exhibiting narrow green emission at 531 nm (FWHM = 36 nm), a high PLQY of 93%, and outstanding CP-OLED performance (EQE = 32.0%; $|g_{EL}| = 7.74 \times 10^{-4}$) [62] (Table 17). Bin's group introduced orthogonal spiro-structures into hetero[6]helicenes **48a–c**, achieving near-unity PLQYs in solution (up to 99%) and OLED external quantum

Table 14: Structure and optical properties of **42a**–**h**.[a]

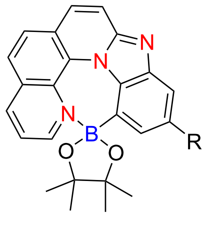

42a R = H
42b R = Me
42c R = CF_3

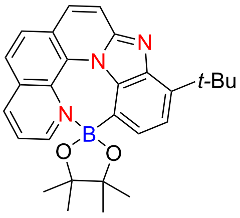

42d

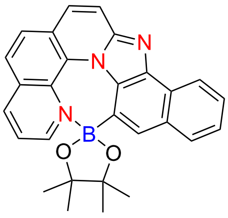

42e

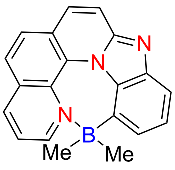

42f

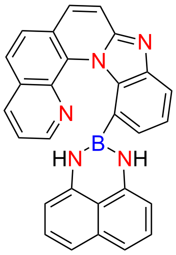

42g

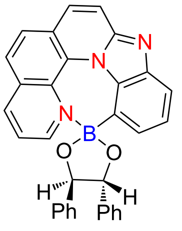

42h

compound	$\lambda_{abs(max)}$ [nm]	$\lambda_{em(max)}$ [nm]	Φ_F
42a	372	520	0.08
42b	373	522	0.08
42c	364	563	0.15
42d	372	530	0.07
42e	407	588	0.05
42f	385	–	–
42g	366	–	–
42h	–	–	–

[a] No g_{abs} or g_{lum} values were reported.

Table 15: Structure and optical properties of **43a**–**h**, **44a**,**b**, and **45a**,**b**.

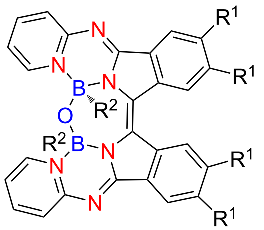

43a–d

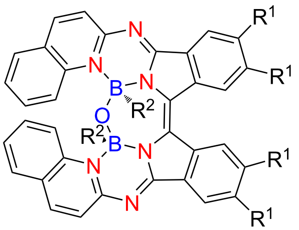

43e–h

43a,**e** R^1 = 4-(*t*-Bu)phenyl, R^2 = F
43b,**f** R^1 = 4-(*t*-Bu)phenyl, R^2 = Ph
43c,**g** R^1 = 4-(*t*-Bu)phenylthio, R^2 = F
43d,**h** R^1 = 4-(*t*-Bu)phenylthio, R^2 = Ph

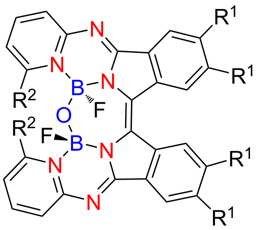

44a R^1 = 4-(*t*-Bu)phenylthio,
R^2 = Me
44b R^1 = 4-(*t*-Bu)phenylthio,
R^2 = Et

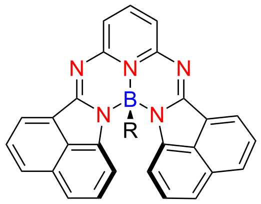

45a R = F
45b R = Ph

compound	$\lambda_{abs(max)}$ [nm]	$\lambda_{em(max)}$ [nm]	Φ_F	$\lvert g_{abs}\rvert$	$\lvert g_{lum}\rvert$
43a	588	625	0.59	4×10^{-5}	3×10^{-5}
43b	623	649	0.56	–	–
43c	601	640	0.31	–	–
43d	634	668	0.12	–	–
43e	646	682	0.30	2.0×10^{-3}	1.3×10^{-3}
43f	677	708	0.24	3.0×10^{-3}	1.3×10^{-3}
43g	660	695	0.16	1.8×10^{-3}	1.2×10^{-3}
43h	691	719	0.10	–	–
44a	624	665	0.08	1.5×10^{-3}	–
44b	625	665	0.07	1.7×10^{-3}	–
45a	548	568	0.26	–	–
45b	554	574	0.18	–	–

Table 16: Structure and optical properties of **46a–d**.

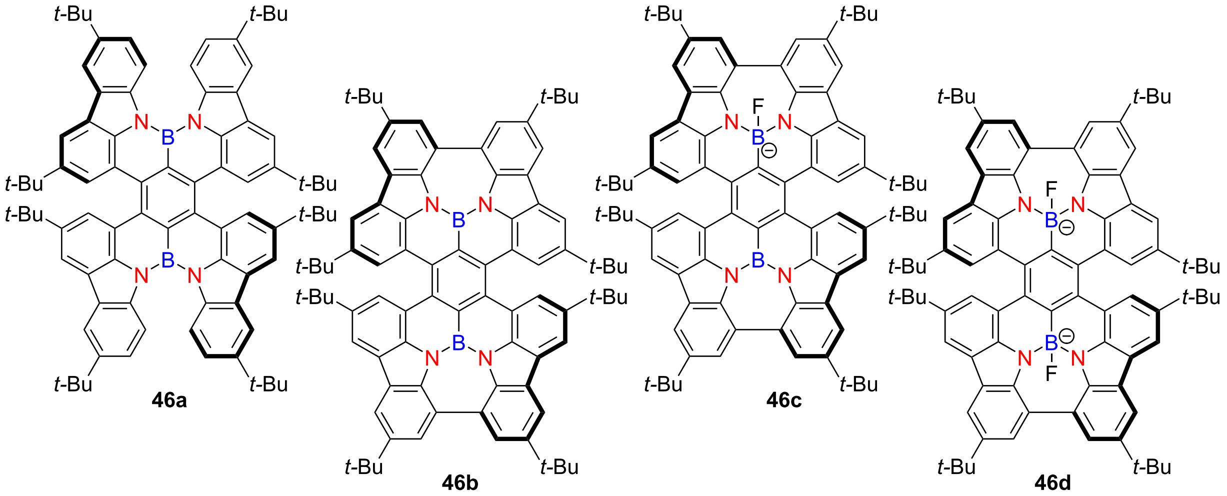

46a **46b** **46c** **46d**

compound	$\lambda_{abs(max)}$ [nm]	$\lambda_{em(max)}$ [nm]	Φ_F	$\lvert g_{abs} \rvert$	$\lvert g_{lum} \rvert$
46a[a]	511	524	0.99	–	–
46b[a]	507	522	0.65	6.2×10^{-3}	1.0×10^{-3}
46c[b]	524	567	0.99	5.0×10^{-3}	6.0×10^{-4}
46d[b]	518	541	0.90	6.0×10^{-3}	7.0×10^{-4}

film	$\lambda_{abs(max)}$ [nm]	$\lambda_{em(max)}$ [nm]	Φ_F	FWHM [nm]
46a in PMMA	–	–	0.95	–
46b in PMMA	–	–	0.55	–
46c in PMMA	–	–	0.80	–
46d in PMMA	–	–	0.77	–

[a] In toluene; [b] in acetone.

efficiencies (EQEs) exceeding 31% [63]. Chen's group reported **49**, a B,N-containing hetero[9]helicene that emits at 578 nm with a PLQY of 98% and showing excellent chiroptical properties ($|g_{lum}| = 5.8 \times 10^{-3}$; $B_{CPL} = 220.75\ M^{-1}\ cm^{-1}$) [64]. OLEDs incorporating compound **49** demonstrated an EQE of 35.5% and $|g_{EL}| = 6.2 \times 10^{-3}$. Zhang's group synthesized **50a–f**, with and without installed heptagons [65]. The heptagon-containing derivatives showed red-shifted emission, broader FWHM, lower PLQYs, and diminished B_{CPL} values, indicating a trade-off between extended conjugation and emissive efficiency. Yin's group introduced 1,4-BN motifs into compounds **51a** and **51b**, which emitted blue-green light at 474 and 465 nm, respectively, and exhibited moderate CPL activity ($|g_{lum}| \approx 5 \times 10^{-4}$) [66] . OLEDs based on compound **51a** emitted at 502 nm and achieved an EQE of 3.18%. Liu's group positioned B and N atoms on the inner rim of **52a** and **52b** [67]. While **52b** exhibited remarkably high $|g_{abs}|$ and $|g_{lum}|$ values (6.1×10^{-2} and 2.4×10^{-2}, respectively), its PLQY was relatively low (24%). Further molecular optimization led to the development of compounds **53a–c**, which demonstrated ultra-narrow emission bands (FWHM = 16–34 nm), high PLQYs (67–82%), and exceptional CPL brightness (B_{CPL}s of 583, 374, and 349 $M^{-1}\ cm^{-1}$, respectively), with compound **53a** setting a new record for BN-containing helicene CPL brightness [68]. These collective findings underscore the critical role of rational BN doping, π-conjugation engineering, and structural rigidity in precisely tuning the photophysical and chiroptical properties of helicene-based materials, thereby advancing the design of next-generation CPL-active optoelectronic systems with superior performance metrics.

However, these findings also suggest that boron may not always be the optimal choice for enhancing charge-transfer properties. The delocalization of electrons between the vacant p-orbital of boron and the electron-rich π-conjugated systems can diminish both the electron-accepting capability of boron and the electron-donating efficiency of the conjugated framework. Additionally, the inherently low electronegativity of boron further limits its

Table 17: Structure and optical properties of **47**, **48a**–**c**, **49**, **50a**–**f**, **51a**,**b**, **52a**,**b**, and **53a**–**c**.

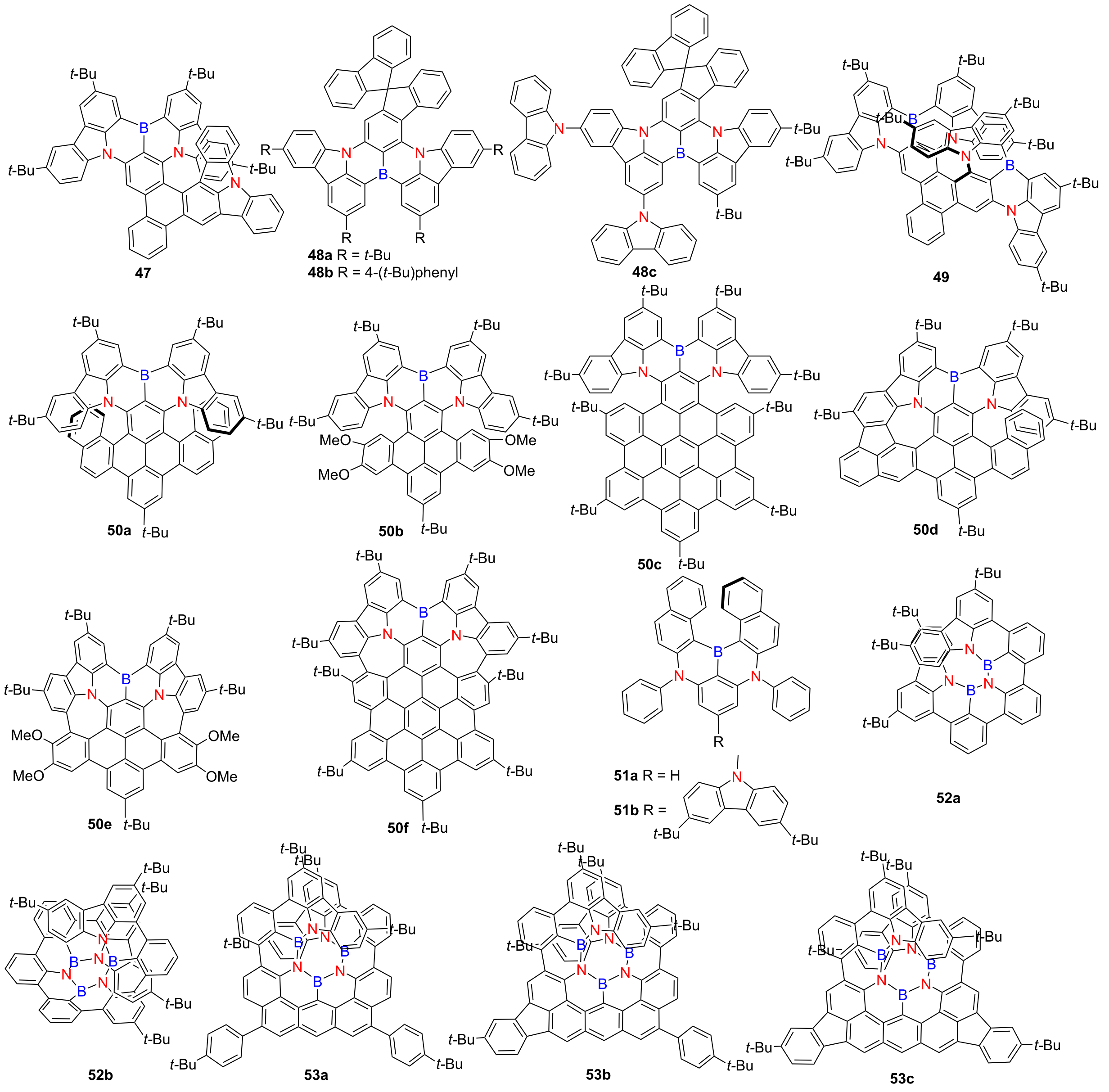

compound	$\lambda_{abs(max)}$ [nm]	$\lambda_{em(max)}$ [nm]	Φ_F	$\lvert g_{abs}\rvert$	$\lvert g_{lum}\rvert$
47	510	531	0.93	1.4×10^{-3}	5.8×10^{-4}
48a	482	503	0.91	–	–
48b	495	516	0.99	–	–
48c	493	515	0.94	–	–
49	546	578	0.98	5.6×10^{-3}	5.8×10^{-3}
50a	548	595	0.68	7.4×10^{-3}	2.7×10^{-3}
50b	545	585	0.66	8.6×10^{-3}	2.5×10^{-3}
50c	553	598	0.74	3.1×10^{-3}	2.7×10^{-3}
50d	622	675	0.11	4.7×10^{-3}	2.9×10^{-3}
50e	563	623	0.27	–	–
50f	595	641	0.02	6.6×10^{-3}	5.0×10^{-3}
51a	453	474	0.83	6.2×10^{-3}	5.1×10^{-4}

Table 17: Structure and optical properties of **47**, **48a–c**, **49**, **50a–f**, **51a**,**b**, **52a**,**b**, and **53a–c**. (continued)

51b	447	465	0.54	2.5×10^{-3}	4.8×10^{-4}
52a	403	409	0.31	3.6×10^{-2}	2.4×10^{-2}
52b	423	430	0.24	6.1×10^{-2}	4.8×10^{-2}
53a	506	515	0.82	2.4×10^{-2}	1.7×10^{-2}
53b	513	529	0.67	1.1×10^{-2}	1.2×10^{-2}
53c	516	535	0.72	1.1×10^{-2}	8.0×10^{-3}
film	$\lambda_{abs(max)}$ [nm]	$\lambda_{em(max)}$ [nm]	Φ_F		FWHM [nm]
46a from $CHCl_3$	–	667	0.02		48
46b from $CHCl_3$	–	632	0.04		35
47 in PhCzBCz	–	≈545	0.92		≈50
51a in DPEPO	–	472	0.32		38
51b in DPEPO	–	467	0.42		29
device	$\lambda_{EL(max)}$ [nm]	$\lvert g_{EL}\rvert$	FWHM [nm]	CIE coordinate	EQE_{max} [%]
47	536	7.7×10^{-4}	38	(0.32, 0.66)	31.1
48a	490	–	30	(0.10, 0.41)	25.2
48b	506	–	37	(0.15, 0.65)	29.2
48c	522	–	37	(0.22, 0.70)	31.0
49	580	6.2×10^{-3}	48	(0.53, 0.46)	35.4
51a	502	–	35	(0.14, 0.55)	3.2

effectiveness as an electron acceptor, thereby restricting the achievable red-shift in emission. To overcome these limitations, alternative electron-withdrawing atoms and functional groups have been introduced into nitrogen-doped helicene frameworks to improve their photophysical performance and extend emission into the longer wavelength region.

X,N-containing helicenes (X = O, S or Se)

Imide functional groups are well recognized for their strong electron-accepting character, making them valuable moieties in the design of optoelectronic materials. When incorporated into π-conjugated frameworks, imide groups can significantly modulate electronic structures and enhance properties such as fluorescence efficiency, charge transport, and chiroptical responses. In this section, we begin by summarizing representative imide-functionalized helicenes, highlighting their structural features and photophysical performances. In 2020, Ravat's group introduced a novel class of helically chiral diimide molecules **54a–c**, which integrate the favorable characteristics of arylene diimides within the chiral architecture of [*n*]helicenes [69]. These compounds exhibit varying PLQYs of 0.22, 0.02, and 0.12 for **54a**, **54b**, and **54c**, respectively, and notably retain fluorescence in the solid state. The $|g_{abs}|$ in the visible region increase systematically with helical length, reaching values as high as $\approx 10^{-2}$ for compounds **54b** and **54c –** among the highest reported to date – highlighting their strong potential in chiral optoelectronic applications (Table 18). In 2023, the same group reported a stable push–pull [7]helicene diimide (compound **55**) that exhibited notable chiroptical performance, with $|g_{abs}|$ and $|g_{lum}|$ values of 1.12×10^{-2} and 5.0×10^{-3}, respectively, in toluene [70]. Furthermore, compound **55** demonstrated solvent-dependent fluorescence and CPL behavior across the visible spectrum, with both emission intensity and chiroptical properties varying in response to solvent polarity. Concurrently, Würthner's group developed two naphthalimide-annulated [*n*]helicenes, compounds **56a** and **56b** (*n* = 5, 6), via a concise two-step synthetic route that afforded excellent yields and notable photophysical properties [71]. Both helicenes display high Φ_F as 73% for **56a** and 69% for **56b**. Notably, compound **56b** exhibits markedly enhanced $|g_{abs}|$ and $|g_{lum}|$ values of 2.1×10^{-3} and 2.3×10^{-3}, approximately 4.5-fold greater than that of compound **56a**. Its red CPL emission at 615 nm and high B_{CPL} of 66.5 M^{-1} cm^{-1} underscore its potential for advanced chiral photonic applications.

Heteroatom engineering in double helicenes has emerged as a powerful strategy for tuning chiroptical properties and excited-state dynamics. In 2021, Sakamaki's group synthesized a novel double N,O-hetero[5]helicene (compound **57b**) by coupling two 12*H*-benzo[*b*]phenoxazine (BPO) units and systematically compared it to its *N*,*N*-analogue (compound **57a**) derived from 13*H*-dibenzo[*b*,*i*]phenoxazine (DBPO) scaffolds [72] (Table 19). Compound **57b** was obtained in significantly higher yield and, like compound **57a**, exhibited electron-rich character and

Table 18: Structures and optical properties of **54a–c**, **55** and **56a**,**b**.

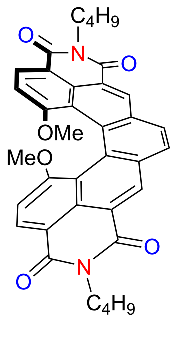

54a

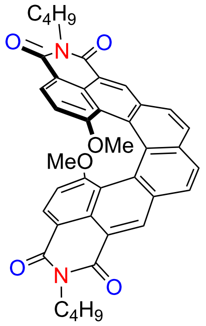

54b

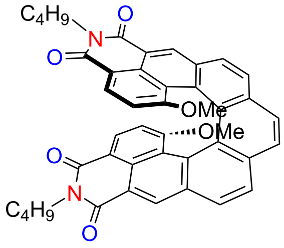

54c

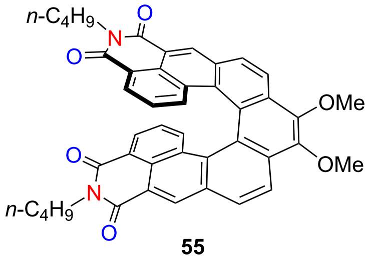

55

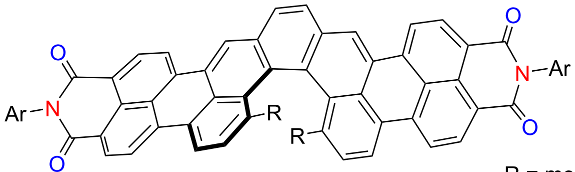

56a

R = methoxy
Ar = 2,6-diisopropylphenyl

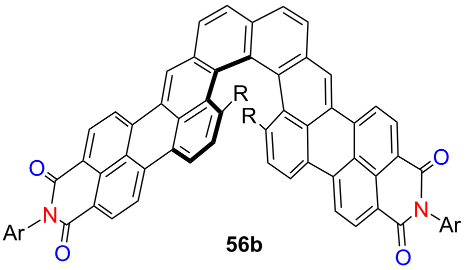

56b

compound	$\lambda_{abs(max)}$ [nm]	$\lambda_{em(max)}$ [nm]	Φ_F	$\lvert g_{abs}\rvert$	$\lvert g_{lum}\rvert$	B_{CPL} [M^{-1} cm^{-1}]
54a	417, 442	471, 499	0.22[a] 0.17[b]	7×10^{-3}	–	–
54b	395	470, 498	0.02[a] 0.02[b]	1.75×10^{-2}	–	–
54c	452	508	0.12[a] 0.06[b]	1.22×10^{-2}	–	–
55[c]	408	532	0.26	8.6×10^{-3}	4.2×10^{-3}	7.8
56a	629	655	0.73	4.5×10^{-4}	5.0×10^{-4}	22.0
56b	588	613	0.69	2.1×10^{-3}	2.3×10^{-3}	66.5
device	$\lambda_{EL(max)}$ [nm]	$\lvert g_{EL}\rvert$	FWHM [nm]	CIE coordinate		EQE_{max} [%]
56b	618	–	50	–		2.3

[a]As detected in solution; [b]as detected in the solid state; [c]all detected in DCM.

compact molecular packing, both favorable for *p*-type transistor performance. Importantly, both helicenes displayed strong CPL in CH_2Cl_2, with $\lvert g_{lum}\rvert$ values exceeding 10^{-2}. Intriguingly, the CPL signals of the two compounds exhibited opposite signs, underscoring the sensitivity of chiral excited-state properties to heteroatom substitution within the helicene framework. Extending this design principle, the group reported a double *N*,*S*-hetero[5]helicene **58** constructed from two benzo[*b*]phenothiazine units in 2023 [73]. Compared to the *N*,*O*-analogue **57b**, this new compound showed more intense phosphorescence and an extended emission lifetime in dilute solution. Notably, it demonstrated room-temperature dual-emission CPL originating from both prompt fluorescence and long-lived phosphorescence, a rare feature in helicene systems. In a subsequent study, the same group reported a bis(*N*,*Se*)-hetero[4]helicene **59b** and systematically compared its structural and dynamic properties with those of its sulfur analogue **59a** [74]. Despite their close structural resemblance, the longer C–Se bond in **59b** led to a markedly higher racemization barrier (145.7 vs 112.8 kJ/mol), thereby illustrating how subtle atomic substitutions can significantly influence the conformational stability of helical molecules (Table 19). These studies illustrate how precise heteroatom modulation enables fine control over CPL directionality and emission lifetimes, offering promising avenues for the development of multifunctional chiral optoelectronic materials – particularly those capable of simultaneous fluorescence and phosphorescence-based CPL.

Recently, thiadiazole-fused helicenes have gradually come into our view. In 2023, Hirose's group synthesized a series of tetraazadithia[*n*]helicenes – **60a**, **60b**, and **60c** – featuring 2,1,3-thiadiazole termini [75] (Table 20). Among them, compound

Table 19: Structures and optical properties of **57a**,**b**, **58**, and **59a**,**b**.

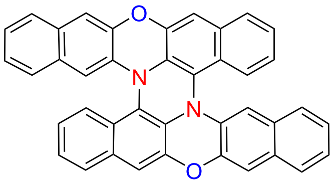

57a

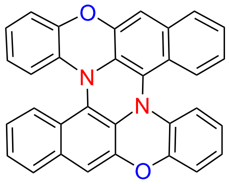

57b

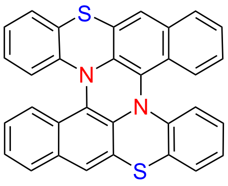

58

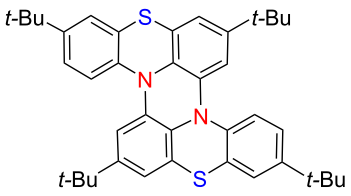

59a

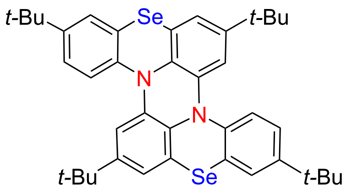

59b

compound	$\lambda_{abs(max)}$ [nm]	$\lambda_{em(max)}$ [nm]	Φ_F	$\lvert g_{abs}\rvert$	$\lvert g_{lum}\rvert$
57a	≈410	569	0.038	1.7×10^{-2}	2.3×10^{-2}
57b	≈380	587	0.035	1.3×10^{-2}	1.3×10^{-2}
58	≈390	547	0.003 0.30[a]	2.0×10^{-2}	1.7×10^{-2} [b]
59a	380	–	–	–	–
59b	380	–	–	–	–

[a]Phosphorescence quantum yield Φ_P; [b]doped in β-estradiol matrix.

Table 20: Structures and optical properties of **60a**–**c** and **61a**,**b**.

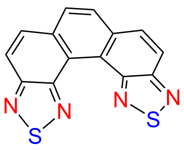

60a

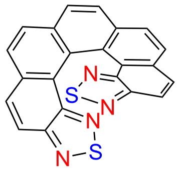

60b

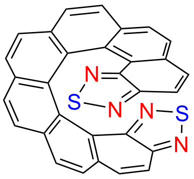

60c

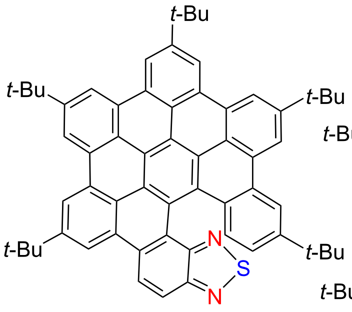

61a

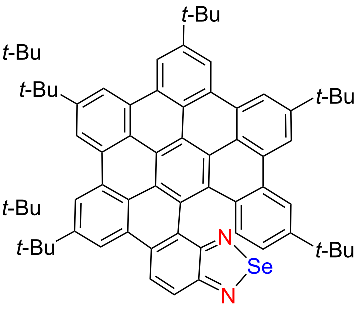

61b

compound	$\lambda_{abs(max)}$ [nm]	$\lambda_{em(max)}$ [nm]	Φ_F	$\lvert g_{abs}\rvert$	$\lvert g_{lum}\rvert$	B_{CPL} [M^{-1} cm^{-1}]
60a	391	398	0.005	–	–	–
60b	431	450	0.008	1.5×10^{-2}	1.0×10^{-2}	2
60c	445	483	0.027	3.7×10^{-2}	4.0×10^{-2}	15
61a	340	536	0.0735	–	–	–
61b	349	556	0.009	–	–	–

60c exhibited pronounced CPL activity in toluene ($|g_{\text{lum}}|$ = 0.04, Φ_F = 3%), demonstrating the efficacy of terminal heterocycle incorporation for boosting chiroptical performance. In 2024, Babu and co-workers developed two π-extended hetero[6]helicenes – **61a** and **61b** – incorporating thiadiazole and selenadiazole moieties, respectively [76]. Substitution of sulfur with selenium enhanced intermolecular interactions and led to a notable reduction in the optical bandgap, highlighting the effectiveness of heteroatom modulation in tuning the electronic and photophysical properties of chiral nanographenes. These studies exemplify how strategic structural and electronic design – through π-extension, end-group heteroatom engineering, and atom-specific substitutions – enables precise tuning of chiroptical and photophysical properties in helicene-based materials, advancing their applicability in next-generation optoelectronic devices.

In 2020, Pittelkow's group developed a unique synthetic strategy that converts a non-planar hetero[7]helicene into a planar hetero[8]circulene featuring an antiaromatic cyclooctatetraene (COT) core (**62a**–**f**) [77] (Table 21). Through controlled oxidation of the thiophene units to sulfones, they achieved a systematic red-shift in both absorption and emission spectra. Remarkably, the emission of these derivatives spans nearly the entire visible spectrum. These studies provide innovative molecular design strategies for constructing helically twisted or planarized chiral π-conjugated systems with tunable optical properties, thereby paving the way for the development of multifunctional materials in advanced photonic and electronic technologies.

In 2021, Viglianisi's group synthesized a series of thia-bridged triarylamine[4]helicene-functionalized polynorbornenes **63a**–**c** via ring-opening metathesis polymerization (ROMP), introducing helicene chirality into polymer backbones with tunable electrochromic behavior [78]. These polymers exhibit reversible pH-responsive color changes. For instance, **63a** transitions from pale yellow to deep blue in the solid state upon exposure to TFA, while **63b** and **63c** in CH_2Cl_2 exhibit new absorption bands at 570 and 575 nm, respectively – reversibly decolorized upon triethylamine treatment (Table 22). This work demonstrates the potential of helicene-containing polymers as stimuli-responsive chiral electrochromic materials. In the same year, You's group developed a transition-metal-catalyzed C–H/C–H-type regioselective C3-arylation of benzothiophenes using molecular oxygen as the oxidant [79]. This strategy afforded the TADF-active compound **64a**, which exhibits efficient blue emission and excellent OLED performance with a maximum EQE of 25.4%. This example highlights the utility of helicene-related heteroaromatic frameworks in the design of high-efficiency emissive materials. Also in 2021, Ema's group reported a concise Scholl-type cyclodehydrogenation strategy for synthe-

Table 21: Structure and optical properties of **62a**–**f**.

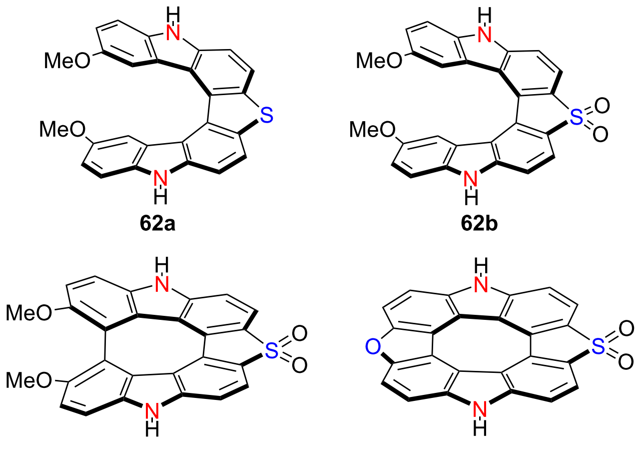

compound	$\lambda_{\text{abs(max)}}$ [nm]	$\lambda_{\text{em(max)}}$ [nm]	Φ_F	$\|g_{\text{abs}}\|$	$\|g_{\text{lum}}\|$
62a	388	429	0.08	–	–
62b	419	484	0.25	–	–
62c	431	518	0.14	–	–
62d	476	574	0.13	–	–
62e	414	436	0.06	–	–
62f	473	485	0.12	–	–

Table 22: Structures and optical properties of **63a–c**, **64a**,**b**, **65a–d**, and **66**.

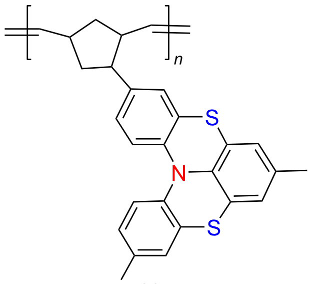

63a

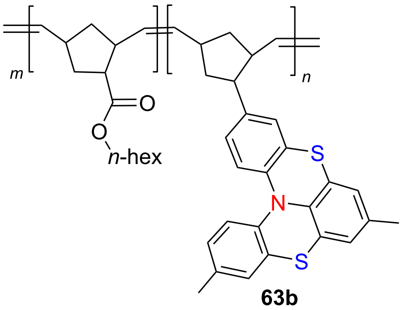

63b

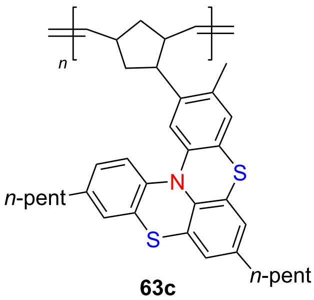

63c

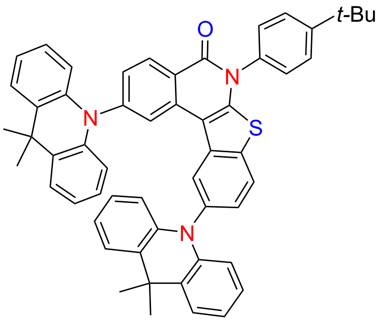

64a

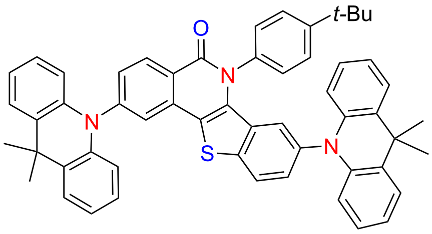

64b

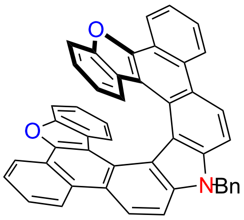

65a

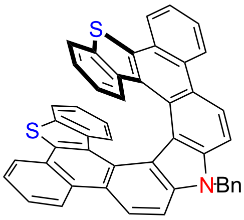

65b

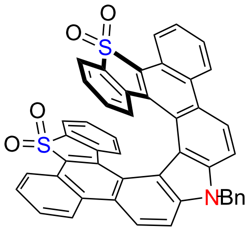

65c

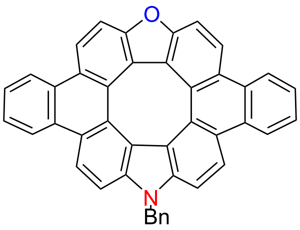

65d

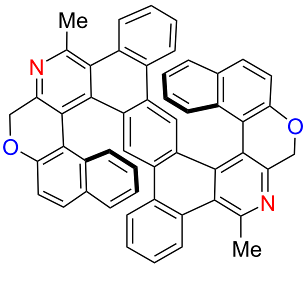

66

compound	$\lambda_{abs(max)}$ [nm]	$\lambda_{em(max)}$ [nm]	Φ_F	$\lvert g_{abs}\rvert$	$\lvert g_{lum}\rvert$
63a	–	–	–	–	–
63b	570	–	–	–	–
63c	575	–	–	–	–
64a	376	456	–	–	–
64b	360	456	–	–	–
65a	401	420, 441	0.30	9.2×10^{-4}	7.2×10^{-4}
65b	414	432, 457	0.08	1.6×10^{-3}	1.1×10^{-3}

Table 22: Structures and optical properties of **63a–c**, **64a**,**b**, **65a–d**, and **66**. (continued)

65c		440	493	0.10	7.3×10^{-4}	2.6×10^{-4}
65d		420	554	0.02	–	–
66		388, 431	489	0.21	5.59×10^{-3}	1.42×10^{-3}
66 (+TFA)		290, 389, 439	555	0.32	4.98×10^{-3}	1.38×10^{-3}
device	$\lambda_{EL(max)}$ [nm]	$\lvert g_{EL} \rvert$	FWHM [nm]	CIE coordinate		EQE_{max} [%]
64a	474	–	–	(0.15, 0.23)		25.4

sizing azahelicenes and diaza[8]circulenes **65a**–**d** [24] (Table 22). These molecules exhibited distinct Cotton effects and CPL, with $|g_{lum}|$ reaching up to 1.6×10^{-3}. This approach offers a generalizable route to structurally diverse chiral polycyclic aromatic hydrocarbons (PAHs) with strong chiroptical responses. Concurrently, Tanaka's group achieved the enantioselective synthesis of aza[6]- and aza[7]helicene-like molecules via Rh(I)/chiral bisphosphine-catalyzed [2 + 2 + 2] cycloaddition [80]. The resulting S-shaped double aza[6]helicene-like compound **66** displayed high enantiomeric excess (up to 89% ee), pronounced chiroptical activity ($|g_{abs}| = 0.0054–0.0056$), and substantial Φ_F of 0.21–0.32 under both neutral and acidic conditions. This work exemplifies the power of transition-metal catalysis for constructing enantioenriched helicenes with tunable photophysical properties. These contributions from 2021 underscore the synthetic versatility and functional diversity of helicene-based systems, spanning electrochromism, thermally activated delayed fluorescence, and circularly polarized luminescence. Such structural innovations provide valuable frameworks for the development of next-generation chiral optoelectronic materials.

In 2022, Furuta's group developed a one-pot synthetic protocol to access (NH)-phenanthridinone derivatives and chiral amide-functionalized [7]helicene-like molecules **67a**,**b** from biaryl dicarboxylic acids, employing a Curtius rearrangement followed by basic hydrolysis [81] (Table 23). Notably, when chalcogen-containing substrates were used, the process afforded phosphorus ester derivatives of aza[5]helicenes. The chiral nature of the products was confirmed by optical rotation and CD measurements. In parallel, Soni's group established an efficient three-step synthesis of coumarin-containing hetero[5]- and [6]helicene-like structures **68a**–**g** in high yields [82]. These compounds display diverse photophysical behaviors: compound **68d** emits yellow fluorescence in both solution and solid state, exhibiting solvatofluorochromism due to a twisted intramolecular charge transfer (TICT) mechanism, while compound **68e** emits blue light ($\Phi_F = 0.37$) and demonstrates pronounced AIE in the solid state. Concurrently, Jiang's group reported **69b**, the first hetero[4]helicene-type molecule exhibiting both CPL and TADF [83]. This compound displays a high Φ_F of 0.51 and a $|g_{lum}|$ of 1.2×10^{-3}. OLED devices fabricated using **69b** emit sky-blue light with a peak EQE of 10.6% and $|g_{EL}|$ values up to 1.6×10^{-3}. Collectively, these studies demonstrate the versatility of helicene-inspired architectures for constructing multifunctional chiral optoelectronic materials, highlighting their growing relevance in next-generation circularly polarized OLED technologies.

Takizawa and co-workers have pioneered electrochemical strategies for synthesizing structurally diverse hetero[7]helicenes with tunable chiroptical properties and excellent configurational stability. In 2022, they introduced two electrochemical routes to construct aza-oxa-dehydro[7]helicenes, yielding helicenes with high racemization barriers and notable chiral stability [84]. The quasicirculenes **70a** and **70b** demonstrated strong blue CPL activity, with $|g_{lum}|$ values of 2.5×10^{-3} at 433 nm and 2.4×10^{-3} at 418 nm, respectively (Table 24). Building on this, the team achieved the enantioselective synthesis of heterodehydrospiroenes on a gram scale using chiral vanadium(V) complexes – marking a significant advancement in asymmetric electrochemical catalysis. In a complementary study that same year, they reported a two-step electrochemical synthesis of a double aza-oxa[7]helicene via oxidative coupling followed by dehydrative cyclization [85]. The resulting meso-isomer (*P*,*M*)**-71** emerged as the major product, exhibiting dual emission bands at 415 and 440 nm and solvent-independent absorption at 407 nm. Expanding the structural diversity, the group developed a two-pot synthesis of unsymmetrical hetero[7]helicenes **72a**–**g** in 2023 [86], employing *p*-benzoquinone and *N*-aryl-2-naphthylamines through acid-promoted cyclization followed by electrochemical domino reactions. This method produced six compounds with yields ranging from 33–45%, all featuring extended π-conjugation and distinct photophysical characteristics. Furthermore, they established a mild electrochemical protocol for synthesizing oxaza[7]helicenes incorporating pyrrole and furan units [87]. This method afforded products in 50–86% yield with Faradaic efficiencies up to 77%. Among them, derivative **73** exhibited CPL activity ($|g_{lum}| = 3.0 \times 10^{-4}$), showcasing the ability to modulate chirop-

Table 23: Structures and optical properties of **67a,b**, **68a–g**, and **69a**,**b**.

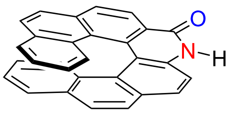

67a

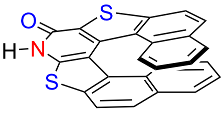

67b

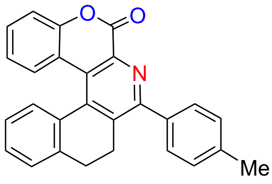

68a

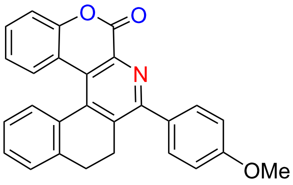

68b

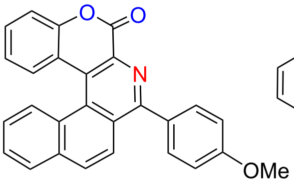

68c

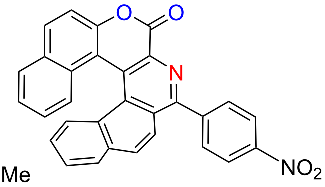

68d

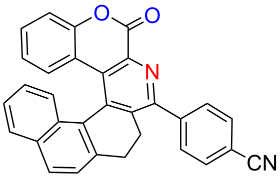

68e

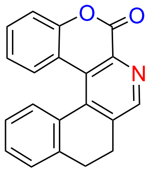

68f

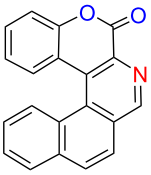

68g

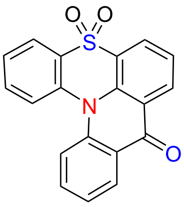

69a

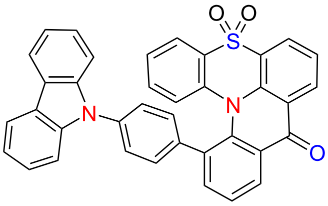

69b

compound	$\lambda_{abs(max)}$ [nm]	$\lambda_{em(max)}$ [nm]	Φ_F	$\lvert g_{abs} \rvert$	$\lvert g_{lum} \rvert$
67a	–	–	–	–	–
67b	–	–	–	–	–
68a	295	411	0.08	–	–
68b	309	422	0.10	–	–
68c	328	439	0.03	–	–
68d	394	514	0.22	–	–
68e	320	423	0.37	–	–
68f	318	389	0.01	–	–
68g	317	411	0.04	–	–
69a	397	431	–	–	–
69b	400	446	0.51	–	1.2×10^{-3}

device	$\lambda_{EL(max)}$ [nm]	$\lvert g_{EL} \rvert$	FWHM [nm]	CIE coordinate	EQE$_{max}$ [%]
69b	488	1.6×10^{-3}	72	(0.17, 0.34)	10.6

tical responses via heteroatom integration. These studies underscore the versatility of electrochemical synthesis in enabling precise structural modulation of heterohelicenes, facilitating access to high-performance chiral optoelectronic materials.

In 2023, Zhang's group introduced a new class of helically chiral double hetero[4]helicenes **74a** and **74b** exhibiting CP-TADF, constructed on a distinct donor–acceptor core architecture [88] (Table 25). These compounds demonstrate excellent configurational stability and robust CPL signals both in solution and in solid-state films, with a $\lvert g_{lum} \rvert$ of 3.1×10^{-3}. Corresponding CP-OLEDs based on compound **74a** achieved outstanding device performance, reaching a maximum EQE of 20.03% and a $\lvert g_{EL} \rvert$ of 2.9×10^{-3} – underscoring their considerable potential for advanced chiral optoelectronic applications.

Table 24: Structures and optical properties of **70a**,**b**, **71**, **72a**–**g**, and **73**.

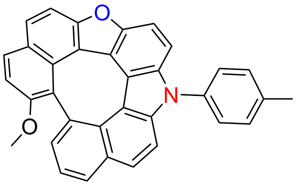

70a

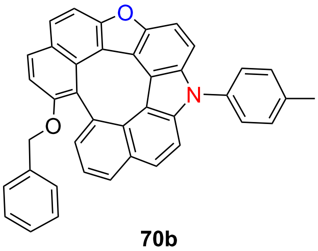

70b

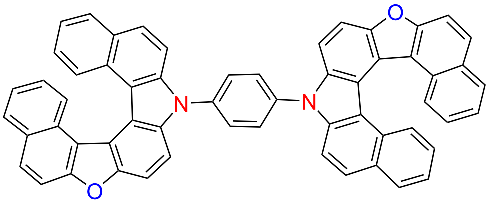

71

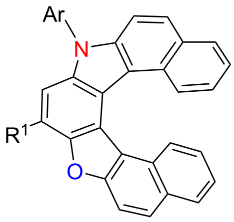

	Ar =	R^1 =
72a	Ph	H
72b	*p*-tolyl	H
72c	*p*-tolyl	H

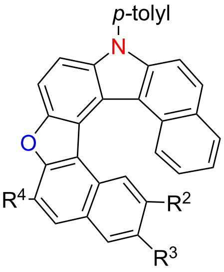

	R^2 =	R^3 =	R^4 =
72d	H	H	H
72e	H	Bpin	H
72f	Ph	H	H
72g	H	H	COOMe

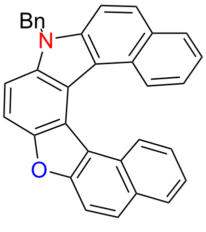

73

compound	$\lambda_{abs(max)}$ [nm]	$\lambda_{em(max)}$ [nm]	Φ_F	$\lvert g_{abs}\rvert$	$\lvert g_{lum}\rvert$
70a	402	433	0.25	–	2.5×10^{-3}
70b	–	418	0.16	–	2.4×10^{-3}
71	407	415, 440	–	–	–
72a	406	439	–	–	–
72b	403	440	0.065	–	–
72c	402	440	–	–	–
72d	413	450	–	–	–
72e	401	440	–	–	–
72g	405	440	–	–	–
73	–	–	–	–	3.0×10^{-4}

Building upon this framework, in 2024, the same group developed a novel cove-region bridging strategy to construct double hetero[4]helicenes with enhanced structural rigidity and persistent chirality [89]. By selectively modifying the bay regions of the SPZ (spiro[fluorene-9,9'-xanthene]) scaffold, they successfully converted initially non-emissive helicenes into efficient TADF luminophores with tunable emission wavelengths ranging from sky-blue to deep red. Particularly, the enantiomeric forms of the **75b** derivatives emerged as rare examples of red-emissive CPL materials. This innovative design approach offers a versatile and modular platform for engineering chiral multi-helicene systems with customizable optoelectronic properties, paving the way for their deployment in next-generation CPL-active materials and high-performance CP-OLED devices.

In 2024, Jančařík and co-workers introduced an intramolecular radical cyclization strategy to synthesize highly luminescent tetraceno[6]helicenone and its aza analogue **76** [90] (Table 26). The incorporation of a carbonyl group into the helicene backbone substantially enhanced fluorescence quantum yields and red-shifted the emission into the visible region. The aza analogue demonstrated promising performance in OLEDs, confirming its potential for optoelectronic applications. Concurrently, Shirinian's group synthesized a series of nitrogen-functionalized quinoline (NFQ)-based aza-oxa[5]helicenes **77a**–**f** exhibiting excellent UV stability and solvent-dependent fluorescence [91]. Protonation significantly enhanced their emission intensity, and the presence of nitrogen facilitated further structural derivatization. In the same year, Alcarazo's group reported an enantioselective gold-catalyzed synthesis of compound **78**, achieving a high enantiomeric excess [92]. They further investigated various post-synthetic modification strategies, demonstrating their potential for application in chiral photonic materials. Collectively, these advances underscore the power of structural tailoring, heteroatom incorporation, and en-

Table 25: Structures and optical properties of **74a**,**b** and **75a**–**c**.

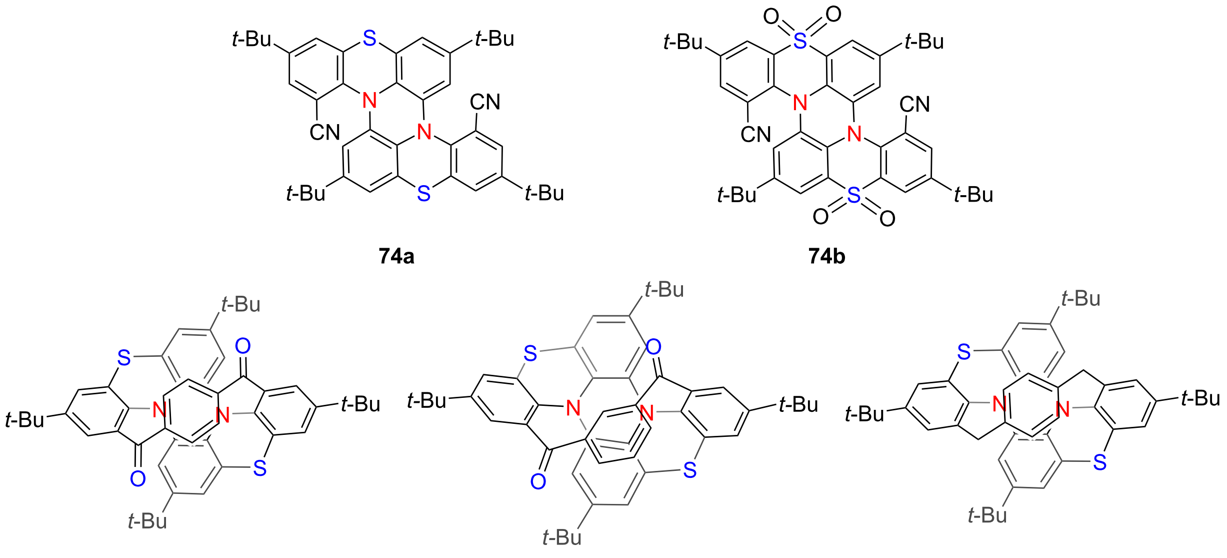

74a **74b**

75a **75b** **75c**

compound	$\lambda_{abs(max)}$ [nm]	$\lambda_{em(max)}$ [nm]	Φ_F	$\lvert g_{abs}\rvert$	$\lvert g_{lum}\rvert$
74a	406	493	0.13/0.67[a]	–	$3.1 \times 10^{-3,a}$
74b	357	450	0.07/0.22[a]	–	–
75a	612	–	–	–	–
75b	495	656	0.02	–	2.7×10^{-3}
75c	436	480	0.09	–	2.5×10^{-2}

device	$\lambda_{EL(max)}$ [nm]	$\lvert g_{EL}\rvert$	FWHM [nm]	CIE coordinate	EQE_{max} [%]
(*M*,*M*)-**74a**	500	2.9×10^{-3}	82	(0.24, 0.50)	20.03
rac-**74a**	500	–	81	(0.24, 0.49)	20.00

[a] Detected as 20 wt % doped films with the mCBP host.

antioselective strategies in finely tuning the photophysical and chiroptical properties of helicenes, providing a versatile foundation for the development of high-performance chiral optoelectronic materials.

Conclusion

Nitrogen-doped helicenes and their heteroatom co-doped analogues constitute a rapidly advancing class of chiral π-conjugated materials, distinguished by exceptional structural tunability, photophysical diversity, and chiroptical functionality. The integration of nitrogen – and its synergistic pairing with heteroatoms such as boron, oxygen, sulfur, and selenium – has significantly expanded the molecular design space, enabling precise control over redox behavior, emission wavelength, CPL, and responsiveness to thermal or redox stimuli. These heteroatom modifications have led to remarkable breakthroughs, including near-unity PLQYs, ultranarrow emission bands, $\lvert g_{lum}\rvert$ values exceeding 10^{-3}, and unprecedented B_{CPL}, particularly in the visible to near-infrared (NIR) spectral regions.

Recent advances in synthetic methodology – including electrochemical, Scholl-type, and enantioselective catalytic strategies – have further enabled access to structurally complex helicene topologies with enhanced configurational stability and integrated multifunctionality. These developments have facilitated a growing range of applications in CP-OLEDs, molecular sensing, chiral switches, and photonic devices. Moving forward, key challenges remain, such as mitigating spectral broadening in red/NIR emission, enhancing the chemical and photostability of electron-deficient helicenes, and developing sustainable, scalable synthetic approaches. The integration of computational design with multifunctional molecular engineering is expected to accelerate the deployment of helicene-based materials in next-generation technologies spanning chiral optoelec-

Table 26: Structures and optical properties of **76**, **77a–f**, and **78**.[a]

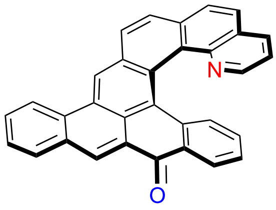

76

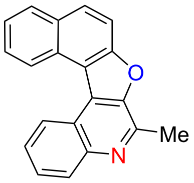

77a

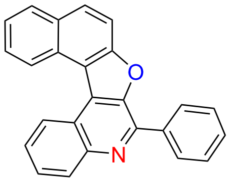

77b

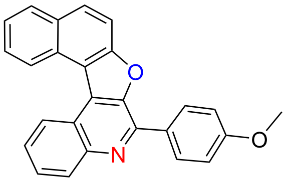

77c

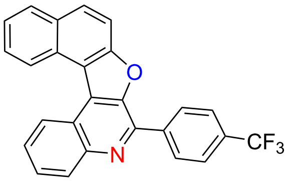

77d

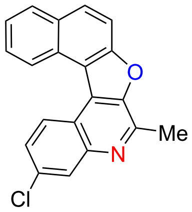

77e

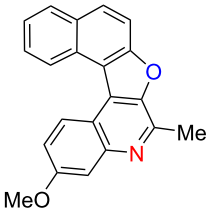

77f

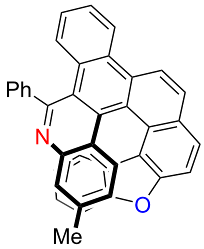

78

compound	$\lambda_{abs(max)}$ [nm]	$\lambda_{em(max)}$ [nm]	Φ_F
76	483	561	0.43
77a in $CHCl_3$	352	379, 399	0.39
77b in $CHCl_3$	359	379, 392	0.04
77c in $CHCl_3$	360	397	0.08
77d in $CHCl_3$	362	390, 403	0.09
77a in heptane	347	388	0.21
77e in heptane	348	391	0.20
77f in heptane	348, 358	383	0.19
77a in toluene	352	394, 421	0.56
77e in toluene	353	380, 400	0.44
77f in toluene	353	388	0.28
77a in acetonitrile	348	375	0.48
77e in acetonitrile	348	383	0.48
77f in acetonitrile	349	391	0.42
77a in methanol	351	383	0.48
77e in methanol	349	391	0.47
77f in methanol	352	396	0.27

device	$\lambda_{EL(max)}$ [nm]	$\lvert g_{EL}\rvert$	FWHM [nm]	CIE coordinate	EQE_{max} [%]
76	580	–	103	–	0.15
76:MADN 95:5	550	–	93	–	0.7

[a]No g_{abs} or g_{lum} values were reported, no optical characterization for **78**.

tronics, bioimaging, spintronics, and quantum information science.

Funding

Prof. Dr. H.-Y. Gong acknowledges the financial support provided by the National Natural Science Foundation of China (Grant No. 92156009). Nai-Te Yao appreciates for the financial support from the Interdisciplinary Research Foundation for Doctoral Candidates of Beijing Normal University (Grant No. BNUXKJC2407).

Author Contributions

Meng Qiu: resources; writing – original draft. Jing Du: writing – original draft. Nai-Te Yao: funding acquisition; writing –

original draft. Xin-Yue Wang: writing – original draft. Han-Yuan Gong: conceptualization; funding acquisition; writing – review & editing.

ORCID® iDs

Nai-Te Yao - https://orcid.org/0000-0003-0740-2275
Han-Yuan Gong - https://orcid.org/0000-0003-4168-7657

Data Availability Statement

Data sharing is not applicable as no new data was generated or analyzed in this study.

References

1. Chen, J.; Captain, B.; Takenaka, N. *Org. Lett.* **2011,** *13,* 1654–1657. doi:10.1021/ol200102c
2. Peng, Z.; Takenaka, N. *Chem. Rec.* **2013,** *13,* 28–42. doi:10.1002/tcr.201200010
3. Zhang, G.; Zhang, J.; Tao, Y.; Gan, F.; Lin, G.; Liang, J.; Shen, C.; Zhang, Y.; Qiu, H. *Nat. Commun.* **2024,** *15,* 5469. doi:10.1038/s41467-024-49865-y
4. Isla, H.; Saleh, N.; Ou-Yang, J.-K.; Dhbaibi, K.; Jean, M.; Dziurka, M.; Favereau, L.; Vanthuyne, N.; Toupet, L.; Jamoussi, B.; Srebro-Hooper, M.; Crassous, J. *J. Org. Chem.* **2019,** *84,* 5383–5393. doi:10.1021/acs.joc.9b00389
5. Meng, D.; Fu, H.; Xiao, C.; Meng, X.; Winands, T.; Ma, W.; Wei, W.; Fan, B.; Huo, L.; Doltsinis, N. L.; Li, Y.; Sun, Y.; Wang, Z. *J. Am. Chem. Soc.* **2016,** *138,* 10184–10190. doi:10.1021/jacs.6b04368
6. Jakubec, M.; Storch, J. *J. Org. Chem.* **2020,** *85,* 13415–13428. doi:10.1021/acs.joc.0c01837
7. Wang, X.-Y.; Yao, X.; Narita, A.; Müllen, K. *Acc. Chem. Res.* **2019,** *52,* 2491–2505. doi:10.1021/acs.accounts.9b00322
8. Feng, Y.; Xu, Y.; Qu, C.; Wang, Q.; Ye, K.; Liu, Y.; Wang, Y. *Adv. Mater. (Weinheim, Ger.)* **2024,** *36,* 2403061. doi:10.1002/adma.202403061
9. Zhu, D.; Jiang, W.; Ma, Z.; Feng, J.; Zhan, X.; Lu, C.; Liu, J.; Liu, J.; Hu, Y.; Wang, D.; Zhao, Y. S.; Wang, J.; Wang, Z.; Jiang, L. *Nat. Commun.* **2022,** *13,* 3454. doi:10.1038/s41467-022-31186-7
10. Kundu, D.; Rio, N. D.; Crassous, J. *Acc. Chem. Res.* **2024,** *57,* 2941–2952. doi:10.1021/acs.accounts.4c00275
11. Dhbaibi, K.; Favereau, L.; Crassous, J. *Chem. Rev.* **2019,** *119,* 8846–8953. doi:10.1021/acs.chemrev.9b00033
12. Nowak-Król, A.; Geppert, P. T.; Naveen, K. R. *Chem. Sci.* **2024,** *15,* 7408–7440. doi:10.1039/d4sc01083c
13. Maeda, C.; Ema, T. *Chem. Commun.* **2025,** *61,* 4757–4773. doi:10.1039/d4cc06307d
14. Reger, D.; Haines, P.; Amsharov, K. Y.; Schmidt, J. A.; Ullrich, T.; Bönisch, S.; Hampel, F.; Görling, A.; Nelson, J.; Jelfs, K. E.; Guldi, D. M.; Jux, N. *Angew. Chem., Int. Ed.* **2021,** *60,* 18073–18081. doi:10.1002/anie.202103253
15. Qiu, S.; Valdivia, A. C.; Zhuang, W.; Hung, F.-F.; Che, C.-M.; Casado, J.; Liu, J. *J. Am. Chem. Soc.* **2024,** *146,* 16161–16172. doi:10.1021/jacs.4c03815
16. Wang, X.-Y.; Bai, J.; Shen, Y.-J.; Li, Z.-A.; Gong, H.-Y. *Angew. Chem., Int. Ed.* **2025,** *64,* e202417745. doi:10.1002/anie.202417745
17. Kumar, V.; Venugopal, G.; Jadhav, A. B.; Dongre, S. D.; Gonnade, R.; Kumar, J.; Ruer, P. C.; Hupp, B.; Steffen, A.; Babu, S. S. *Angew. Chem., Int. Ed.* **2025,** *64,* e202422125. doi:10.1002/anie.202422125
18. Yanagi, T.; Tanaka, T.; Yorimitsu, H. *Chem. Sci.* **2021,** *12,* 2784–2793. doi:10.1039/d1sc00044f
19. Taniguchi, T.; Nishii, Y.; Mori, T.; Nakayama, K.-i.; Miura, M. *Chem. – Eur. J.* **2021,** *27,* 7356–7361. doi:10.1002/chem.202100327
20. Yen-Pon, E.; Buttard, F.; Frédéric, L.; Thuéry, P.; Taran, F.; Pieters, G.; Champagne, P. A.; Audisio, D. *JACS Au* **2021,** *1,* 807–818. doi:10.1021/jacsau.1c00084
21. Kos, M.; Rodríguez, R.; Storch, J.; Sýkora, J.; Caytan, E.; Cordier, M.; Císařová, I.; Vanthuyne, N.; Williams, J. A. G.; Žádný, J.; Církva, V.; Crassous, J. *Inorg. Chem.* **2021,** *60,* 11838–11851. doi:10.1021/acs.inorgchem.1c01379
22. Yang, S.-Y.; Zou, S.-N.; Kong, F.-C.; Liao, X.-J.; Qu, Y.-K.; Feng, Z.-Q.; Zheng, Y.-X.; Jiang, Z.-Q.; Liao, L.-S. *Chem. Commun.* **2021,** *57,* 11041–11044. doi:10.1039/d1cc04405b
23. Petdum, A.; Kaewnok, N.; Panchan, W.; Sahasithiwat, S.; Sooksimuang, T.; Sirirak, J.; Chaiyaveij, D.; Wanichacheva, N. *J. Mol. Struct.* **2021,** *1245,* 131250. doi:10.1016/j.molstruc.2021.131250
24. Maeda, C.; Nomoto, S.; Akiyama, K.; Tanaka, T.; Ema, T. *Chem. – Eur. J.* **2021,** *27,* 15699–15705. doi:10.1002/chem.202102269
25. Maeda, C.; Yasutomo, I.; Ema, T. *Angew. Chem., Int. Ed.* **2024,** *63,* e202404149. doi:10.1002/anie.202404149
26. Wu, Y.-F.; Ying, S.-W.; Su, L.-Y.; Du, J.-J.; Zhang, L.; Chen, B.-W.; Tian, H.-R.; Xu, H.; Zhang, M.-L.; Yan, X.; Zhang, Q.; Xie, S.-Y.; Zheng, L.-S. *J. Am. Chem. Soc.* **2022,** *144,* 10736–10742. doi:10.1021/jacs.2c00794
27. Váňa, L.; Jakubec, M.; Sýkora, J.; Císařová, I.; Žádný, J.; Storch, J.; Církva, V. *J. Org. Chem.* **2022,** *87,* 7150–7166. doi:10.1021/acs.joc.2c00375
28. Gong, X.; Li, C.; Cai, Z.; Wan, X.; Qian, H.; Yang, G. *J. Org. Chem.* **2022,** *87,* 8406–8412. doi:10.1021/acs.joc.2c00371
29. Hong, J.; Xiao, X.; Liu, H.; Dmitrieva, E.; Popov, A. A.; Yu, Z.; Li, M.-D.; Ohto, T.; Liu, J.; Narita, A.; Liu, P.; Tada, H.; Cao, X.-Y.; Wang, X.-Y.; Zou, Y.; Müllen, K.; Hu, Y. *Chem. – Eur. J.* **2022,** *28,* e202202243. doi:10.1002/chem.202202243
30. Yu, Z.; Shi, G.; Wang, K.-P.; Xu, L.-Z.; Chen, S.; Hu, Z.-Q. *Tetrahedron* **2023,** *130,* 133178. doi:10.1016/j.tet.2022.133178
31. Ausekle, E.; Ehlers, P.; Villinger, A.; Langer, P. *Chem. – Eur. J.* **2024,** *30,* e202303225. doi:10.1002/chem.202303225
32. Liu, W.; Qin, T.; Xie, W.; Zhou, J.; Ye, Z.; Yang, X. *Angew. Chem., Int. Ed.* **2023,** *62,* e202303430. doi:10.1002/anie.202303430
33. Qiua, S.; Liu, J. *Org. Mater.* **2023,** *5,* 202–206. doi:10.1055/a-2172-1216
34. Nishimura, Y.; Harimoto, T.; Suzuki, T.; Ishigaki, Y. *Chem. – Eur. J.* **2023,** *29,* e202301759. doi:10.1002/chem.202301759
35. Li, C.; Zhang, C.; Li, P.; Jia, Y.; Duan, J.; Liu, M.; Zhang, N.; Chen, P. *Angew. Chem., Int. Ed.* **2023,** *62,* e202302019. doi:10.1002/anie.202302019
36. Shi, Y.; Li, C.; Di, J.; Xue, Y.; Jia, Y.; Duan, J.; Hu, X.; Tian, Y.; Li, Y.; Sun, C.; Zhang, N.; Xiong, Y.; Jin, T.; Chen, P. *Angew. Chem., Int. Ed.* **2024,** *63,* e202402800. doi:10.1002/anie.202402800
37. Gan, F.; Zhang, G.; Liang, J.; Shen, C.; Qiu, H. *Angew. Chem., Int. Ed.* **2024,** *63,* e202320076. doi:10.1002/anie.202320076
38. Gross, M.; Zhang, F.; Arnold, M. E.; Ravat, P.; Kuehne, A. J. C. *Adv. Opt. Mater.* **2024,** *12,* 2301707. doi:10.1002/adom.202301707

39. Wang, Y.; Liao, Q.; Feng, Y.; Wang, Y.; Li, Y.; Meng, Q. *Chem. Commun.* **2024,** *60,* 8292–8295. doi:10.1039/d4cc02747g
40. Xia, Y.; Jiang, L.; Yang, Q.; Yu, X.; Chen, F. *Chin. J. Org. Chem.* **2024,** *44,* 2841–2846. doi:10.6023/cjoc202405006
41. Yadagiri, B.; Kumar, V.; Singh, S. P. *Mater. Adv.* **2024,** *5,* 2328–2334. doi:10.1039/d3ma01045g
42. Huo, G.-F.; Xu, W.-T.; Han, Y.; Zhu, J.; Hou, X.; Fan, W.; Ni, Y.; Wu, S.; Yang, H.-B.; Wu, J. *Angew. Chem., Int. Ed.* **2024,** *63,* e202403149. doi:10.1002/anie.202403149
43. Borstelmann, J.; Schneider, L.; Rominger, F.; Deschler, F.; Kivala, M. *Angew. Chem., Int. Ed.* **2024,** *63,* e202405570. doi:10.1002/anie.202405570
44. Borstelmann, J.; Zank, S.; Krug, M.; Berger, G.; Fröhlich, N.; Glotz, G.; Gnannt, F.; Schneider, L.; Rominger, F.; Deschler, F.; Clark, T.; Gescheidt, G.; Guldi, D. M.; Kivala, M. *Angew. Chem., Int. Ed.* **2025,** *64,* e202423516. doi:10.1002/anie.202423516
45. Matsuo, Y.; Gon, M.; Tanaka, K.; Seki, S.; Tanaka, T. *J. Am. Chem. Soc.* **2024,** *146,* 17428–17437. doi:10.1021/jacs.4c05156
46. Matsuo, Y.; Gon, M.; Tanaka, K.; Seki, S.; Tanaka, T. *Chem. – Asian J.* **2024,** *19,* e202400134. doi:10.1002/asia.202400134
47. Matsuo, Y.; Seki, S.; Tanaka, T. *Chem. Lett.* **2024,** *53,* upae159. doi:10.1093/chemle/upae159
48. Kusy, D.; Górski, K.; Bertocchi, F.; Galli, M.; Vanthuyne, N.; Terenziani, F.; Gryko, D. T. *Chem. – Eur. J.* **2025,** *31,* e202404632. doi:10.1002/chem.202404632
49. Maeda, C.; Nagahata, K.; Shirakawa, T.; Ema, T. *Angew. Chem., Int. Ed.* **2020,** *59,* 7813–7817. doi:10.1002/anie.202001186
50. Maeda, C.; Michishita, S.; Yasutomo, I.; Ema, T. *Angew. Chem., Int. Ed.* **2025,** *64,* e202418546. doi:10.1002/anie.202418546
51. Oda, S.; Kawakami, B.; Yamasaki, Y.; Matsumoto, R.; Yoshioka, M.; Fukushima, D.; Nakatsuka, S.; Hatakeyama, T. *J. Am. Chem. Soc.* **2022,** *144,* 106–112. doi:10.1021/jacs.1c11659
52. Zhang, Y.; Zhang, D.; Huang, T.; Gillett, A. J.; Liu, Y.; Hu, D.; Cui, L.; Bin, Z.; Li, G.; Wei, J.; Duan, L. *Angew. Chem., Int. Ed.* **2021,** *60,* 20498–20503. doi:10.1002/anie.202107848
53. Li, J.-K.; Chen, X.-Y.; Guo, Y.-L.; Wang, X.-C.; Sue, A. C.-H.; Cao, X.-Y.; Wang, X.-Y. *J. Am. Chem. Soc.* **2021,** *143,* 17958–17963. doi:10.1021/jacs.1c09058
54. Meng, G.; Zhou, J.; Han, X.-S.; Zhao, W.; Zhang, Y.; Li, M.; Chen, C.-F.; Zhang, D.; Duan, L. *Adv. Mater. (Weinheim, Ger.)* **2024,** *36,* 2307420. doi:10.1002/adma.202307420
55. Yang, W.; Li, N.; Miao, J.; Zhan, L.; Gong, S.; Huang, Z.; Yang, C. *CCS Chem.* **2022,** *4,* 3463–3471. doi:10.31635/ccschem.022.202101661
56. Ye, Z.; Wu, H.; Xu, Y.; Hua, T.; Chen, G.; Chen, Z.; Yin, X.; Huang, M.; Xu, K.; Song, X.; Huang, Z.; Lv, X.; Miao, J.; Cao, X.; Yang, C. *Adv. Mater. (Weinheim, Ger.)* **2024,** *36,* 2308314. doi:10.1002/adma.202308314
57. Zhang, X.; Rauch, F.; Niedens, J.; da Silva, R. B.; Friedrich, A.; Nowak-Król, A.; Garden, S. J.; Marder, T. B. *J. Am. Chem. Soc.* **2022,** *144,* 22316–22324. doi:10.1021/jacs.2c10865
58. Xu, Y.; Ni, Z.; Xiao, Y.; Chen, Z.; Wang, S.; Gai, L.; Zheng, Y.-X.; Shen, Z.; Lu, H.; Guo, Z. *Angew. Chem., Int. Ed.* **2023,** *62,* e202218023. doi:10.1002/anie.202218023
59. Yu, C.-Y.; Xu, Y.; Bi, X.; Ni, Z.; Xiao, H.; Hu, X.; Lu, H. *Tetrahedron Lett.* **2023,** *133,* 154833. doi:10.1016/j.tetlet.2023.154833
60. Kage, Y.; Jiang, Y.; Minakuchi, N.; Mori, S.; Shimizu, S. *Chem. Commun.* **2024,** *60,* 3543–3546. doi:10.1039/d4cc00168k
61. Tan, D.; Dong, J.; Ma, T.; Feng, Q.; Wang, S.; Yang, D.-T. *Angew. Chem., Int. Ed.* **2023,** *62,* e202304711. doi:10.1002/anie.202304711
62. Huang, T.; Yuan, L.; Lu, X.; Qu, Y.; Qu, C.; Xu, Y.; Zheng, Y.-X.; Wang, Y. *Chem. Sci.* **2024,** *15,* 15170–15177. doi:10.1039/d4sc03854a
63. Cheng, H.; Lan, J.; Yang, Y.; Bin, Z. *Mater. Horiz.* **2024,** *11,* 4674–4680. doi:10.1039/d4mh00634h
64. Guo, W.-C.; Zhao, W.-L.; Tan, K.-K.; Li, M.; Chen, C.-F. *Angew. Chem., Int. Ed.* **2024,** *63,* e202401835. doi:10.1002/anie.202401835
65. Ju, Y.-Y.; Xie, L.-E.; Xing, J.-F.; Deng, Q.-S.; Chen, X.-W.; Huang, L.-X.; Nie, G.-H.; Tan, Y.-Z.; Zhang, B. *Angew. Chem., Int. Ed.* **2025,** *64,* e202414383. doi:10.1002/anie.202414383
66. Liu, M.; Li, C.; Liao, G.; Zhao, F.; Yao, C.; Wang, N.; Yin, X. *Chem. – Eur. J.* **2024,** *30,* e202402257. doi:10.1002/chem.202402257
67. Yu, Y.; Wang, C.; Hung, F.-F.; Chen, C.; Pan, D.; Che, C.-M.; Liu, J. *J. Am. Chem. Soc.* **2024,** *146,* 22600–22611. doi:10.1021/jacs.4c06997
68. Yu, Y.; Wang, C.; Hung, F.-F.; Jiang, L.; Che, C.-M.; Liu, J. *Angew. Chem., Int. Ed.* **2025,** *64,* e202501645. doi:10.1002/anie.202501645
69. Saal, F.; Zhang, F.; Holzapfel, M.; Stolte, M.; Michail, E.; Moos, M.; Schmiedel, A.; Krause, A.-M.; Lambert, C.; Würthner, F.; Ravat, P. *J. Am. Chem. Soc.* **2020,** *142,* 21298–21303. doi:10.1021/jacs.0c11053
70. Saal, F.; Swain, A.; Schmiedel, A.; Holzapfel, M.; Lambert, C.; Ravat, P. *Chem. Commun.* **2023,** *59,* 14005–14008. doi:10.1039/d3cc04470j
71. Tian, X.; Shoyama, K.; Mahlmeister, B.; Brust, F.; Stolte, M.; Würthner, F. *J. Am. Chem. Soc.* **2023,** *145,* 9886–9894. doi:10.1021/jacs.3c03441
72. Sakamaki, D.; Tanaka, S.; Tanaka, K.; Takino, M.; Gon, M.; Tanaka, K.; Hirose, T.; Hirobe, D.; Yamamoto, H. M.; Fujiwara, H. *J. Phys. Chem. Lett.* **2021,** *12,* 9283–9292. doi:10.1021/acs.jpclett.1c02896
73. Tanaka, S.; Sakamaki, D.; Haruta, N.; Sato, T.; Gon, M.; Tanaka, K.; Fujiwara, H. *J. Mater. Chem. C* **2023,** *11,* 4846–4854. doi:10.1039/d3tc00871a
74. Sakamaki, D.; Inoue, Y.; Shimomura, K.; Taura, D.; Yashima, E.; Seki, S. *Tetrahedron Lett.* **2023,** *114,* 154294. doi:10.1016/j.tetlet.2022.154294
75. Zhang, Z.; Murata, Y.; Hirose, T. *Tetrahedron* **2023,** *142,* 133514. doi:10.1016/j.tet.2023.133514
76. Kumar, V.; Dongre, S. D.; Venugopal, G.; Narayanan, A.; Babu, S. S. *Chem. Commun.* **2024,** *60,* 11944–11947. doi:10.1039/d4cc03707c
77. Lousen, B.; Pedersen, S. K.; Bols, P.; Hansen, K. H.; Pedersen, M. R.; Hammerich, O.; Bondarchuk, S.; Minaev, B.; Baryshnikov, G. V.; Ågren, H.; Pittelkow, M. *Chem. – Eur. J.* **2020,** *26,* 4935–4940. doi:10.1002/chem.201905339
78. Lupi, M.; Menichetti, S.; Stagnaro, P.; Utzeri, R.; Viglianisi, C. *Synthesis* **2021,** *53,* 2602–2611. doi:10.1055/s-0040-1706743
79. Shi, Y.; Yang, G.; Shen, B.; Yang, Y.; Yan, L.; Yang, F.; Liu, J.; Liao, X.; Yu, P.; Bin, Z.; You, J. *J. Am. Chem. Soc.* **2021,** *143,* 21066–21076. doi:10.1021/jacs.1c11277
80. Hanada, K.; Nogami, J.; Miyamoto, K.; Hayase, N.; Nagashima, Y.; Tanaka, Y.; Muranaka, A.; Uchiyama, M.; Tanaka, K. *Chem. – Eur. J.* **2021,** *27,* 9313–9319. doi:10.1002/chem.202005479

81. Murai, T.; Xing, Y.; Kurokawa, M.; Kuribayashi, T.; Nikaido, M.; Elboray, E. E.; Hamada, S.; Kobayashi, Y.; Sasamori, T.; Kawabata, T.; Furuta, T. *J. Org. Chem.* **2022,** *87,* 5510–5521. doi:10.1021/acs.joc.1c02769
82. Soni, R.; Soman, S. S. *Asian J. Org. Chem.* **2022,** *11,* e202100770. doi:10.1002/ajoc.202100770
83. Yang, S.-Y.; Tian, Q.-S.; Liao, X.-J.; Wu, Z.-G.; Shen, W.-S.; Yu, Y.-J.; Feng, Z.-Q.; Zheng, Y.-X.; Jiang, Z.-Q.; Liao, L.-S. *J. Mater. Chem. C* **2022,** *10,* 4393–4401. doi:10.1039/d1tc06125a
84. Khalid, M. I.; Salem, M. S. H.; Sako, M.; Kondo, M.; Sasai, H.; Takizawa, S. *Commun. Chem.* **2022,** *5,* 166. doi:10.1038/s42004-022-00780-7
85. Salem, M. S. H.; Sabri, A.; Khalid, M. I.; Sasai, H.; Takizawa, S. *Molecules* **2022,** *27,* 9068. doi:10.3390/molecules27249068
86. Salem, M. S. H.; Khalid, M. I.; Sasai, H.; Takizawa, S. *Tetrahedron* **2023,** *133,* 133266. doi:10.1016/j.tet.2023.133266
87. Salem, M. S. H.; Khalid, M. I.; Sako, M.; Higashida, K.; Lacroix, C.; Kondo, M.; Takishima, R.; Taniguchi, T.; Miura, M.; Vo-Thanh, G.; Sasai, H.; Takizawa, S. *Adv. Synth. Catal.* **2023,** *365,* 373–380. doi:10.1002/adsc.202201262
88. Qu, C.; Zhu, Y.; Liang, L.; Ye, K.; Zhang, Y.; Zhang, H.; Zhang, Z.; Duan, L.; Wang, Y. *Adv. Opt. Mater.* **2023,** *11,* 2203030. doi:10.1002/adom.202203030
89. Qu, C.; Xu, Y.; Wang, Y.; Nie, Y.; Ye, K.; Zhang, H.; Zhang, Z. *Angew. Chem., Int. Ed.* **2024,** *63,* e202400661. doi:10.1002/anie.202400661
90. Sturm, L.; Banasiewicz, M.; Deperasinska, I.; Kozankiewicz, B.; Morawski, O.; Dechambenoit, P.; Bock, H.; Nagata, Y.; Salvagnac, L.; Séguy, I.; Šámal, M.; Jančařík, A. *Chem. – Eur. J.* **2024,** *30,* e202403482. doi:10.1002/chem.202403482
91. Balakhonov, R. Y.; Gaeva, E. B.; Mekeda, I. S.; Dolotov, R. A.; Metelitsa, A. V.; Shirinian, V. Z. *Dyes Pigm.* **2024,** *225,* 112032. doi:10.1016/j.dyepig.2024.112032
92. Fu, W.; Pelliccioli, V.; Casares-López, R.; Cuerva, J. M.; Simon, M.; Golz, C.; Alcarazo, M. *CCS Chem.* **2024,** *6,* 2439–2451. doi:10.31635/ccschem.024.202404088

License and Terms

The definitive version of this article is the electronic one which can be found at:
https://doi.org/10.3762/bjoc.21.106

BEILSTEIN JOURNAL OF ORGANIC CHEMISTRY

Wittig reaction of cyclobisbiphenylenecarbonyl

Taito Moribe[1], Junichiro Hirano[1], Hideaki Takano[1,2], Hiroshi Shinokubo[1,3]
and Norihito Fukui*[1]

Letter

Open Access

Address:
[1]Department of Molecular and Macromolecular Chemistry, Graduate School of Engineering, Nagoya University, Furo-cho, Chikusa-ku, Nagoya, Aichi 464-8603, Japan, [2]Institute for Advanced Research, Nagoya University, Furo-cho, Chikusa-ku, Nagoya, Aichi 464-8601, Japan and [3]Research Institute for Quantum and Chemical Innovation, Institutes of Innovation for Future Society and Integrated Research Consortium on Chemical Science (IRCCS), Nagoya University, Furo-cho, Chikusa-ku, Nagoya, 464-8603, Japan

Email:
Norihito Fukui* - fukui@chembio.nagoya-u.ac.jp

* Corresponding author

Keywords:
bathtub; chirality; cyclobisbiphenylenecarbonyl; figure-eight; Wittig reaction

Beilstein J. Org. Chem. **2025,** *21,* 1454–1461.
https://doi.org/10.3762/bjoc.21.107

Received: 28 March 2025
Accepted: 04 July 2025
Published: 14 July 2025

This article is part of the thematic issue "Non-central chirality in organic chemistry".

Associate Editor: N. Yoshikai

Abstract

Cyclobisbiphenylenecarbonyl (CBBC) represents a readily available chiral figure-eight macrocycle containing two carbonyl groups. However, the transformation of the carbonyl groups has been unexplored. Herein, we conducted the Wittig reaction of CBBC with methylenetriphenylphosphorane to furnish two chiral macrocycles containing one or two exocyclic olefin units. Owing to the transformation of carbonyl groups, the resulting products exhibit several unique physical and chemical properties: (1) the enhancement of configurational stability, (2) the appearance of fluorescence, and (3) the reductive carbon–carbon-bond formation between carbonyl and alkene units.

Introduction

Figure-eight π-conjugated molecules represent chiral macrocycles with a twisted crossover structure [1-15]. Various figure-eight π-systems including aromatic hydrocarbons, belt-type extended π-systems, and porphyrinoids have been reported. The structural twisting in figure-eight macrocycles leads to cross-linked conjugation at the molecular center and a highly symmetric chiral structure with D_2-symmetry. Consequently, figure-eight molecules often exhibit fascinating properties, such as unusual rearrangement reactions [9] and efficient circularly polarized luminescence (CPL) [10-12].

Cyclobisbiphenylenecarbonyl (CBBC) **1** is a figure-eight macrocycle, which is readily synthesized from commercially available dibenzo[*g*,*p*]chrysene (DBC, **2**) via oxidative inner-bond cleavage (Figure 1) [16,17]. CBBC **1** was first synthesized by Suszko and Schillak in 1934 using sodium dichromate as an oxidant [16]. Recently, our group developed a scalable, catalytic, and enantioselective protocol to furnish CBBC **1** [17]. Several peripherally modified CBBC derivatives have also been prepared and were shown to have fascinating properties [17-21]. For example, carbazole-substituted donor–acceptor-type CBBC derivatives exhibit both efficient circularly polarized luminescence (CPL) and thermally activated delayed fluorescence (TADF), demonstrating that CBBC represents a promising building block for the design of advanced functional materials [17,21]. However, the transformation of the carbonyl groups in CBBC has been underexplored. Herein, we report the Wittig reaction of CBBC **1**. CBBC **1** undergoes structural change from a stable figure-eight conformation **A** to a metastable bathtub conformation **B** with a small energy difference of approximately 2 kcal mol^{-1} [21]. In this paper, we discuss the effect of the transformation of the carbonyl groups on the conformational change of the figure-eight structure. We thus intentionally depict flattened chemical structures in the reaction schemes.

Results and Discussion

Synthesis and characterization

Methylenetriphenylphosphorane was generated by mixing equimolar amounts of methyltriphenylphosphonium iodide ([MePPh$_3$]I) and sodium *tert*-butoxide (NaO*t*-Bu) in THF. The Wittig reaction of CBBC **1** with 1.2 equiv of methylenetriphenylphosphorane afforded mono-olefin **3** in 49% yield as well as an internally functionalized dibenzo[*g*,*p*]chrysene (DBC) derivative **4** in 5% yield (Scheme 1). The use of an excess amount of methylenetriphenylphosphorane (5.0 equiv) afforded compound **4** in a higher yield of 50%. In addition, the reaction furnished bis-olefin **5** in 2% isolated yield which is lower than the estimated yield by ^{1}H NMR measurement of the crude mixture (11%). This is due to the partial loss of the product during purification to remove a trace amount of DBC **2**, which was generated as a byproduct and exhibited similar polarity as compound **5**. The obtained compounds **3**, **4**, and **5** were identified using nuclear magnetic resonance (NMR) spectroscopy and mass spectrometry (MS) (see Supporting Information File 1) as well as single crystal X-ray diffraction analysis (vide infra). Furthermore, the absence of carbonyl groups in bis-olefin **5** has been corroborated by Fourier transform infrared (FTIR) spectroscopy (Figure S16 in Supporting Information File 1).

Compound **4** could be generated through the reaction of compound **3** with phosphorus ylide. However, a reliable reaction mechanism remains unclear. A tentative mechanism that may be plausible is shown in Supporting Information File 1, Figure S21, which consists of (1) the nucleophilic attack of methylenetriphenylphosphorane to the *exo*-methylene group of **3**, (2) the intramolecular carbon–carbon-bond formation at the carbonyl group, and (3) the nucleophilic substitution of the thus generated alkoxide to form an oxygen-containing five-membered ring. At least, density functional theory (DFT) calculations support that the nucleophilic attack of methylenetriphenylphosphorane to the *exo*-methylene unit is slightly favorable over reaction with the carbonyl group (Figure S20, Supporting Information File 1), which will be due to the disrupted nucleophilic

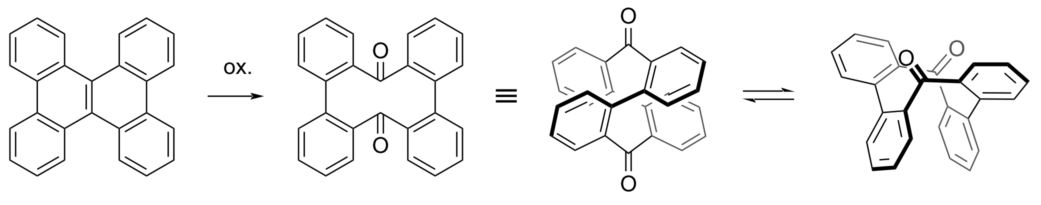

DBC **2** CBBC **1** figure-eight **A** bathtub **B**

Figure 1: Synthesis and structures of CBBC **1**.

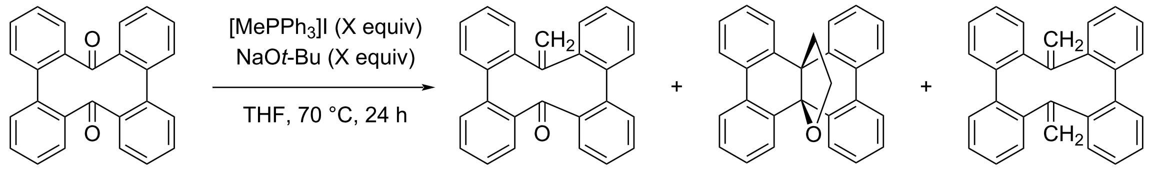

	1	**3**	**4**	**5**
X = 1.2		49%	5%	n.d.
X = 5.0		n.d.	50%	2%

Scheme 1: Wittig reactions of CBBC **1**.

attack to the carbonyl group by the intramolecular steric repulsion toward the Bürgi–Dunitz angle. However, alternative mechanisms initiated by a conventional oxaphosphetane formation cannot not yet be ruled out.

The structures of compounds **3**, **4**, and **5** were determined by X-ray diffraction analysis (Figure 2). Mono-olefin **3** and bis-olefin **5** adopt a bathtub-like chiral macrocyclic structure rather than figure-eight conformation. Both compounds crystallize as a racemic pair of enantiomers with $P2_1/c$ and Cc space groups, respectively. The bond lengths at the exocyclic olefin units of **3** and **5** are 1.336(2) and 1.333(3)–1.337(3) Å, respectively, which are typical for carbon–carbon double bonds. The (CH_2CH_2O)-substituted DBC derivative **4** adopts a double-helicene-like structure similarly to other internally functionalized DBC derivatives [22]. The dihedral angle between the mean planes of the two terminal benzene units is 83°, which is comparable to those of other derivatives.

Next, products **3** and **5** were analyzed by variable temperature (VT) ^{1}H NMR spectroscopy. The ^{1}H NMR spectrum of bis-olefin **5** in CD_2Cl_2 at 298 K shows a symmetric pattern, in which the signal due to the methylene protons appears as one singlet (Figure 3). The decrease of temperature to 243 K resulted in the broadening of the ^{1}H NMR spectrum and the appearance of two sets of signals which sharpened upon further

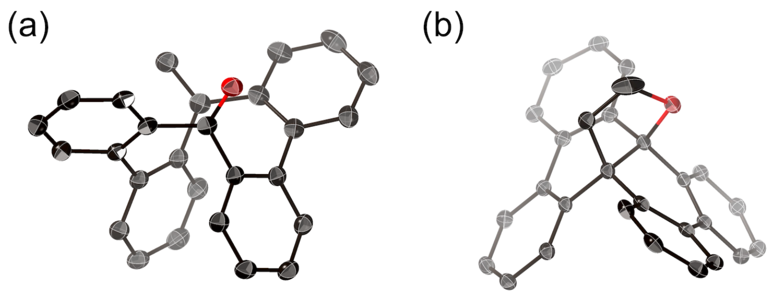

Figure 2: X-ray crystal structures of (a) **3**, (b) **4**, and (c) **5** with thermal ellipsoids at 50% probability; all hydrogen atoms are omitted for clarity.

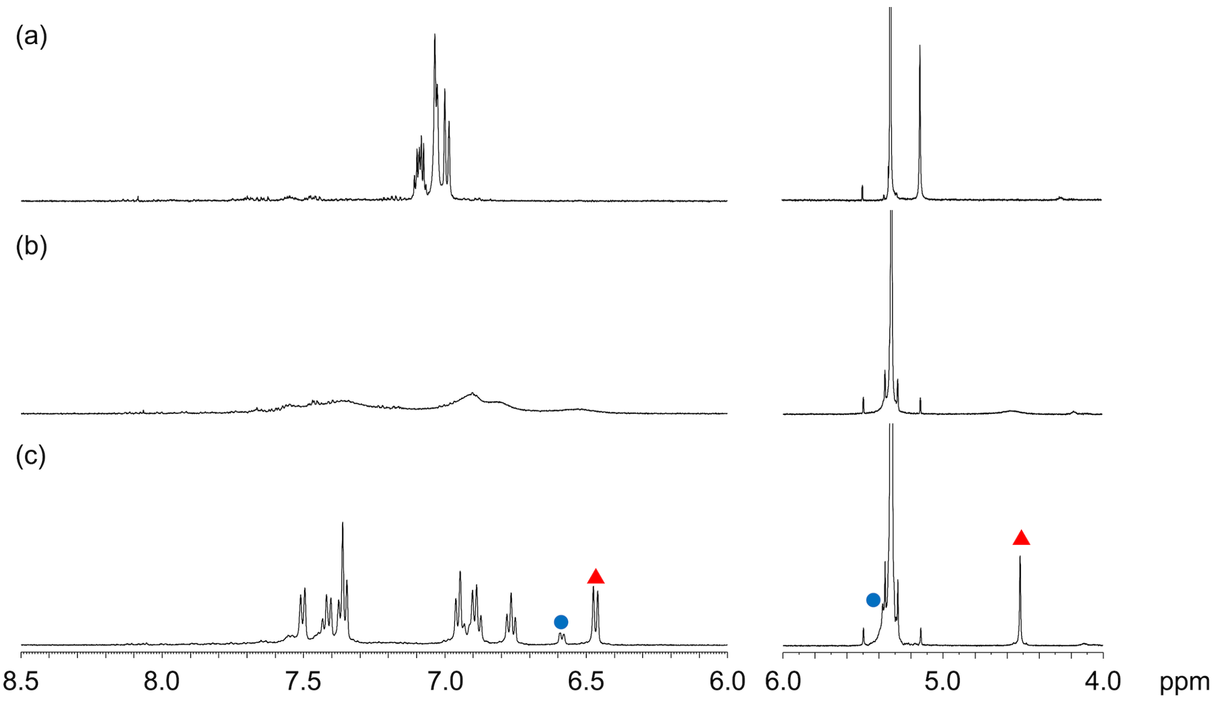

Figure 3: VT ^{1}H NMR spectra of **5** in CD_2Cl_2 at (a) 298 K, (b) 243 K, and (c) 203 K. Blue circle and red triangle mean selected signals due to figure-eight and bathtub conformations, respectively.

decrease of the temperature. These are attributable to the mixture of conformers with the figure-eight conformation as minor and the bathtub conformation as major conformer with a ratio of ca. 1:7. The obtained temperature-dependent ^{1}H NMR data were subjected to the van't Hoff plot, affording an enthalpy ΔH and an entropy ΔS of 1.5 kcal mol^{-1} and 3.2 cal K^{-1} mol^{-1}, respectively (Figure S26 in Supporting Information File 1). These physical parameters give a free energy ΔG_{298} of 0.55 kcal mol^{-1}, indicating approximately a 2:5 ratio of figure-eight and bathtub conformations at room temperature. Mono-olefin **3** exhibited similar temperature-dependent ^{1}H NMR changes, which furnished ΔH of 3.1 kcal mol^{-1} and ΔS of 11 cal K^{-1} mol^{-1} for the (figure-eight)–bathtub interconversion (Figure S25 in Supporting Information File 1). These parameters afforded ΔG_{298} of −0.22 kcal mol^{-1}, indicating that the figure-eight conformation is slightly preferred at room temperature with approximately a 3:2 ratio of figure-eight and bathtub conformations. We have also estimated the activation barriers of the interconversion of **3** and **5** between the figure-eight and bathtub conformations by measuring VT ^{1}H NMR spectra in toluene-d_8 because the signals due to the *exo*-methylene groups overlapped with the solvent signal in CD_2Cl_2. The thus obtained activation barriers of **3** and **5** were 11 and 12 kcal mol^{-1} at 263 and 253 K, respectively (Figure S27 in Supporting Information File 1).

Previous DFT calculations at the B3LYP/6-31G(d) level of theory suggested that the bathtub conformation of CBBC **1** is slightly unfavorable than the figure-eight conformation by 2.4 kcal mol^{-1} [21]. On the other hand, the current DFT calculations suggest that the bathtub conformation of bis-olefin **5** is rather favorable by 0.3 kcal mol^{-1}, which is in accordance with the temperature-dependent ^{1}H NMR measurements. The relatively preferable formation of bathtub conformation is attributable to the destabilization of the figure-eight structures by the intramolecular steric repulsion between the *exo*-methylene units and neighboring benzene rings.

Resolution

The resolution of rac-**3** and rac-**5** was conducted using high-performance liquid chromatography (HPLC) equipped with DAICEL CHIRALPAK IE as the chiral stationary phase (eluent: CH_2Cl_2/hexane 3:2 for **3** and 1:9 for **5**). The absolute configurations of the enantiomers were determined by transformation of enantiomerically pure CBBC (*P*,*P*)-**1**, whose configuration was previously confirmed [17]. The (*P*,*P*)-figure-eight conformation of CBBC **1** corresponds to the (R_a,R_a)-bathtub conformation, whose configuration is based on the axial chirality of the biaryl segment. Consequently, the 1st fractions of **3** and **5** were determined to be (S_a,S_a) and (R_a,R_a), respectively (see Supporting Information File 1, Figures S1 and S2).

The resolution of (CH_2CH_2O)-substituted DBC derivative **4** at ambient temperature was examined using DAICEL CHIRALPAK IA–IE (eluent: CH_2Cl_2/hexane and 2-propanol/hexane). However, the resolution was unsuccessful due to the low racemization barrier as with structurally similar methylenedioxy-substituted DBC derivative [22].

Racemization dynamics

The racemization barriers of CBBC **1**, mono-olefin **3**, and bis-olefin **5** were evaluated by monitoring the decrease of circular dichroism (CD) signals in 1,2-dichlorobenzene at 170 °C (Supporting Information File 1, Figures S22–S24). The decrease of CD intensity was fitted by a single exponential curve, affording half-lifes of 1.3 h for **1**, 6.4 h for **3**, and 29 h for **5**. These results indicate that the transformation of carbonyl groups to exocyclic olefins is effective to retard racemization.

The racemization dynamics of **5** was investigated by DFT calculations at the B3LYP/6-31G(d) level of theory, employing the Gaussian 16 software package and the global reaction route mapping (GRRM17) [23] program (Figure 4). The interconversion between figure-eight conformation (*M*,*M*)-**B** and bathtub conformation (S_a,S_a)-**A** is feasible with a small activation barrier of 9.9 kcal mol^{-1}. The figure-eight conformer (*M*,*M*)-**B** untwists to adopt an achiral conformation **C** with the *exo*-alkene units rotated inwards in opposite directions. These conformational changes are almost identical to those of CBBC **1**. However, the racemization barrier of **5** (34.8 kcal mol^{-1}) is larger than that of CBBC **1** (33.7 kcal mol^{-1}), which accords with the experimental results. In the transition state TS2, the exocyclic olefin unit **a** is close to the adjacent benzene ring **b**, which causes intramolecular steric repulsion to increase the racemization barrier.

Optical and chiroptical properties

The UV–vis absorption spectra of CBBC **1**, mono-olefin **3**, and bis-olefin **5** are shown in Figure 5a. The absorption of **3** tails to 370 nm, which is comparable to the absorption end of CBBC **1**. On the other hand, the absorption of bis-olefin **5** is blue-shifted, tailing to 325 nm. In the case of CBBC **1**, the contribution of n–π* transition due to the carbonyl groups affords weak absorption in the 300–380 nm range [17]. Consequently, the blue-shifted absorption of **5** compared to those of **1** and **3** could result from the loss of carbonyl groups. The relatively large optical HOMO–LUMO gap of **5** despite the presence of 26 sp^2 carbons is due to the cross-conjugation at the exocyclic olefins. Mono-olefin **3** is virtually non-emissive, similarly to CBBC **1**, which could originate from the non-radiative decay via intersystem crossing due to the carbonyl group. In sharp contrast, bis-olefin **5** fluoresces at 389 nm with a quantum yield of

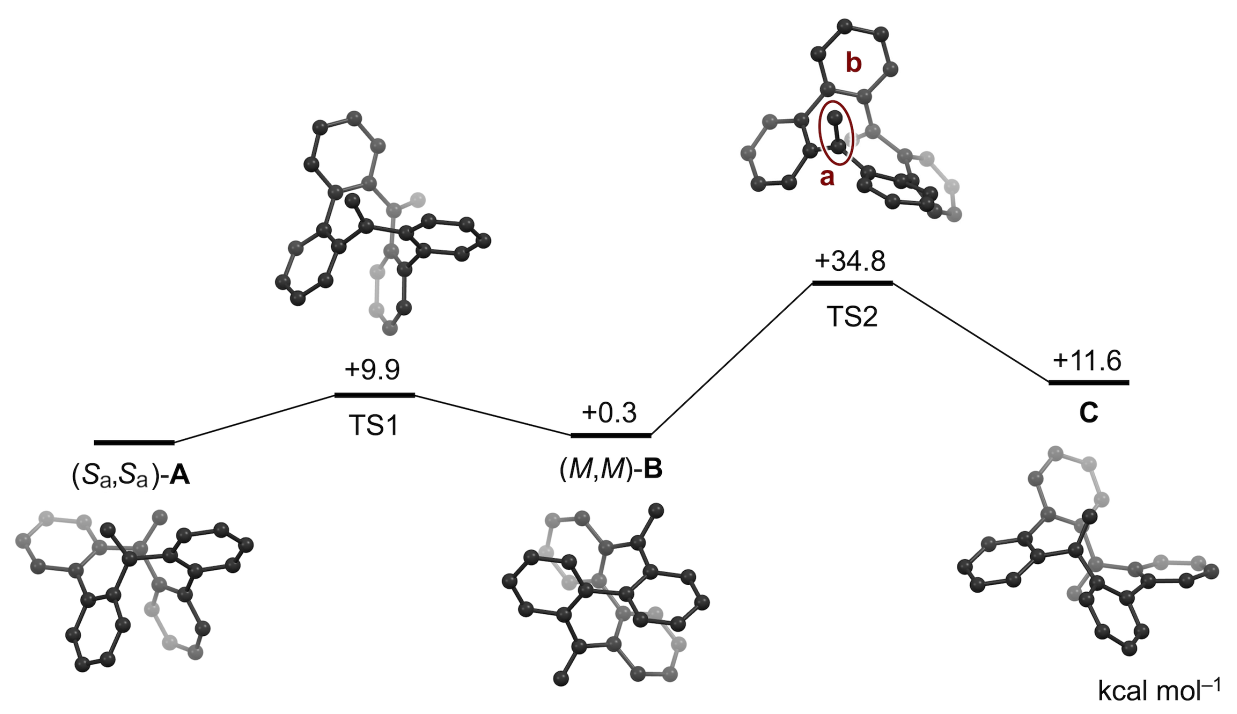

Figure 4: Simulated dynamics of bis-olefin **5** at the B3LYP/6-31G(d) level of theory. The description for the configuration of **A** and **B** are based on the helical chirality of the 1,1-diphenylethylene units and the axial chirality of the biaryl segments, respectively.

7.5% and a lifetime of 6.0 ns. The radiative and non-radiative decay rate constants are calculated to be 1.3×10^7 s^{-1} and 1.5×10^8 s^{-1}, respectively.

The CD spectra and the dissymmetry factors (g) of enantiomers of CBBC **1**, mono-olefin **3**, and bis-olefin **5** are shown in Figure 5b and Figure 5c, respectively. These spectra are observed as mirror images for enantiomers. The shapes of the CD spectra of mono-olefin **3** and bis-olefin **5** are essentially identical except for nearly forbidden transitions of **3** in the 340–400 nm range. While the maximum g value of CBBC **1** is approximately 0.03, the g values of mono-olefin **3** and bis-olefin **5** are lower than 0.006. We conducted TD-DFT calculations for both the bathtub and figure-eight conformations of compounds **3** and **5**, indicating that the signs of CD signals are reversal in most spectral range (Figure S18 and Figure S19 in Supporting Information File 1). Consequently, the low g values of **3** and **5** are attributable to the offset of CD signals due to the coexistence of two conformations.

Reactivity

The reactivity of the Wittig products was examined. Mono-olefin **3** was treated with $TiCl_4$ and zinc powder in THF at 65 °C, which are typical conditions for the McMurry coupling (Scheme 2) [24,25]. This reaction afforded an internally functionalized DBC derivative **6** in 60% yield, which adopts an unsymmetric structure with methyl and hydroxy groups on the central carbon atoms. The structure of compound **6** has been confirmed by X-ray diffraction analysis. On the other hand, the treatment of bis-olefin **5** under the same conditions recovered the starting material, which highlights the distinctive role of the carbonyl group for the reductive carbon–carbon-bond formation from **3**.

Conclusion

The Wittig reaction of CBBC **1** with methylenetriphenylphosphorane furnished two (exocyclic olefin)-containing macrocycles **3** and **5** as well as an internally functionalized DBC derivative **4**. Compounds **3** and **5** adopt a bathtub-like conformation in the solid state. In solution, both figure-eight and bathtub conformations exist as an equilibrium mixture, in which the bathtub conformation is rather preferable at low temperature. Mono-olefin **3** and bis-olefin **5** exhibit enhanced configurational persistency compared to CBBC **1**. Bis-olefin **5** fluoresces with a quantum yield of 7.5%, while CBBC **1** is non-emissive under ambient conditions. Mono-olefin **3** undergoes a reductive carbon–carbon-bond formation between carbonyl and alkene units upon treatment with $TiCl_4$. The current study demonstrates that the transformation of the carbonyl groups of CBBC results in products with altered physical and chemical properties which may be beneficial for the development of advanced materials.

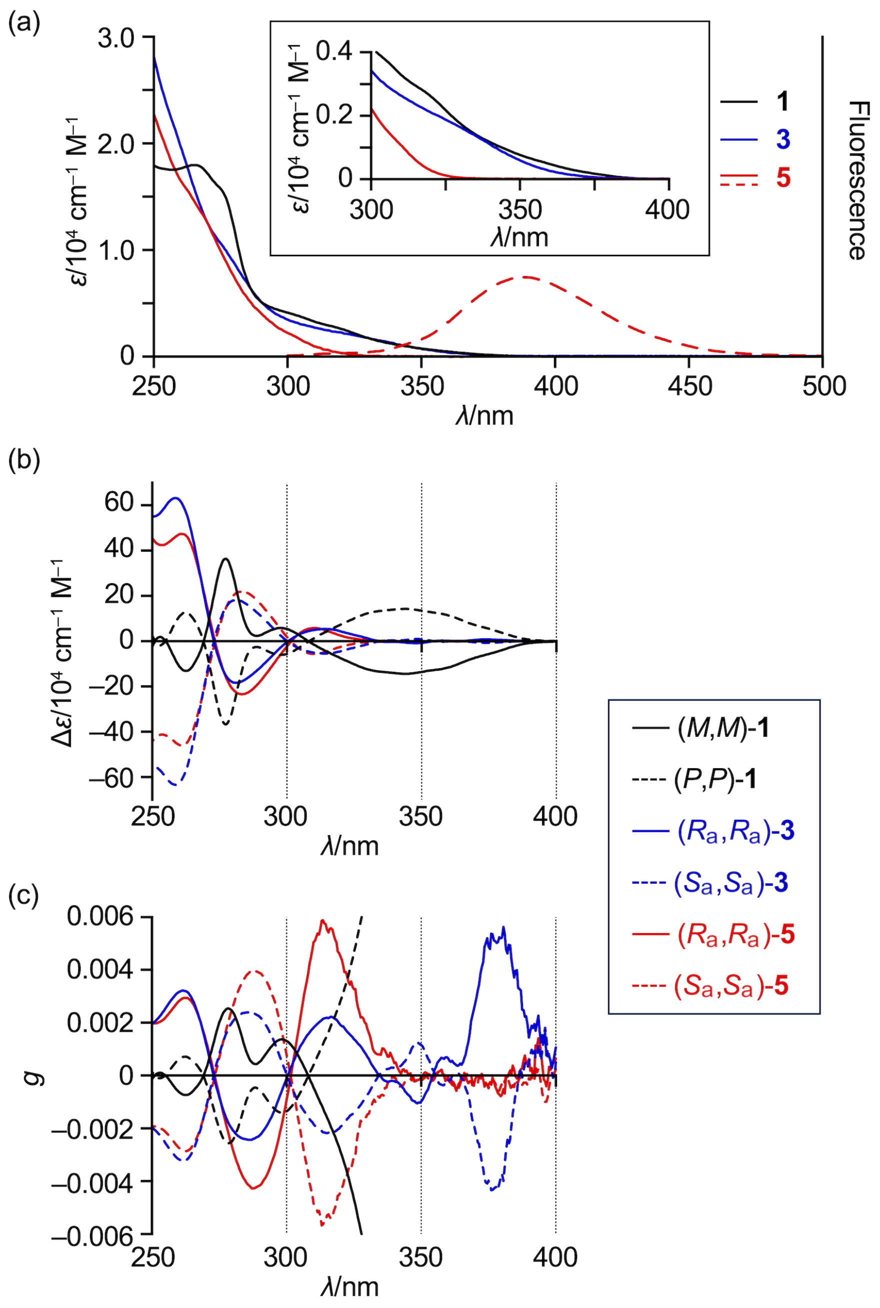

Figure 5: (a) UV–vis absorption (solid lines) and emission (dashed lines) spectra of **1** (black), **3** (blue), and **5** (red). (b) CD spectra of **1** (black), **3** (blue), and **5** (red). (c) CD *g* values of **1** (black), **3** (blue), and **5** (red). λ = wavelength; ε = extinction coefficient; solvent = CH_2Cl_2.

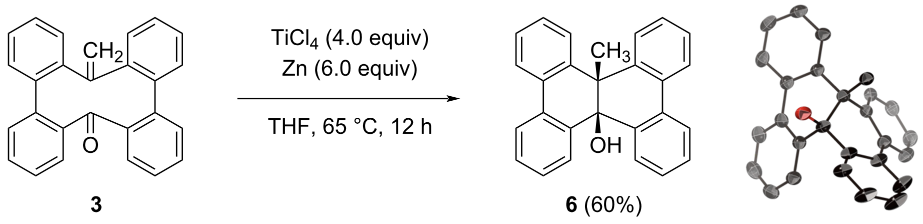

Scheme 2: Conversion of mono-olefin **3** to internally functionalized DBC derivative **6**.

Supporting Information

Supporting Information File 1

Experimental details and spectral data for all new compounds.
[https://www.beilstein-journals.org/bjoc/content/supplementary/1860-5397-21-107-S1.pdf]

Funding

This work was supported by JSPS KAKENHI grants JP20H05862 (H.S., N.F.), JP20H05863 (H.S.), JP20H05867 (N.F.), JP23H03947 (N.F.), JP24K01467 (N.F.), and JP24K21766 (N.F.) as well as JST PRESTO grant JPMJPR21Q7 (N.F.) and FOREST grant JPMJFR232G (N.F.).

Author Contributions

Taito Moribe: investigation. Junichiro Hirano: investigation. Hideaki Takano: investigation. Hiroshi Shinokubo: funding acquisition; writing – review & editing. Norihito Fukui: conceptualization; funding acquisition; project administration; visualization; writing – original draft.

ORCID® iDs

Hiroshi Shinokubo - https://orcid.org/0000-0002-5321-2205
Norihito Fukui - https://orcid.org/0000-0002-0466-0116

Data Availability Statement

All data that supports the findings of this study is available in the published article and/or the supporting information of this article.

References

1. Staab, H. A.; Wehinger, E. *Angew. Chem., Int. Ed. Engl.* **1968,** *7,* 225–226. doi:10.1002/anie.196802251
2. Sessler, J. L.; Weghorn, S. J.; Lynch, V.; Johnson, M. R. *Angew. Chem., Int. Ed. Engl.* **1994,** *33,* 1509–1512. doi:10.1002/anie.199415091
3. Bröring, M.; Jendrny, J.; Zander, L.; Schmickler, H.; Lex, J.; Wu, Y.-D.; Nendel, M.; Chen, J.; Plattner, D. A.; Houk, K. N.; Vogel, E. *Angew. Chem., Int. Ed. Engl.* **1995,** *34,* 2515–2517. doi:10.1002/anie.199525151
4. Nakanishi, W.; Matsuno, T.; Ichikawa, J.; Isobe, H. *Angew. Chem., Int. Ed.* **2011,** *50,* 6048–6051. doi:10.1002/anie.201102210
5. Senthilkumar, K.; Kondratowicz, M.; Lis, T.; Chmielewski, P. J.; Cybińska, J.; Zafra, J. L.; Casado, J.; Vives, T.; Crassous, J.; Favereau, L.; Stępień, M. *J. Am. Chem. Soc.* **2019,** *141,* 7421–7427. doi:10.1021/jacs.9b01797
6. Kiel, G. R.; Bay, K. L.; Samkian, A. E.; Schuster, N. J.; Lin, J. B.; Handford, R. C.; Nuckolls, C.; Houk, K. N.; Tilley, T. D. *J. Am. Chem. Soc.* **2020,** *142,* 11084–11091. doi:10.1021/jacs.0c03177
7. Fan, W.; Matsuno, T.; Han, Y.; Wang, X.; Zhou, Q.; Isobe, H.; Wu, J. *J. Am. Chem. Soc.* **2021,** *143,* 15924–15929. doi:10.1021/jacs.1c08468
8. Krzeszewski, M.; Ito, H.; Itami, K. *J. Am. Chem. Soc.* **2022,** *144,* 862–871. doi:10.1021/jacs.1c10807
9. Tanaka, Y.; Hoshino, W.; Shimizu, S.; Youfu, K.; Aratani, N.; Maruyama, N.; Fujita, S.; Osuka, A. *J. Am. Chem. Soc.* **2004,** *126,* 3046–3047. doi:10.1021/ja031935t
10. Morisaki, Y.; Gon, M.; Sasamori, T.; Tokitoh, N.; Chujo, Y. *J. Am. Chem. Soc.* **2014,** *136,* 3350–3353. doi:10.1021/ja412197j
11. Robert, A.; Naulet, G.; Bock, H.; Vanthuyne, N.; Jean, M.; Giorgi, M.; Carissan, Y.; Aroulanda, C.; Scalabre, A.; Pouget, E.; Durola, F.; Coquerel, Y. *Chem. – Eur. J.* **2019,** *25,* 14364–14369. doi:10.1002/chem.201902637
12. Kubo, H.; Shimizu, D.; Hirose, T.; Matsuda, K. *Org. Lett.* **2020,** *22,* 9276–9281. doi:10.1021/acs.orglett.0c03506
13. Wang, L.-H.; Nogami, J.; Nagashima, Y.; Tanaka, K. *Org. Lett.* **2023,** *25,* 4225–4230. doi:10.1021/acs.orglett.3c00895
14. Nogami, J.; Hashizume, D.; Nagashima, Y.; Miyamoto, K.; Uchiyama, M.; Tanaka, K. *Nat. Synth.* **2023,** *2,* 888–897. doi:10.1038/s44160-023-00318-2
15. Robert, A.; Dechambenoit, P.; Hillard, E. A.; Bock, H.; Durola, F. *Chem. Commun.* **2017,** *53,* 11540–11543. doi:10.1039/c7cc06798d
16. Suszko, S.; Schillak, R. *Rocz. Chem.* **1934,** *14,* 1216–1225.
17. Yoshina, R.; Hirano, J.; Nishimoto, E.; Sakamoto, Y.; Tajima, K.; Minabe, S.; Uyanik, M.; Ishihara, K.; Ikai, T.; Yashima, E.; Omine, T.; Ishiwari, F.; Saeki, A.; Kim, J.; Oh, J.; Kim, D.; Liu, G.; Yasuda, T.; Shinokubo, H.; Fukui, N. *J. Am. Chem. Soc.* **2024,** *146,* 29383–29390. doi:10.1021/jacs.4c07985
18. Suzuki, K. *Bull. Chem. Soc. Jpn.* **1962,** *35,* 735–740. doi:10.1246/bcsj.35.735
19. Suzuki, K.; Maeda, T.; Nawa, N.; Sōda, Y. *Bull. Chem. Soc. Jpn.* **1962,** *35,* 1299–1302. doi:10.1246/bcsj.35.1299
20. Clar, E.; Guye-Vuillème, J. F.; Stephen, J. F. *Tetrahedron* **1964,** *20,* 2107–2117. doi:10.1016/s0040-4020(01)98484-4
21. Nishimoto, E.; Ikai, T.; Shinokubo, H.; Fukui, N. *Chem. – Eur. J.* **2025,** *31,* e202404194. doi:10.1002/chem.202404194
22. Takeo, Y.; Hirano, J.; Fukui, N.; Shinokubo, H. *Org. Lett.* **2023,** *25,* 8484–8488. doi:10.1021/acs.orglett.3c03428
23. Maeda, S.; Harabuchi, Y.; Takagi, M.; Saita, K.; Suzuki, K.; Ichino, T.; Sumiya, Y.; Sugiyama, K.; Ono, Y. *J. Comput. Chem.* **2018,** *39,* 233–251. doi:10.1002/jcc.25106
24. McMurry, J. E. *Chem. Rev.* **1989,** *89,* 1513–1524. doi:10.1021/cr00097a007
25. Jiao, J.; Li, Z.; Qiao, Z.; Li, X.; Liu, Y.; Dong, J.; Jiang, J.; Cui, Y. *Nat. Commun.* **2018,** *9,* 4423. doi:10.1038/s41467-018-06872-0

License and Terms

The definitive version of this article is the electronic one which can be found at:
https://doi.org/10.3762/bjoc.21.107

BEILSTEIN JOURNAL OF ORGANIC CHEMISTRY

Synthesis of an aza[5]helicene-incorporated macrocyclic heteroarene via oxidation of an *o*-phenylene-pyrrole-thiophene icosamer

Yusuke Matsuo[1,2], Aoi Nakagawa[1], Shu Seki[1] and Takayuki Tanaka[*1]

Full Research Paper

Open Access

Address:
[1]Department of Molecular Engineering, Graduate School of Engineering, Kyoto University, Kyotodaigakukatsura, Nishikyo-ku, Kyoto, Japan and [2]Department of Chemistry, Graduate School of Science, Kyoto University, Kitashirakawa Oiwake-cho, Sakyo-ku, Kyoto, Japan

Email:
Takayuki Tanaka* - tanaka@moleng.kyoto-u.ac.jp

* Corresponding author

Keywords:
cyclophane; fluorescence; heterohelicene; intramolecular oxidative coupling

Beilstein J. Org. Chem. **2025,** *21,* 1561–1567.
https://doi.org/10.3762/bjoc.21.119

Received: 01 June 2025
Accepted: 23 July 2025
Published: 31 July 2025

This article is part of the thematic issue "Non-central chirality in organic chemistry".

Associate Editor: N. Yoshikai

Abstract

The intramolecular oxidative fusion reaction of macrocyclic heteroaromatic arrays has provided strained polycyclic heteroaromatic macrocycles as promising functional molecules. In this study, we prepared an *ortho*-phenylene-pyrrole-thiophene hybrid icosamer, as the largest cyclic array in the series. The oxidative fusion reaction with [bis(trifluoroacetoxy)iodo]benzene (PIFA) afforded a cyclophane-type aza[5]helicene-incorporated macrocycle, the structure of which was unambiguously revealed by X-ray diffraction analysis. Its optical properties have been investigated in detail.

Introduction

Conjugated macrocyclic polyarenes have attracted significant attention due to their stimuli-responsive optoelectronic properties, dynamic structural changes, and host–guest interactions [1-5]. In addition to these promising functionalities, their cyclic polyaromatic frameworks can be further transformed into fused structures. To this end, belt-like polyaromatic architectures can be developed, inspiring ongoing efforts toward the construction of carbon nanotube analogs (Figure 1) [6-12]. Nevertheless, partially fused macrocyclic intermediates are also important as they exhibit structural strain associated with both the polycyclic segments and the inherent strain stemming from the macrocyclic structure. For instance, cyclic chrysenylenes [13-16] and pyrenylenes [17,18] were reported to adopt unique chiral arrangements depending on their stereochemistry. Helical motifs such as carbo[4]helicene and oxa[5]helicene were incorporated into cyclic structures, giving rise to cyclic carbo[4]helicenylene **A** and cyclic oxa[5]helicenylene-biphenylene **B**, respectively [19,20]. Recently, our group established an efficient synthetic strategy for strained macrocyclic polyarenes, such as compound **C**, in which *o*-phenylene units preorganize adjacent

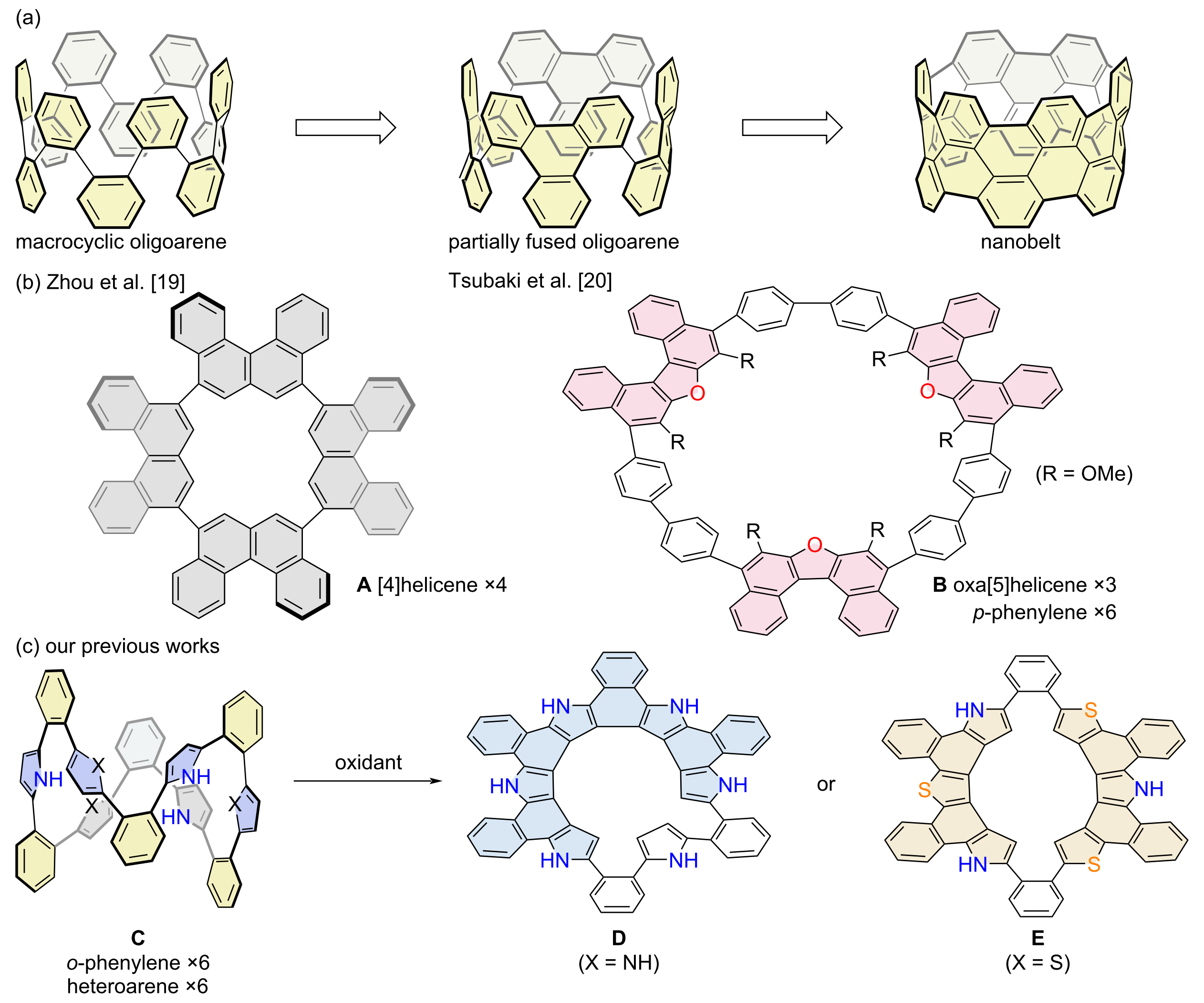

Figure 1: (a) Increased ring-strain from macrocyclic oligoarene to partially fused oligoarene and nanobelt. (b) Cyclo[4]helicenylene and cyclo(oxa[5]helicenylene-biphenylene). (c) Intramolecular oxidative coupling of cyclic *o*-phenylene-pyrrole-thiophene dodecamers.

heteroaromatics into close proximity, thereby facilitating oxidative ring-closure reactions [21]. Among these, the largest macrocycle ever synthesized is a dodecameric hybrid array of 1,2-phenylene, 2,5-thienylene, and 2,5-pyrrolylene units [22,23]. The intramolecular oxidative coupling of these arrays afforded heterohelicene-incorporated macrocycles **D** and **E**, depending on the relative arrangements of the pyrrole and thiophene units [24,25]. The influence of heteroaromatic positioning on the reaction outcome has been rationalized in our previous work [25]. As a further extension of this molecular design, herein we report the synthesis of an *o*-phenylene-pyrrole-thiophene hybrid icosamer and its oxidative fusion to yield an aza[5]helicene-incorporated macrocycle. The resulting cyclophane-like structure and its optical properties have been analyzed in detail.

Results and Discussion

Synthesis and characterization

Synthesis

We obtained *o*-phenylene-pyrrole-thiophene hybrid icosamer **4** during our attempt to synthesize hybrid decamer **3** in a previous report [26], via a Suzuki–Miyaura cross-coupling reaction between dibromo precursor **1** and borylated precursor **2** (Scheme 1). The resulting mixture was successfully separated by column chromatography on silica using CH_2Cl_2/*n*-hexane as an eluent to give icosamer **4** in 6% yield, along with decamer **3** (30%). High-resolution atmospheric-pressure-chemical-ionization time-of-flight mass-spectrometry (HR-APCI-TOF-MS) showed a molecular ion peak for **4** at *m/z* = 1479.4320 (calcd for $C_{100}H_{66}N_6S_4$, *m/z* = 1479.4305). The ^{1}H NMR spectrum of **4** in acetone-d_6 exhibited two NH signals at 9.07 and 8.98 ppm

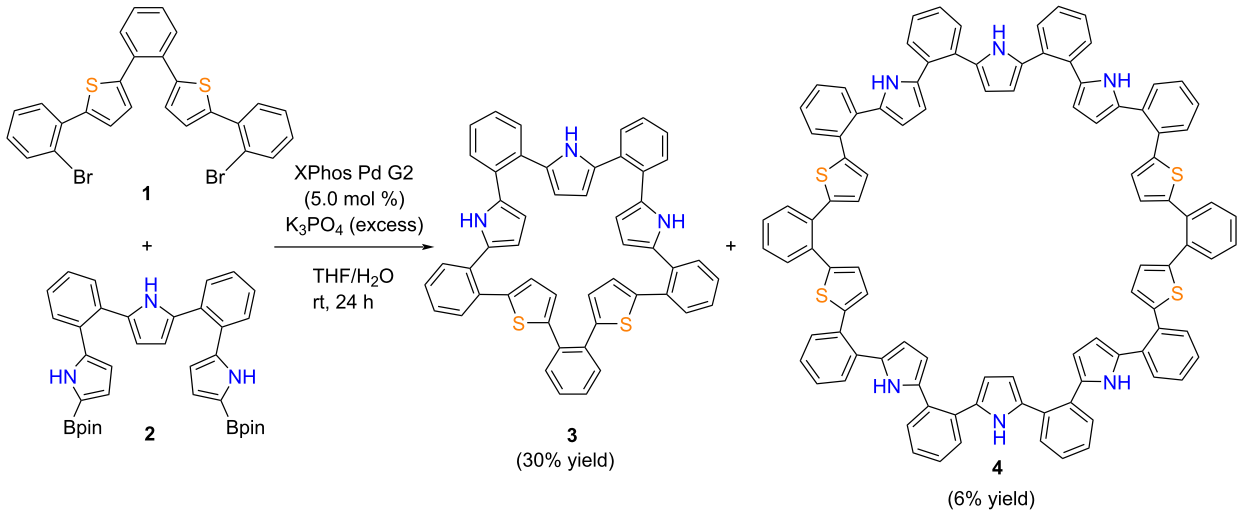

Scheme 1: Synthesis of *o*-phenylene-pyrrole-thiophene hybrid macrocycles.

and five doublet signals due to the heterole β-protons in the range of 6.7–5.8 ppm, along with *o*-phenylene protons around 7 ppm.

Single crystals suitable for X-ray diffraction analysis were obtained from a mixture of acetone/*n*-hexane and the solid-state structure was successfully determined (Figure 2). Similar to other previously reported *o*-phenylene-bridged hybrid nanorings [22,23], the average dihedral angles were 40.66° between the phenylene and pyrrole units, and 57.22° between the phenylene and thiophene units. This represents the largest *o*-phenylene-bridged heteroaromatic macrocycle whose structure has been confirmed by X-ray diffraction analysis.

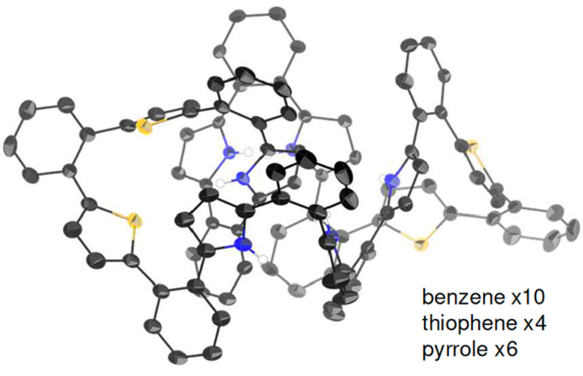

Figure 2: X-ray crystal structure of **4**. Thermal ellipsoids are scaled to 50% probability level. Solvent molecules and hydrogen atoms except for NHs are omitted for clarity.

Next, oxidation of **4** was attempted using [bis(trifluoroacetoxy)iodo]benzene (PIFA) in CH_2Cl_2 at −78 °C (Scheme 2). These reaction conditions had previously proven effective for the oxidation of **3** and other *o*-phenylene-bridged acyclic heteroaromatics [26,27]. Thus, to a solution of **4** in CH_2Cl_2 was added 15 equivalents of PIFA at −78 °C and stirred for 3 h. The mixture was then allowed to warm to room temperature to give a dark solution. The system was worked-up with $NaBH_4$/MeOH for 10 minutes followed by extraction with CH_2Cl_2 and evaporation of the solvent to afford a crude product, which was recrystallized from THF to give **5** in 58% yield. Due to its poor solubility in common organic solvents, the ^1H NMR spectrum could only be recorded in DMSO. At room temperature, the ^1H NMR spectrum in DMSO-d_6 exhibited broad signals in the range of 6–7 ppm, which sharpened significantly at 100 °C (Figure 3). The ^1H NMR spectrum at 100 °C displayed distinct signals at 12.01 and 11.54 ppm due to NH protons, a singlet for the pyrrole β-protons at 6.97 ppm, and doublets for the thiophene β-protons at 6.26 and 5.95 ppm. HR-APCI-TOF-MS revealed a molecular ion peak at m/z = 1471.3682 (calcd for $C_{100}H_{58}N_6S_4$, m/z = 1471.3679), indicating the loss of eight hydrogen atoms from **4**, suggesting the formation of a fused structure at the pyrrole segments. Finally, the structure was unambiguously revealed by X-ray diffraction analysis to display an aza[5]helicene-incorporated macrocyclic structure (Figure 4). In the solid-state, the distance between the two aza[5]helicene moieties was found to be 3.185 Å, closely consistent with the DFT-optimized value of 3.136 Å (see Supporting Information File 1). The average dihedral angles between the *o*-phenylene and aza[5]helicene segments, and between the *o*-phenylene and thiophene segments, were 37.52° and 44.28°, respectively. Four NH sites of the aza[5]helicene moiety formed hydrogen bonds with DMSO molecules in the crystal lattice, as observed in aza[*n*]helicenes recently reported

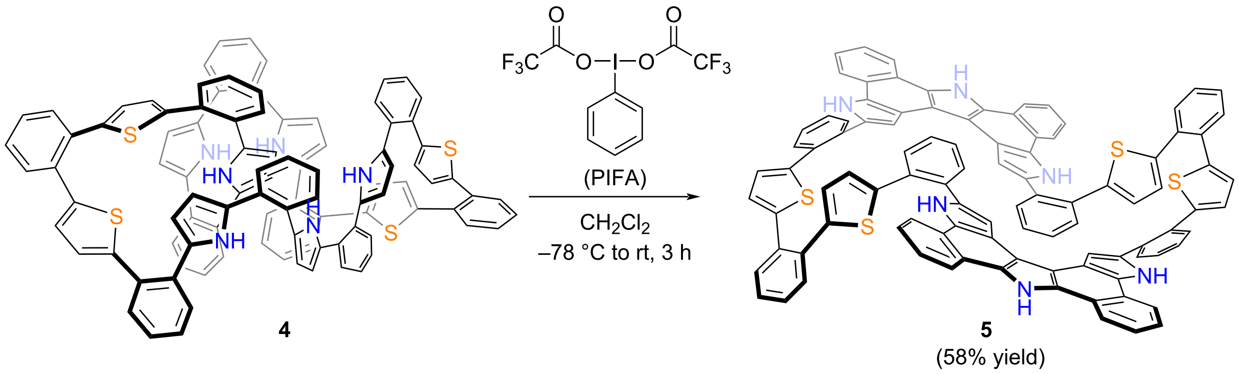

Scheme 2: Synthesis of aza[5]helicene-incorporated macrocyclic heteroarene **5**.

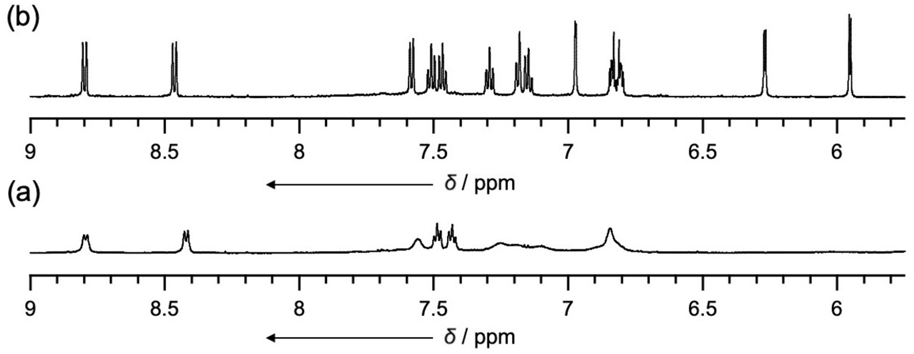

Figure 3: ^{1}H NMR spectra of **5** in DMSO-d_6 (a) at room temperature and (b) at 100 °C.

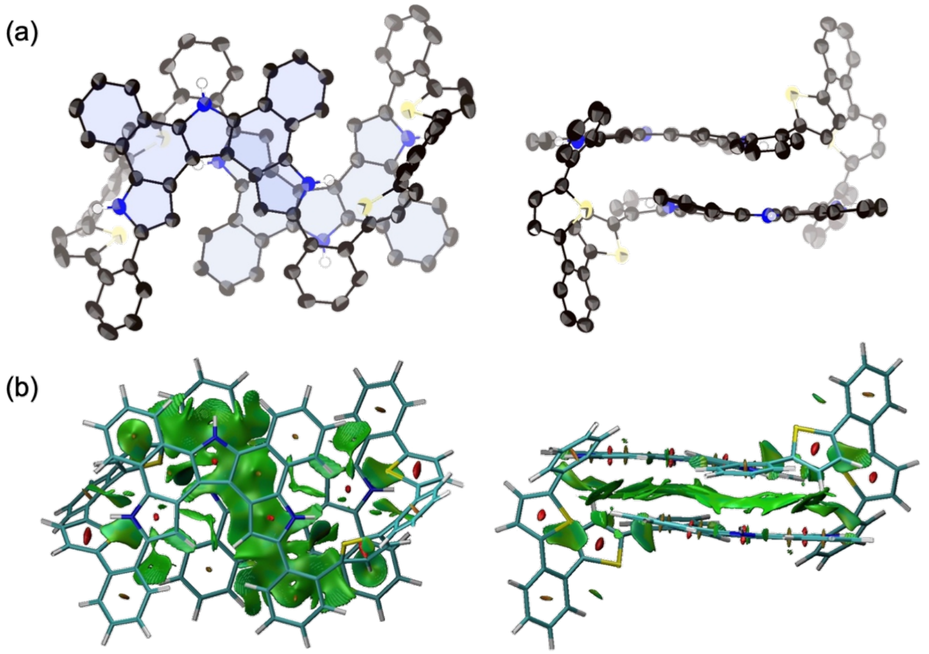

Figure 4: (a) X-ray crystal structure of **5**; (left) top view, (right) side view. Thermal ellipsoids are scaled to 50% probability level. Solvent molecules and hydrogen atoms except for NHs are omitted for clarity. (b) NCI plot of **5**; (left) top view, (right) side view (isosurface: 0.50, range: $-0.03 < \mathrm{sign}(\lambda_2)\rho < 0.03$).

[28], while the other two NH sites remained uncoordinated due to steric hindrance. Non-covalent interaction (NCI) plot analysis revealed distinct intramolecular π–π dispersion interactions between the two aza[5]helicene moieties (green surface in Figure 4b) [29-31].

Optical properties

The electronic absorption and emission spectra of **4** were measured in DMSO (Figure 5a). As observed for other *o*-phenylene-bridged cyclic heteroarenes in previous reports, compound **4** exhibited a broad featureless absorption band up to 450 nm, with emission peaked at 546 nm. The red-shifted emission is likely due to a significant structural relaxation in the excited state. The fluorescence quantum yield (Φ_F) was determined as 0.078 (λ_{ex} = 300 nm), and the fluorescence lifetime (τ) using biexponential decay model fitting as 1.7 and 4.4 ns. The partially fused structure of **5** exhibited a well-defined lowest-energy absorption band peaked at 399 nm (Figure 5b). A broad emission was observed at 528 nm, resulting in a relatively large Stokes shift of 6100 cm^{-1}, which can be attributed to the structural relaxation in the excited state, as inferred by the observed broad ^1H NMR spectrum at room temperature. Due to the thermal energy loss, the Φ_F value was modest (0.072), which is lower than those of related aza[*n*]helicene analogs [27,28]. The fluorescence lifetime (τ) was determined by biexponential decay model fitting as 0.65 and 3.2 ns. DFT calculation was conducted to investigate the electronic structure. The HOMO and HOMO−1 are primarily localized on the aza[5]helicene moieties, while the orbital coefficients are distributed to the bridging thiophene and *o*-phenylene units in LUMO, indicating a charge-transfer (CT)-like transition. However, further optical characterization of compound **5** was limited due to its poor solubility in common organic solvents.

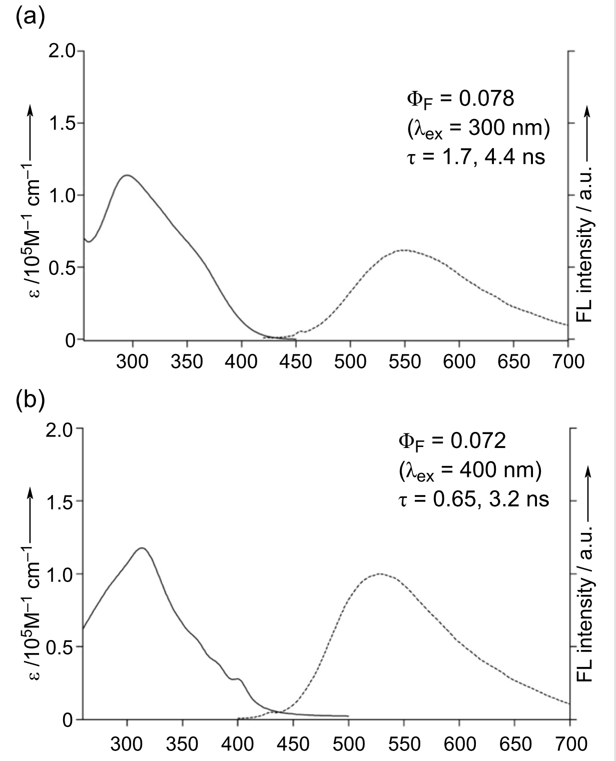

Figure 5: UV–vis absorption and emission spectra of (a) **4** and (b) **5** in DMSO.

Conclusion

A novel *o*-phenylene-pyrrole-thiophene hybrid macrocycle (icosamer **4**) was synthesized via Suzuki–Miyaura cross-coupling and isolated in 6% yield. Oxidation of **4** with PIFA produced a partially fused aza[5]helicene-containing macrocycle **5** in 58% yield, which was also characterized by X-ray analysis and NMR spectroscopy at elevated temperatures. Optical studies showed that compound **4** had broad absorption (up to 450 nm) and emission at 546 nm, while macrocycle **5** showed an emission peak at 528 nm, presumably as a consequence of structural relaxation and CT character. This study illuminated that a partially fused macrocyclic molecule is an intriguing structural motif which comprises a rigid backbone, yet showing somewhat flexible structural dynamics under ambient temperature conditions.

Supporting Information

Supporting Information File 1

Experimental procedures, characterization data of all products, copies of ^1H and ^{13}C NMR spectra, optical data, and DFT calculation results.
[https://www.beilstein-journals.org/bjoc/content/supplementary/1860-5397-21-119-S1.pdf]

Supporting Information File 2

Crystallographic Information File for compound **4**.
[https://www.beilstein-journals.org/bjoc/content/supplementary/1860-5397-21-119-S2.cif]

Supporting Information File 3

Crystallographic Information File for compound **5**.
[https://www.beilstein-journals.org/bjoc/content/supplementary/1860-5397-21-119-S3.cif]

Funding

This work was supported by the JST FOREST program Grant Number JPMJFR232D and JSPS KAKENHI Grant Numbers (22H00314 and 23K17942) and CREST, Japan Science and Technology Agency (JST). T.T. gratefully acknowledges the

Asahi Glass Foundation and Murata Science and Education Foundation (M24AN152). Y. M. acknowledges the JSPS fellowships for young scientists.

Author Contributions

Yusuke Matsuo: data curation; formal analysis; investigation; methodology. Aoi Nakagawa: data curation; investigation. Shu Seki: funding acquisition; resources; writing – review & editing. Takayuki Tanaka: conceptualization; funding acquisition; investigation; project administration; supervision; validation; visualization; writing – original draft; writing – review & editing.

ORCID® iDs

Shu Seki - https://orcid.org/0000-0001-7851-4405
Takayuki Tanaka - https://orcid.org/0000-0001-8018-7984

Data Availability Statement

All data that supports the findings of this study is available in the published article and/or the supporting information of this article.

Preprint

A non-peer-reviewed version of this article has been previously published as a preprint: https://doi.org/10.3762/bxiv.2025.39.v1

References

1. Iyoda, M.; Yamakawa, J.; Rahman, M. J. *Angew. Chem., Int. Ed.* **2011,** *50,* 10522–10553. doi:10.1002/anie.201006198
2. Lewis, S. E. *Chem. Soc. Rev.* **2015,** *44,* 2221–2304. doi:10.1039/c4cs00366g
3. Li, Y.; Kono, H.; Maekawa, T.; Segawa, Y.; Yagi, A.; Itami, K. *Acc. Mater. Res.* **2021,** *2,* 681–691. doi:10.1021/accountsmr.1c00105
4. Roy, R.; Brouillac, C.; Jacques, E.; Quinton, C.; Poriel, C. *Angew. Chem., Int. Ed.* **2024,** *63,* e202402608. doi:10.1002/anie.202402608
5. Sun, X.; Bai, J.; Wang, X.-Y.; Gong, H.-Y. *Coord. Chem. Rev.* **2024,** *518,* 216063. doi:10.1016/j.ccr.2024.216063
6. Povie, G.; Segawa, Y.; Nishihara, T.; Miyauchi, Y.; Itami, K. *Science* **2017,** *356,* 172–175. doi:10.1126/science.aam8158
7. Povie, G.; Segawa, Y.; Nishihara, T.; Miyauchi, Y.; Itami, K. *J. Am. Chem. Soc.* **2018,** *140,* 10054–10059. doi:10.1021/jacs.8b06842
8. Cheung, K. Y.; Watanabe, K.; Segawa, Y.; Itami, K. *Nat. Chem.* **2021,** *13,* 255–259. doi:10.1038/s41557-020-00627-5
9. Cheung, K. Y.; Gui, S.; Deng, C.; Liang, H.; Xia, Z.; Liu, Z.; Chi, L.; Miao, Q. *Chem* **2019,** *5,* 838–847. doi:10.1016/j.chempr.2019.01.004
10. Nogami, J.; Tanaka, Y.; Sugiyama, H.; Uekusa, H.; Muranaka, A.; Uchiyama, M.; Tanaka, K. *J. Am. Chem. Soc.* **2020,** *142,* 9834–9842. doi:10.1021/jacs.0c03684
11. Nogami, J.; Nagashima, Y.; Sugiyama, H.; Miyamoto, K.; Tanaka, Y.; Uekusa, H.; Muranaka, A.; Uchiyama, M.; Tanaka, K. *Angew. Chem., Int. Ed.* **2022,** *61,* e202200800. doi:10.1002/anie.202200800
12. Nogami, J.; Hashizume, D.; Nagashima, Y.; Miyamoto, K.; Uchiyama, M.; Tanaka, K. *Nat. Synth.* **2023,** *2,* 888–897. doi:10.1038/s44160-023-00318-2
13. Hitosugi, S.; Nakanishi, W.; Isobe, H. *Chem. – Asian J.* **2012,** *7,* 1550–1552. doi:10.1002/asia.201200187
14. Hitosugi, S.; Yamasaki, T.; Isobe, H. *J. Am. Chem. Soc.* **2012,** *134,* 12442–12445. doi:10.1021/ja305723j
15. Sun, Z.; Sarkar, P.; Suenaga, T.; Sato, S.; Isobe, H. *Angew. Chem., Int. Ed.* **2015,** *54,* 12800–12804. doi:10.1002/anie.201506424
16. Yang, Y.; Nanjo, Y.; Isobe, H.; Sato, S. *Org. Biomol. Chem.* **2020,** *18,* 4949–4955. doi:10.1039/d0ob01064b
17. Kurosaki, R.; Suzuki, M.; Hayashi, H.; Fujiki, M.; Aratani, N.; Yamada, H. *Chem. Commun.* **2019,** *55,* 9618–9621. doi:10.1039/c9cc03123e
18. Kurosaki, R.; Morimoto, H.; Matsuo, K.; Hayashi, H.; Yamada, H.; Aratani, N. *Chem. – Eur. J.* **2023,** *29,* e202203848. doi:10.1002/chem.202203848
19. Zhou, Z.; Yang, Y.; Liang, J.; Sato, S.; Zhang, Z.; Wei, Z. *Precis. Chem.* **2025,** *3,* 27–34. doi:10.1021/prechem.4c00064
20. Shouda, T.; Nakanishi, K.; Sasamori, T.; Tokitoh, N.; Kuramochi, K.; Tsubaki, K. *J. Org. Chem.* **2017,** *82,* 7850–7855. doi:10.1021/acs.joc.7b01053
21. Tanaka, T. *Bull. Chem. Soc. Jpn.* **2022,** *95,* 602–610. doi:10.1246/bcsj.20220030
22. Chen, F.; Tanaka, T.; Hong, Y.; Kim, W.; Kim, D.; Osuka, A. *Chem. – Eur. J.* **2016,** *22,* 10597–10606. doi:10.1002/chem.201601452
23. Chen, F.; Kim, J.; Matsuo, Y.; Hong, Y.; Kim, D.; Tanaka, T.; Osuka, A. *Asian J. Org. Chem.* **2019,** *8,* 994–1000. doi:10.1002/ajoc.201900168
24. Chen, F.; Tanaka, T.; Hong, Y. S.; Mori, T.; Kim, D.; Osuka, A. *Angew. Chem., Int. Ed.* **2017,** *56,* 14688–14693. doi:10.1002/anie.201708429
25. Matsuo, Y.; Osuka, A.; Tanaka, T. *Synthesis* **2022,** *54,* 147–152. doi:10.1055/a-1577-7972
26. Matsuo, Y.; Maeda, C.; Tsutsui, Y.; Tanaka, T.; Seki, S. *Angew. Chem., Int. Ed.* **2023,** *62,* e202314968. doi:10.1002/anie.202314968
27. Chen, F.; Tanaka, T.; Mori, T.; Osuka, A. *Chem. – Eur. J.* **2018,** *24,* 7489–7497. doi:10.1002/chem.201800617
28. Matsuo, Y.; Gon, M.; Tanaka, K.; Seki, S.; Tanaka, T. *J. Am. Chem. Soc.* **2024,** *146,* 17428–17437. doi:10.1021/jacs.4c05156
29. Johnson, E. R.; Keinan, S.; Mori-Sánchez, P.; Contreras-García, J.; Cohen, A. J.; Yang, W. *J. Am. Chem. Soc.* **2010,** *132,* 6498–6506. doi:10.1021/ja100936w
30. Contreras-García, J.; Johnson, E. R.; Keinan, S.; Chaudret, R.; Piquemal, J.-P.; Beratan, D. N.; Yang, W. *J. Chem. Theory Comput.* **2011,** *7,* 625–632. doi:10.1021/ct100641a
31. Boto, R. A.; Peccati, F.; Laplaza, R.; Quan, C.; Carbone, A.; Piquemal, J.-P.; Maday, Y.; Contreras-Garcıa, J. *J. Chem. Theory Comput.* **2020,** *16,* 4150–4158. doi:10.1021/acs.jctc.0c00063

License and Terms

BEILSTEIN JOURNAL OF ORGANIC CHEMISTRY

pH-Controlled isomerization kinetics of *ortho*-disubstituted benzamidines: *E*/*Z* isomerism and axial chirality

Ryota Kimura[1], Satoshi Ichikawa[*,‡1,2] and Akira Katsuyama[*,‡1,2]

Letter

Open Access

Address:
[1]Faculty of Pharmaceutical Sciences, Hokkaido University, Kita-12, Nishi-6, Kita-ku, Sapporo 060-0812, Japan and [2]Center for Research and Education on Drug Discovery, Faculty of Pharmaceutical Sciences, Hokkaido University, Kita-12, Nishi-6, Kita-ku, Sapporo 060-0812, Japan

Email:
Satoshi Ichikawa[*] - ichikawa@pharm.hokudai.ac.jp;
Akira Katsuyama[*] - katsuyama@pharm.hokudai.ac.jp

* Corresponding author ‡ Equal contributors

Keywords:
atropisomer; conformation; isomerization; molecular switch; organobase

Beilstein J. Org. Chem. **2025,** *21,* 1568–1576.
https://doi.org/10.3762/bjoc.21.120

Received: 30 May 2025
Accepted: 25 July 2025
Published: 04 August 2025

This article is part of the thematic issue "Non-central chirality in organic chemistry".

Associate Editor: N. Yoshikai

Abstract

pH-Responsive molecular switches and motors are a class of organic molecules whose three-dimensional structure can be changed by acid–base stimuli. To date, pH-responsive molecular switches have been developed using various functional groups, but further advances require expanding the range of pH-responsive systems and discovering new molecular architectures. Here, we investigate the pH-responsive behavior of *ortho*-disubstituted benzamidine, which generates atropisomers and *E*/*Z* isomers. The amidine moiety allows modulation of the C–N and C–N/C–C rotational barriers by protonation, providing a novel approach to control the kinetics of isomerization via pH adjustment. The results showed that protonation of the amidine moiety significantly suppresses both C–N bond rotation and C–N/C–C concerted rotation, demonstrating the potential of *ortho*-disubstituted benzamidine derivatives as a novel pH-responsive molecular switch.

Introduction

pH-Responsive molecular motors and switches are a class of functional organic molecules capable of reversible structural and electronic changes triggered by protonation and deprotonation [1-19]. This class of molecules has the capacity to regulate three-dimensional structures and motions of molecules through simple acid–base stimuli. This provides a high degree of control over their behavior, allowing for both tunability and predictability. Among the various types of pH-sensitive molecular switches, those that rely on isomerism caused by the rotation of molecular bonds are attracting attention because they can apply the most basic property of molecular conformation to molecular switches [19]. For example, hydrazone-based molecular switches undergo reversible *E*/*Z* isomerization around the C=N bond [1-7], with protonation significantly shifting the equilibrium. Beyond double-bond isomerization, pH stimuli have also been employed to modulate rotational barriers in axially chiral anilines [10,11] and a triazine molecule [9]. In particular, protonation of a remote basic site in N–C axially chiral anilines significantly increases the rotational barrier by attenuating resonance stabilization in the transition state. One important issue in this field is the development of molecules that can precisely control the range of pH to which they can respond. Furthermore, it is also important to discover new molecular skeletons, as there is a lack of variation in the substructures that act as pH-responsive molecular switches.

Previously, we reported that chalcogen substitution of an *ortho*-disubstituted benzamide (DiBA) increases the rotational barrier of the C–N and C–N/C–C concerted rotation (Figure 1a,b) [20]. The observation can be explained mainly by the double-bond nature of the chalcogen amide C–N bond, which is attributed to a zwitterionic resonance structure of chalcogen amide. It has been shown that a late periodic chalcogen amide has a lower energy π^* orbital (C=S or C=Se), resulting in an increase in the contribution of the zwitterionic resonance structure [21-23]. Based on this consideration, an *ortho*-disubstituted benzamidine, which is generated by formal substitution of the carbonyl oxygen atom of DiBA to an NH group, could act as a pH-responsive molecular switch (Figure 1c). Namely, the double-bond nature of an amidine moiety can be altered by the protonation of the amidine nitrogen atom. This suggests the possibility of controlling the rate of C–N rotation and C–N/C–C rotation by adjusting the pH of the solvent and the pK_a of the amidine. Herein, we report our findings on the structural properties of an *ortho*-disubstituted benzamidine. Similar to DiBA, an *ortho*-disubstituted benzamidine has two types of stereoisomers: *E*/*Z* isomers arising from the amidine C–N bond and atropisomers generated from the constrained C–C axis. Both C–N rotation and C–N/C–C rotation are suppressed by the protonation of the amidine moiety, and the rate of the isomerization can be controlled by the basicity of the amidine moiety.

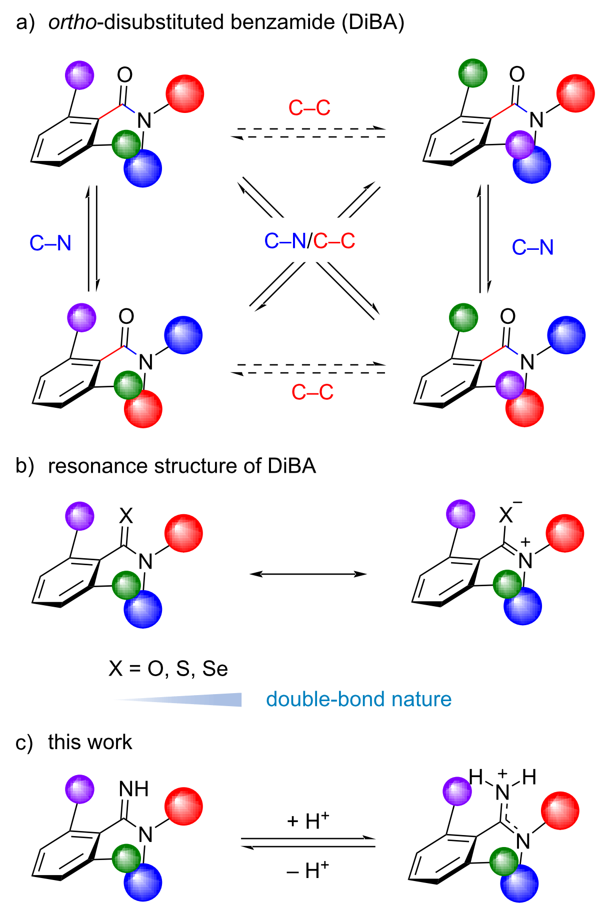

Figure 1: a) Structural features of DiBA. b) Resonance structure of the amide moiety of DiBA. c) Molecular form and protonated structure of *ortho*-disubstituted benzamidine.

Results and Discussion

To the best of our knowledge, although the structural analysis of the *E*/*Z* isomerism of amidine [24,25] and the effect of the protonation of an amidine moiety on the rotational barrier of the C–N bond [26] have been studied, the separation of amidine *E*/*Z* isomers has not been reported yet. To verify our hypothesis that the rotational barrier of the benzamidine changes upon protonation, density functional theory (DFT) calculations were performed for the C–N and C–N/C–C rotations of the molecular form and of the protonated 2-bromo-*N*,*N*,6-trimethylbenzimidamide as a model compound (Figure 2). Several transition states (TSs) were found depending on the configuration of the amidine N–H and the rotational direction. The C–N bond rotation of the molecular form of amidine was calculated to be 68 kJ·mol^{-1} for *Z*-amidine and 71 kJ·mol^{-1} for *E*-amidine. Protonation of the amidine moiety drastically increases the rotational barrier (132 kJ·mol^{-1}), suggesting that the protonation suppresses the C–N bond rotation via the increased double-bond nature of the C–N axis. A similar trend was found for the C–N/C–C concerted rotation (Figure 2). Compared with the C–N bond rotation, the C–N/C–C bond rotation requires a higher rotational barrier as in the parent chalcogen amides, regardless of whether it is in the molecular form or protonated state, and the protonation of the nitrogen atom increases the activation energy by 33–43 kJ·mol^{-1}. To investigate how protonation affects the double-bond nature of the amidine moiety, we calculated the distance between the imino carbon atom and the nitrogen atom of the NMe_2 moiety (*d*) for local minimum and transition-state structures (Figure 2). In the local minimum and transition state of the C–N rotation and C–N/C–C concerted rotation, protonation leads to a shortening of the C–N bond by 0.6 Å and 0.3–0.4 Å, respectively. This result indicates that protonation has a greater impact on the local minimum structures,

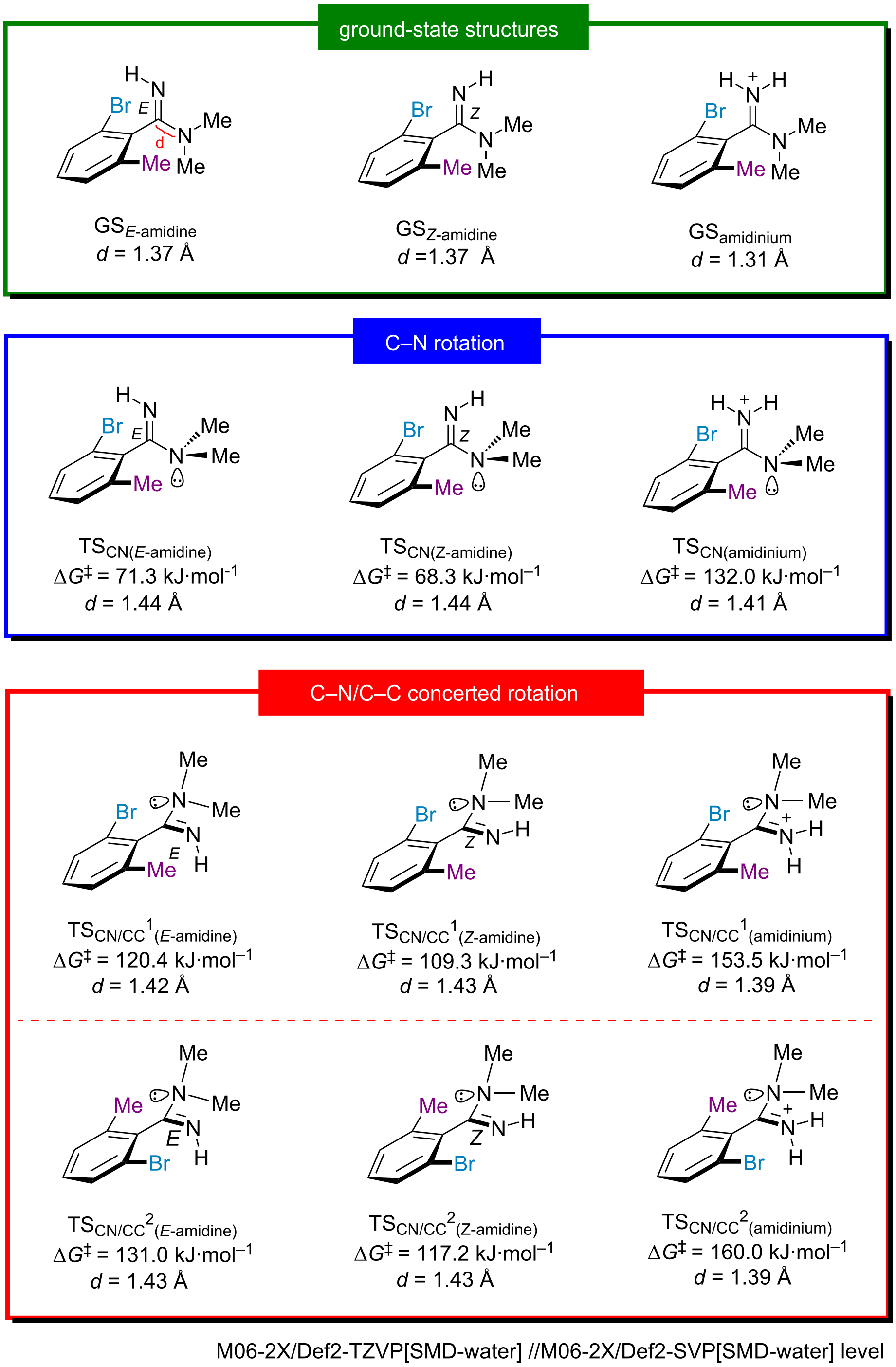

Figure 2: Rotational barriers of 2-bromo-*N*,*N*,6-trimethylbenzimidamide and its protonated form calculated by the DFT method.

as the p orbital of the nitrogen atom in the NMe_2 moiety and the C=N π orbital are located in the same plane, allowing for effective conjugation between them. The DFT study clearly showed that the rotational barriers of *ortho*-disubstituted benzamidine can be modulated by the protonation or deprotonation of the amidine moiety.

Next, we experimentally examined the C–N rotation of 2-bromo-*N*,*N*-diethyl-6-methylbenzimidamide (**1**). First, the effect of the protonation on the C–N bond rotation was investigated by variable temperature nuclear magnetic resonance (VT-NMR) spectra (Figure 3) in DMSO-d_6 [27]. In the case of the molecular form of amidine **1** (Figure 3a), the signals corre-

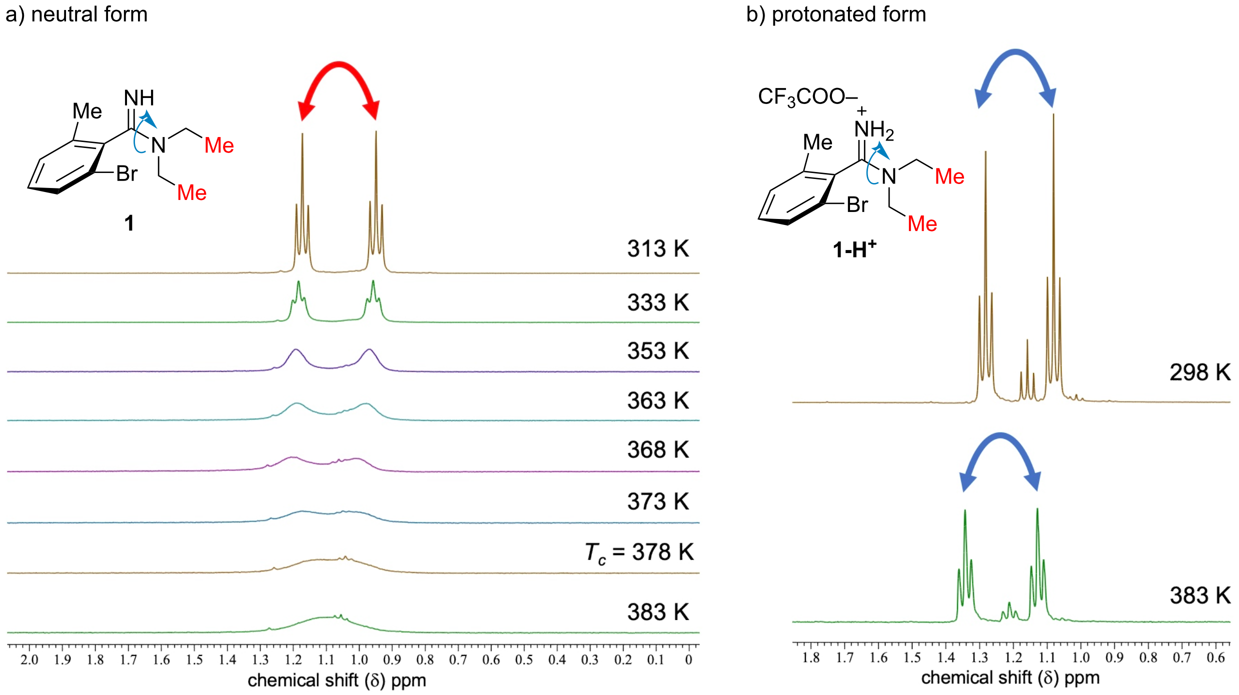

Figure 3: Comparison of VT-NMR spectra of a) amidine **1** and b) its trifluoroacetate salt **1-H$^+$** in DMSO-d_6 (400 MHz).

sponding to the two methyl groups resulting from the amidine *E*/*Z* isomerism were observed separately at 313 K (1.17 and 0.95 ppm), and they gradually fused as the temperature increased. The activation energy of *E*/*Z* isomerization was calculated to be 77 kJ·mol^{-1} from the observed coalescence temperature (T_c = 378 K). On the other hand, the two methyl signals of amidine **1** trifluoroacetate salt were not coalesced even at 383 K, indicating that the C–N bond rotation was sufficiently slow on the NMR time scale (Figure 3b).

To separate each *E*/*Z* isomer, amidine **2** with two different substituents on the same nitrogen atom, was prepared, and racemic **2** was analyzed by reversed-phase high performance liquid chromatography (RP-HPLC) using an acidic mobile phase [H_2O (0.1% CF_3CO_2H)/MeCN 72:28]. As shown in Figure 4, the HPLC analysis of amidine **2** showed two peaks corresponding to the *E* and *Z* isomers which could be explained by the existence of *E*/*Z* isomers of amidine **2** trifluoroacetate salt. After separation of the two peaks, HPLC analysis of each separated component showed single peaks, suggesting that the *E* and *Z* isomers of amidine **2** trifluoroacetate salt could be separated by standard RP-HPLC. The configuration of the amidine moiety of each component was characterized by NOE experiments (for details, see Supporting Information File 1). The NMR and HPLC experiments clearly indicate that protonation of the amidine moiety increases the rotational barrier of the C–N bond, a result which is consistent with our DFT study.

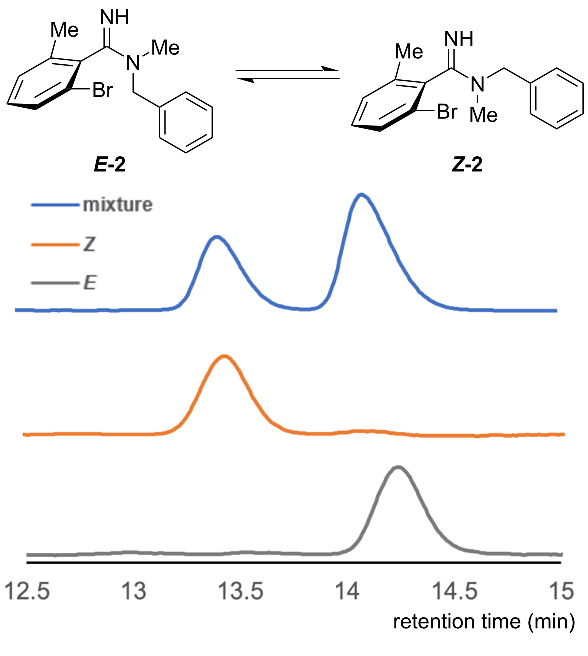

Figure 4: Separation and isolation of amidine *E*/*Z* isomers by RP-HPLC. The mobile phase contained CF_3CO_2H to protonate the amidine moiety.

Since it was found that the *E*/*Z* isomers of amidine could be isolated as a TFA salt, the kinetics of the C–N bond rotation at different pH values was then evaluated. The *E*/*Z* ratio of the isolated **Z-2** trifluoroacetate salt (**Z-2-H$^+$**) in three buffers (pH 4.6, 5.5, and 6.5, respectively) was calculated by RP-HPLC at different times at 20 °C (Figure 5). The curve fitting analysis of the obtained data points yielded an apparent first-order rate constant (k) of $8.3 \times 10^{-7} \cdot s^{-1}$ at pH 4.6, $4.8 \times 10^{-6} \cdot s^{-1}$ at pH 5.5, and $6.0 \times 10^{-5} \cdot s^{-1}$ at pH 6.5. These results indicate that isomerization was suppressed as pH decreased, as expected. Plotting log(k) versus pH showed a linear relationship with a slope of 1 (Figure 6). This result means that a change of one unit in pH results in about a 10-fold change in the isomerization rate, considering the Henderson–Hasselbalch equation, where pH changes of one increases or decreases the amount of molecular form by a factor of ten. The experimental results, showing that the pH dependence of the isomerization rate closely matches

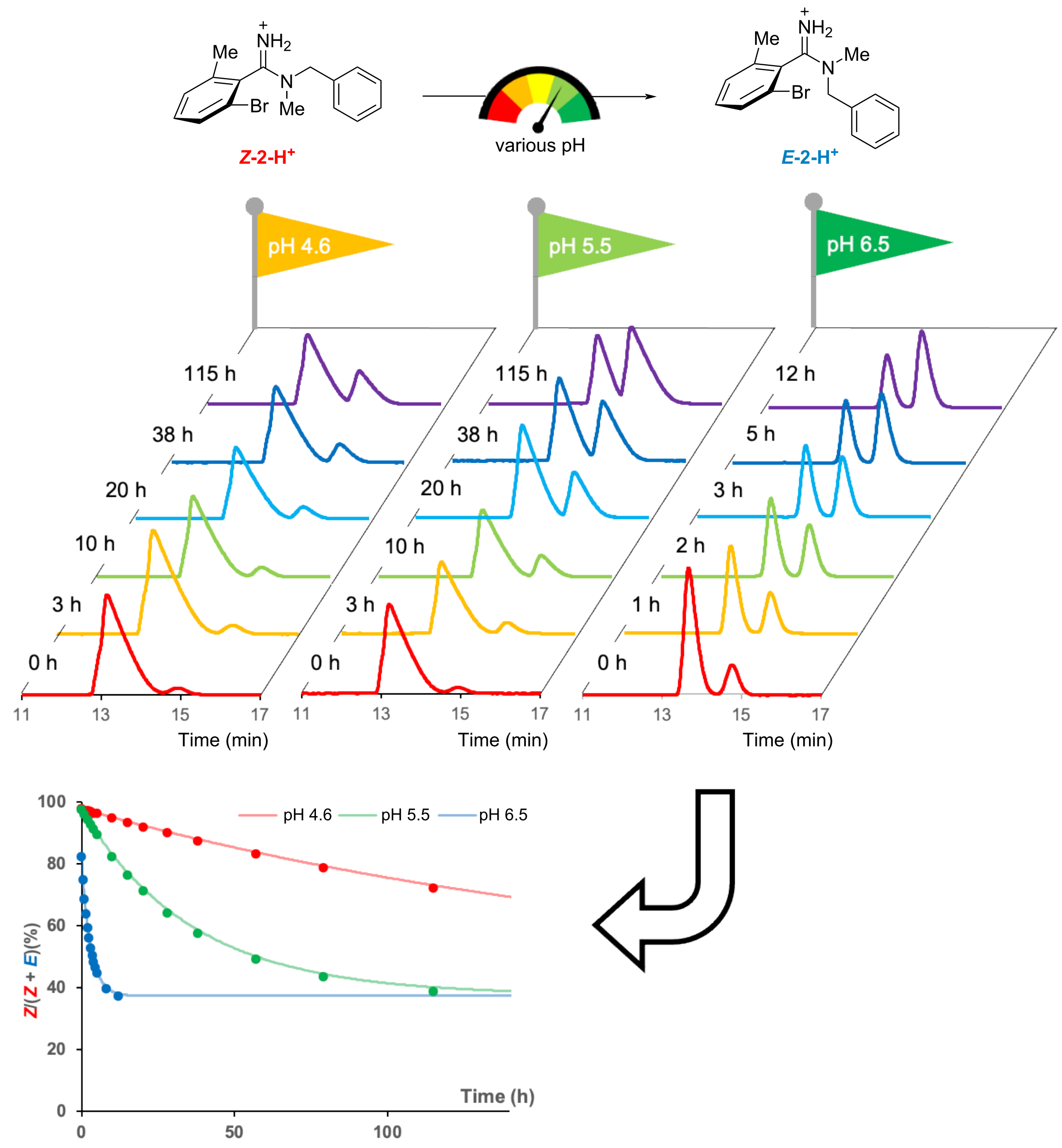

Figure 5: Kinetic analysis of the isomerization of ***Z*-2-H$^+$** to ***E*-2-H$^+$** at different pH (pH 4.6, 5.5, and 6.5). In the bottom graph, each circle represents the experimental ratio of the *Z* isomer at each time point, and each curve shows the theoretical value obtained from the curve-fitting analysis of the experimental data.

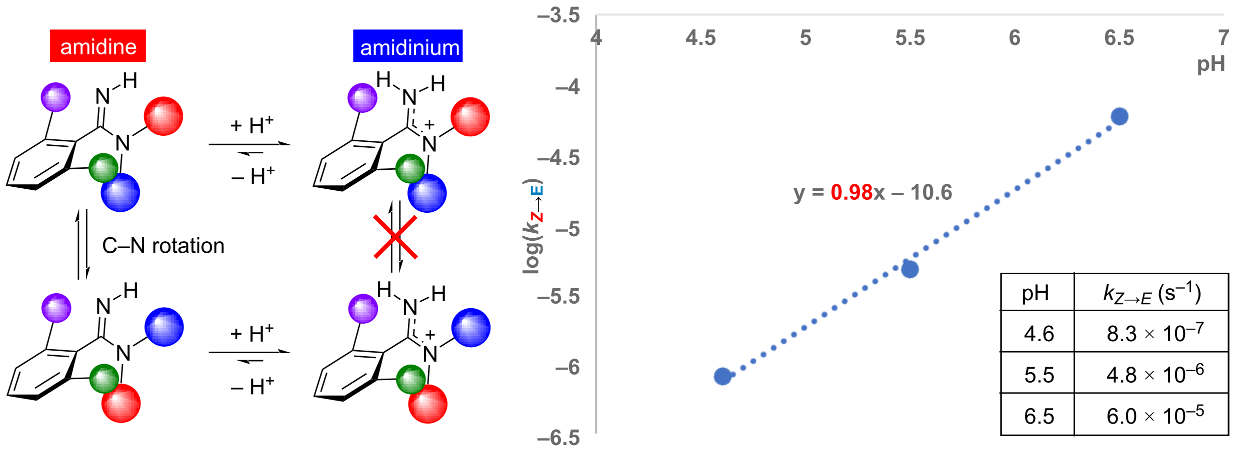

pH	$k_{Z\to E}$ (s^{-1})
4.6	8.3×10^{-7}
5.5	4.8×10^{-6}
6.5	6.0×10^{-5}

Figure 6: Correlation between *E*/*Z* isomerization rate constant and pH. The result indicates that C–N rotation from the molecular form of amidine was dominant in the observed isomerization.

that of the molecular form of the amidine fraction, suggest that the observed C–N isomerization mainly proceeds from the molecular form. These results suggest that the C–N bond rotation in amidines may be governed by the fraction of the molecular form species present at a given pH, reflecting the basicity of the amidine. Motivated by this finding, we next investigated the relationship between amidine basicity and the isomerization rate.

To systematically modulate the basicity of amidine, we designed *N*-phenylbenzimidamides **3**–**7**, with different electron-donating or electron-withdrawing substituents at the *para*-position of the phenyl ring conjugated with the amidine moiety. The same kinetic analysis was performed for compounds **3**–**7** at pH 4.0, 4.5, 5.0, and 5.5, and the results are summarized in Table 1. In addition, the calculated pK_a values of the amidines are also shown in Table 1. As a result, the C–N isomerization was accelerated by an electron-withdrawing chloro substituent, and electron-donating substituents (Me, OMe and NMe_2 groups) decreased the isomerization rate. Figure 7a illustrates the effect of the electronic property of each substituent, which is represented as the Hammett substituent constant [28], on the rate constant at different pH. Consistent with the results for amidine **2**, amidines **3**–**7** showed smaller rate constants at more acidic pH, suggesting that isomerization of the molecular form species was also predominant for amidines **3**–**7**. The results at the same pH suggest that the isomerization rate varies systematically depending on the electron-donating or electron-withdrawing property of the substituent, indicating that the isomerization rate can be controlled by the basicity of the amidine. It is noteworthy that the pH dependence was relatively smaller in the case of amidine **7** (X = NMe_2). This fact could be rationalized by the existence of different protonation states of amidine **7**

Table 1: The pK_a value of each compound and rate constants of *E*/*Z* isomerization at various pH values.

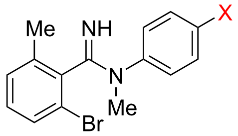

3: X = Cl
4: X = H
5: X = Me
6: X = OMe
7: X = NMe_2

compound	pK_a[a]	pH	*k* ($10^{-6}\cdot s^{-1}$)	
			Z to *E*	*E* to *Z*
3	9.36	4.0	14.0	20.6
		4.5	36.6	53.4
		5.0	115.0	159.8
		5.5	305.3	427.8
4	10.02	4.0	5.4	10.8
		4.5	12.7	24.5
		5.0	34.3	66.3
		5.5	97.7	186.2
5	10.31	4.0	2.8	4.6
		4.5	7.1	12.5
		5.0	18.8	32.4
		5.5	54.7	97.8
6	10.32	4.0	2.4	4.1
		4.5	5.6	10.5
		5.0	18.8	32.4
		5.5	47.0	85.8
7	10.82	4.0	10.1	15.1
		4.5	12.2	18.2
		5.0	18.7	28.1
		5.5	37.9	57.1

[a] Calculated by Jaguar program (Schrödinger, LLC, 2024).

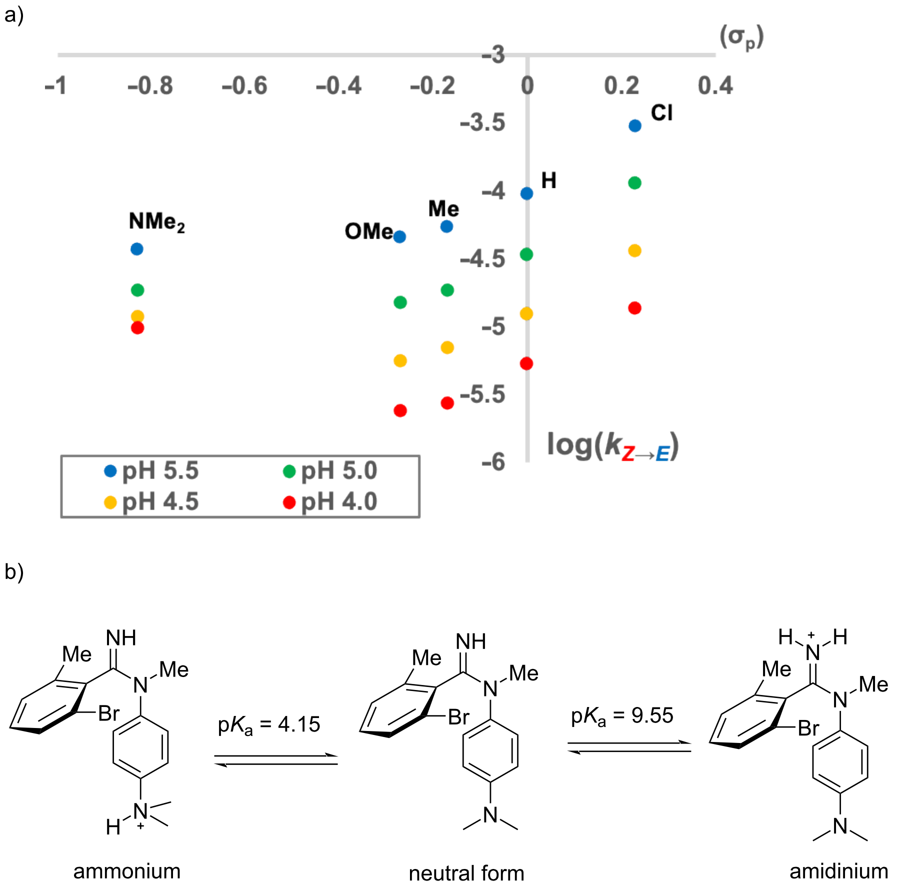

Figure 7: a) Correlation between isomerization rate constant and electronic effects of the substituents. b) Possible protonated states of compound **7**.

(Figure 7b). In the case of amidine **7**, both the amidine moiety and the NMe_2 group could be protonated under acidic conditions, and the NMe_2-protonated species has a similar double-bond nature for the C–N bond as the molecular form. Thus, it can be assumed that the presence of the NMe_2-protonated species reduced the apparent population of the protonated amidine under acidic conditions, resulting in a decrease in the inhibitory effect of the C–N rotation due to the decrease in pH.

As the rotation of the C–N bond of the *ortho*-disubstituted benzamidine could be controlled by the protonation of the amidine moiety, we then focused on the chiral axis of the *ortho*-disubstituted benzamidine. Our DFT calculations suggested that the double-bond nature of the C–N bond in the transition state of the C–N/C–C concerted rotation was decreased due to the twisted structure, and the activation energy varies depending on whether the amidine was protonated or in its molecular form (Figure 2). To investigate the effect of protonation on the stability of the chiral axis, amidine **1**, which has identical substituents on the amidine nitrogen and thus does not generate *E*/*Z* isomers, was selected. In the chiral HPLC analysis using an acidic eluent [$MeCN/H_2O$ (containing 0.5% CF_3CO_2H) 20:80], the trifluoroacetate salt of amidine **1** was observed as two peaks corresponding to the atropisomers arising from the C–C axis. Each atropisomer could be separated by chiral HPLC, and the isomer eluting earlier was used for the following kinetic analysis. The effect of pH on the kinetics of the racemization was investigated. The isomer was heated in the buffer (pH 9.2, 10.3, 11.7, and 12.7) at 70 °C, and the er value was monitored at each time point (Figure 8). The rate constants obtained from the curve fitting analysis of the experimental results significantly changed in the examined pH range (Table 2), and the rate constants increased with rising pH. Notably, at pH 9.2, racemization proceeded minimally, even under high temperature conditions. Furthermore, it was confirmed that racemization requires a higher pH where a higher proportion of the amidine exists in its molecular form. This result was consistent with our DFT calculations, which showed that the rotational barrier of the C–N/C–C concerted rotation is higher than that of C–N rotation. This finding is consistent with the calculated pK_a of 10.6 for amidine **1**, indicating that racemization is minimal under the conditions where most of the amidine remains in its protonated form. As pH was increased above the pK_a, the proportion of the molecular form of amidine increased, leading to a significant increase in the isomerization rate. These observations underscore the significant influence of pH on the racemization kinetics of amidine **1**, as shown in Table 1. As a result, it was found that as well as the C–N bond rotation the racemization rate could be controlled by the protonation of the basic amidine moiety. This result indicates the possibility of controlling the stability of the chiral axis by the basicity of the amidine, as well as the C–N bond, as mentioned above.

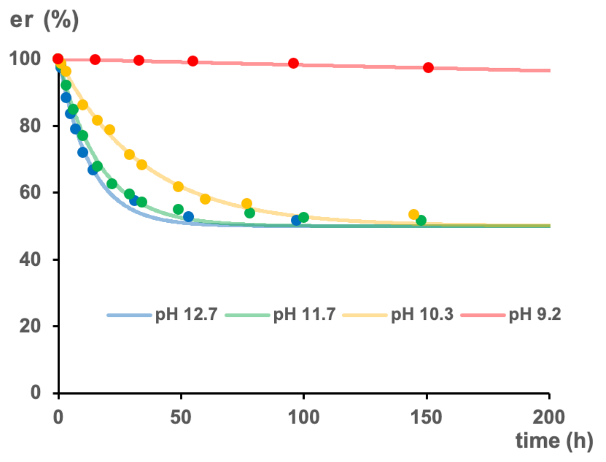

Figure 8: Analysis of the rate of racemization of **1** at various pH at 70 °C. Each circle shows the experimental er at each time point, and each curve shows the theoretical value obtained from the curve fitting analysis of the experimental data.

Table 2: Rate constants of racemization of **1** at various pH at 70 °C.

pH	k_{rac} ($10^{-6}{\cdot}\text{s}^{-1}$)
9.2	0.05
10.3	4.0
11.7	8.3
12.7	10.7

Conclusion

In conclusion, we demonstrated that the rate of the C–N bond rotation and racemization of *ortho*-disubstituted benzamidine could be controlled by the protonation of the amidine moiety and showed the potential for application as a pH-responsive molecular switch based on changes in the rotation rate of the two axes. For the C–N bond rotation, the basicity of the amidine moiety had a clear impact on the rate of bond rotation, and the finding could be helpful to the rational design of pH-responsive molecular switches based on the *ortho*-disubstituted benzamidine. The study presented here also shows the usefulness of the single-atom substitution strategy on DiBA. By replacing the oxygen atom of DiBA with a nitrogen atom (and thus NH), which has been shown to be photo-responsive when replaced with sulfur or selenium, the pH-responsive property was acquired. Such minimal changes in physical properties can be made with little effect on the molecular structure and are widely used in areas such as carbon materials. If the three-dimensional structure of molecules can be manipulated by various external stimuli through such modifications, we can expect to develop useful molecular switches that can be applied to various fields, such as functional materials, biological probes, and drugs.

Supporting Information

Supporting Information File 1

Detailed experimental procedures, spectral data and HPLC charts.
[https://www.beilstein-journals.org/bjoc/content/supplementary/1860-5397-21-120-S1.pdf]

Acknowledgements

HRMS analysis of the synthesized compounds was performed by Hokkaido University, Global Facility Center (GFC), Pharma Science Open Unit (PSOU), funded by MEXT under "Support Program for Implementation of New Equipment Sharing System".

Funding

This research was supported in part by JSPS KAKENHI Grant-in-Aid for Challenging Research (Exploratory) (S.I., Grant Number JP18K19384), Grant Platform Project for Supporting Drug Discovery and Life Science Research (Basis for Supporting Innovative Drug Discovery and Life Science Research (BINDS)) from AMED (S.I., Grant Number JP25ama121039), JSPS Grant-in-Aid for Scientific Research (C) (A.K., Grant Number JP24K09703).

Author Contributions

Ryota Kimura: investigation; methodology; visualization; writing – original draft. Satoshi Ichikawa: conceptualization; funding acquisition; supervision; writing – review & editing. Akira Katsuyama: conceptualization; funding acquisition; methodology; project administration; writing – original draft; writing – review & editing.

ORCID® iDs

Satoshi Ichikawa - https://orcid.org/0000-0001-5345-5007
Akira Katsuyama - https://orcid.org/0000-0002-4062-5561

Data Availability Statement

All data that supports the findings of this study is available in the published article and/or the supporting information of this article.

References

1. Landge, S. M.; Aprahamian, I. *J. Am. Chem. Soc.* **2009,** *131,* 18269–18271. doi:10.1021/ja909149z
2. Tatum, L. A.; Su, X.; Aprahamian, I. *Acc. Chem. Res.* **2014,** *47,* 2141–2149. doi:10.1021/ar500111f
3. Ray, D.; Foy, J. T.; Hughes, R. P.; Aprahamian, I. *Nat. Chem.* **2012,** *4,* 757–762. doi:10.1038/nchem.1408
4. Foy, J. T.; Ray, D.; Aprahamian, I. *Chem. Sci.* **2015,** *6,* 209–213. doi:10.1039/c4sc02882a
5. Dial, B. E.; Pellechia, P. J.; Smith, M. D.; Shimizu, K. D. *J. Am. Chem. Soc.* **2012,** *134,* 3675–3678. doi:10.1021/ja2120184
6. Kassem, S.; Lee, A. T. L.; Leigh, D. A.; Markevicius, A.; Solà, J. *Nat. Chem.* **2016,** *8,* 138–143. doi:10.1038/nchem.2410
7. Kassem, S.; Lee, A. T. L.; Leigh, D. A.; Marcos, V.; Palmer, L. I.; Pisano, S. *Nature* **2017,** *549,* 374–378. doi:10.1038/nature23677
8. Kyba, E. P.; Gokel, G. W.; De Jong, F.; Koga, K.; Sousa, L. R.; Siegel, M. G.; Kaplan, L.; Sogah, G. D. Y.; Cram, D. J. *J. Org. Chem.* **1977,** *42,* 4173–4184. doi:10.1021/jo00862a001
9. Claton, L. E.; Pan, H.; Simanek, E. E. *J. Org. Chem.* **2024,** *89,* 5480–5484. doi:10.1021/acs.joc.3c02918
10. Iwasaki, Y.; Morisawa, R.; Yokojima, S.; Hasegawa, H.; Roussel, C.; Vanthuyne, N.; Caytan, E.; Kitagawa, O. *Chem. – Eur. J.* **2018,** *24,* 4453–4458. doi:10.1002/chem.201706115
11. Homma, D.; Taketani, S.; Shirai, T.; Caytan, E.; Roussel, C.; Elguero, J.; Alkorta, I.; Kitagawa, O. *J. Org. Chem.* **2022,** *87,* 8118–8125. doi:10.1021/acs.joc.2c00845
12. Mandal, D.; Sarkar, A.; Behera, K. C.; Ravikanth, M. *Chem. Sci.* **2025,** *16,* 1772–1782. doi:10.1039/d4sc07016j
13. Wu, Y.; Wang, G.; Li, Q.; Xiang, J.; Jiang, H.; Wang, Y. *Nat. Commun.* **2018,** *9,* 1953. doi:10.1038/s41467-018-04323-4
14. Mock, W. L.; Pierpont, J. *J. Chem. Soc., Chem. Commun.* **1990,** 1509–1511. doi:10.1039/c39900001509
15. Jun, S. I.; Lee, J. W.; Sakamoto, S.; Yamaguchi, K.; Kim, K. *Tetrahedron Lett.* **2000,** *41,* 471–475. doi:10.1016/s0040-4039(99)02094-8
16. Harris, J. D.; Moran, M. J.; Aprahamian, I. *Proc. Natl. Acad. Sci. U. S. A.* **2018,** *115,* 9414–9422. doi:10.1073/pnas.1714499115
17. Su, X.; Aprahamian, I. *Chem. Soc. Rev.* **2014,** *43,* 1963–1981. doi:10.1039/c3cs60385g
18. Fitzmaurice, O.; Bartkowski, M.; Giordani, S. *Front. Chem. (Lausanne, Switz.)* **2022,** *10,* 859450. doi:10.3389/fchem.2022.859450
19. Zhou, H.-Y.; Han, Y.; Chen, C.-F. *Mater. Chem. Front.* **2020,** *4,* 12–28. doi:10.1039/c9qm00546c
20. Nagami, S.; Kaguchi, R.; Akahane, T.; Harabuchi, Y.; Taniguchi, T.; Monde, K.; Maeda, S.; Ichikawa, S.; Katsuyama, A. *Nat. Chem.* **2024,** *16,* 959–969. doi:10.1038/s41557-024-01461-9
21. Radael, G. N.; Pontes, R. M. *Comput. Theor. Chem.* **2020,** *1187,* 112938. doi:10.1016/j.comptc.2020.112938
22. Nieuwland, C.; Fonseca Guerra, C. *Chem. – Eur. J.* **2022,** *28,* e202200755. doi:10.1002/chem.202200755
23. Zhao, Q.; Li, G.; Nareddy, P.; Jordan, F.; Lalancette, R.; Szostak, R.; Szostak, M. *Angew. Chem., Int. Ed.* **2022,** *61,* e202207346. doi:10.1002/anie.202207346
24. Cunningham, I. D.; Hegarty, A. F. *J. Chem. Soc., Perkin Trans. 2* **1986,** 537–541. doi:10.1039/p29860000537
25. Kalz, K. F.; Hausmann, A.; Dechert, S.; Meyer, S.; John, M.; Meyer, F. *Chem. – Eur. J.* **2016,** *22,* 18190–18196. doi:10.1002/chem.201603850
26. McKennis, J. S.; Smith, P. A. S. *J. Org. Chem.* **1972,** *37,* 4173–4178. doi:10.1021/jo00798a045
27. Huggins, M. T.; Kesharwani, T.; Buttrick, J.; Nicholson, C. *J. Chem. Educ.* **2020,** *97,* 1425–1429. doi:10.1021/acs.jchemed.0c00057
28. Hansch, C.; Leo, A.; Taft, R. W. *Chem. Rev.* **1991,** *91,* 165–195. doi:10.1021/cr00002a004

License and Terms

The definitive version of this article is the electronic one which can be found at:
https://doi.org/10.3762/bjoc.21.120

BEILSTEIN JOURNAL OF ORGANIC CHEMISTRY

Synthesis of optically active folded cyclic dimers and trimers

Ena Kumamoto, Kana Ogawa, Kazunori Okamoto and Yasuhiro Morisaki*

Full Research Paper

Open Access

Address:
Department of Applied Chemistry for Environment, School of Biological and Environmental Sciences, Kwansei Gakuin University, 1 Gakuen Uegahara, Sanda, Hyogo 669-1330, Japan

Email:
Yasuhiro Morisaki* - ymo@kwansei.ac.jp

* Corresponding author

Keywords:
circularly polarized luminescence; oligomer; [2.2]paracyclophane; planar chirality

Beilstein J. Org. Chem. **2025,** *21,* 1603–1612.
https://doi.org/10.3762/bjoc.21.124

Received: 29 May 2025
Accepted: 30 July 2025
Published: 11 August 2025

This article is part of the thematic issue "Non-central chirality in organic chemistry".

Associate Editor: N. Yoshikai

Abstract

Optically active higher-ordered structures, such as one-handed helical and propeller-shaped structures, can be constructed by folding the π-conjugated system using [2.2]paracyclophane as the chiral crossing unit, leading to circularly polarized luminescence (CPL) properties. Chiral cyclic dimers and trimers were synthesized using planar chiral [2.2]paracyclophane-containing enantiopure ribbon-shaped compounds as the chiral monomers. Unicursal π-conjugated systems were folded at the [2.2]paracyclophane units, and exhibited good photoluminescence quantum efficiencies and CPL anisotropy factors. Opposite chiroptical properties were observed between the dimer and trimer, despite the same absolute configuration of the planar chiral [2.2]paracyclophane units, which was reproduced by theoretical studies.

Introduction

Cyclophane is a general term for cyclic compounds with at least one aromatic ring in the main chain backbone [1]. Cyclophane compounds have long been known; [2.2]paracyclophane was first reported as a cyclic dimer of paraxylylene by Brown et al. in 1949 [2]. In 1951, Cram et al. reported the practical synthesis of [2.2]paracyclophanes via Wurtz-type intramolecular cyclization [3]. [2.2]Paracyclophane has a molecular structure in which two benzene rings are stacked face-to-face with ethylene chains at the para positions. Various studies have been conducted on their reactivities and physical properties derived from their unique molecular structure with stacked π-electron clouds [1,4-6]. The distance between benzene rings in [2.2]paracyclophane is extremely short (2.8–3.1Å), and thus the rotational motion of benzene rings is completely suppressed; therefore, planar chirality without chiral centers [7] appears by introducing substituent(s) at appropriate position(s) on the benzene rings [8]. Enantiopure planar chiral [2.2]paracyclophanes have been used as chiral auxiliaries and chiral ligands for transition metals in the fields of organic and organometallic chemistry [9-20]. In 2012, enantiopure [2.2]paracyclophane was used as a chiral monomer to prepare optically active conjugated polymers and cyclic trimers [21], in which π-electron systems were stacked to form zigzag and triangular structures, respectively. The conjugated polymers and cyclic trimers exhibited circularly polarized luminescence (CPL) [22-25] with high photoluminescence (PL) quantum efficiency (Φ_{PL}) and anisotropy. Additionally, the π-stacked structure of [2.2]paracyclophane can be applied at a crossing point. By folding the π-conjugated system using [2.2]paracyclophane as the chiral crossing unit, optically active higher-ordered structures, such as one-handed helical [26,27] and propeller-shaped structures [28-30], can be constructed, leading to the excellent CPL behaviors. Recently, planar chiral [2.2]paracyclophane-containing cyclic molecules have been received attention; for examples, the one-handed double helical compounds [31-34] and chiral nanohoops [35,36] emitting circularly polarized fluorescence have been reported. In this study, enantiopure ribbon-shaped compounds based on planar chiral tetrasubstituted [2.2]paracyclophane were used as chiral monomers, and optically active cyclic dimers and trimers, in which π-conjugated systems were folded in two and three places, respectively, were synthesized. Planar chiral [2.2]paracyclophane served as crosspoints to construct unicursal cyclic π-conjugated structures. The synthetic procedures and optically properties were investigated.

Results and Discussion

Scheme 1 illustrates the synthetic routes to optically active cyclic dimer and trimer based on planar chiral tetrasubstituted [2.2]paracyclophane. Bis-(*para*)-pseudo-*ortho*-typed [15] [2.2]paracyclophane (S_p)-**1** was prepared according to a literature's procedure [31]. The Sonoghashira–Hagihara cross-coupling [37,38] of (S_p)-**1** with diiodotolane **2** afforded the corresponding ribbon-shaped compound (S_p)-**3** in 39% isolated yield. Triisopropylsilyl (TIPS) groups in (S_p)-**3** were removed using Bu_4NF to afford diyne (S_p)-**4** as a monomer in 45% isolated yield. The reaction of (S_p)-**4** with diiodobenzene **5** using a $Pd_2(dba)_3/PPh_3/CuI$ catalytic system in toluene and Et_3N under diluted conditions (monomer concentration = approximately 1.3×10^{-3} M) was performed. The corresponding cyclic dimer (S_p)-**6** and trimer (S_p)-**7** were detected mainly by thin-layer chromatography (TLC) and separated roughly using simple SiO_2 column chromatography. In addition, they were purified using a recyclable high-performance liquid chromatography (HPLC) to remove unidentified impurities to obtain (S_p)-**6** and (S_p)-**7** in 16% and 3% isolated yields, respectively.

The ultraviolet–visible (UV–vis) absorption spectra and normalized photoluminescence (PL) spectra of (S_p)-**6** and (S_p)-**7** in diluted $CHCl_3$ solutions (1.0×10^{-5} M) are depicted in Figure 1. The absorption bands are derived from the π–π* transitions of a phenylene–ethynylene conjugation system. The spectra of (S_p)-**6** and (S_p)-**7** are similar, and the absorption peak top of (S_p)-**7** is red-shifted compared with that of (S_p)-**6** because of the bent structure of the *p*-phenylene–ethynylene moieties in (S_p)-**6** and extended π-conjugation of (S_p)-**7**. Such a red-shift of a UV–vis absorption spectrum has been observed in previously reported [2.2]paracyclophane-based cyclic oligomers [39].

$CHCl_3$ solutions (1.0×10^{-5} M) of (S_p)-**6** and (S_p)-**7** were photo-excited around their absorption peak maxima, and both oligomers emitted blue fluorescence as shown in Figure 1. Their PL spectra with vibrational structures were identical, and the PL quantum efficiencies (Φ_{PL}) of both (S_p)-**6** and (S_p)-**7** were estimated to be 0.65. Their PL of the cast films fabricated from the toluene solutions were also measured, and weak and inefficient luminescence were observed because of the aggregation-caused PL quenching. The PL lifetimes of (S_p)-**6** and (S_p)-**7** in the $CHCl_3$ solutions were measured at each PL peak maximum; and the PL decay curves (Figure S17, Supporting Information File 1) were fitted with the single exponential function. The lifetimes (τ) were estimated to be 1.6 ns and 1.0 ns, respectively.

Circular dichroism (CD) and CPL spectra of (S_p)-**6** and (S_p)-**7** were obtained in $CHCl_3$ solutions (1.0×10^{-5} M), and the spectra are shown in Figure 2. As illustrated in Figure 2A, the mirror-image Cotton effect of (S_p)- and (R_p)-**6** was observed throughout the absorption band, and the absolute molar ellipticity |[θ]| reached on the order of 10^6. Intense CPL signals were also obtained, and the $|g_{lum}|$ value [23-25] was estimated as 1.0×10^{-3}. The g_{lum} plots of **6** and **7** are shown in Figure S18A, Supporting Information File 1. Figure 2B shows the CD and CPL spectra of (S_p)- and (R_p)-**7**. Mirror-image CD signals were observed, and the absolute molar ellipticity (|[θ]|) was smaller than that of **6**. The first Cotton effect of (S_p)-**7** was negative, in contrast to that of (S_p)-**6**. The sign of the first Cotton effect was consistent with that of CPL signal; the CPL sign of (S_p)-**7** was also negative. Thus, the CD and CPL signs of (S_p)-**6** and (S_p)-**7** were opposite, despite the planar chiral [2.2]paracyclophane units having the same absolute configuration. The $|g_{lum}|$ value of **7** was 0.4×10^{-3} (Figure S18A, Supporting Information File 1), which was lower than that of **6**. In the case of the film states of **6** and **7**, low PL brightness and intermolecular random orientation of fluorophores resulted in noisy CPL signals.

The CD spectra were simulated by time-dependent density functional theory (TD-DFT) calculations (TD-MN15/6-31G(d)//MN15/6-31G(d). The calculated rotatory strengths of (S_p)-**6** and (S_p)-**7** were plotted with their observed CD spectra in Figure 3A and 3B, respectively, and the calculated CD spectra are shown in Supporting Information File 1, Figure S19A and S19B, respectively. Thus, the rotatory strengths corresponded well the observed CD spectra (Figure 3A and 3B). The signs of the simulated CD spectrum of (S_p)-**6** were positive and negative from the long wavelength to the short wavelength (Figure S19A, Supporting Information File 1), which reproduced the

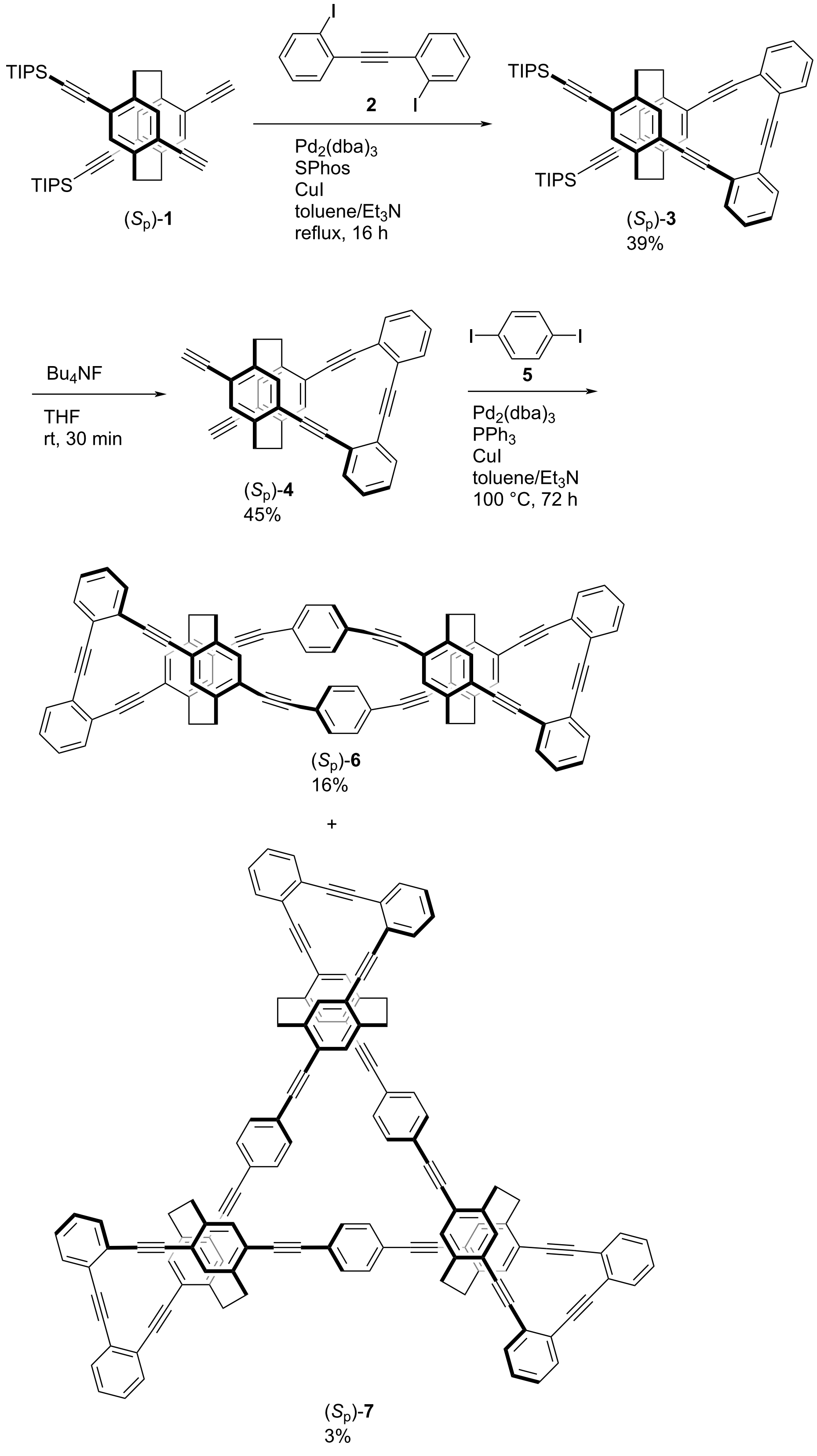

Scheme 1: Synthesis of cyclic dimer (S_p)-**6** and trimer (S_p)-**7**.

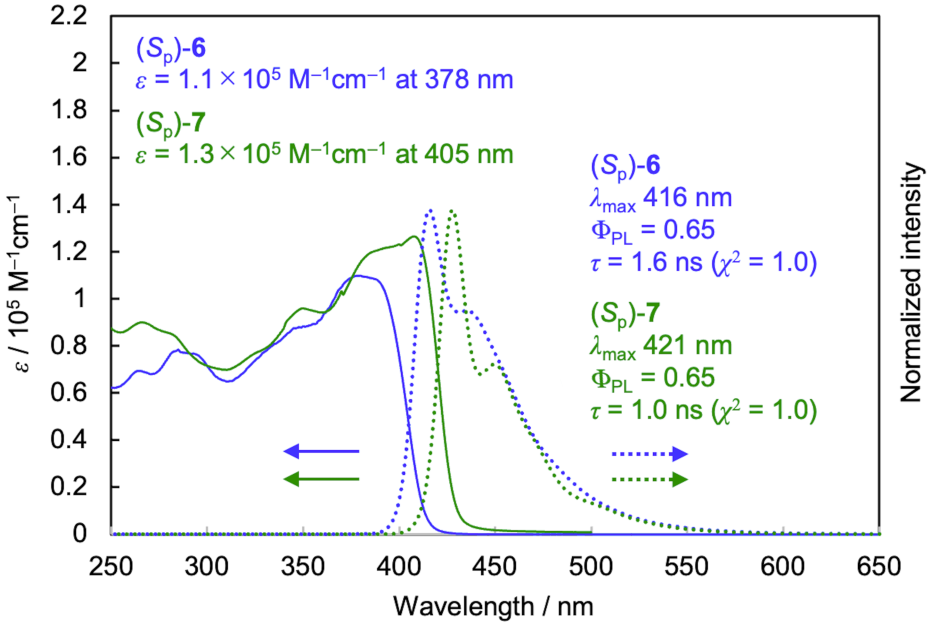

Figure 1: UV–vis and PL spectra of (S_p)-**6** and (S_p)-**7** in $CHCl_3$ (1.0×10^{-5} M). Excitation wavelength 370 nm and 378 nm for (S_p)-**6** and (S_p)-**7**, respectively.

experimental CD spectrum of (S_p)-**6**. In addition, the signs of the experimental CD spectrum of (S_p)-**7**, negative and positive from the long wavelength to the short wavelength, were reproduced using the simulated CD spectrum (Figure S19B, Supporting Information File 1).

Molecular orbitals of (S_p)-**6** and (S_p)-**7** in their ground and excited states were calculated using DFT and TD-DFT calculations (Figures S20–S23, Supporting Information File 1). In both molecules, the orbitals were localized to part of the π-conjugation systems rather than the whole system in the ground and excited states due to the twisted structures by the π-stacked [2.2]paracyclophane moieties. The CPL behaviors of (S_p)-**6** and (S_p)-**7** were investigated by TD-DFT calculations; namely, the electric transition dipole moment (μ), magnetic transition dipole moment (m), and the angle (θ) between μ and m in the S_1 states were simulated. The g_{lum} value was theoretically calculated by the following equation: $g_{lum} = 4|\mu||m|\cos\theta/(|\mu|^2 + |m|^2) \approx 4|m|\cos\theta/|\mu|$. The molecular orbitals of (S_p)-**6** and (S_p)-**7** in the S_1 states involved in CPL are illustrated in Supporting Information File 1, Figure 4A and 4B. The molecular orbitals of (S_p)-**6** were localized in one curved π-electron system, and the μ extended along the long axis of the molecule. The value of the angle θ of (S_p)-**6** was calculated to be 76°, which supported the positive CPL sign. The molecular orbitals of (S_p)-**7** in the S_1 states are shown in Figure 4B. The orbitals are linearly localized in the portion of the extended π-electron system rather than the entire molecule. Therefore, the elongation of the μ could not be suppressed, and thus a lower $|g_{lum}|$ value was obtained. The angle θ of (S_p)-**7** was 97°; it is consistent with the negative CPL sign. As described above, the experimental CD and CPL signs of (S_p)-**6** and (S_p)-**7** were reproduced by the TD-DFT calculations. Molecular orbitals of (S_p)-**6** involved in the CPL are obviously curved and twisted, resulting in the opposite chiroptical signs. Twisted chirality is known to result in CPL of π-conjugated molecules; for example, twisted anthracene is a good CPL emitter [40-47]; the more the anthracene is twisted, the better the CPL properties [46]. As for the π-stacked cyclic oligomers, the trimers and tetramers exhibited good CPL properties, whereas the cyclic dimer consisting of curved π-electron systems was not a good CPL emitter [39]. Thus, one of our next targets is to clarify experimentally and theoretically the CPL behavior of linear π-electron systems such as p-phenylene-ethynylene, when they are curved and twisted.

Conclusion

In summary, two types of optically active oligomers using planar chiral tetrasubstituted [2.2]paracyclophane as chiral crossing units were prepared, in which π-extended conjugated systems were folded in either two or three places. The oligomers exhibited good optical properties such as PL and CPL properties with good Φ_{PL} values (>0.6) and $|g_{lum}|$ values of the ordered of 10^{-4}–10^{-3}. The chiroptical properties of dimers and trimers showed opposite Cotton effects and CPL signals, despite the same absolute configuration of the planar chiral [2.2]paracyclophane crossing points. The π-conjugation

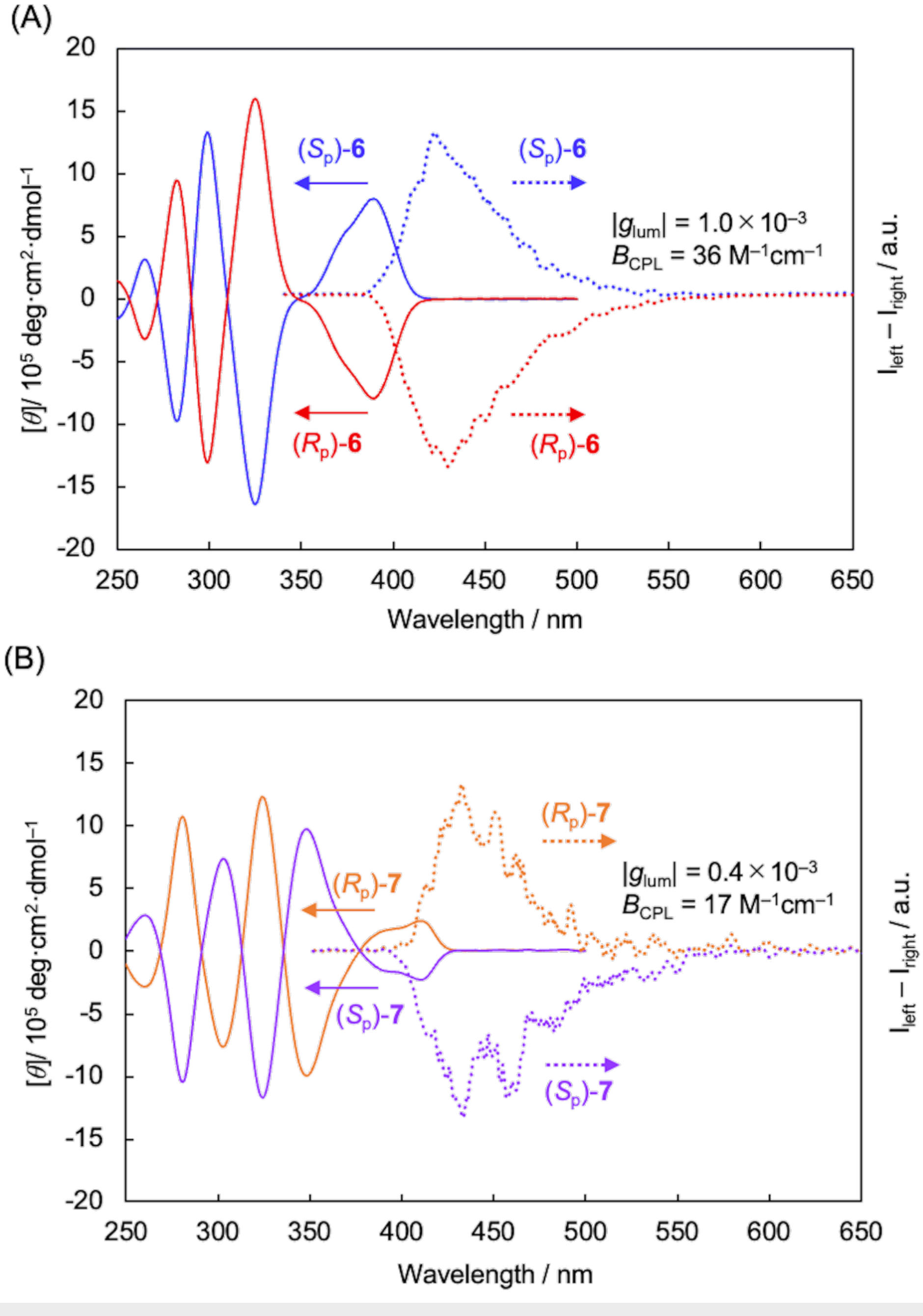

Figure 2: (A) UV, CD, PL, and CPL spectra of (*S*$_p$)- and (*R*$_p$)-**6** in $CHCl_3$ (1.0 × 10^{-5} M). (B) UV, CD, PL, and CPL spectra of (*S*$_p$)- and (*R*$_p$)-**7** in $CHCl_3$ (1.0 × 10^{-5} M). Excitation wavelength for CPL of both (*S*$_p$)-**6** and (*S*$_p$)-**7** = 300 nm.

system of the dimer that exhibited CPL was highly curved and twisted, which caused the different chiroptical properties.

Experimental

General

^{1}H and ^{13}C NMR spectra were recorded on a JEOL JNM ECZ-500R instrument at 500 and 125 MHz, respectively. Samples were analyzed in $CDCl_3$, and the chemical shift values were expressed relative to Me_4Si as an internal standard. Analytical thin-layer chromatography (TLC) was performed with silica gel 60 Merck F_{254} plates. Column chromatography was performed with silica gel 60N (spherical neutral). Recyclable preparative high-performance liquid chromatography (HPLC) was carried out on a Japan Analytical Industry Model LC918R (JAIGEL 1H and 2H gel-permeation columns) using CH_2Cl_2 as an eluent. Recyclable chiral chromatography (HPLC) was carried out on a YMC LC Forte/R (Chiralpak® IA column). High-resolution mass spectra (HRMS) was obtained on a Bruker Daltonics

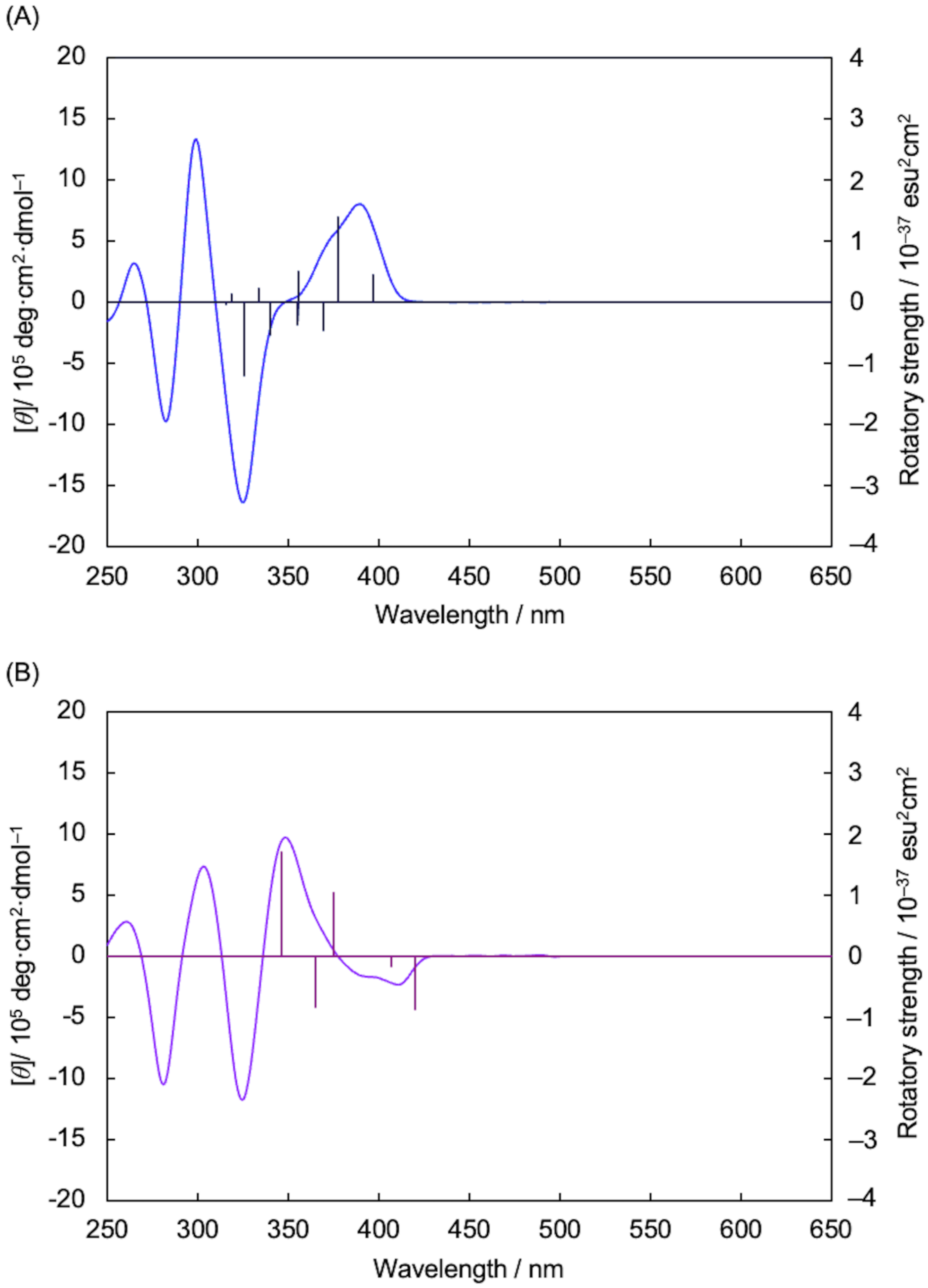

Figure 3: (A) CD spectrum of (S_p)-**6** in $CHCl_3$ (1.0 × 10^{-5} M), and the plot of the calculated rotatory strengths (TD-MN15/6-31G(d)//MN15/6-31G(d)). (B) CD spectrum of (S_p)-**7** in $CHCl_3$ (1.0 × 10^{-5} M), and the plot of the calculated rotatory strengths (TD-MN15/6-31G(d)//MN15/6-31G(d)).

microTOF II spectrometer (APCI) by using sodium formate and tuning mix as internal standard or on a JEOL JMS-S3000 spectrometer for matrix-assisted desorption/ionization (MALDI) with *trans*-2-[3-(4-*tert*-butylphenyl)-2-methyl-2-propenylidene]malononitrile (DCTB) as a matrix. UV–vis absorption spectra were recorded on a JASCO V-730 spectrophotometer, and samples were analyzed in $CHCl_3$ at room temperature. Photoluminescence (PL) spectra were recorded on a JASCO FP-8500 spectrofluorometer, and samples were analyzed in $CHCl_3$ at room temperature. Absolute PL quantum efficiency was calculated on a JASCO FP-8500 with an ILF-835 integrating sphere. The PL lifetime measurement was performed on a Hamamatsu Photonics Quantaurus-Tau fluorescence lifetime spectrometer system. Specific rotations ($[\alpha]_D^t$) were measured with a HORIBA SEPA-500 polarimeter: concentration "*c*" is g/dL. Circular dichroism (CD) spectra were recorded on a JASCO J-1500 spectropolarimeter with $CHCl_3$ as a solvent at room temperature. Circularly polarized luminescence (CPL)

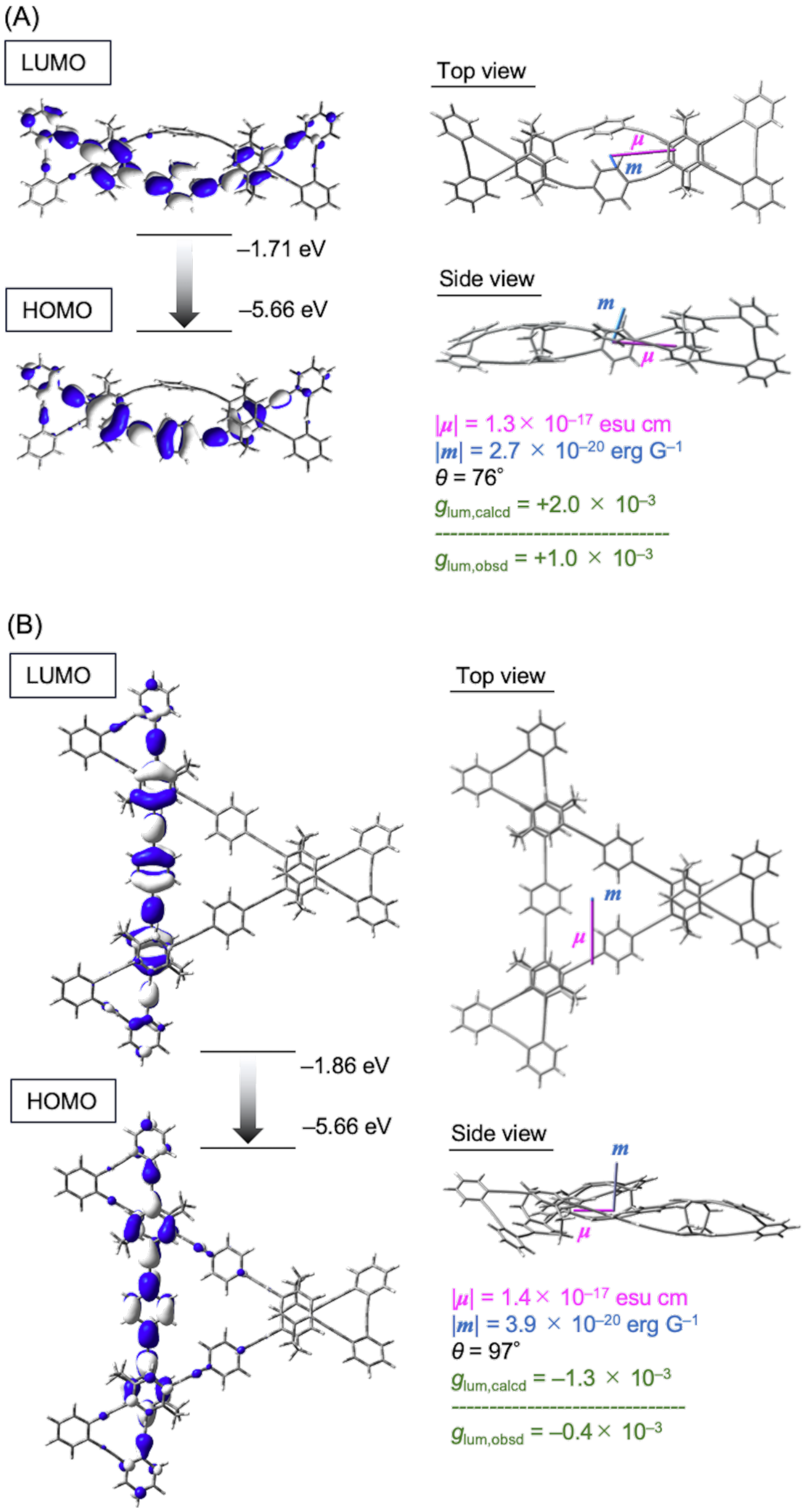

Figure 4: Molecular orbitals and simulated CPL profiles in the S_1 states of (A) (S_p)-**6** and (B) (S_p)-**7** (TD-MN15/6-31G(d)).

spectra were recorded on a JASCO CPL-300 with $CHCl_3$ as a solvent at room temperature.

Materials

Commercially available compounds used without purification are as follows: $Pd_2(dba)_3$, SPhos (2-dicyclohexylphosphino-2',6'-dimethoxybiphenyl), PPh_3, CuI, Bu_4NF, MeOH, dehydrated THF, dehydrated toluene, and 1,4-diiodobenzene (**5**). Et_3N was purchased and distilled over KOH. (S_p)-**1** [31], (R_p)-**1** [31], and **2** [48] were prepared as described in the literature.

Synthesis of (S_p)-3

A mixture of (S_p)-**1** (49.6 mg, 0.081 mmol), **2** (25.3 mg, 0.059 mmol), $Pd_2(dba)_3$ (6.1 mg, 0.0067 mmol), SPhos (5.6 mg, 0.014 mmol), CuI (1.8 mg, 0.0095 mmol), toluene (40 mL) and Et_3N (40 mL) was placed in a round-bottom flask equipped with a magnetic stirring bar. After degassing the reaction mixture several times, the mixture was heated at reflux temperature for 16 h. After the reaction mixture was cooled to room temperature, the solvent was removed with a rotary evaporator. The residue was purified by column chromatography on SiO_2 ($CHCl_3$/hexane = 1/4 v/v as an eluent) and by recyclable HPLC (CH_2Cl_2 as an eluent) to afford (S_p)-**3** (24.6 mg, 0.031 mmol, 39%) as a light yellow solid. R_f = 0.73 ($CHCl_3$/hexane = 1:2 v/v); ^{1}H NMR ($CDCl_3$, 500 MHz) δ 1.20 (s, 42H), 2.97–3.08 (m, 4H), 3.49–3.53 (m, 4H), 7.06 (s, 2H), 7.21 (s, 2H), 7.37–7.40 (m, 4H), 7.60–7.62 (m, 2H), 7.70–7.73 (m, 2H) ppm; ^{13}C NMR ($CDCl_3$, 125 MHz) δ 11.48, 18.84, 32.32, 32.57, 92.38, 93.65, 93.81, 95.72, 105.99, 125.16, 125.33, 125.42, 125.91, 128.07, 128.27, 131.99, 133.24, 134.65, 135.30, 141.30, 142.58 ppm: HRMS (APCI+) (*m*/*z*): $[M + H]^+$ calcd. for $C_{56}H_{62}Si_2$, 791.4463; found, 791.4472; $[\alpha]_D^{25}$ –203.25 (*c* 0.04, $CHCH_3$).

(R_p)-**3** was obtained by the same procedure of (S_p)-**3**. HRMS (APCI+) (*m*/*z*): $[M + H]^+$ calcd. for $C_{56}H_{62}Si_2$, 791.4463; found, 791.4442; $[\alpha]_D^{25}$ = +199.73 (*c* 0.04, $CHCH_3$).

Synthesis of (S_p)-4

(S_p)-**3** (43.0 mg, 0.054 mmol) was dissolved in THF (2 mL), followed by the addition of Bu_4NF (1.0 M in THF solution, 0.11 mL). The reaction was carried out at room temperature for 30 min, and then H_2O was added to the reaction mixture. The organic layer was extracted three times with CH_2Cl_2, and the combined organic layers were washed with saturated aqueous $NaHCO_3$ and brine. After drying over $MgSO_4$ and filtration, the solvent was removed under reduced pressure. The residue was purified by recyclable HPLC (CH_2Cl_2 as an eluent) to afford (S_p)-**4** (11.8 mg, 0.025 mmol, 45%) as a light yellow solid. R_f = 0.43 ($CHCl_3$/hexane = 1:2 v/v). ^{1}H NMR ($CDCl_3$, 500 MHz) δ 2.98–3.09 (m, 4H), 3.39 (s, 2H), 3.43–3.55 (m, 4H), 7.09 (s, 2H), 7.21 (s, 2H), 7.37–7.41 (m, 4H), 7.62–7.65 (m, 2H), 7.70–7.73 (m, 2H) ppm; ^{13}C NMR ($CDCl_3$, 125 MHz) δ 32.31, 32.43, 81.96, 83.04, 92.45, 93.34, 93.94, 124.30, 125.18, 125.98, 126.02, 128.25, 128.37, 132.22, 133.29, 135.15, 135.42, 141.47, 142.64 ppm; HRMS (APCI+) (*m*/*z*): $[M + H]^+$ calcd. for $C_{38}H_{22}$, 479.1794; found, 479.1774. $[\alpha]_D^{25}$ –278.90 (*c* 0.04, $CHCH_3$).

(R_p)-**4** was obtained by the same procedure of (S_p)-**4**. HRMS (APCI+) (*m*/*z*): $[M + H]^+$ calcd. for $C_{38}H_{22}$, 479.1794; found, 479.1816. $[\alpha]_D^{25}$ = +278.68 (*c* 0.04, $CHCH_3$).

Synthesis and isolation of cyclic dimer (S_p)-6 and trimer (S_p)-7

A mixture of (S_p)-**4** (18.2 mg, 0.038 mmol), 1,4-diiodobenzene (**5**, 13.2 mg, 0.040 mmol), $Pd_2(dba)_3$ (9.0 mg, 0.0098 mmol), PPh_3 (12.2 mg, 0.047 mmol), CuI (2.3 mg, 0.012 mmol), toluene (15 mL) and Et_3N (15 mL) was placed in a round-bottom flask equipped with a magnetic stirring bar. After degassing the reaction mixture several times, the mixture was heated at reflux temperature for 72 h. After the reaction mixture was cooled to room temperature, the solvent was removed with a rotary evaporator. The residue was purified by column chromatography on SiO_2 (hexane/ethyl acetate = 4:1 v/v as an eluent). The first and second fractions included mainly dimer (S_p)-**6** and trimer (S_p)-**7**, respectively. Dimer (S_p)-**6** (6.8 mg, 0.0062 mmol, 16%) was isolated from the first fraction by recyclable HPLC (CH_2Cl_2 as an eluent) as a light yellow solid. Trimer (S_p)-**7** was isolated from the second fraction by recyclable HPLC (CH_2Cl_2 as an eluent). Further purification of (S_p)-**7** was carried out using chiral HPLC (CH_2Cl_2/hexane = 5:5 v/v as an eluent) to obtain (S_p)-**7** (2.0 mg, 0.0012 mmol, 3%) as a yellow solid. Enantiomers were obtained by the same procedure from (R_p)-**4**.

(S_p)-**6**. R_f = 0.40 (hexane/ethyl acetate = 4:1 v/v). ^{1}H NMR ($CDCl_3$, 500 MHz) δ 3.12 (m, 8H), 3.46 (m, 4H), 3.60 (m, 4H), 7.23 (s, 8H), 7.31 (s, 8H), 7.38 (m, 8H), 7.64 (m, *J* = 8.59 Hz, 4H), 7.70 (m, *J* = 8.59 Hz, 4H) ppm; ^{13}C{^{1}H} NMR ($CDCl_3$, 125 MHz) δ 29.8, 32.5, 32.8, 92.4, 92.7, 93.3, 93.7, 95.0, 123.5, 125.4, 125.8, 126.0, 128.2, 128.4, 131.5, 132.5, 133.1, 135.3, 136.7, 140.7, 141.7 ppm. HRMS (MALDI) (*m*/*z*): $[M + Ag]^+$: calcd. for $C_{88}H_{48}Ag$, 1211.2802; found, 1211.2823. $[\alpha]_D^{25}$ +386.63 (*c* 0.02, $CHCl_3$).

(R_p)-**6**. HRMS (MALDI) (*m*/*z*): $[M + Ag]^+$calcd. for $C_{88}H_{48}Ag$ 1211.2802; found, 1211.2848. $[\alpha]_D^{25}$ –386.63 (*c* 0.02, $CHCl_3$).

(S_p)-**7**. R_f = 0.29 (hexane/ethyl acetate = 4/1 v/v). ^{1}H NMR ($CDCl_3$, 500 MHz) δ 3.10–3.18 (m, 12H), 3.60–3.66 (m, 12H), 7.23 (s, 6H), 7.28 (s, 6H), 7.45–7.47 (m, 12H), 7.70–7.71 (m, 6H), 7.76–7.79 (m, 18H) ppm; $^{13}C\{^1H\}$ NMR ($CDCl_3$, 125 MHz) δ 32.60, 32.75, 91.31, 92.41, 93.47, 93.99, 94.29, 123.59, 125.14, 125.75, 125.91, 128.17, 128.27, 128.32, 131.70, 132.16, 133.24, 134.60, 135.59, 141.52, 142.25 ppm; HRMS (MALDI) (*m*/*z*): $[M + Ag]^+$ calcd. for $C_{132}H_{72}Ag$ 1763.4680; found, 1763.4729; $[\alpha]_D^{25} = -739.17$ (*c* 0.01, $CHCl_3$).

(R_p)-**7**. HRMS (MALDI) (*m*/*z*): $[M + Ag]^+$ calcd. for $C_{132}H_{72}Ag$, 1763.4680; found, 1763.4647; $[\alpha]_D^{25}$ +739.75 (*c* 0.01, $CHCl_3$).

Supporting Information

Supporting Information File 1

Statement of computational methods, NMR and HRMS spectra, PL decay curves, g_{lum} charts, calculated ECD spectra, and cartesian coordinates.
[https://www.beilstein-journals.org/bjoc/content/supplementary/1860-5397-21-124-S1.pdf]

Acknowledgements

The authors are grateful to Professor Kazuo Tanaka and Dr. Masayuki Gon (Graduate School of Engineering, Kyoto University) for CD and CPL spectroscopy.

Funding

The financial support by Grant-in-Aid for Scientific Research (A) (No. 24H00470) and (B) (25K01822) from the Japan Society for the Promotion of Science (Y.M.) is greatly acknowledged. This work was also partly supported by the Toshiaki Ogasawara Memorial Foundation (Y.M.).

Author Contributions

Ena Kumamoto: investigation. Kana Ogawa: investigation. Kazunori Okamoto: formal analysis; investigation. Yasuhiro Morisaki: conceptualization; data curation; funding acquisition; project administration; supervision; writing – original draft.

ORCID® iDs

Yasuhiro Morisaki - https://orcid.org/0000-0002-9125-2670

Data Availability Statement

All data that supports the findings of this study is available in the published article and/or the supporting information of this article.

Preprint

A non-peer-reviewed version of this article has been previously published as a preprint: https://doi.org/10.3762/bxiv.2025.38.v1

References

1. Cyclophanes. *Compendium of Chemical Terminology;* International Union of Pure and Applied Chemistry (IUPAC). doi:10.1351/goldbook.c01504
2. Brown, C. J.; Farthing, A. C. *Nature* **1949,** *164,* 915–916. doi:10.1038/164915b0
3. Cram, D. J.; Steinberg, H. *J. Am. Chem. Soc.* **1951,** *73,* 5691–5704. doi:10.1021/ja01156a059
4. Vögtle, F., Ed. *Cyclophane Chemistry: Synthesis, Structures and Reactions;* John Wiley & Sons: Chichester, UK, 1993.
5. Gleiter, R.; Hopf, H., Eds. *Modern Cyclophane Chemistry;* Wiley-VCH: Weinheim, Germany, 2004. doi:10.1002/3527603964
6. Hopf, H. *Angew. Chem., Int. Ed.* **2008,** *47,* 9808–9812. doi:10.1002/anie.200800969
7. Planar chirality. *Compendium of Chemical Terminology;* International Union of Pure and Applied Chemistry (IUPAC). doi:10.1351/goldbook.p04681
8. Cram, D. J.; Allinger, N. L. *J. Am. Chem. Soc.* **1955,** *77,* 6289–6294. doi:10.1021/ja01628a067
9. Rozenberg, V.; Sergeeva, E.; Hopf, H. Cyclophanes as Templates in Stereoselective Synthesis. In *Modern Cyclophane Chemistry;* Gleiter, R.; Hopf, H., Eds.; Wiley-VCH: Weinheim, Germany, 2004; pp 435–462. doi:10.1002/3527603964.ch17
10. Rowlands, G. J. *Org. Biomol. Chem.* **2008,** *6,* 1527–1534. doi:10.1039/b800698a
11. Gibson, S. E.; Knight, J. D. *Org. Biomol. Chem.* **2003,** *1,* 1256–1269. doi:10.1039/b300717k
12. Aly, A. A.; Brown, A. B. *Tetrahedron* **2009,** *65,* 8055–8089. doi:10.1016/j.tet.2009.06.034
13. Paradies, J. *Synthesis* **2011,** 3749–3766. doi:10.1055/s-0031-1289296
14. Delcourt, M.-L.; Felder, S.; Turcaud, S.; Pollok, C. H.; Merten, C.; Micouin, L.; Benedetti, E. *J. Org. Chem.* **2019,** *84,* 5369–5382. doi:10.1021/acs.joc.9b00372
15. Vorontsova, N. V.; Rozenberg, V. I.; Sergeeva, E. V.; Vorontsov, E. V.; Starikova, Z. A.; Lyssenko, K. A.; Hopf, H. *Chem. – Eur. J.* **2008,** *14,* 4600–4617. doi:10.1002/chem.200701683
16. David, O. R. P. *Tetrahedron* **2012,** *68,* 8977–8993. doi:10.1016/j.tet.2012.08.009
17. Hassan, Z.; Spuling, E.; Knoll, D. M.; Lahann, J.; Bräse, S. *Chem. Soc. Rev.* **2018,** *47,* 6947–6963. doi:10.1039/c7cs00803a
18. Morisaki, Y.; Chujo, Y. *Bull. Chem. Soc. Jpn.* **2019,** *92,* 265–274. doi:10.1246/bcsj.20180259
19. Hassan, Z.; Spuling, E.; Knoll, D. M.; Bräse, S. *Angew. Chem., Int. Ed.* **2020,** *59,* 2156–2170. doi:10.1002/anie.201904863
20. Felder, S.; Wu, S.; Brom, J.; Micouin, L.; Benedetti, E. *Chirality* **2021,** *33,* 506–527. doi:10.1002/chir.23335
21. Morisaki, Y.; Hifumi, R.; Lin, L.; Inoshita, K.; Chujo, Y. *Polym. Chem.* **2012,** *3,* 2727–2730. doi:10.1039/c2py20530k
22. Berova, N.; Nakanishi, K.; Woody, R., Eds. *Circular Dichroism,* 2nd ed.; Wiley-VCH: New York, NY, USA, 2000.
23. Riehl, J. P.; Muller, F. *Comprehensive Chiroptical Spectroscopy;* John Wiley & Sons: New York, NY, USA, 2012.
24. Richardson, F. S.; Riehl, J. P. *Chem. Rev.* **1977,** *77,* 773–792. doi:10.1021/cr60310a001
25. Riehl, J. P.; Richardson, F. S. *Chem. Rev.* **1986,** *86,* 1–16. doi:10.1021/cr00071a001
26. Miki, N.; Inoue, R.; Morisaki, Y. *Bull. Chem. Soc. Jpn.* **2022,** *95,* 110–115. doi:10.1246/bcsj.20210368

27. Matsumura, K.; Inoue, R.; Morisaki, Y. *Adv. Funct. Mater.* **2024,** *34,* 2310566. doi:10.1002/adfm.202310566
28. Morisaki, Y.; Gon, M.; Sasamori, T.; Tokitoh, N.; Chujo, Y. *J. Am. Chem. Soc.* **2014,** *136,* 3350–3353. doi:10.1021/ja412197j
29. Gon, M.; Morisaki, Y.; Chujo, Y. *J. Mater. Chem. C* **2015,** *3,* 521–529. doi:10.1039/c4tc02339k
30. Gon, M.; Kozuka, H.; Morisaki, Y.; Chujo, Y. *Asian J. Org. Chem.* **2016,** *5,* 353–359. doi:10.1002/ajoc.201500468
31. Morisaki, Y.; Sawada, R.; Gon, M.; Chujo, Y. *Chem. – Asian J.* **2016,** *11,* 2524–2527. doi:10.1002/asia.201601028
32. Inoue, R.; Kondo, R.; Morisaki, Y. *Chem. Commun.* **2020,** *56,* 15438–15441. doi:10.1039/d0cc06205g
33. Lian, Z.; He, J.; Liu, L.; Fan, Y.; Chen, X.; Jiang, H. *Nat. Commun.* **2023,** *14,* 2752. doi:10.1038/s41467-023-38405-9
34. He, J.; Fan, Y.; Lian, Z.; Guo, S.; Wang, Y.; Jiang, H. *Adv. Opt. Mater.* **2024,** *12,* 2302221. doi:10.1002/adom.202302221
35. He, J.; Yu, M.-H.; Lian, Z.; Fan, Y.-Q.; Guo, S.-Z.; Li, X.-N.; Wang, Y.; Wang, W.-G.; Cheng, Z.-Y.; Jiang, H. *Chem. Sci.* **2023,** *14,* 4426–4433. doi:10.1039/d2sc06825g
36. Fan, Y.; He, J.; Liu, L.; Liu, G.; Guo, S.; Lian, Z.; Li, X.; Guo, W.; Chen, X.; Wang, Y.; Jiang, H. *Angew. Chem., Int. Ed.* **2023,** *62,* e202304623. doi:10.1002/anie.202304623
37. Sonogashira, K.; Tohda, Y.; Hagihara, N. *Tetrahedron Lett.* **1975,** *16,* 4467–4470. doi:10.1016/s0040-4039(00)91094-3
38. Sonogashira, K. Palladium-Catalyzed Alkynylation: Sonogashira Alkyne Synthesis. In *Handbook of Organopalladium Chemistry for Organic Synthesis;* Negishi, E., Ed.; John Wiley & Sons: New York, NY, USA, 2002; pp 493–529. doi:10.1002/0471473804
39. Tanaka, K.; Inoue, R.; Morisaki, Y. *Chem. – Asian J.* **2022,** *17,* e202101267. doi:10.1002/asia.202101267
40. Bedi, A.; Shimon, L. J. W.; Gidron, O. *J. Am. Chem. Soc.* **2018,** *140,* 8086–8090. doi:10.1021/jacs.8b04447
41. Bedi, A.; Gidron, O. *Chem. – Eur. J.* **2019,** *25,* 3279–3285. doi:10.1002/chem.201805728
42. Bedi, A.; Gidron, O. *Acc. Chem. Res.* **2019,** *52,* 2482–2490. doi:10.1021/acs.accounts.9b00271
43. Armon, A. M.; Bedi, A.; Borin, V.; Schapiro, I.; Gidron, O. *Eur. J. Org. Chem.* **2021,** 5424–5429. doi:10.1002/ejoc.202100865
44. Malakar, P.; Borin, V.; Bedi, A.; Schapiro, I.; Gidron, O.; Ruhman, S. *Phys. Chem. Chem. Phys.* **2022,** *24,* 2357–2362. doi:10.1039/d1cp05728f
45. Bedi, A.; Manor Armon, A.; Diskin-Posner, Y.; Bogosalvsky, B.; Gidron, O. *Nat. Commun.* **2022,** *13,* 451. doi:10.1038/s41467-022-28072-7
46. Tsuchiya, M.; Inoue, R.; Tanaka, K.; Morisaki, Y. *Chem. – Asian J.* **2022,** *17,* e202200418. doi:10.1002/asia.202200418
47. Bedi, A.; Schwartz, G.; Hananel, U.; Manor Armon, A.; Shioukhi, I.; Markovich, G.; Gidron, O. *Chem. Commun.* **2023,** *59,* 2011–2014. doi:10.1039/d2cc07074j
48. Bentley, K. W.; de los Santos, Z. A.; Weiss, M. J.; Wolf, C. *Chirality* **2015,** *27,* 700–707. doi:10.1002/chir.22489

License and Terms

The definitive version of this article is the electronic one which can be found at:
https://doi.org/10.3762/bjoc.21.124

BEILSTEIN JOURNAL OF ORGANIC CHEMISTRY

Catalytic asymmetric reactions of isocyanides for constructing non-central chirality

Jia-Yu Liao

Perspective

Open Access

Address:
College of Pharmaceutical Sciences, Zhejiang University, Hangzhou, 310058, China

Email:
Jia-Yu Liao - jyliao@zju.edu.cn

Keywords:
axial chirality; helical chirality; inherent chirality; isocyanide; planar chirality

Beilstein J. Org. Chem. **2025,** *21,* 1648–1660.
https://doi.org/10.3762/bjoc.21.129

Received: 31 May 2025
Accepted: 05 August 2025
Published: 19 August 2025

This article is part of the thematic issue "Non-central chirality in organic chemistry".

Associate Editor: N. Yoshikai

Abstract

Beyond the conventional carbon-centered chirality, catalytic asymmetric transformations of isocyanides have recently emerged as a powerful strategy for the efficient synthesis of structurally diverse scaffolds featuring axial, planar, helical, and inherent chirality. Herein, we summarize the exciting achievements in this rapidly evolving field. These elegant examples have been organized and presented based on the reaction type as well as the resulting chirality form. Additionally, we provide a perspective on the current limitations and future opportunities, aiming to inspire further advances in this area.

Introduction

Chirality represents a fundamental property of molecules and manifests in diverse forms (Figure 1a). While central chirality based on stereogenic centers (e.g., C, P, S, etc.) is the most conventional type, non-central chirality, such as axial [1-4], planar [5-7], helical [8-10], and inherent chirality [11,12], has gained increasing attention due to its broad applications in various fields, including but not limited to drug discovery, asymmetric catalysis, and materials science (Figure 1b). Consequently, the development of efficient and stereoselective methods for assembling such scaffolds with respect to structural diversity has become a hot topic in synthetic organic chemistry.

Isocyanides (also termed isonitriles) are a class of highly versatile building blocks in organic synthesis, participating in a wide range of transformations including multicomponent reactions (e.g., the well-known Passerini and Ugi reactions) [13-15], insertion reactions [16-18], cycloaddition reactions (e.g., [4 + 1], [3 + 2]) [19,20], and others [21-23]. Particularly, isocyanides have been widely exploited toward the preparation of centrally chiral structures through transition-metal-catalyzed or organocatalytic asymmetric reactions [24-26]. Beyond these great developments, recent efforts have successfully expanded the utility of isocyanides to access structurally diverse non-central chiral frameworks, further expanding their synthetic

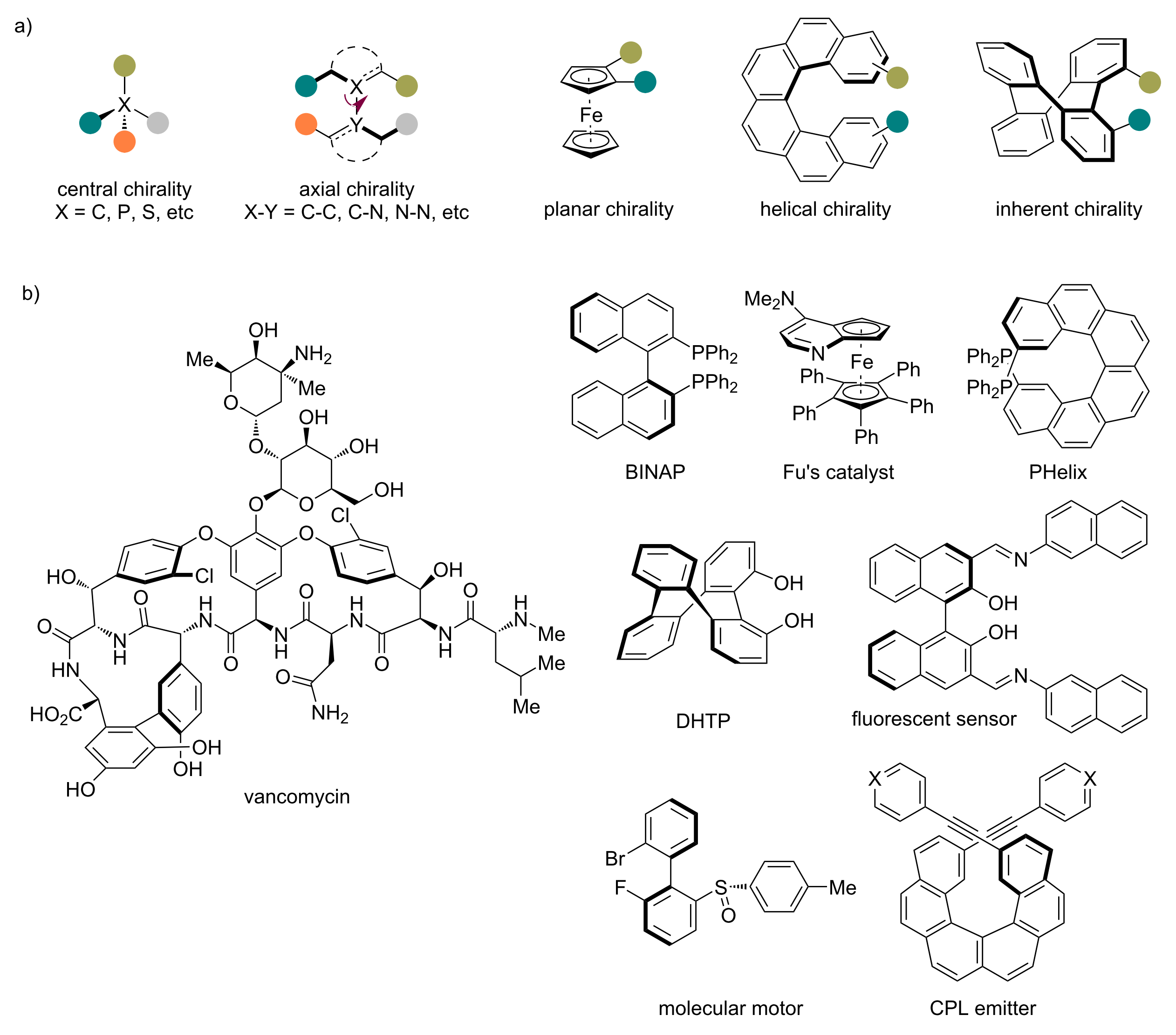

Figure 1: a) Common types of chirality. b) Representative functional molecules bearing non-central chirality.

potential. The following sections highlight these fruitful achievements, organized by both the reaction type and the chirality type of resulting products.

Perspective

Isocyanide-based transformations

Palladium-catalyzed isocyanide insertion reactions

In 2018, Luo, Zhu, and co-workers developed a palladium-catalyzed enantioselective reaction between ferrocene-derived vinyl isocyanides **1** and aryl iodides (Scheme 1a) [27]. This transformation proceeded via two key steps, isocyanide insertion and desymmetric C(sp^2)–H bond activation. By using phosphoramidite **L1** as the chiral ligand, planar chiral pyridoferrocenes **2** were obtained in 61–99% yield with 72–99% ee. In addition, this catalytic system could be applied to synthesize more complex structures. As shown in Scheme 1b, when *N*-(2-iodophenyl)methacrylamide **3** and **1a** were employed as starting materials, compound **4** bearing nonadjacent planar and central chirality was obtained in good yield and enantioselectivity (**4a**, 54%, 90% ee; **4b**, 32%, 97% ee). However, the diastereoselectivity is modest (1.7:1), likely resulting from insufficient chiral induction during the indolinone-forming step.

Moving forward, this strategy was applied in the construction of axial chirality by the same group. In 2021, they reported a Pd(OAc)$_2$/**L2**-catalyzed imidoylative cycloamidation of *N*-alkyl-2-isocyanobenzamides **5** with 2,6-disubstituted aryl iodides **6** (Scheme 2a) [28]. Through a coupling–cyclization reaction sequence, axially chiral 2-arylquinazolinones **7** were synthesized in 35–93% yield with 71–95% ee. Interestingly, by using *N*-(2,4-dimethoxyphenyl)-2-isocyanobenzamide (**8**) and aryl iodide **6a** as the reactants, diastereomeric products

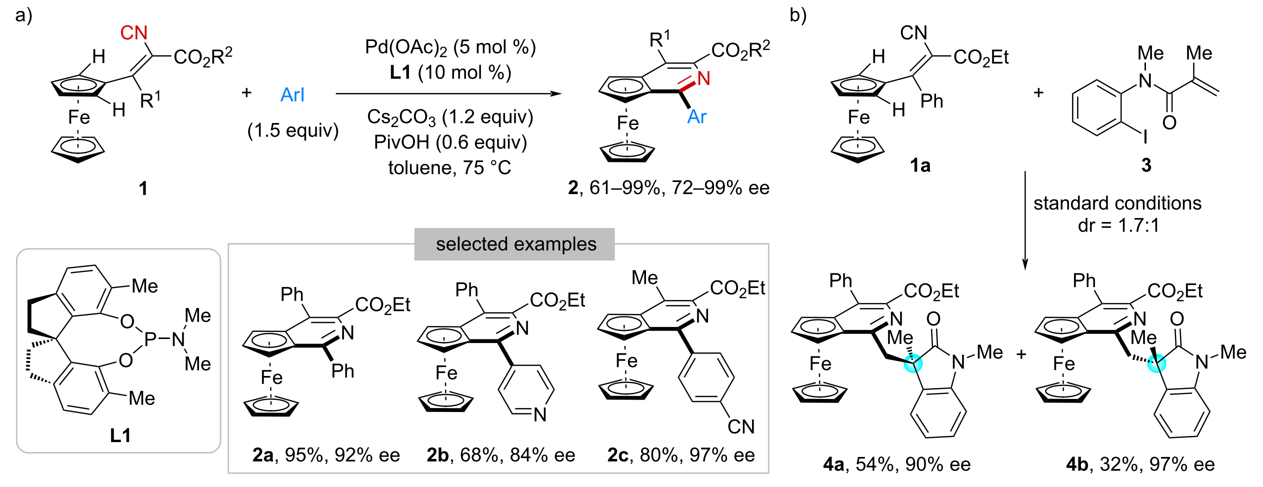

Scheme 1: Construction of planar chirality.

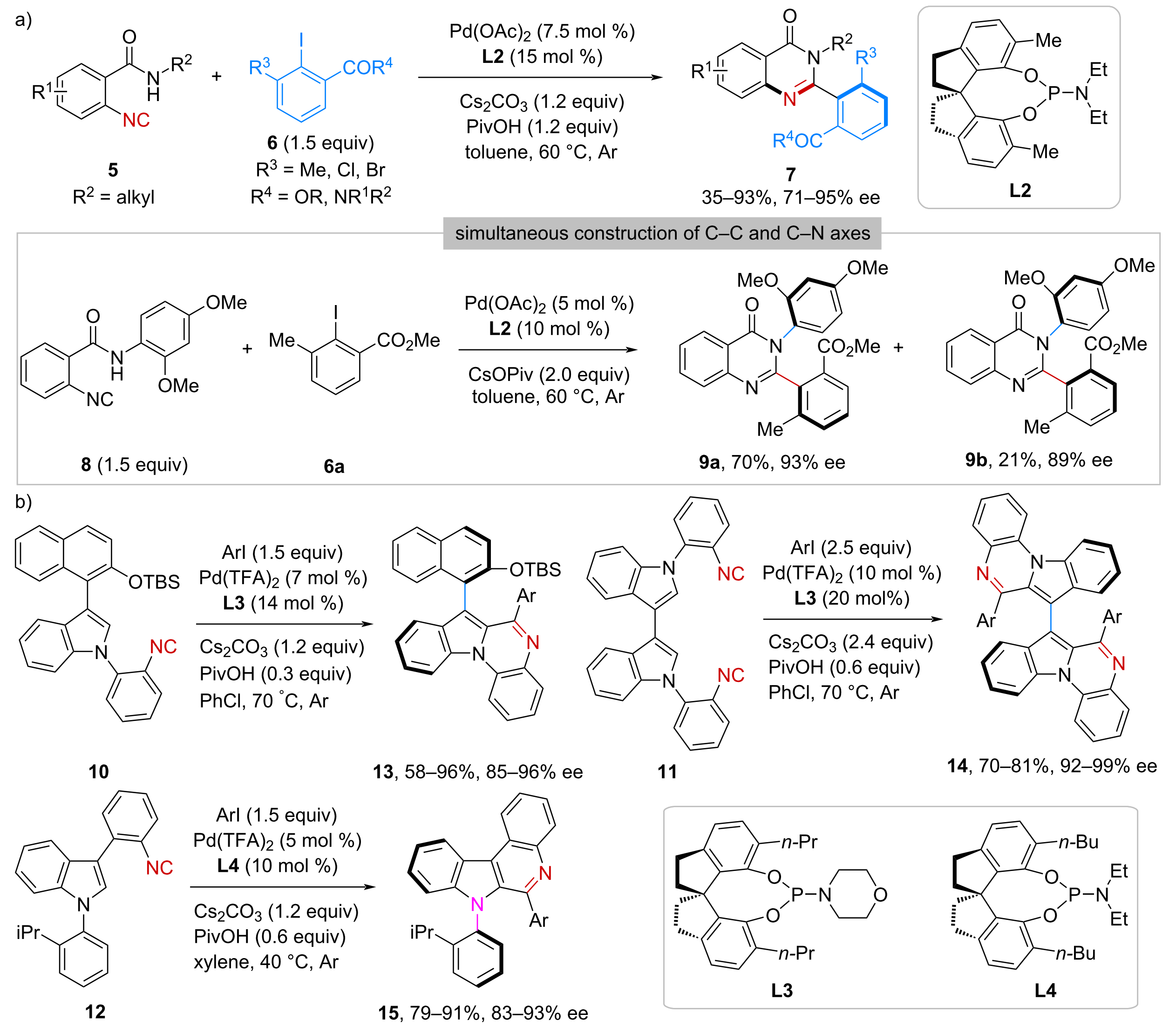

Scheme 2: Construction of axial chirality.

9a and **9b**, each containing two distinct stereogenic axes (C–C and C–N), were obtained in 93% and 89% ee, respectively.

Very recently, Luo and co-workers implemented an efficient palladium-catalyzed atroposelective C(sp^2)–H imidoylative cyclization of functionalized phenyl isocyanides, guided by DFT calculations (Scheme 2b) [29]. Three types of isocyanides (**10**–**12**) were evaluated in reactions with aryl iodides, affording indole-fused N-heteroaryl scaffolds **13**–**15**, featuring either a C–C or C–N stereogenic axis, in moderate-to-high yields with high enantioselectivities.

Beyond planar and axial chirality, the same group developed a three-component coupling reaction of 2,2′-diisocyano-1,1′-biphenyls **16**, aryl iodides, and carboxylates (Scheme 3a) [30].

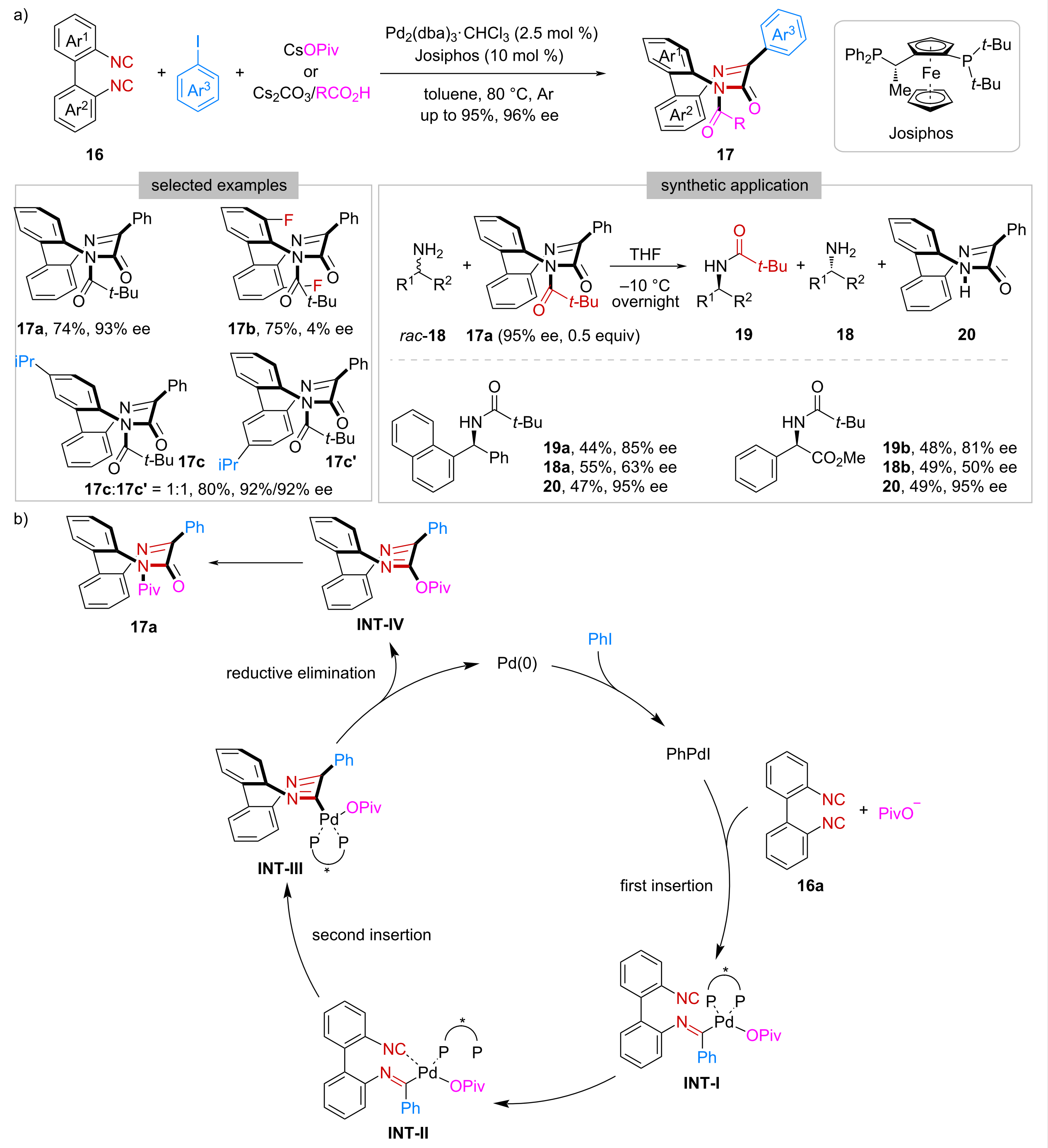

Scheme 3: Construction of inherent chirality.

Under chiral palladium catalysis, unique inherently chiral saddle-shaped bridged biaryls **17** were formed through a reaction sequence involving double isocyanide insertion, reductive elimination, and acyl transfer. To be noted, the introduction of a substituent at the *ortho*-position of the isocyanide group in **16** caused a significant drop in the enantioselectivity (e.g., **17b**). Besides, when unsymmetrical diisocyanide was used, the initial isocyanide insertion was found to be non-regioselective, delivering a 1:1 mixture of regioisomers (**17c** and **17c'**). Intriguingly, **17a** could act as a chiral acylating reagent, applying in the kinetic resolution of racemic primary amines *rac*-**18**. Additionally, after the reaction, the resulting deacylated compound **20** could be recovered in almost quantitative yield without any erosion of the enantiopurity. A possible reaction mechanism for this Pd-catalyzed three-component reaction was proposed (Scheme 3b). As shown, the reaction started with the oxidative addition of phenyl iodide to Pd(0) to generate the phenyl Pd(II) species. After that, coordination and migratory insertion of the first isocyanide group of **16a** to Pd(II) delivered **INT-I**. Then, coordination and migratory insertion of the second isocyanide group occurred to give **INT-III**, which underwent reductive elimination to afford **INT-IV**. Finally, migration of the Piv group from O to N gave the product **17a**.

Moreover, the Pd-catalyzed isocyanide insertion approach has been successfully extended to the generation of helical chirality [31]. As shown in Scheme 4a, phenyl diisocyanides **21** or **22** underwent double C(sp^2)–H imidoylative cyclization with aryl iodides, furnishing symmetrical pyrido[6]helicenes **23** or furan-incorporating pyrido[7]helicenes **24** with stable helical chirality, respectively. Furthermore, pre-cyclized monoisocyanides, such as **25a** and **25b**, were identified as another class of suitable substrates under the standard conditions (Scheme 4b). On one hand, such findings demonstrated that the second cyclization determines enantioselectivity; on the other hand, it provided a practical way to the preparation of unsymmetrical pyrido[6]helicenes **26**.

Isocyanide-based multicomponent reactions

Except for Pd-catalyzed isocyanide insertion reactions, organocatalytic isocyanide-based multicomponent reactions have been explored for the synthesis of axially chiral compounds. In 2024, Yang and co-workers reported a catalytic asymmetric version of the Groebke–Blackburn–Bienaymé reaction [32-34] involving 6-aryl-2-aminopyridines **27**, aldehydes, and isocyanides (Scheme 5a) [35]. By employing chiral phosphoric acid (CPA) **C1** as the catalyst, this reaction worked well to afford axially chiral imidazo[1,2-*a*]pyridines **28** in high-to-excellent yields (up to 99%) and enantioselectivities (up to >99% ee). It is worth noting that the presence of a hydrogen bonding donor in **27** is crucial for achieving high enantioselectivity. As shown, while replacing the OH with NHMe led to a slight decrease of ee (**28c** versus **28b**), the protection of the OH with methyl caused a severe drop (**28d** versus **28b**). The application of the resulting

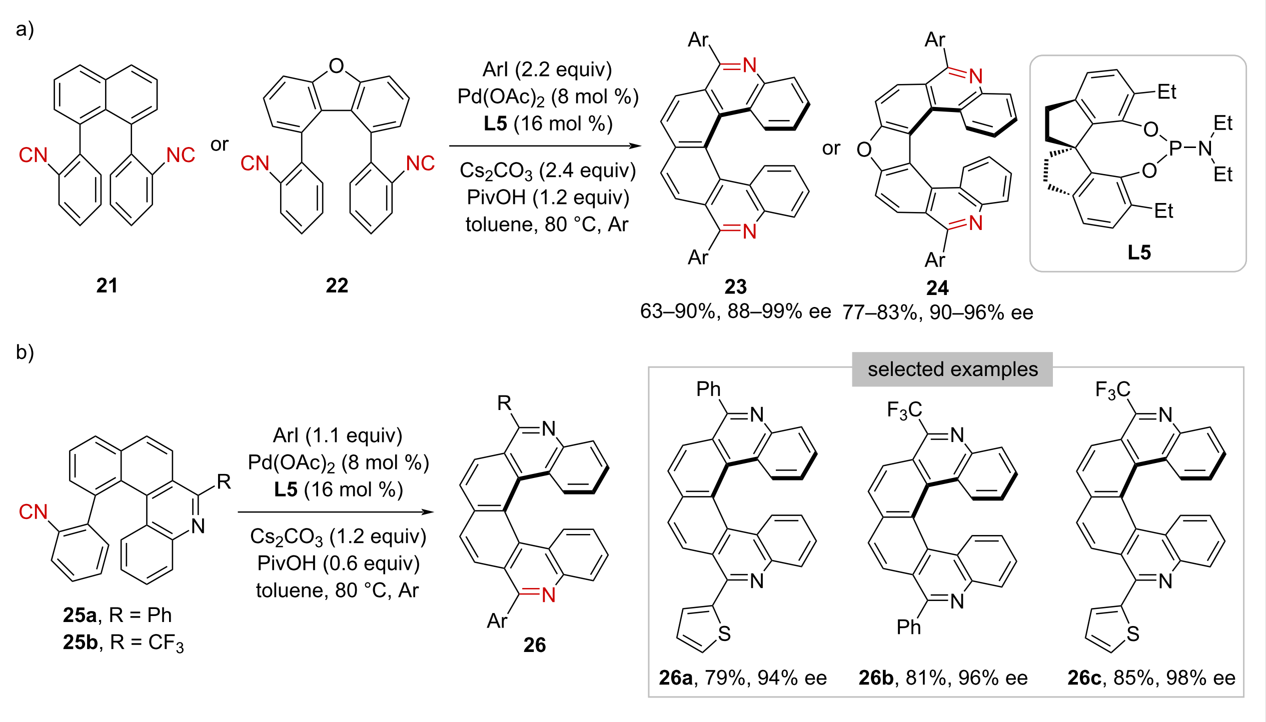

Scheme 4: Construction of helical chirality.

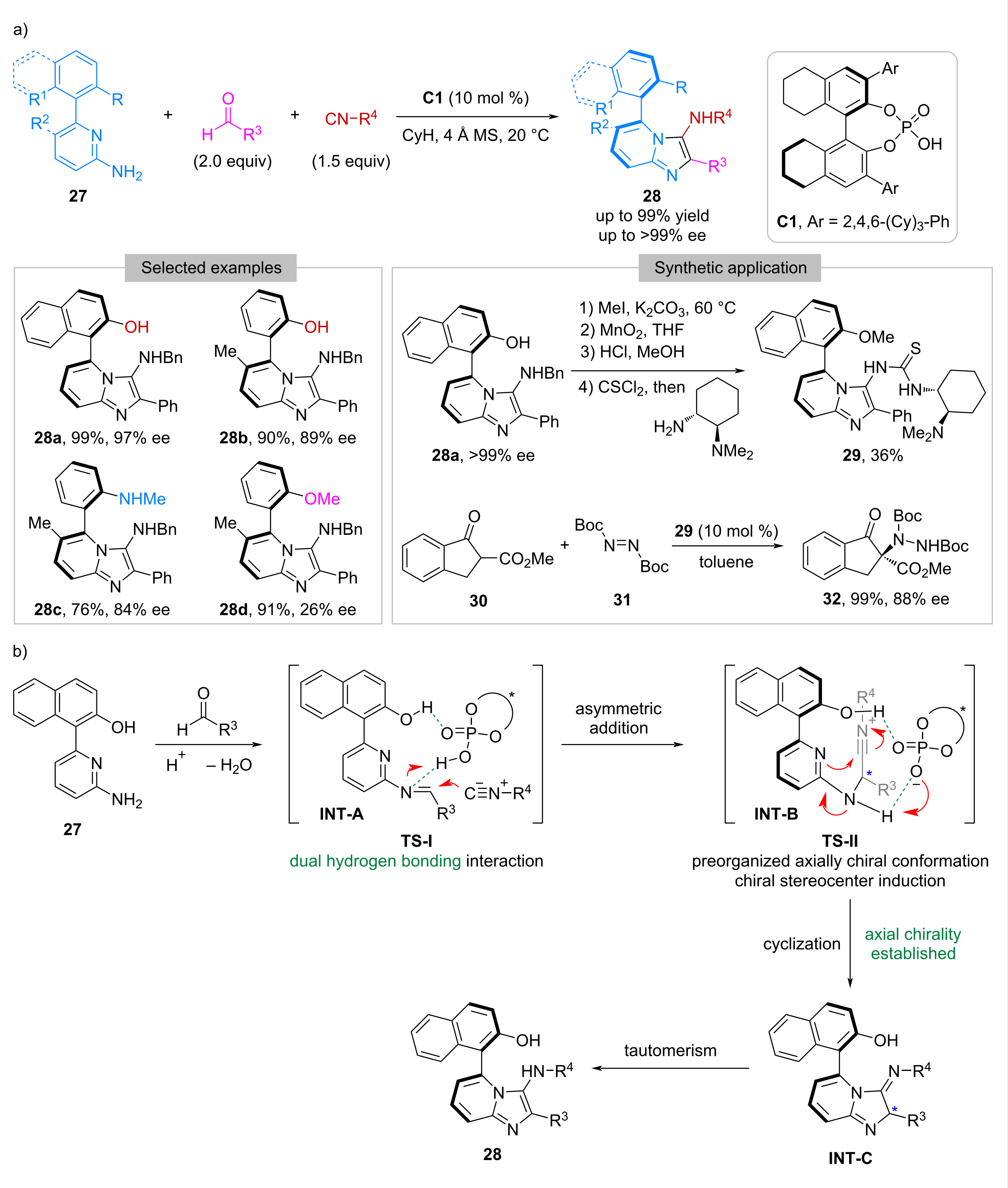

Scheme 5: CPA-catalyzed enantioselective Groebke–Blackburn–Bienaymé reaction.

products in developing chiral organocatalysts was investigated as well. For instance, **28a** was converted to a thiourea-tertiary amine **29** through a four-step procedure in an overall 36% yield. This compound was then utilized as the catalyst in the electrophilic amination reaction between β-ketoester **30** and di-*tert*-butyl azodicarboxylate (**31**), and the corresponding product **32** was obtained in 99% yield with 88% ee. A plausible reaction mechanism was proposed for this CPA-catalyzed enantioselective Groebke–Blackburn–Bienaymé reaction. As illustrated in Scheme 5b, the imine condensation between **27** and the aldehyde afforded **INT-A**, which was activated by the CPA catalyst through hydrogen bonding interaction. The nucleophilic addition of isocyanide to **Int-A** produced **INT-B** bearing a stereogenic center. Subsequently, **INT-B** underwent intramolecular cyclization to generate axially chiral **INT-C**, which, after imine-enamine tautomerization, led to the formation of final product **28**.

α-Acidic isocyanide-based transformations

De novo arene formation

In 2019, Zhu and co-workers developed the first example of catalytic enantioselective Yamamoto–de Meijere pyrrole synthesis [36,37] between alkynyl ketones **33** and isocyanoacetates (Scheme 6) [38]. The success of this study not only adds a new entry to the de novo arene formation strategy [39,40] but also initiates the application of isocyanoacetates in constructing axial chirality. With Ag_2O and quinine-derived amino-phosphine ligand **L6** as the chiral catalyst, atropisomeric 3-arylpyrroles **34** were generated in 43–98% yield with 82–96% ee. Notably, two by-products **35** and **36** were observed during the reaction, resulting from the aldol reaction of isocyanoacetates with the ketone moiety in **33**. The authors have also demonstrated that **34f** could be used as the starting material to prepare the axially chiral olefin-oxazole **37**, which might be a potentially useful ligand in asymmetric catalysis. A possible stereochemical model was proposed as well, involving synergistic activation of both the alkynyl ketone and isocyanoacetate by the chiral catalyst.

Central-to-axial chirality transfer

In parallel with Zhu's work, Du, Chen, and co-workers reported an alternative way for the preparation of axially chiral 3-arylpyrroles [41] through a catalytic asymmetric Barton–Zard reaction [42] via central-to-axial chirality transfer strategy [43,44]. Under a similar silver-based catalytic system, nitroolefins **38** bearing a β-*ortho*-substituted aryl group reacted smoothly with α-acidic isocyanides to give the corresponding products **39** in 55–99% yield and 57–96% ee (Scheme 7). In addition, nitroolefins **40** possessing a β-five-membered heteroaryl ring were proven to be suitable substrates to react with *tert*-butyl isocyanoacetate, affording 3-heteroarylpyrroles **41** in 55–99% yield with 70–96% ee. In these cases, additional 2.0 equivalents of DBU were required to facilitate the conversion from the [3 + 2] cycloadducts to the final products. Moreover, an axially chiral tertiary alcohol-phosphine **42** was prepared from **39a** through a three-step procedure including

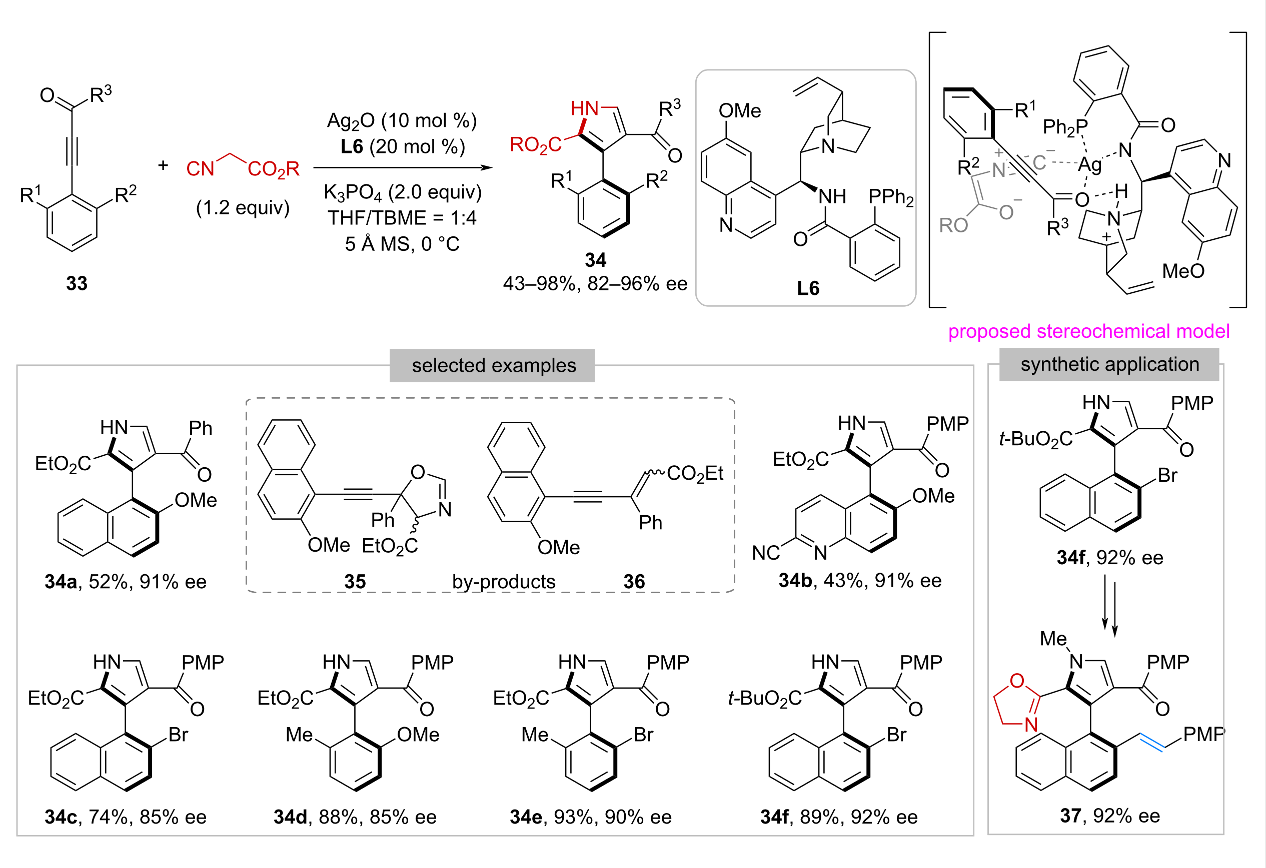

Scheme 6: Construction of axially chiral 3-arylpyrroles via de novo pyrrole formation.

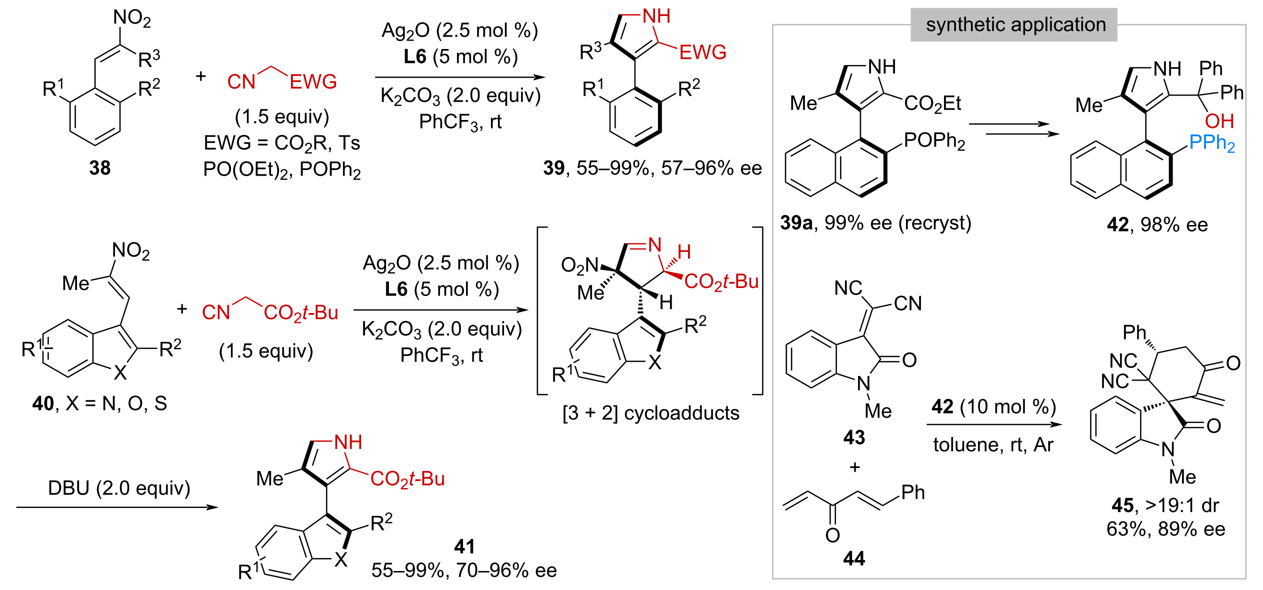

Scheme 7: Synthesis of atropoisomeric 3-arylpyrroles via central-to-axial chirality transfer.

N-methylation, reduction of phosphine oxide, and Grignard addition to ester. Subsequently, **42** was applied as a bifunctional Lewis base organocatalyst in the formal [4 + 2] cyclization reaction between alkene **43** and 2,2′-dienone **44**. The corresponding spirooxindole **45** was obtained in >19:1 dr, 63% yield, and 89% ee.

Dynamic kinetic resolution of configurationally labile bridged biaryls

The catalytic asymmetric dynamic kinetic resolution (DKR) of configurationally labile bridged biaryls, pioneered by Bringmann and co-workers [45], has proven to be a powerful approach for synthesizing axially chiral biaryls, particularly in the challenging case of sterically hindered tetra-*ortho*-substituted scaffolds [46,47]. In this context, α-acidic isocyanides have been successfully employed as carbon nucleophiles in the DKR of various bridged biaryls bearing different linkages to give diverse nitrogen heterocycle-substituted atropoisomeric biaryls.

In 2021, our group achieved the catalytic enantioselective DKR of biaryl lactones **46** with α-acidic isocyanides (Scheme 8a) [48]. By using Ag_2CO_3 and cinchonine-derived amino-phosphine **L7** as the catalyst, a wide range of oxazole-containing tetra-*ortho*-substituted axially chiral phenols **47** bearing diverse scaffolds, including naphthyl-phenyl (e.g., **47a**), phenyl-naphthyl (e.g., **47b**), biphenyl (e.g., **47c**), and binaphthyl (e.g., **47d**), were obtained in high yields with high enantioselectivities. In terms of isocyanides, isocyanoacetates with different ester groups, *p*-toluenesulfonylmethyl isocyanide (**47e**), and isocyanoacetamide (**47f**), were all compatible. It is noteworthy that this work represents the first example of catalytic asymmetric DKR of Bringmann's lactones with carbon nucleophiles. The success lies in the tandem enantioselective ring-opening of lactones with α-acidic isocyanides, followed by a rapid cyclization driven by aromatization, overcoming the long-standing stereochemical leakage problem caused by the undesired lactol formation [45].

Encouraged by the above results, we turned our attention to biaryl lactams [49]. However, in this case, the inherent resonance stability of the amide bond makes the ring-opening process rather challenging. To solve this problem, we envisioned that a cooperative catalytic system merging silver catalysis and organocatalysis could be employed to activate both reactants simultaneously. After extensive screening, the combination of Ag_2CO_3 and quinidine-derived squaramide **C2** was identified to be the optimal choice of catalyst. A variety of *ortho*,*ortho*-disubstituted biaryl lactams **48** were facilely transformed into the corresponding tetra-*ortho*-substituted atropisomeric anilines **49** in high yields with excellent enantioselectivities (Scheme 8b). In contrast, lactams possessing only one *ortho* substituent suffered from much lower reactivity (e.g., **49c**), presumably due to the lack of sufficient torsional strain [50], whereas substrates bearing strong electron-withdrawing groups resulted in almost no reactivity (e.g., **49d**).

Additionally, it was found that the N-substituent R^3 in **48** has a significant effect on both reactivity and enantioselectivity. While replacing Ts with Bn led to no reaction at all (**49e** versus **49a**), substituting it with Cbz gave the desired product **49f** in only 6% yield with <5% ee.

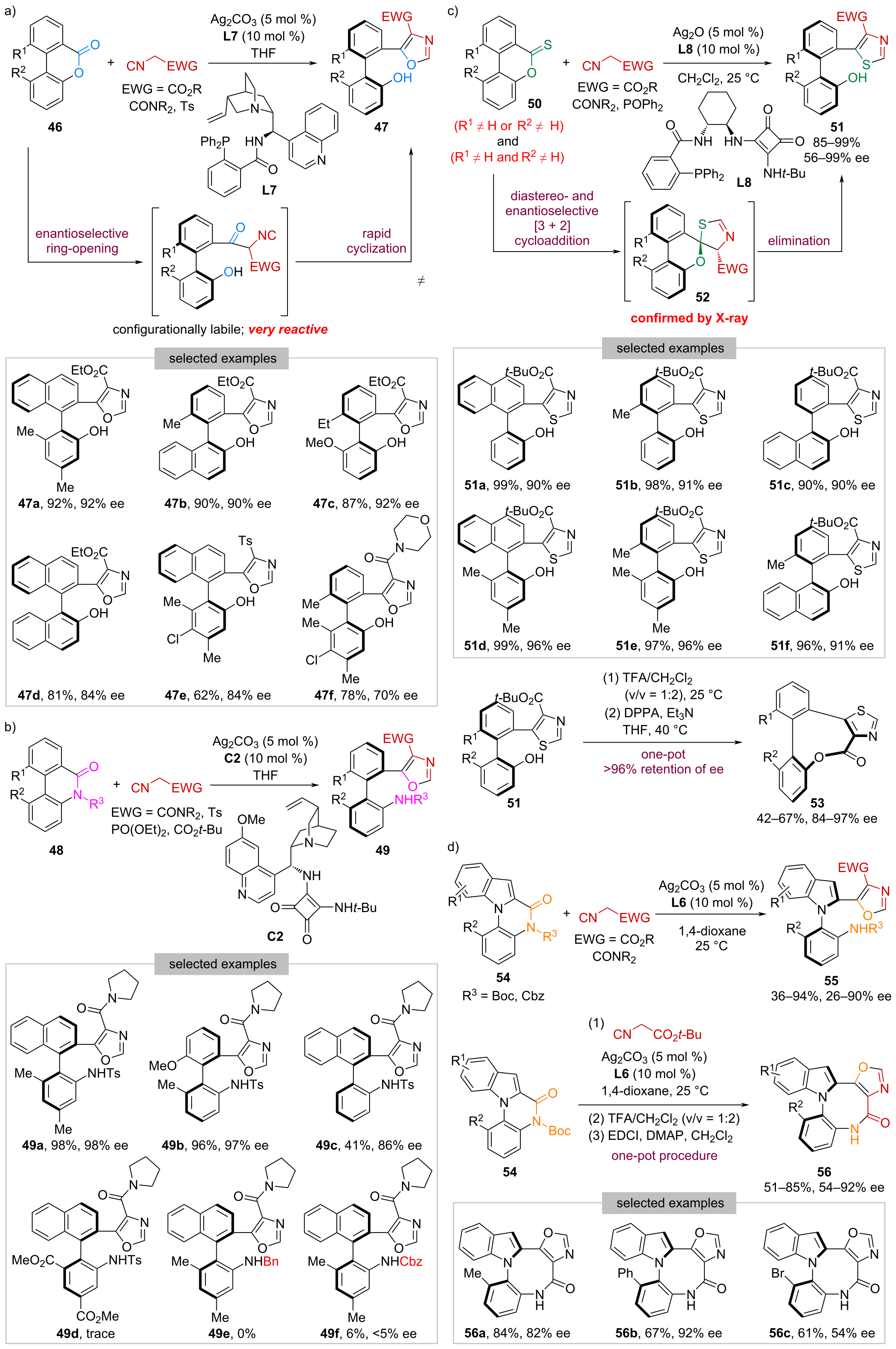

Scheme 8: Dynamic kinetic resolution of bridged biaryls with α-acidic isocyanides.

In 2022, we reported the discovery and development of a torsional strain-independent reaction between biaryl thionolactones **50** and α-acidic isocyanides (Scheme 8c) [51]. Using Ag_2O and 1,2-diaminocyclohexane-derived phosphine-squaramide bifunctional ligand **L8** as the catalyst, a universal synthesis of tri- and tetra-*ortho*-substituted biaryl phenols **51** containing a thiazole moiety was achieved in 85–99% yield with 56–99% ee. It is worth mentioning that this work represents the first example of catalytic asymmetric DKR of biaryl thionolactones, getting rid of the pre-formation of stoichiometric Ru-complexes [52,53]. Mechanistic investigations indicated that this transformation proceeds through a two-step sequence promoted by the same catalyst: 1) the diastereo- and enantioselective [3 + 2] cycloaddition to generate spiro-*S*,*O*-ketal **52** with both axial and central chirality, followed by 2) ring-strain and aromatization-driven elimination, which elucidating the observed unusual torsional strain-independent reactivity. In addition, products bearing a *tert*-butyl ester group were smoothly converted into structurally novel axially chiral eight-membered lactones **53** in 42–67% yield with excellent retention of enantiopurity via an overall lactonization process.

In addition to C–C axial chirality, we have demonstrated that our Ag-catalyzed DKR protocol could be applied for the generation of C–N atropisomers by using *N*-arylindole lactams **54** as the cross-partner [54]. By employing Ag_2CO_3 and **L6** as the catalyst, axially chiral *N*-arylindoles **55** were synthesized in 36–94% yield with 26–90% ee (Scheme 8d). Building on such results, a one-pot procedure involving DKR, hydrolysis, and lactamization was developed, enabling a practical synthesis of structurally novel atropisomeric *N*-arylindoles **56** bearing an eight-membered lactam in 51–85% yield with 54–92% ee. Of note, these scaffolds exhibited remarkably large Stokes shifts, showing great potential in the development of fluorescent dyes.

Desymmetrization of prochiral compounds

Beyond DKR of bridged biaryls, our group has successfully applied α-acidic isocyanides in the catalytic asymmetric desymmetrization of substrates featuring a prochiral axis, realizing the preparation of structurally complex scaffolds possessing both axial and central chirality. Notably, in these cases, both issues of diastereo- and enantioselectivity are required to be addressed appropriately to prevent forming a complex mixture of stereoisomers.

In 2022, our group developed a silver-catalyzed desymmetric [3 + 2] cycloaddition between prochiral *N*-aryl maleimides **57** and α-substituted α-acidic isocyanides (Scheme 9a) [55]. With Ag_2CO_3 and **L9** as the chiral catalyst, this reaction proceeded smoothly to produce highly functionalized bicyclic 1-pyrrolines **58** bearing a remote C–N stereogenic axis and three contiguous stereogenic carbon centers in high yields (up to 97%) with high stereoselectivities (up to >20:1 dr, 99% ee).

Subsequently, we expanded this methodology to prochiral *N*-quinazolinone maleimides **59**, achieving the simultaneous generation of N–N axial and central chirality within a single step (Scheme 9b) [56]. Of particular note, an interesting ligand-induced diastereodivergent profile was identified. While the employment of **L9** afforded *endo*-selective [3 + 2] cycloadducts **60**, using Trost ligand **L10** resulted in a complete reversal to the *exo*-cycloadducts **61**. DFT calculations were performed and indicated that these two ligands act in different ways in the cyclization process, providing explanations for such a diastereodivergence. Specifically, **L9** functions as a monodentate ligand, and the stronger ligand–substrate hydrogen-bonding interaction and smaller distortion of the ligand resulted in *endo*-cycloadducts (**L9-TS**). In contrast, Trost ligand **L10** serves as a bidentate ligand, and the smaller distortion of isocyanoacetate–Ag coordination combing with better Ag–C σ-orbital overlap led to *exo*-cycloadducts (**L10-TS**).

Except for constructing C–N and N–N axial chirality, we have developed a highly diastereo- and enantioselective method to access tri- and tetra-*ortho*-substituted biaryl aldehydes **63** bearing both C–C axial and central chirality (Scheme 9c) [57]. Key to this work relies on the implementation of an efficient Ag_2O/**L7**-catalyzed desymmetric [3 + 2] cycloaddition of prochiral biaryl dialdehydes **62** with α-substituted α-acidic isocyanides. We have also demonstrated that the retained aldehyde functionality in **63** allowed for versatile derivatizations, such as reduction, reductive amination, condensation, and olefination, which further expanded the structural diversity of the resulting products.

Summary and Outlook

The past few years have witnessed exciting progress in developing catalytic asymmetric transformations of isocyanides for generating architectures bearing axial, planar, helical, and inherent chirality. These advances not only offer efficient routes to enantioenriched non-central chiral compounds but also significantly broaden the utility of isocyanides in organic synthesis. Nevertheless, despite these notable accomplishments, this research field remains in its nascent stage with ample room for further exploration. First, existing studies have predominantly focused on the construction of axial chirality, while synthetic methods for other forms of non-central chirality, such as planar, helical, and inherent chirality, remain largely underdeveloped. To date, only a single example has been reported for each case, all of which are restricted to palladium-catalyzed isocyanide insertion reactions. Second, the catalytic systems employed thus far are relatively limited. Although transition metal catalysis,

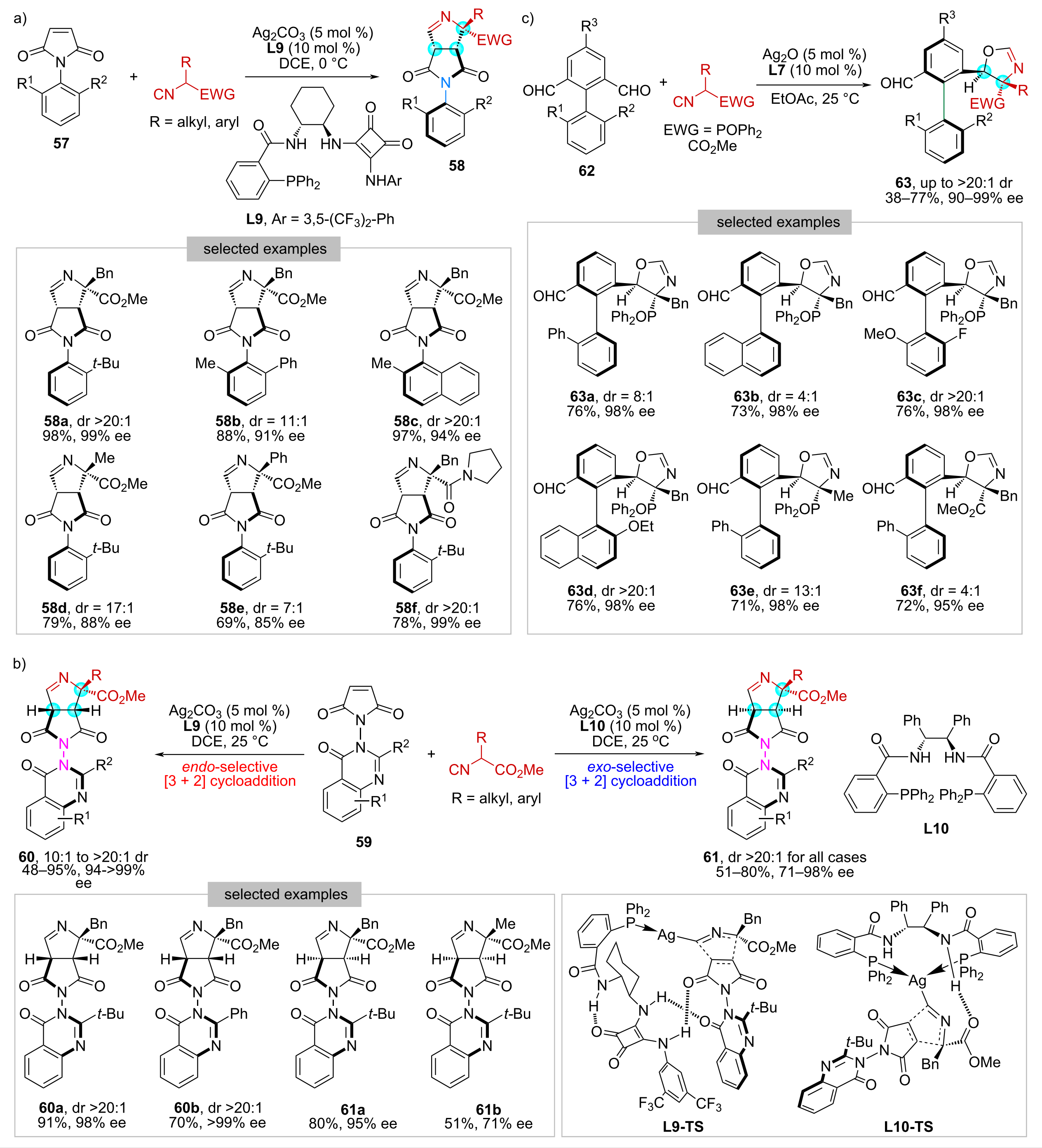

Scheme 9: Desymmetrization of prochiral compounds with α-acidic isocyanides.

particularly with palladium and silver, has proven to be highly effective, expanding the scope as well as the activation mode of chiral catalysts could greatly enrich reaction types and accessible structural diversity. Third, further investigation into the potential applications of the resulting chiral products, e.g., biological activities and utility as chiral organocatalysts or ligands, warrants greater attention. We anticipate that considerable efforts in these directions would be crucial for advancing this field and fully unlocking the synthetic potential of isocyanides in the preparation of non-central chiral compounds.

Funding

Financial support from the Joint Funds of the Zhejiang Provincial Natural Science Foundation of China (LTZ22B020001) and Zhejiang University is acknowledged.

ORCID® iDs

Jia-Yu Liao - https://orcid.org/0000-0001-6847-4825

Data Availability Statement

Data sharing is not applicable as no new data was generated or analyzed in this study.

References

1. Wencel-Delord, J.; Panossian, A.; Leroux, F. R.; Colobert, F. *Chem. Soc. Rev.* **2015,** *44,* 3418–3430. doi:10.1039/c5cs00012b
2. Cheng, J. K.; Xiang, S.-H.; Li, S.; Ye, L.; Tan, B. *Chem. Rev.* **2021,** *121,* 4805–4902. doi:10.1021/acs.chemrev.0c01306
3. Carmona, J. A.; Rodríguez-Franco, C.; Fernández, R.; Hornillos, V.; Lassaletta, J. M. *Chem. Soc. Rev.* **2021,** *50,* 2968–2983. doi:10.1039/d0cs00870b
4. Schmidt, T. A.; Hutskalova, V.; Sparr, C. *Nat. Rev. Chem.* **2024,** *8,* 497–517. doi:10.1038/s41570-024-00618-x
5. López, R.; Palomo, C. *Angew. Chem., Int. Ed.* **2022,** *61,* e202113504. doi:10.1002/anie.202113504
6. Laws, D.; Poff, C. D.; Heyboer, E. M.; Blakey, S. B. *Chem. Soc. Rev.* **2023,** *52,* 6003–6030. doi:10.1039/d3cs00325f
7. Yang, G.; Wang, J. *Angew. Chem., Int. Ed.* **2024,** *63,* e202412805. doi:10.1002/anie.202412805
8. Tanaka, K.; Morita, F. *J. Synth. Org. Chem., Jpn.* **2022,** *80,* 1019–1027. doi:10.5059/yukigoseikyokaishi.80.1019
9. Wang, Y.; Wu, Z.-G.; Shi, F. *Chem Catal.* **2022,** *2,* 3077–3111. doi:10.1016/j.checat.2022.10.011
10. Huang, Q.; Tang, Y.-P.; Zhang, C.-G.; Wang, Z.; Dai, L. *ACS Catal.* **2024,** *14,* 16256–16265. doi:10.1021/acscatal.4c05345
11. Tang, M.; Yang, X. *Eur. J. Org. Chem.* **2023,** *26,* e202300738. doi:10.1002/ejoc.202300738
12. Luo, Y.; Luo, S.; Zhu, Q. *J. Org. Chem.* **2025,** *90,* 5307–5322. doi:10.1021/acs.joc.5c00479
13. Dömling, A.; Ugi, I. *Angew. Chem., Int. Ed.* **2000,** *39,* 3168–3210. doi:10.1002/1521-3773(20000915)39:18<3168::aid-anie3168>3.0.co;2-u
14. Dömling, A. *Chem. Rev.* **2006,** *106,* 17–89. doi:10.1021/cr0505728
15. Sadjadi, S.; Heravi, M. M.; Nazari, N. *RSC Adv.* **2016,** *6,* 53203–53272. doi:10.1039/c6ra02143c
16. Qiu, G.; Ding, Q.; Wu, J. *Chem. Soc. Rev.* **2013,** *42,* 5257–5269. doi:10.1039/c3cs35507a
17. Song, B.; Xu, B. *Chem. Soc. Rev.* **2017,** *46,* 1103–1123. doi:10.1039/c6cs00384b
18. Collet, J. W.; Roose, T. R.; Ruijter, E.; Maes, B. U. W.; Orru, R. V. A. *Angew. Chem., Int. Ed.* **2020,** *59,* 540–558. doi:10.1002/anie.201905838
19. Kaur, T.; Wadhwa, P.; Bagchi, S.; Sharma, A. *Chem. Commun.* **2016,** *52,* 6958–6976. doi:10.1039/c6cc01562j
20. Doraghi, F.; Baghershahi, P.; Gilaninezhad, F.; Darban, N. M. Z.; Dastyafteh, N.; Noori, M.; Mahdavi, M. *Adv. Synth. Catal.* **2025,** *367,* e202400994. doi:10.1002/adsc.202400994
21. Gulevich, A. V.; Zhdanko, A. G.; Orru, R. V. A.; Nenajdenko, V. G. *Chem. Rev.* **2010,** *110,* 5235–5331. doi:10.1021/cr900411f
22. Boyarskiy, V. P.; Bokach, N. A.; Luzyanin, K. V.; Kukushkin, V. Y. *Chem. Rev.* **2015,** *115,* 2698–2779. doi:10.1021/cr500380d
23. Giustiniano, M.; Basso, A.; Mercalli, V.; Massarotti, A.; Novellino, E.; Tron, G. C.; Zhu, J. *Chem. Soc. Rev.* **2017,** *46,* 1295–1357. doi:10.1039/c6cs00444j
24. van Berkel, S. S.; Bögels, B. G. M.; Wijdeven, M. A.; Westermann, B.; Rutjes, F. P. J. T. *Eur. J. Org. Chem.* **2012,** 3543–3559. doi:10.1002/ejoc.201200030
25. Wang, Q.; Wang, D.-X.; Wang, M.-X.; Zhu, J. *Acc. Chem. Res.* **2018,** *51,* 1290–1300. doi:10.1021/acs.accounts.8b00105
26. Luo, J.; Chen, G.-S.; Chen, S.-J.; Li, Z.-D.; Liu, Y.-L. *Chem. – Eur. J.* **2021,** *27,* 6598–6619. doi:10.1002/chem.202003224
27. Luo, S.; Xiong, Z.; Lu, Y.; Zhu, Q. *Org. Lett.* **2018,** *20,* 1837–1840. doi:10.1021/acs.orglett.8b00348
28. Teng, F.; Yu, T.; Peng, Y.; Hu, W.; Hu, H.; He, Y.; Luo, S.; Zhu, Q. *J. Am. Chem. Soc.* **2021,** *143,* 2722–2728. doi:10.1021/jacs.1c00640
29. Wang, X.; Xu, J.; Luo, Y.; Wang, Y.; Huang, J.; Zhu, Q.; Luo, S. *ACS Catal.* **2025,** *15,* 201–210. doi:10.1021/acscatal.4c06720
30. Luo, Y.; Cheng, S.; Peng, Y.; Wang, X.; Li, J.; Gan, C.; Luo, S.; Zhu, Q. *CCS Chem.* **2022,** *4,* 2897–2905. doi:10.31635/ccschem.021.202101486
31. Yu, T.; Li, Z.-Q.; Li, J.; Cheng, S.; Xu, J.; Huang, J.; Zhong, Y.-W.; Luo, S.; Zhu, Q. *ACS Catal.* **2022,** *12,* 13034–13041. doi:10.1021/acscatal.2c04461
32. Groebke, K.; Weber, L.; Mehlin, F. *Synlett* **1998,** 661–663. doi:10.1055/s-1998-1721
33. Blackburn, C.; Guan, B.; Fleming, P.; Shiosaki, K.; Tsai, S. *Tetrahedron Lett.* **1998,** *39,* 3635–3638. doi:10.1016/s0040-4039(98)00653-4
34. Bienaymé, H.; Bouzid, K. *Angew. Chem., Int. Ed.* **1998,** *37,* 2234–2237. doi:10.1002/(sici)1521-3773(19980904)37:16<2234::aid-anie2234>3.3.co;2-i
35. Hong, S.; Liu, W.; Zhang, C.; Yang, X. *Sci. Adv.* **2024,** *10,* eadr6135. doi:10.1126/sciadv.adr6135
36. Kamijo, S.; Kanazawa, C.; Yamamoto, Y. *J. Am. Chem. Soc.* **2005,** *127,* 9260–9266. doi:10.1021/ja051875m
37. Larionov, O. V.; de Meijere, A. *Angew. Chem., Int. Ed.* **2005,** *44,* 5664–5667. doi:10.1002/anie.200502140
38. Zheng, S.-C.; Wang, Q.; Zhu, J. *Angew. Chem., Int. Ed.* **2019,** *58,* 1494–1498. doi:10.1002/anie.201812654
39. Zhang, X.; Liu, Y.-Z.; Shao, H.; Ma, X. *Molecules* **2022,** *27,* 8517. doi:10.3390/molecules27238517
40. Sun, H.-R.; Sharif, A.; Chen, J.; Zhou, L. *Chem. – Eur. J.* **2023,** *29,* e202300183. doi:10.1002/chem.202300183
41. He, X.-L.; Zhao, H.-R.; Song, X.; Jiang, B.; Du, W.; Chen, Y.-C. *ACS Catal.* **2019,** *9,* 4374–4381. doi:10.1021/acscatal.9b00767
42. Barton, D. H. R.; Zard, S. Z. *J. Chem. Soc., Chem. Commun.* **1985,** 1098–1100. doi:10.1039/c39850001098
43. Yang, H.; Chen, J.; Zhou, L. *Chem. – Asian J.* **2020,** *15,* 2939–2951. doi:10.1002/asia.202000681
44. Min, X.-L.; Zhang, X.-L.; Shen, R.; Zhang, Q.; He, Y. *Org. Chem. Front.* **2022,** *9,* 2280–2292. doi:10.1039/d1qo01699g
45. Bringmann, G.; Breuning, M.; Tasler, S. *Synthesis* **1999,** 525–558. doi:10.1055/s-1999-3435
46. Wang, G.; Huang, J.; Zhang, J.; Fu, Z. *Org. Chem. Front.* **2022,** *9,* 4507–4521. doi:10.1039/d2qo00946c
47. Wu, C.; Jin, Y.; Zhang, X.; Gao, R.; Dou, X. *Eur. J. Org. Chem.* **2024,** *27,* e202400402. doi:10.1002/ejoc.202400402
48. Qian, L.; Tao, L.-F.; Wang, W.-T.; Jameel, E.; Luo, Z.-H.; Zhang, T.; Zhao, Y.; Liao, J.-Y. *Org. Lett.* **2021,** *23,* 5086–5091. doi:10.1021/acs.orglett.1c01632
49. Wang, W.-T.; Zhang, S.; Tao, L.-F.; Pan, Z.-Q.; Qian, L.; Liao, J.-Y. *Chem. Commun.* **2022,** *58,* 6292–6295. doi:10.1039/d2cc01625g

50. Zhao, K.; Duan, L.; Xu, S.; Jiang, J.; Fu, Y.; Gu, Z. *Chem* **2018,** *4,* 599–612. doi:10.1016/j.chempr.2018.01.017
51. Luo, Z.-H.; Wang, W.-T.; Tang, T.-Y.; Zhang, S.; Huang, F.; Hu, D.; Tao, L.-F.; Qian, L.; Liao, J.-Y. *Angew. Chem., Int. Ed.* **2022,** *61,* e202211303. doi:10.1002/anie.202211303
52. Schenk, W. A.; Kümmel, J.; Reuther, I.; Burzlaff, N.; Wuzik, A.; Schupp, O.; Bringmann, G. *Eur. J. Inorg. Chem.* **1999,** 1745–1756. doi:10.1002/(sici)1099-0682(199910)1999:10<1745::aid-ejic1745>3.3.co;2-t
53. Bringmann, G.; Wuzik, A.; Kümmel, J.; Schenk, W. A. *Organometallics* **2001,** *20,* 1692–1694. doi:10.1021/om001040e
54. Tao, L.-F.; Huang, F.; Zhao, X.; Qian, L.; Liao, J.-Y. *Cell Rep. Phys. Sci.* **2023,** *4,* 101697. doi:10.1016/j.xcrp.2023.101697
55. Zhang, S.; Luo, Z.-H.; Wang, W.-T.; Qian, L.; Liao, J.-Y. *Org. Lett.* **2022,** *24,* 4645–4649. doi:10.1021/acs.orglett.2c01761
56. Wang, W.-T.; Zhang, S.; Lin, W.; Luo, Z.-H.; Hu, D.; Huang, F.; Bai, R.; Lan, Y.; Qian, L.; Liao, J.-Y. *Org. Chem. Front.* **2024,** *11,* 3308–3319. doi:10.1039/d4qo00294f
57. Huang, F.; Tao, L.-F.; Liu, J.; Qian, L.; Liao, J.-Y. *Chem. Commun.* **2023,** *59,* 4487–4490. doi:10.1039/d3cc00708a

License and Terms

The definitive version of this article is the electronic one which can be found at:
https://doi.org/10.3762/bjoc.21.129

BEILSTEIN JOURNAL OF ORGANIC CHEMISTRY

Unique halogen–π association detected in single crystals of C–N atropisomeric *N*-(2-halophenyl)quinolin-2-one derivatives and the thione analogue

Mai Uchibori[1], Nanami Murate[1], Kanako Shima[1], Tatsunori Sakagami[1], Ko Kanehisa[2], Gary James Richards[2], Akiko Hori[2] and Osamu Kitagawa*[1]

Full Research Paper

Address:
[1]Chemistry and Materials Program, College of Engineering, Shibaura Institute of Technology, 3-7-5 Toyosu, Kohto-ku, Tokyo 135-8548, Japan and [2]Graduate School of Engineering and Science, Shibaura Institute of Technology, 307 Fukasaku, Minuma-ku, Saitama 337-8570, Japan

Email:
Osamu Kitagawa* - kitagawa@shibaura-it.ac.jp

* Corresponding author

Keywords:
atropisomers; C–N bond; halogen bond; quinolinones; single crystals; thiones

Beilstein J. Org. Chem. **2025,** *21,* 1748–1756.
https://doi.org/10.3762/bjoc.21.138

Received: 30 May 2025
Accepted: 12 August 2025
Published: 01 September 2025

This article is part of the thematic issue "Non-central chirality in organic chemistry".

Associate Editor: N. Yoshikai

Abstract

In single crystals of C–N atropisomeric *N*-(2-halophenyl)quinolin-2-one and the thione analogue, a unique association based on a halogen–π interaction was detected. In racemic and optically pure *N*-(2-bromo- or 2-chlorophenyl)quinolin-2-ones, homochiral layered polymers, which consist of (*P*)- or (*M*)-atropisomers, were formed through intermolecular halogen–π association. The halogen–π association in the racemates is due to a halogen bond (C–X···π) between a σ-hole on the halogen atom and a π-electron on the quinolinone benzene ring, while that in optically pure forms is caused by an n–π* interaction between a lone electron pair on the halogen atom and a π* orbital of the quinolinone. In contrast to the formation of the homochiral layered polymer in quinolinones, in racemic *N*-(2-bromophenyl)quinoline-2-thione, heterochiral layered polymers, in which (*P*)- and (*M*)-atropisomers were alternately connected, were formed through an n–π* interaction between a lone electron pair on the bromine atom and a π* orbital of the quinoline-2-thione.

Introduction

In the past several years, C–N atropisomers (C–N axially chiral compounds) owing to the rotational restriction around a C–N single bond have received great attention as new target molecules for catalytic asymmetric reactions. Highly enantioselective syntheses of diverse C–N atropisomeric compounds possessing carboxamide, imide, lactam, sulfonamide, indole, pyrrole, imidazole, carbazole and amine skeletons have been reported by many groups [1-9]. C–N atropisomers are attractive compounds from the viewpoint of not only synthetic organic chemistry but also medicinal chemistry [10-13]. For example, 3-(2-bromophenyl)-2-methylquinazolin-4-one (**I**), which has a high rotational barrier about the N3–Ar bond, is known as mebroqualone possessing GABA agonist activity (Figure 1) [14,15].

Our group has been exploring asymmetric synthesis of C–N atropisomers and their structural properties for over 25 years [16,17]. As a part of the C–N atropisomeric chemistry, we succeeded in the asymmetric synthesis of mebroqualone (**I**) and the thione analogue **II** [18,19]. In the course of this study, it was found that intermolecular association in the single crystals of racemates significantly differs from that of optically pure forms (chirality-dependent halogen bonding, Figure 1) [20,21].

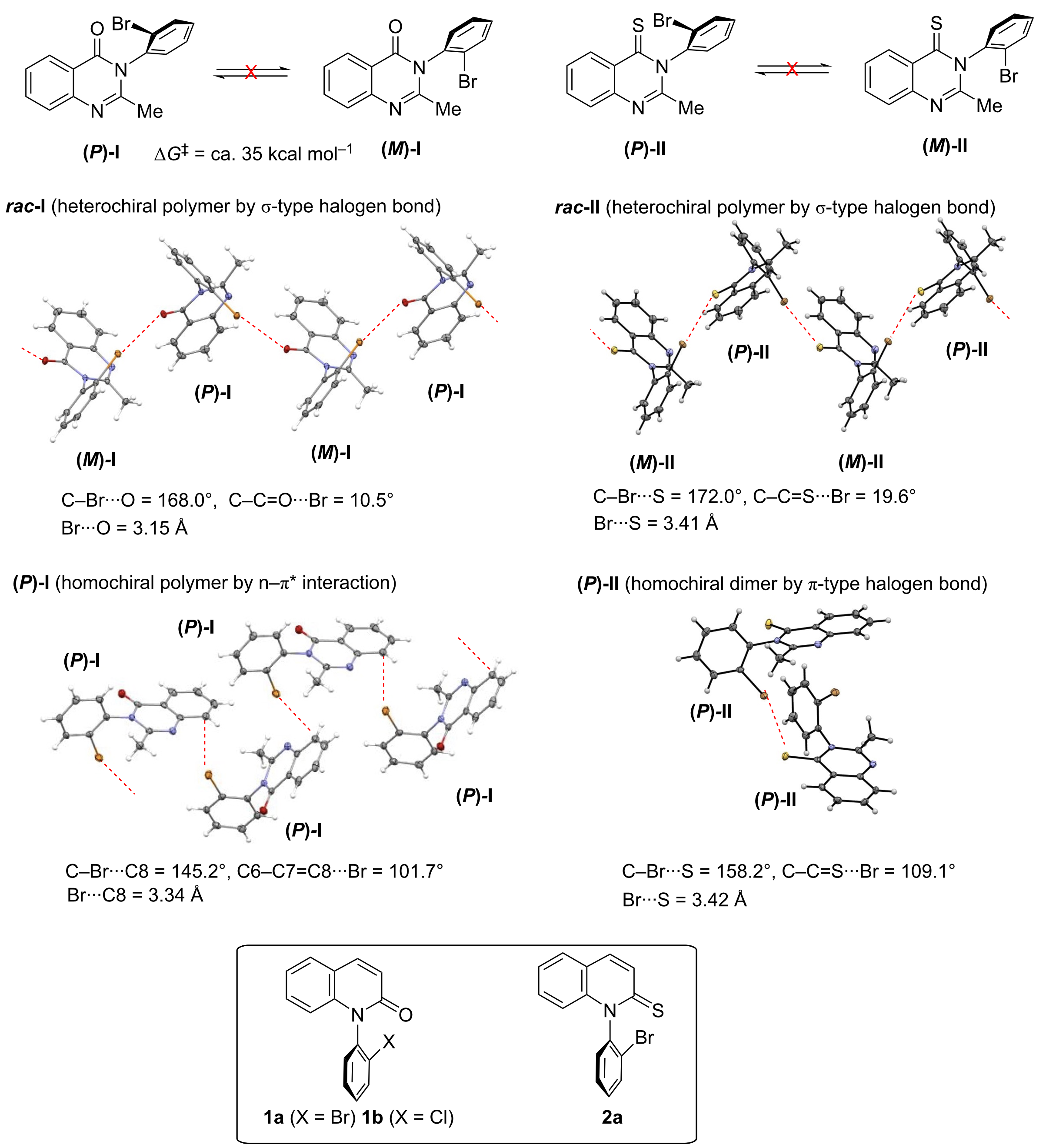

Figure 1: Various C–N atropisomeric compounds and their intermolecular interactions in single crystals.

That is, in crystals of racemic mebroqualone ***rac*-I**, heterochiral zig-zag polymer chains, in which **(*P*)-I** and **(*M*)-I** were alternately connected, were formed through a σ-type intermolecular halogen bonding (C–Br···O) between the *ortho*-bromine atom and the carbonyl oxygen. The formation of similar heterochiral polymers through a σ-type intermolecular halogen bond (C–Br···S) was also found in crystals of the thio-analogue ***rac*-II**. On the other hand, in the optically pure mebroqualone **(*P*)-I**, the homochiral layered polymer was formed through a bromine–π association. The association is due to an n–π* interaction between a lone electron pair on the bromine atom and a π* orbital of the quinazolinone ring. In the optically pure thio-analogue **(*P*)-II**, the formation of homochiral dimers, rather than homochiral polymer chains, was detected. Furthermore, the homochiral dimers were constructed through a π-type halogen bonding (C–Br···S), rather than a σ-type such as ***rac*-I** and ***rac*-II**.

Halogen bonding has aroused great interest as a new type of noncovalent interaction as an alternative to hydrogen bonding and has been widely used as an important supramolecular tool in broad fields such as materials science, crystal engineering, liquid crystals, synthetic organic chemistry and medicinal chemistry [22-26]. Typically, halogen bonding has been classified into two major types: (1) σ-type halogen bonding, where the electrophilic region (σ-hole) of a halogen atom interacts with a lone pair on an electron-rich atom (e.g., C–X···Y), and (2) π-type halogen bonding (or halogen–π interaction), where the σ-hole interacts with an electron-rich π-system (e.g., C–X···π). The σ-hole typically forms on the extension of the C–X bond, opposite the bonding electron density, hence, the interaction is highly directional, with σ-type halogen bonds favoring nearly linear geometries (C–X···Y ≈ 180°). When the C–X···π angle significantly deviates from linearity, the halogen may act as an electron donor rather than an acceptor, and the interaction can be better described as an n–π* interaction involving the lone pair on the halogen atom.

The results shown in Figure 1 suggest that in the case of chiral compounds, the corresponding racemic and enantioenriched forms, ought to have different halogen bonding properties, and should be explored as different chemical entities. Meanwhile, there are very few studies on halogen bonding related to molecular chirality such as those shown in Figure 1 [27-30]. In addition, the studies on the comparison of intermolecular interaction (halogen bonding) between chiral compounds possessing an amide group and a thioamide group are quite rare [21].

We were curious as to whether the chirality (racemate/optically pure form)- and the functional group (C=O/C=S)-dependent halogen bonds found in **I** and **II** are also observed in other C–N atropisomeric compounds. In this article, we report the synthesis of atropisomeric *N*-(2-halophenyl)quinolin-2-ones (**1a**: X = Br, **1b**: X = Cl) and *N*-(2-bromophenyl)quinoline-2-thione (**2a**), and the analysis of halogen–mediated intermolecular interactions (halogen bonding and n–π* interaction) observed in their single crystals.

Results and Discussion

Synthesis of quinoline-2-ones (thione), their enantiomer separation and rotational stability

We focused on *N*-(2-halophenyl)quinolin-2-ones **1** and the thione analogue **2** as alternative substrates to verify chirality- and functional group-dependent halogen bonding observed in C–N atropisomeric quinazolinone **I** and quinazoline-thione **II**. Although the catalytic asymmetric synthesis of *N*-(2-bromo- or 2-chloro-phenyl)quinolin-2-ones **1a**,**b** was recently attempted by Doerfler et al., the yields were moderate (33% and 48%) and the enantioselectivities were poor (11% ee and 9% ee) [31]. In addition, rotational stability about the C–N bond in **1a**,**b** was not mentioned at all. We prepared racemates ***rac*-1a**,**b** in accordance with Scheme 1 and separated their enantiomers [**(*P*)-1a**,**b** and **(*M*)-1a**,**b**] through medium pressure liquid chromatography (MPLC) using a semi-preparative chiral IH column. The rotational barriers of **1a** and **1b** were evaluated to be 32.0 and 30.8 kcal mol^{-1}, respectively, by a thermal racemization experiment of the separated **(*P*)-1a** and **(P)-1b**. In contrast to quinolinones **1a,b**, the atropisomers in the precursors (3,4-dihydroquinolinones **4a,b**) could not be isolated because of the low rotational stability [32].

Quinolinone ***rac*-1a** was converted to quinoline-thione ***rac*-2a** by reaction with Lawesson's reagent, and subsequently, the enantiomers [**(*P*)-2a** and **(*M*)-2a**] were separated by MPLC using a chiral IH column. Unfortunately, the barrier value of quinoline-thione **2a** could not be evaluated because of the high rotational stability.

Chirality dependent halogen–π interaction detected in single crystals of racemic and optically pure *N*-(2-halophenyl)quinolin-2-ones

Single crystals of ***rac*-1a,b** were prepared (single crystals of ***rac*-1a,b** were obtained by vapour diffusion of hexane into a methanol solution of the compound at room temperature) and their X-ray crystal structural analyses were performed (Figure 2) [33]. In the crystals of ***rac*-1a**, a π-type intermolecular interaction between the bromine atom and the benzene ring of the quinolinone was found (the torsion angle: C8–C7–C6···Br = −80.3°). That is, the bromine atom interacts with three car-

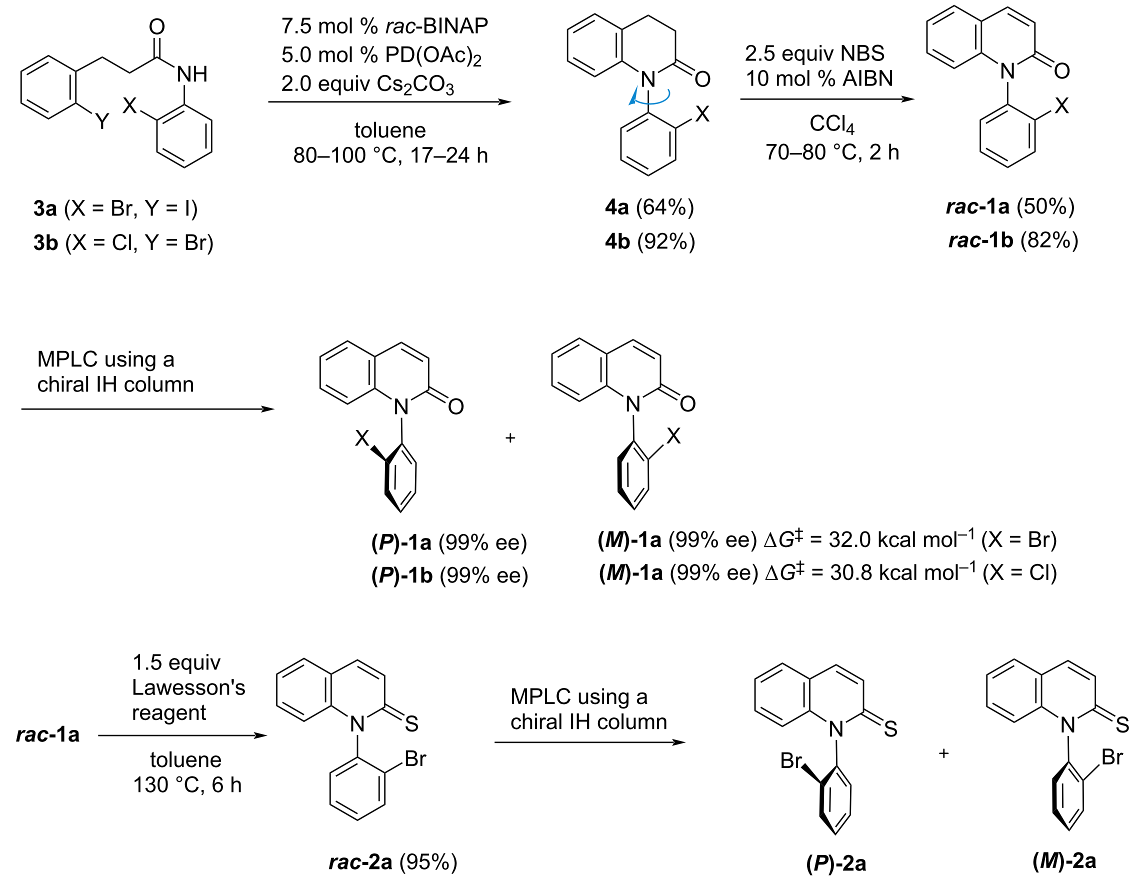

Scheme 1: Synthesis of *N*-(2-halophenyl)quinolin-2-ones **1a**,**b** and quinoline-2-thione **2a**.

bon atoms (C5–7); the three bond distances (Br···C5–7) and three bond angles (C–Br···C5–7) were 3.44, 3.30, 3.50 Å and 166.6, 155.9, 134.0°, respectively. Although a racemate, homochiral layered polymer chains, which consist of **(*P*)-1a** or **(*M*)-1a**, were formed through the Br–π interactions. The formation of homochiral layered polymers through halogen–π-type intermolecular interactions was also found in crystals of the *ortho*-chloro derivative ***rac*-1b** (the torsion angle: C8–C7–C6···Cl = −81.7°). In ***rac*-1b**, the chlorine atom interacts with two carbon atoms (C5 and C6) of the benzene ring, the two bond distances (Cl···C5,6) and two bond angles (C–Cl···C5,6) were 3.42, 3.27 Å and 164.5, 154.4°, respectively.

The formation of homochiral layered polymers through intermolecular halogen–π interactions was also observed in the crystals of optically pure forms **(*P*)-1a**,**b** (Figure 3, single crystals of **(*P*)-1a,b** were obtained by vapour diffusion of hexane into a methanol solution of the compound at room temperature) [34]. Meanwhile, the halogen atoms in **(*P*)-1a**,**b** were found to interact with the C4 atom on the lactam ring [the torsion angles of **(*P*)-1a** and **(*P*)-1b**: C2–C3–C4···Br = −102.6° and C2–C3–C4···Cl = −103.3°] but not with the benzene moiety as observed in racemates ***rac*-1a**,**b**. The bond length (Br···C4) and bond angle (C–Br···C4) in **(*P*)-1a** were 3.44 Å and 133.4 °, respectively, and the bond length (Cl···C4) and bond angle (C–Cl···C4) in **(*P*)-1b** were 3.40 Å and 132.8 °, respectively. The C–X···C4 bonds (133.4 ° and 132.8°) in the optically pure forms **(*P*)-1a,b** were considerably bent in comparison with the C–X···C5 bonds (166.6° and 164.5°) in racemates ***rac*-1a,b**.

Figure 4 shows the distances “*d*” and the two kinds of angles “θ”, ”α" in ***rac*-1a,b** and **(*P*)-1a,b**. The *d* values (distance between the centroid of the benzene ring and halogen X) in ***rac*-1a** and ***rac*-1b** were approximately 3.4 Å (3.36 Å and 3.35 Å, respectively), while the *d* values (distance between the centroid of the lactam ring and halogen X) in **(*P*)-1a** and **(*P*)-1b** were approximately 4.0 Å (4.01 Å and 3.99 Å, respectively). Although the *d* values in **(*P*)-1a**,**b** were 0.6 Å longer than those of

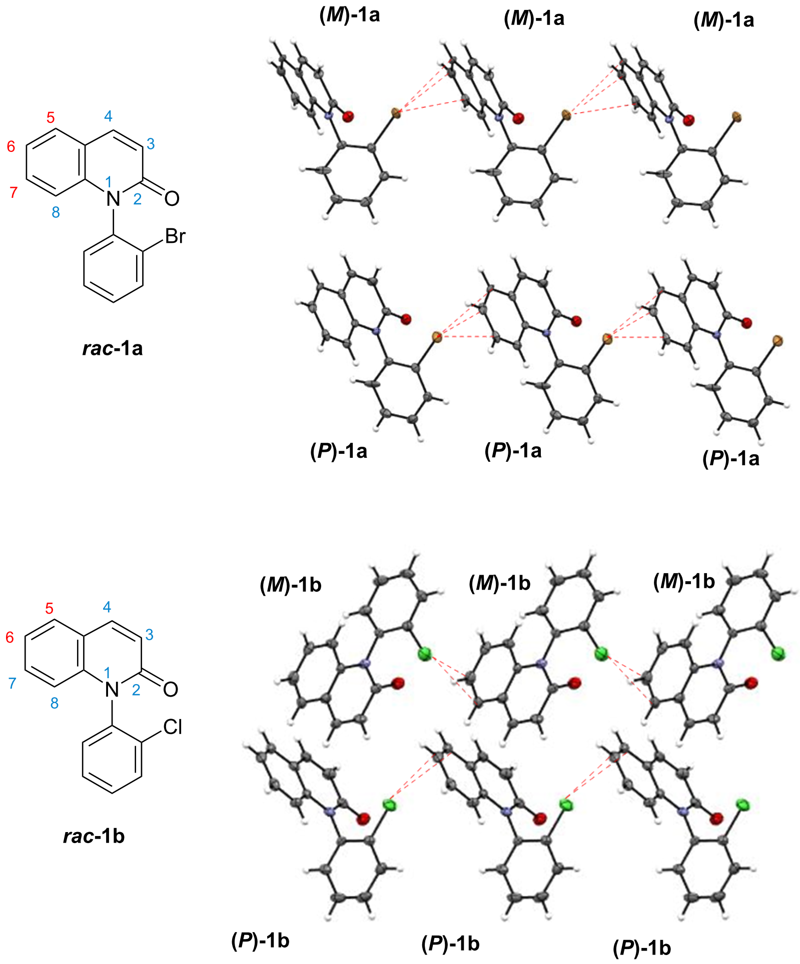

Br···C5 = 3.44 Å
Br···C6 = 3.30 Å
Br···C7 = 3.50 Å
C–Br···C5 = 166.6°
C–Br···C6 = 155.9°
C–Br···C7 = 134.0°
C8–C7–C6···Br = –80.3°

Cl···C5 = 3.42 Å
Cl···C6 = 3.27 Å
C–Cl··C5 = 164.5°
C–Cl···C6 = 154.4°
C8–C7–C6···Cl = –81.7°

Figure 2: Intramolecular associations detected in crystals of ***rac*-1a** and ***rac*-1b**.

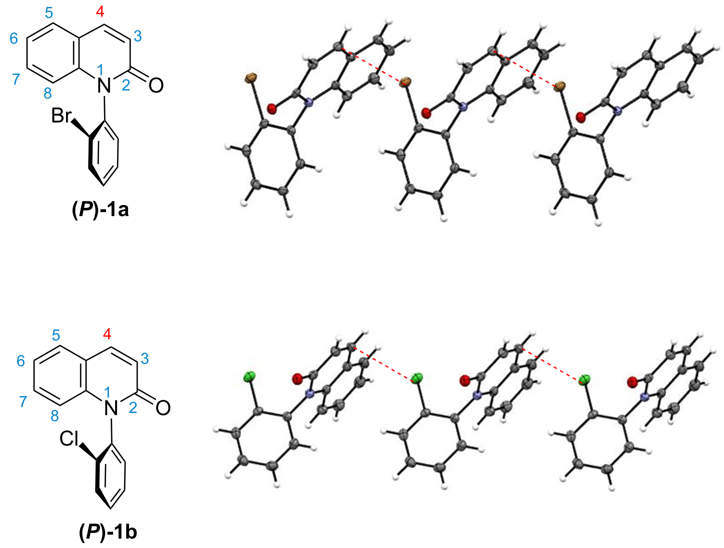

Br···C4 = 3.44 Å
C–Br···C4 = 133.4°
C2–C3–C4···Br = –102.6

Cl···C4 = 3.40 Å
C–Cl···C4 = 132.8°
C2–C3–C4···Cl = –103.3°

Figure 3: Intramolecular association detected in the crystals of **(*P*)-1a** and **(*P*)-1b**.

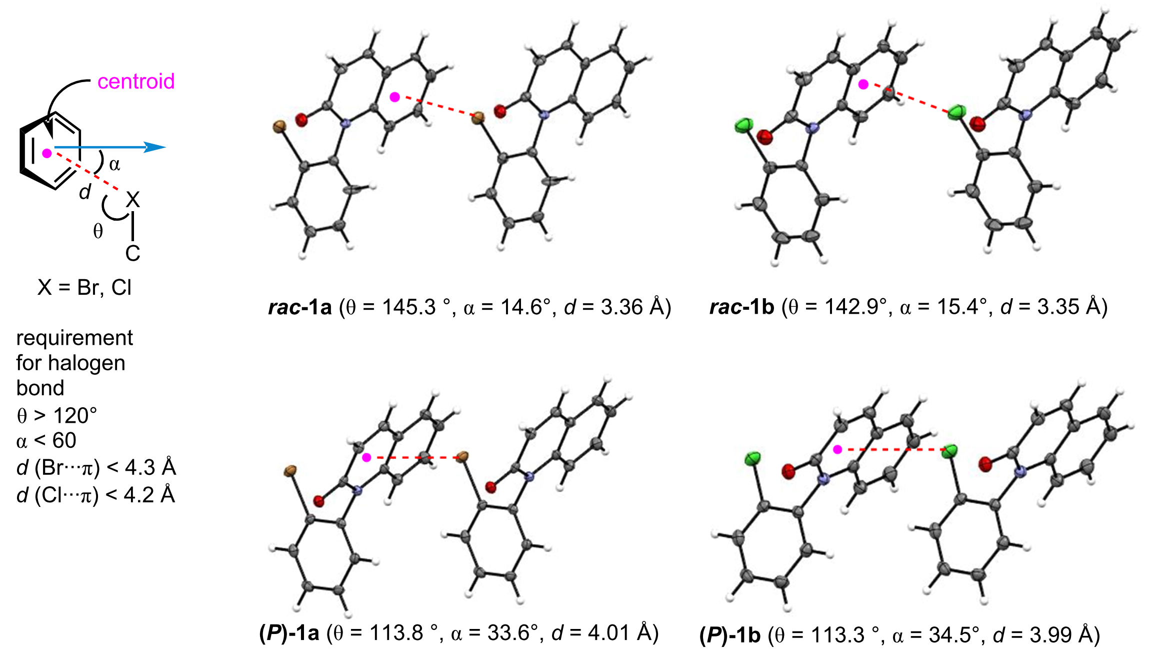

***rac*-1a** (θ = 145.3 °, α = 14.6°, *d* = 3.36 Å) ***rac*-1b** (θ = 142.9°, α = 15.4°, *d* = 3.35 Å)

(*P*)-1a (θ = 113.8 °, α = 33.6°, *d* = 4.01 Å) **(*P*)-1b** (θ = 113.3 °, α = 34.5°, *d* = 3.99 Å)

Figure 4: Angles (θ, α) and distances (*d*) in racemate ***rac*-1a,b** and **(*P*)-1a,b**.

***rac*-1a**,**b**, they (4.01 Å and 3.99 Å) were within the acceptable range for halogen bonding [*d* < 4.3 Å (Br···π), *d* < 4.2 Å (Cl···π)]. The angles (θ) of C–X···(centroid) in ***rac*-1a** and ***rac*-1b** were 145.3° and 142.9°, respectively, and the angles (α) in ***rac*-1a** and ***rac*-1b** were 14.6° and 15.4°, respectively. Since both angles (θ and α) met the requirements for halogen bonding (θ > 120°, α < 60°) [33,34], the X···π interaction in ***rac*-1a**,**b** was judged to be due to halogen bonding between a σ-hole on the halogen atom and a π-electron of the aromatic ring.

On the other hand, in **(*P*)-1a** and **(*P*)-1b**, although the angles (α) were 33.6 ° and 34.5° which are acceptable for a halogen bond (α < 60°), the angles (θ) did not meet the requirement for halogen bonding (θ > 120°) [35,36]. That is, the angles (θ) in **(*P*)-1a** and **(*P*)-1b** were 113.8° and 113.3°, respectively, which are approximately 30° narrower than those in ***rac*-1a** and ***rac*-1b**. These results suggest that the C–X···π association in the optically pure forms **(*P*)-1a**,**b** is not due to halogen bonding but rather originates from an n–π* interaction between a lone electron pair on the halogen atom and a π* orbital of the quinolinone ring.

Halogen–π interaction detected in a single crystal of racemic *N*-(2-bromophenyl)quinoline-2-thione

As mentioned in Figure 1, the intermolecular association of racemic C–N atropisomeric mebroqualone ***rac*-I** was very similar to that of the thione analogue ***rac*-II** [the formation of heterochiral polymers through a σ-type halogen bond (C–Br···O or C–Br···S)]. In contrast, the intermolecular associations in the crystals of racemic quinoline-2-thione ***rac*-2a** significantly differed from those of the racemic quinolinones ***rac*-1** in Figure 2 (single crystals of ***rac*-2a** were obtained from slow evaporation of hexane/methanol (1:1) mixture at room temperature) [37].

That is, in contrast to ***rac*-1**, in which homochiral layered polymer chains were formed, crystallization of quinoline-2-thione ***rac*-2a** led to the formation of heterochiral layered polymer chains in which **(*P*)-2a** and **(*M*)-2a** were alternately connected (Figure 5). The association between **(*P*)-2a** and **(*M*)-2a** emerged through a π-type interaction between the bromine atom and the thiolactam moiety (C4–C3–C2···Br = −90.7°). The bromine atom interacts with C2 and C3 carbons on the thiolactam ring. The *d* value of Br···(centroid of the thiolactam ring) was 3.55 Å, and the angles (θ and α) were 112.7° and 19.9°, respectively. Thus, since the angle (θ) is narrower than 120°, the Br···π association in ***rac*-2a** may be due to an n–π* interaction between a lone electron pair on the bromine atom and a π* orbital of the quinoline-thione ring, rather than a π-type halogen bonding.

Although we attempted the preparation of single crystals of the optically pure form of **2a**, unfortunately, crystals suitable for

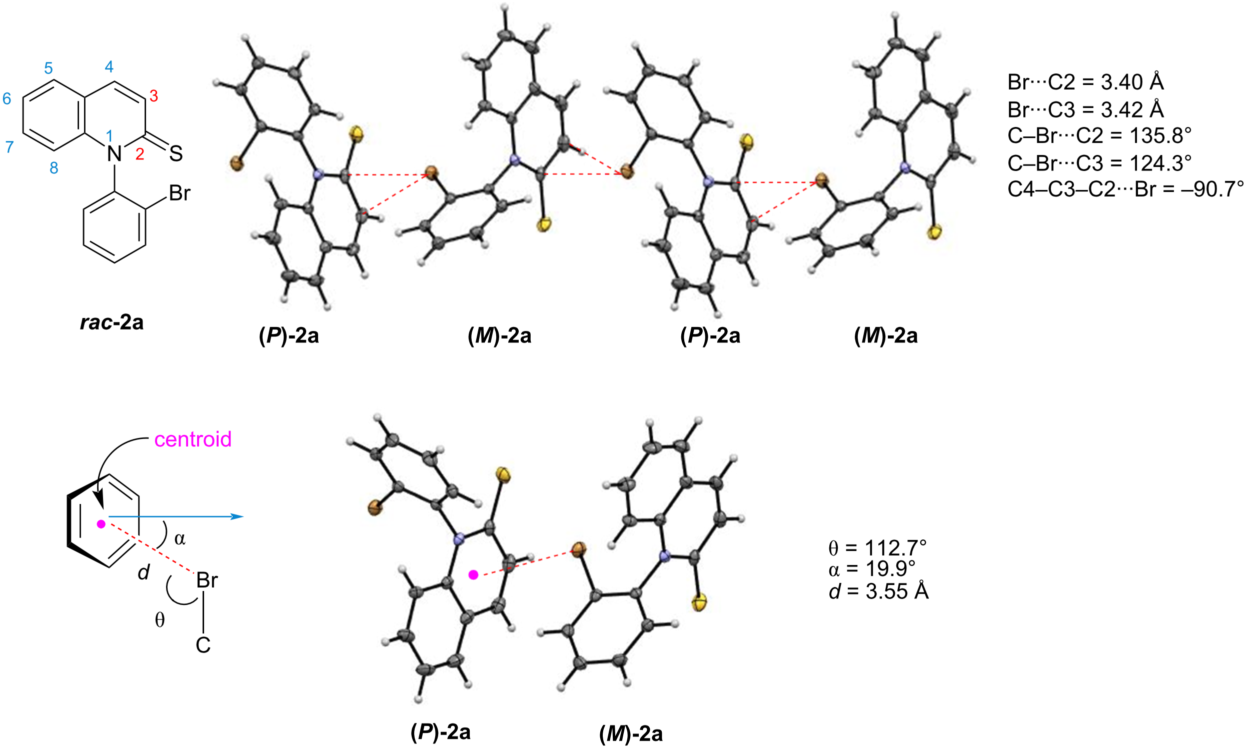

Figure 5: Crystal structure of racemic quinoline-2-thione ***rac*-2a**.

X-ray measurement could not be obtained (**2a** is chemically unstable and standing for a long period in the solution state resulted in several decomposed products).

Conclusion

We found that crystallization of racemic and optically pure C–N atropisomeric *N*-(halophenyl)quinolin-2-one derivatives led to the formation of homochiral layered polymer chains, which consist of (*P*)- or (*M*)-atropisomers, through different types of halogen–π interactions. Homochiral layered polymers in the racemate were constructed through a π-type halogen bonding (C–X···π) between a σ-hole on the halogen atom and a π-electron of the quinoline ring, while those in the optically pure form were formed through an n–π* interaction between a lone electron pair on the halogen atom and a π*orbital of the quinolinone ring. Thus, chirality (racemic/optically pure)-dependent halogen bonding was observed in single crystals of not only 3-(2-halophenyl)quinazolin-4-one derivatives but also *N*-(2-halophenyl)quinolin-2-one derivatives. Furthermore, it was revealed that the intermolecular association of C–N atropisomeric quinoline-2-thione significantly differs from that of quinolinones. That is, in contrast to the homochiral layered polymer found in quinolinone derivatives, in the single crystal of racemic *N*-(2-bromophenyl)quinoline-2-thione, the formation of heterochiral layered polymers, in which (*P*)- and (*M*)-atropisomers were alternately connected, was detected. In addition, the heterochiral layered polymers were constructed through an n–π* interaction between the lone electron pair on the bromine atom and the π*-orbital of the quinoline-2-thione ring, rather than through π-type halogen bonding.

Supporting Information

Crystallographic data for compounds **1** and **2** was obtained from the Cambridge Crystallographic Data Centre under deposition numbers 2448885–2448888 and 2448893. These can be obtained from the CCDC website (https://www.ccdc.cam.ac.uk/structures/).

Supporting Information File 1

Experimental procedures for synthesis of compounds **1**–**4** and their spectral data, copies of ^{1}H and ^{13}C{^{1}H} NMR charts of compounds **1–4**, chiral MPLC and HPLC chart in compounds **1a**,**b**, **2a**, evaluation of rotational barriers of compounds **1a**,**b**, and X-ray crystal data of ***rac*-1a**,**b**, **(*P*)-1a**,**b**, ***rac*-2a** (check CIF).
[https://www.beilstein-journals.org/bjoc/content/supplementary/1860-5397-21-138-S1.pdf]

Funding

This work was partly supported by JSPS KAKENHI (C 23K04755).

Author Contributions

Mai Uchibori: investigation; writing – review & editing. Nanami Murate: investigation. Kanako Shima: investigation. Tatsunori Sakagami: investigation. Ko Kanehisa: investigation; writing – review & editing. Gary James Richards: investigation; writing – review & editing. Akiko Hori: investigation; writing – review & editing. Osamu Kitagawa: conceptualization; funding acquisition; writing – original draft.

ORCID® iDs

Gary James Richards - https://orcid.org/0000-0002-5262-2587
Akiko Hori - https://orcid.org/0000-0002-0969-8500
Osamu Kitagawa - https://orcid.org/0000-0001-7964-1879

Data Availability Statement

All data that supports the findings of this study is available in the published article and/or the supporting information of this article.

References

1. Takahashi, I.; Suzuki, Y.; Kitagawa, O. *Org. Prep. Proced. Int.* **2014,** *46,* 1–23. doi:10.1080/00304948.2014.866467
2. Frey, J.; Choppin, S.; Colobert, F.; Wencel-Delord, J. *Chimia* **2020,** *74,* 883–889. doi:10.2533/chimia.2020.883
3. Thönnißen, V.; Patureau, F. W. *Chem. – Eur. J.* **2021,** *27,* 7189–7192. doi:10.1002/chem.202004151
4. Wu, Y.-J.; Liao, G.; Shi, B.-F. *Green Synth. Catal.* **2022,** *3,* 117–136. doi:10.1016/j.gresc.2021.12.005
5. Sweet, J. S.; Knipe, P. C. *Synthesis* **2022,** *54,* 2119–2132. doi:10.1055/s-0040-1719896
6. Rodríguez-Salamanca, P.; Fernández, R.; Hornillos, V.; Lassaletta, J. M. *Chem. – Eur. J.* **2022,** *28,* e202104442. doi:10.1002/chem.202104442
7. Mei, G.-J.; Koay, W. L.; Guan, C.-Y.; Lu, Y. *Chem* **2022,** *8,* 1855–1893. doi:10.1016/j.chempr.2022.04.011
8. Xiao, X.; Chen, B.; Yao, Y.-P.; Zhou, H.-J.; Wang, X.; Wang, N.-Z.; Chen, F.-E. *Molecules* **2022,** *27,* 6583. doi:10.3390/molecules27196583
9. Campbell, A. D. G.; Armstrong, R. J. *Synthesis* **2023,** *55,* 2427–2438. doi:10.1055/a-2039-5424
10. Clayden, J.; Moran, W. J.; Edwards, P. J.; LaPlante, S. R. *Angew. Chem., Int. Ed.* **2009,** *48,* 6398–6401. doi:10.1002/anie.200901719
11. Glunz, P. W. *Bioorg. Med. Chem. Lett.* **2018,** *28,* 53–60. doi:10.1016/j.bmcl.2017.11.050
12. Perreault, S.; Chandrasekhar, J.; Patel, L. *Acc. Chem. Res.* **2022,** *55,* 2581–2593. doi:10.1021/acs.accounts.2c00485
13. Wang, Z.; Meng, L.; Liu, X.; Zhang, L.; Yu, Z.; Wu, G. *Eur. J. Med. Chem.* **2022,** *243,* 114700. doi:10.1016/j.ejmech.2022.114700
14. Jackman, G. B.; Petrow, V.; Stephenson, O. *J. Pharm. Pharmacol.* **1960,** *12,* 529–538. doi:10.1111/j.2042-7158.1960.tb12705.x
15. Ghosh, S. K.; Nagarajan, R. *RSC Adv.* **2016,** *6,* 27378–27387. doi:10.1039/c6ra00855k
16. Kitagawa, O. *Acc. Chem. Res.* **2021,** *54,* 719–730. doi:10.1021/acs.accounts.0c00767
17. Kitagawa, O. *J. Org. Chem.* **2024,** *89,* 11089–11099. doi:10.1021/acs.joc.4c01065
18. Hirai, M.; Terada, S.; Yoshida, H.; Ebine, K.; Hirata, T.; Kitagawa, O. *Org. Lett.* **2016,** *18,* 5700–5703. doi:10.1021/acs.orglett.6b02865
19. Niijima, E.; Imai, T.; Suzuki, H.; Fujimoto, Y.; Kitagawa, O. *J. Org. Chem.* **2021,** *86,* 709–715. doi:10.1021/acs.joc.0c02319
20. Imai, T.; Niijima, E.; Terada, S.; Wzorek, A.; Soloshonok, V. A.; Hori, A.; Kitagawa, O. *CrystEngComm* **2019,** *21,* 3385–3389. doi:10.1039/c9ce00320g
21. Matsui, R.; Niijima, E.; Imai, T.; Kobayashi, H.; Hori, A.; Sato, A.; Nakamura, Y.; Kitagawa, O. *Molecules* **2022,** *27,* 2369. doi:10.3390/molecules27072369
22. Parisini, E.; Metrangolo, P.; Pilati, T.; Resnati, G.; Terraneo, G. *Chem. Soc. Rev.* **2011,** *40,* 2267–2278. doi:10.1039/c0cs00177e
23. Gilday, L. C.; Robinson, S. W.; Barendt, T. A.; Langton, M. J.; Mullaney, B. R.; Beer, P. D. *Chem. Rev.* **2015,** *115,* 7118–7195. doi:10.1021/cr500674c
24. Cavallo, G.; Metrangolo, P.; Milani, R.; Pilati, T.; Priimagi, A.; Resnati, G.; Terraneo, G. *Chem. Rev.* **2016,** *116,* 2478–2601. doi:10.1021/acs.chemrev.5b00484
25. Bulfield, D.; Huber, S. M. *Chem. – Eur. J.* **2016,** *22,* 14434–14450. doi:10.1002/chem.201601844
26. Mendez, L.; Henriquez, G.; Sirimulla, S.; Narayan, M. *Molecules* **2017,** *22,* 1397–1412. doi:10.3390/molecules22091397
27. Lim, J. Y. C.; Marques, I.; Félix, V.; Beer, P. D. *J. Am. Chem. Soc.* **2017,** *139,* 12228–12239. doi:10.1021/jacs.7b06144
28. Kuwano, S.; Suzuki, T.; Hosaka, Y.; Arai, T. *Chem. Commun.* **2018,** *54,* 3847–3850. doi:10.1039/c8cc00865e
29. Kikkawa, S.; Okayasu, M.; Hikawa, H.; Azumaya, I. *Cryst. Growth Des.* **2021,** *21,* 1148–1158. doi:10.1021/acs.cgd.0c01469
30. Kikkawa, S.; Takeno, M.; Nakayama, T.; Koike, D.; Saito, Y.; Tashiro, M.; Aoyama, Y.; Hikawa, H.; Azumaya, I. *Cryst. Growth Des.* **2024,** *24,* 9564–9570. doi:10.1021/acs.cgd.4c01092
31. Arunachalampillai, A.; Chandrappa, P.; Cherney, A.; Crockett, R.; Doerfler, J.; Johnson, G.; Kommuri, V. C.; Kyad, A.; McManus, J.; Murray, J.; Myren, T.; Fine Nathel, N.; Ndukwe, I.; Ortiz, A.; Reed, M.; Rui, H.; Silva Elipe, M. V.; Tedrow, J.; Wells, S.; Yacoob, S.; Yamamoto, K. *Org. Lett.* **2023,** *25,* 5856–5861. doi:10.1021/acs.orglett.3c02117
32. Wu, L.; Zhou, H.; Sun, L.; Cui, J.; Liu, W.; Wang, Y.; Xie, L. *Russ. J. Org. Chem.* **2024,** *60,* 459–466. doi:10.1134/s1070428024030138
33. ***rac*-1a**: $C_{15}H_{10}BrNO$, CCDC2448893. ***rac*-1b**: $C_{15}H_{10}ClNO$, CCDC2448885.
34. **(*P*)-1a**: $C_{15}H_{10}BrNO$, CCDC2448886. **(*P*)-1b**: $C_{15}H_{10}ClNO$, CCDC2448887.
35. Lu, Y.; Wang, Y.; Zhu, W. *Phys. Chem. Chem. Phys.* **2010,** *12,* 4543–4551. doi:10.1039/b926326h
36. Xu, Z.; Yang, Z.; Liu, Y.; Lu, Y.; Chen, K.; Zhu, W. *J. Chem. Inf. Model.* **2014,** *54,* 69–78. doi:10.1021/ci400539q
37. ***rac*-2a**: $C_{15}H_{10}BrNS$, CCDC 2448888.

License and Terms

The definitive version of this article is the electronic one which can be found at:
https://doi.org/10.3762/bjoc.21.138

BEILSTEIN JOURNAL OF ORGANIC CHEMISTRY

Chiral phosphoric acid-catalyzed asymmetric synthesis of helically chiral, planarly chiral and inherently chiral molecules

Wei Liu*[1] and Xiaoyu Yang*[2]

Review

Address:
[1]Key Laboratory of Subcritical High-Efficiency Extraction, College of Chemistry and Environmental Engineering, Anyang Institute of Technology, Anyang, Henan 455000, China and [2]School of Physical Science and Technology, ShanghaiTech University, Shanghai 201210, China

Email:
Wei Liu* - liuwei@shanghaitech.edu.cn; Xiaoyu Yang* - yangxy1@shanghaitech.edu.cn

* Corresponding author

Keywords:
asymmetric catalysis; chiral phosphoric acid; helical chirality; inherent chirality; planar chirality

Beilstein J. Org. Chem. **2025,** *21,* 1864–1889.
https://doi.org/10.3762/bjoc.21.145

Received: 03 June 2025
Accepted: 26 August 2025
Published: 10 September 2025

This article is part of the thematic issue "Non-central chirality in organic chemistry".

Associate Editor: N. Yoshikai

Abstract

Chiral molecules, distinguished by nonsuperimposability with their mirror image, play crucial roles across diverse research fields. Molecular chirality is conventionally categorized into the following types: central chirality, axial chirality, planar chirality and helical chirality, along with the more recently introduced inherent chirality. As one of the most prominent chiral organocatalysts, chiral phosphoric acid (CPA) catalysis has proven highly effective in synthesizing centrally and axially chiral molecules. However, its potential in the asymmetric construction of other types of molecular chirality has been investigated comparatively less. This Review provides a comprehensive overview of the recent emerging advancements in asymmetric synthesis of planarly chiral, helically chiral and inherently chiral molecules using CPA catalysis, while offering insights into future developments within this domain.

Introduction

Since the seminal works by Akiyama [1] and Terada [2] et al. in 2004 demonstrated the application of BINOL-derived chiral phosphoric acids (CPAs) in asymmetric Mannich reactions, the past two decades have witnessed the remarkable evolution of CPA catalysis into one of the most versatile platforms for achieving diverse enantioselective transformations [3-8]. CPA catalysts are generally recognized as bifunctional catalysts with two distinct catalytic sites. The OH group on the phosphorus atom functions as a Brønsted acid site, while P=O serves as a Lewis base site, which enables the simultaneous activation of both nucleophiles and electrophiles in one reaction (Figure 1). The chiral properties of the catalysts are derived from the chiral framework of the diol precursors, predominantly axially chiral structures such as BINOL, H_8-BINOL, SPINOL and VAPOL scaffolds, which are widely used in the development of CPA catalysts. Furthermore, the *ortho*-aryl substitutions of the CPA

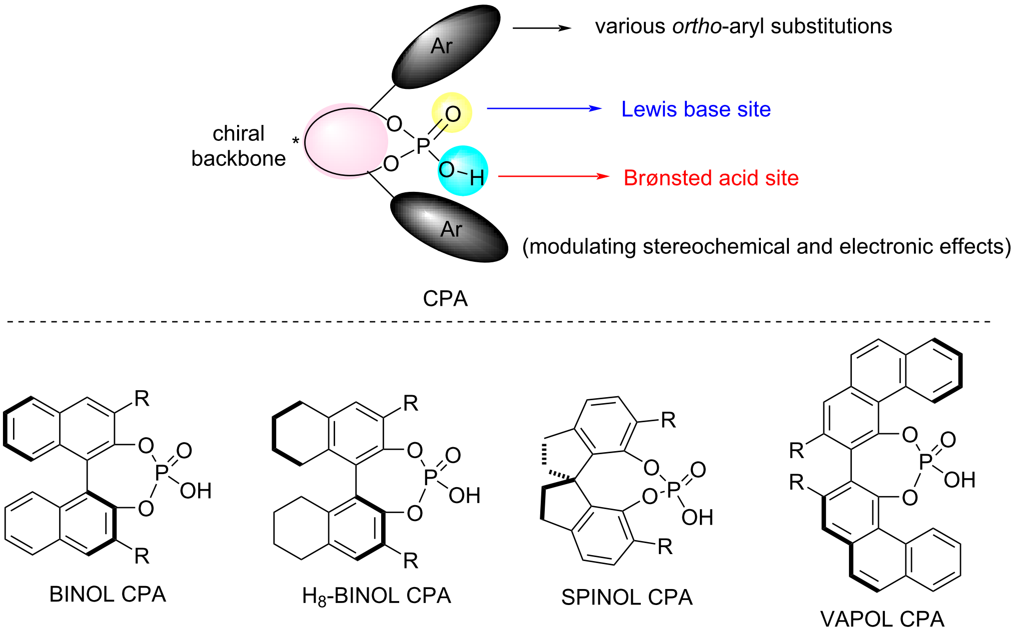

Figure 1: General structure of CPAs and selected CPAs with various chiral scaffolds.

catalyst can efficiently modulate the stereochemical and electronic effects of the CPAs, which establish a chiral microenvironment within the chiral scaffold that governs the stereoselectivity of asymmetric reactions.

Chiral molecules, characterized as three-dimensional structures that are nonsuperimposable with their mirror image, have significant applications in pharmaceutical, agrochemical and asymmetric synthesis as well as materials science, to name a few examples. Molecular chirality is typically classified into four types of chiral elements: central (point) chirality, axial chirality, planar chirality and helical chirality (Figure 2). Moreover, unique forms of chirality originating from the rigid conformation of molecules lacking symmetry, which do not fit into the aforementioned four categories, are termed inherent chirality. Notable examples include inherently chiral calix[4]arenes and saddle-shaped medium-sized cyclic compounds. Catalytic asymmetric synthesis has been recognized as the most straightforward and efficient strategy for synthesizing chiral molecules, with early development primarily targeting compounds featuring stereogenic centers. In the past decade, significant progress has been made in the asymmetric synthesis of diverse axially chiral molecules [9]. However, the exploration of catalytic asymmetric synthesis toward other forms of chiral elements has been relatively limited, with only a few notable instances having emerged recently.

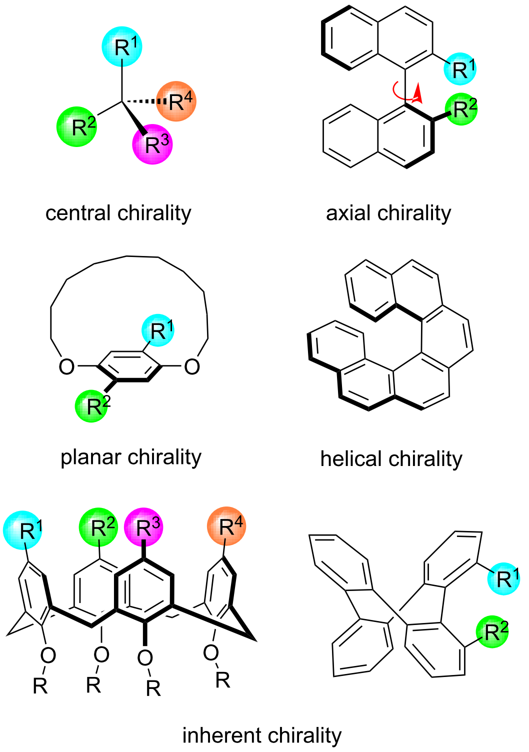

Figure 2: Representative elements of molecular chirality.

Similarly, since the initial introduction of CPA catalysts in asymmetric synthesis in 2004, a plethora of asymmetric catalytic reactions to synthesize chiral molecules with stereogenic centers has been developed. Moreover, the rapid advancement of axially chiral molecules in asymmetric synthesis has been made possible by employing CPA catalysis, notably pioneered by Akiyama [10], Tan [11] and others. However, the application of CPA catalysis in the asymmetric synthesis of other forms of molecular chirality has received less attention. While List and co-workers reported the first CPA-catalyzed asymmetric synthesis of helically chiral azahelicenes through the Fischer indole synthesis back in 2014 [12], the second CPA-catalyzed asymmetric synthesis of helicenes was not achieved until 2023 [13,14]. Similarly, the CPA-catalyzed asymmetric synthesis of planarly chiral [15] and inherently chiral [16] molecules was not disclosed until 2022. In this Review, we have comprehensively summarized the recent advancements in the CPA-catalyzed asymmetric synthesis of various distinct chiral elements, encompassing helically, planarly and inherently chiral molecules. The Review is structured based on the various types of chiral elements, presenting a representative substrate scope for each method, showcasing the reaction mechanisms and applications of the chiral products for selected examples.

Review

Helical chirality

Helicenes are a group of rigid polycyclic aromatic compounds composed of *ortho*-fused aromatic (hetero)cyclic rings, with their helically twisted conformation enforced by steric hindrance between terminal aromatic rings [17]. Despite lacking asymmetric stereogenic centers, this nonplanar scaffold exhibits intrinsic *P*/*M* chirality due to the helical arrangement of the π-extended skeleton. Renowned for their high thermal stability and structural rigidity, chiral helicenes have emerged as prominent molecular platforms in various applications, such as circularly polarized luminescence (CPL) materials, chiral liquid crystals and asymmetric catalysis. Currently, the asymmetric catalytic synthesis of helicenes predominantly revolves around transition metal-catalyzed asymmetric annulation reactions, including the asymmetric [2 + 2 + 2] cycloaddition of aryl-substituted polyynes and hydroarylation of alkynes [18,19]. In contrast, the application of asymmetric organocatalysis for enantioselective synthesis of chiral helicenes remains relatively underdeveloped compared to transition metal-catalyzed approaches [20].

In 2014, List and co-workers reported the pioneering CPA-catalyzed asymmetric synthesis of helically chiral molecules, which also marked the first organocatalyzed asymmetric synthesis of such compounds [12]. By employing a CPA-catalyzed asymmetric Fischer indolization reaction of hydrazine **1** and polycyclic ketone **2**, they achieved the efficient asymmetric synthesis of various helically chiral azahelicenes **3** (Scheme 1). To address the inherent length-scale challenges of molecular helicene frameworks, the authors designed and synthesized novel CPAs bearing extended π-substituents at the *ortho*-positions. The dual hydrogen-bonding interactions were critical for this reaction, ensuring that the reaction proceeded within the chiral pocket of the CPA catalyst. Moreover, the authors proposed that the extended π-substituents at the *ortho*-positions of CPA could engage in π–π-stacking interactions with the enehydrazine intermediate, which is essential for achieving high levels of stereocontrol. Using the optimal catalyst **CPA 1**, a series of aza[6]helicenes **3a**,**b** was synthesized with excellent enantioselectivity and high yield. However, this method demonstrated notably reduced efficiency and stereoselectivity for the more sterically demanding aza[5]helicene **3c** and aza[7]helicenes **3d–f**. Furthermore, the authors expanded this methodology to a double Fischer indolization reaction between hydrazine **1i** and ketone **2i**, which yielded diaza[8]helicene **4** with moderate yield and high enantioselectivity after chloranil-mediated dehydrogenation.

Despite the early demonstration of CPA catalysis in synthesizing chiral helicenes, the next instance of CPA-catalyzed asymmetric synthesis of helicenes was not achieved until 2023. Employing a sequential CPA-catalyzed asymmetric Povarov reaction and oxidative aromatization process, in 2023 our group reported the asymmetric synthesis of various azahelicenes **8** from polycyclic arylamines **5**, dienamides **6** and aldehydes **7** (Scheme 2) [13]. This methodology demonstrates a broad substrate scope, enabling the efficient asymmetric synthesis of diverse aza[5]helicenes **8a–d** and aza[4]helicene **8e** from various aldehydes with high enantioselectivity. In addition, dienamides were found to be compatible with this method, albeit requiring a switch to **CPA 3** as the optimal catalyst, which generated the 1-enamide-substituted azahelicenes **8f**,**g**, with significant potential for diverse derivatizations. Based on experimental and computational studies, the origin of helical chirality in this method was elucidated. We proposed that the asymmetric Povarov reaction would generate a pair of diastereomeric tetrahydroquinoline derivatives displaying helical conformation, with a modest energetic barrier for interconversion. However, steric repulsion between the C-1 substitutions and the terminal arene moieties in the *M*-conformational diastereomer resulted in the *P*-conformational diastereomer being thermodynamically favored. This led to the formation of (*P*)-helicene products following DDQ-mediated dehydrogenation.

Almost simultaneously, the Li group independently reported the asymmetric synthesis of chiral quinohelicenes using a similar sequential asymmetric Povarov reaction and oxidative aromatization strategy [14]. In their study, they employed 3-vinylindoles **10** in the CPA-catalyzed asymmetric Povarov reaction with polycyclic arylamines **9** and various aromatic aldehydes **11**, resulting in a range of quinoline-containing azahelicenes **12** with moderate yield and excellent enantioselectivity after DDQ-mediated oxidative aromatization (Scheme 3). Notably, they not

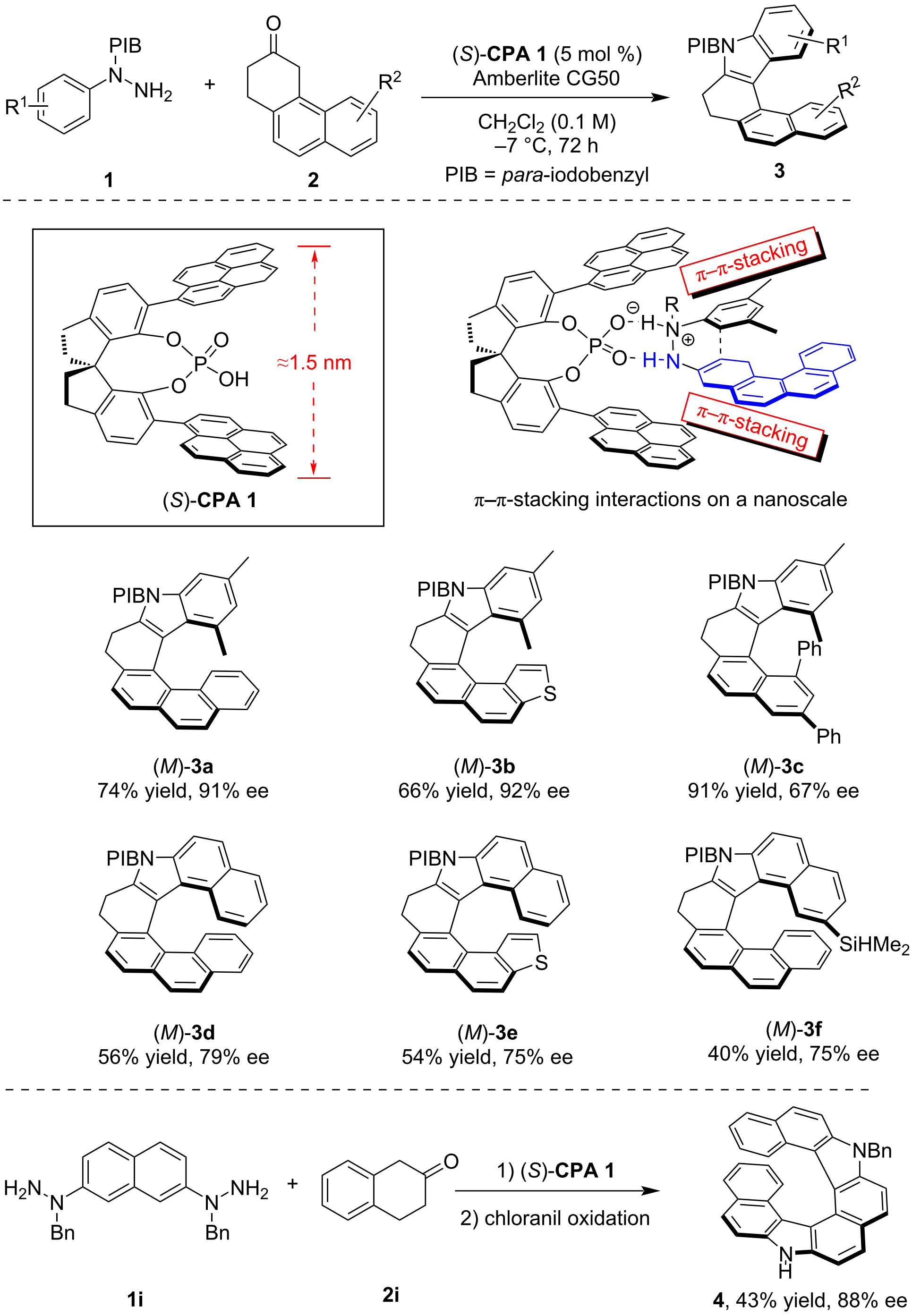

Scheme 1: CPA-catalyzed asymmetric synthesis of azahelicenes via Fischer indole synthesis.

only expanded the substrate scope to encompass various aldehydes and 3-vinylindoles but also conducted extensive structural modifications on the polycyclic arylamine components, which enabled the asymmetric synthesis of azahelicenes with diverse frameworks, including the chromene- and furan-containing quinohelicenes **12d**,**e**, respectively. They also conducted a thorough evaluation of the stability of the helical chirality across the synthesized quinohelicenes, indicating a high racemization barrier.

In 2024, our group further extended the CPA-catalyzed sequential Povarov reaction and aromatization strategy by using

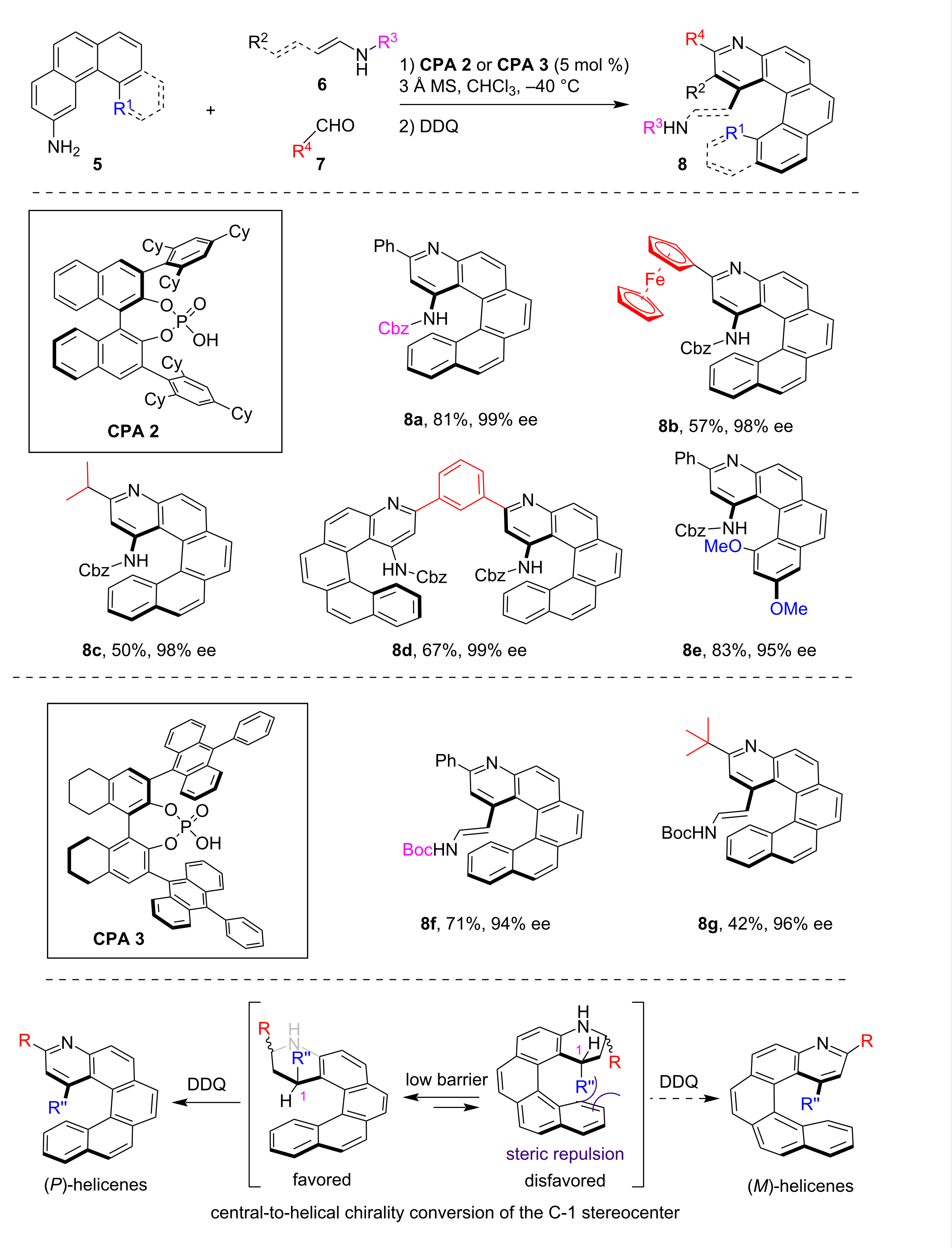

Scheme 2: CPA-catalyzed asymmetric synthesis of azahelicenes via sequential Povarov reaction and oxidative aromatization.

2-vinylphenols **14** as the olefin component, which facilitated the asymmetric synthesis of substituted [5]- and [6]pyridohelicenes **15** with *ortho*-phenolic substituents in position C1 with high enantioselectivity (Scheme 4) [21]. Notably, utilizing one equivalent of DDQ for semioxidation of the tetrahydroquinoline product of the Povarov reaction produced the imine **16a** which, upon

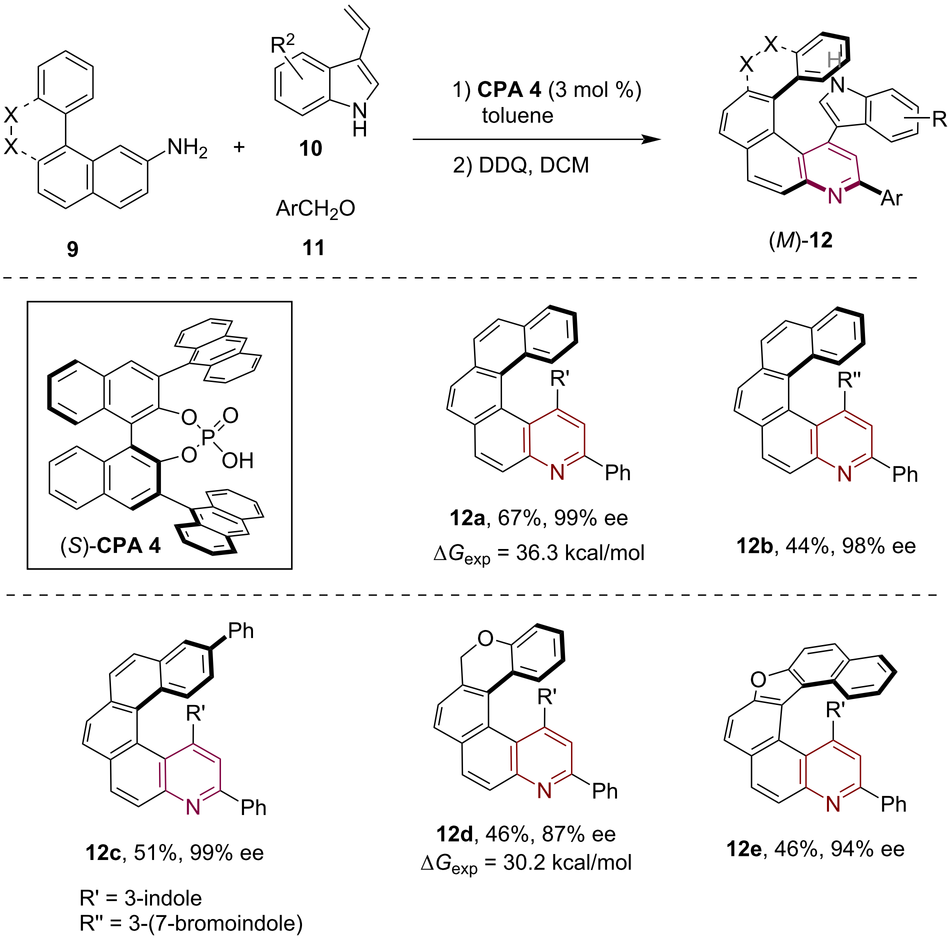

Scheme 3: CPA-catalyzed asymmetric synthesis of azahelicenes via sequential Povarov reaction involving 3-vinylindoles and oxidative aromatization.

treatment with $Pd(PPh_3)_2Cl_2$ and KHMDS, led to furan ring formation and the generation of hetero[7]helicene **17a** while maintaining the stereochemical configuration. Through this methodology, a range of elongated [7]- and [8]heterohelicenes **17b–d** incorporating both furan and pyridine moieties were successfully synthesized with high enantioselectivity. These compounds would be challenging to access using alternative asymmetric methods.

In 2025, our group disclosed a highly efficient catalytic enantioselective double annulation approach for the asymmetric synthesis of hetero[7]helicenes [22]. By employing a sequential CPA-catalyzed three-component double Povarov reaction involving a pentacyclic diamine substrate **18**, enamide **6a** and various aldehydes **7**, followed by oxidative aromatization, a range of bispyridine-containing hetero[7]helicenes was produced with good yield and excellent enantioselectivity (Scheme 5). Notably, two distinct oxidative aromatization methods have been developed to yield diverse heterohelicene products. For instance, using DDQ as an oxidant selectively delivered hetero[7]helicenes **19** with monoamido substitution at the *peri*-positions, while utilizing MnO_2 as an oxidant selectively yielded heterohelicenes **20** with bisamido substitution at the *peri*-positions.

In 2024, Zhou, Chen and co-workers disclosed an efficient method for the asymmetric synthesis of indolohelicenoids through a sequential enantioselective annulation, followed by an eliminative aromatization sequence [23]. The CPA-catalyzed asymmetric [3 + 2]-cycloaddition of cycloenecarbamates **21** and carbalkoxy-substituted azonaphthalenes **22** produced the hexacyclic products **23'** with two contiguous stereogenic centers, which then underwent an eliminative aromatization process to yield various indolohelicenoids **23** with excellent enantioselectivity (Scheme 6). The helical chirality of the products **23** was believed to stem from a notably stereospecific central-to-helical chirality conversion process, maintaining high enantioselectivity even when the eliminative aromatization occurred without

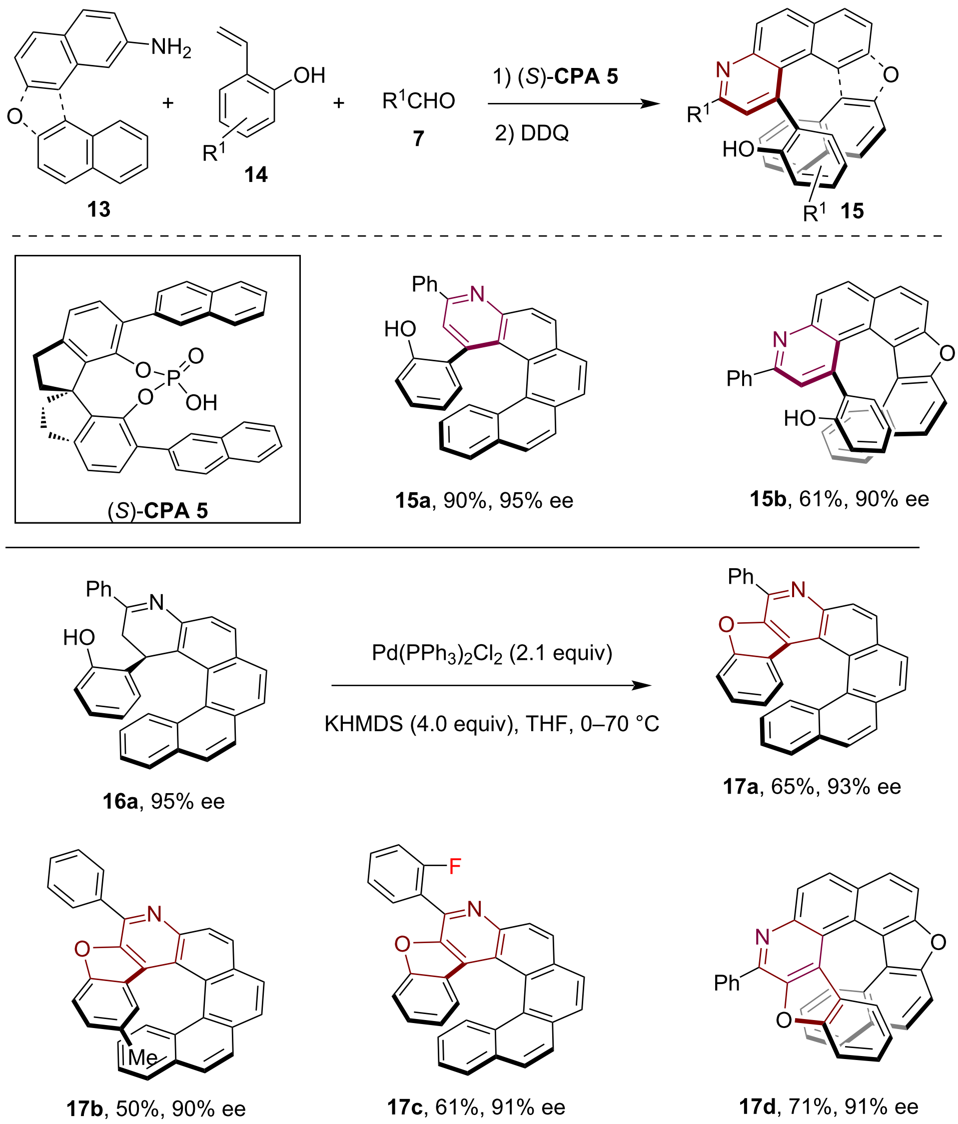

Scheme 4: CPA-catalyzed asymmetric synthesis of heterohelicenes via sequential Povarov reaction involving 2-vinylphenols and aromatization.

the CPA catalyst. Notably, indolohelicenoid **23e** could effectively be converted into the fully aromatic indolohelicene **24e** under DDQ-mediated oxidative conditions without compromising the enantiopurity of the compound.

Kinetic resolution stands as one of the most practical and efficient strategies for accessing chiral compounds. Starting from racemic starting materials, this method entails selective conversion of one enantiomer facilitated by a chiral catalyst, yielding enantioenriched products and allowing for the recovery of unreacted substrate with a high level of enantiopurity [24,25]. While CPAs have been extensively utilized in kinetic resolution of centrally chiral [26-28] and axially chiral compounds [29], their application in the kinetic resolution of helically chiral compounds remains largely unexplored.

In 2024, Liu and co-workers developed an effective method for catalytic kinetic resolution of racemic helical polycyclic phenols through an organocatalyzed enantioselective dearomative amination reaction [30]. The racemic polycyclic phenol derivatives **25**, which exist as single diastereomers featuring both central chirality and helical chirality, were readily prepared through a [3 + 3]-cycloaddition reaction. By employing the CPA-catalyzed asymmetric electrophilic amination reaction with azodicarboxylate on the phenol moiety, efficient kinetic resolution of **25** proceeded to yield both the amination products **26** and the recovered starting material with high enantioselectivity, with an s-factor up to >259 (Scheme 7). Notably, this reaction did not produce the typical arene C–H amination products but instead the dearomative amination products **26**, which is believed to be due to the significant steric hindrance surround-

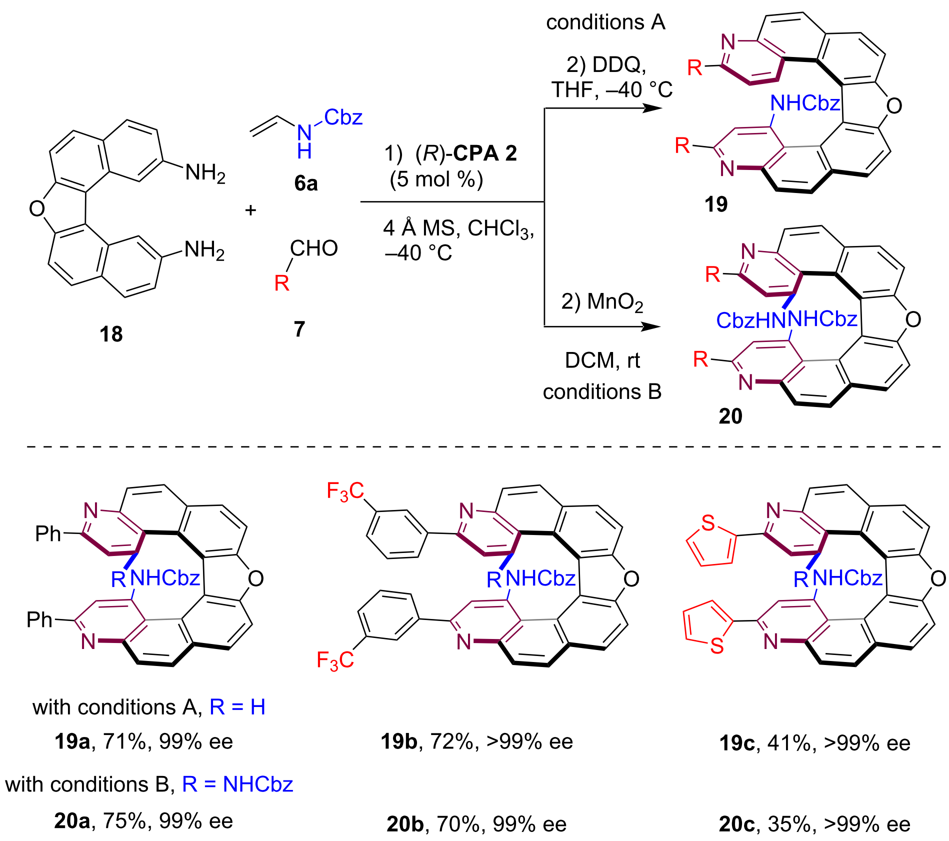

Scheme 5: Diverse enantioselective synthesis of hetero[7]helicenes via a CPA-catalyzed double annulation strategy.

ing the amination site that impeded the subsequent aromatization process. Moreover, the terminal ring of the polycyclic phenol substrates was not limited to a pyranoid moiety as helical polycyclic phenols incorporating a furan ring also efficiently yielded both the dearomatized amination product (*P*,*R*,*R*)**-28a** and the recovered enantioenriched phenolic compound (*M*,*R*)**-27a** with high enantioselectivity.

In 2025, Cai, Ji and co-workers reported a practical approach for the kinetic resolution of racemic aza[6]helicenes through CPA-catalyzed asymmetric transfer hydrogenation [31]. Commencing with the readily available racemic pyrido[6]helicene **29**, the CPA-catalyzed asymmetric transfer hydrogenation employing Hantzsch ester **HEH-1** as the reductant afforded both helically chiral tetrahydroquinoline derivatives (*M*)-**30** and the recovered aza[6]helicene starting material (*P*)-**29** with good to high enantioselectivity, achieving an s-factor of up to 121 (Scheme 8). Moreover, by leveraging the synthesized enantioenriched aza[6]helicene **29a** and tetrahydro[6]helicene **30a** as chiral building blocks, a series of helically chiral organocatalysts and ligands could be easily prepared, such as the helically chiral pyridine *N*-oxide **31a** and helically chiral monophosphine ligands **31b**,**c**, whose potential applications in catalytic asymmetric reactions have also been showcased.

Planar chirality

Planarly chiral cyclophanes, a unique class of macrocyclic compounds featuring planar chirality, can be found in various natural products and are widely utilized in asymmetric catalysis, host–guest chemistry and materials science [32]. These macrocycles typically consist of a substituted aromatic ring and a macrocyclic side chain (*ansa* chain), with the planar chirality arising from the restricted flipping of the substituted aromatic ring caused by steric constraints imposed by the *ansa* chain. Recent advances in asymmetric catalytic synthesis of planarly chiral macrocycles have attracted significant attention, leading to the development of several distinctive strategies, such as (dynamic) kinetic resolution and asymmetric macrocyclizations [33-36].

In 2022, our group reported the enantioselective synthesis of planarly chiral macrocycles through a dynamic kinetic resolution approach [15]. Despite bearing an amino group on the phenyl ring, the configuration of the macrocyclic paracyclophane **32** was found to be unstable at room temperature. Conse-

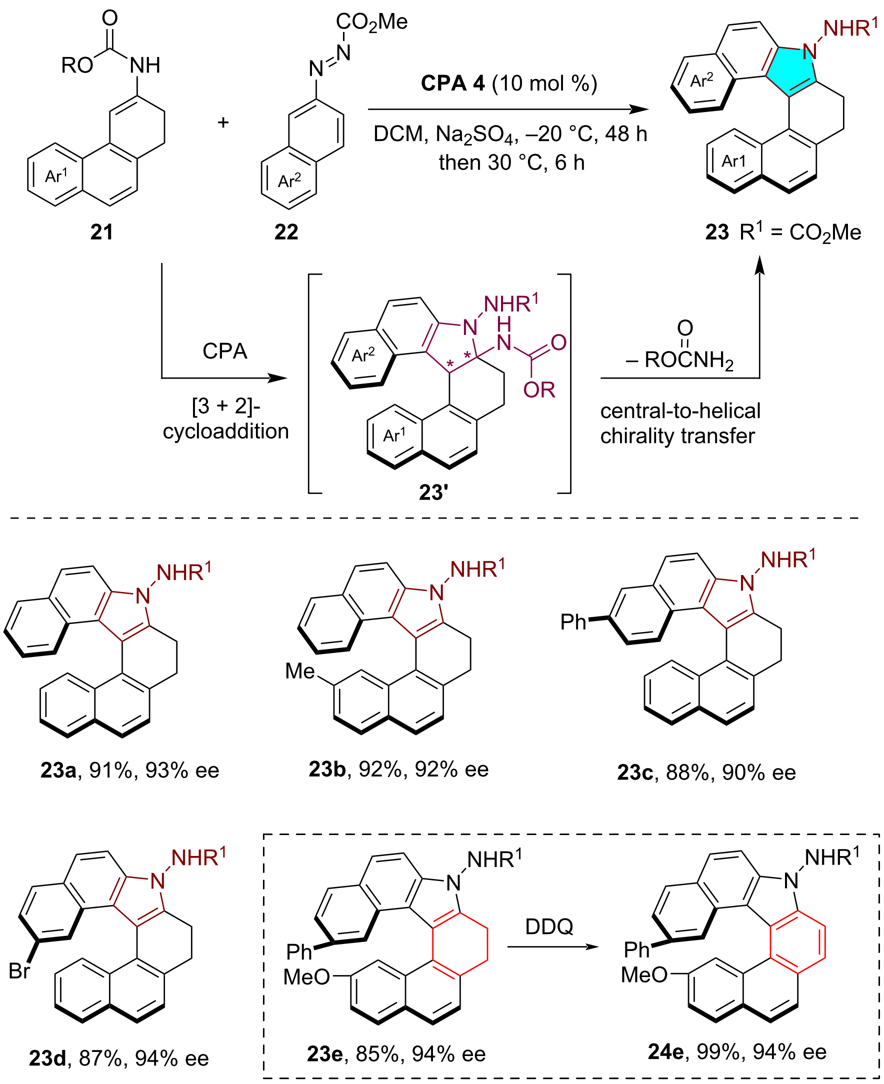

Scheme 6: CPA-catalyzed asymmetric synthesis of indolohelicenoids through enantioselective cycloaddition and eliminative aromatization sequence.

quently, by employing a CPA-catalyzed asymmetric electrophilic amination reaction of the aniline moiety with azodicarboxylates [37,38], the introduction of a bulky hydrazine group restricted the free flipping of the benzene ring, leading to the formation of planar chiral macrocycle **33** with high enantioselectivity (Scheme 9). Substrate scope studies demonstrated the successful construction of planarly chiral macrocycles with 12- to 14-membered *ansa* chains with high enantioselectivity when using NH_2 as the directing group (see **33a**,**b**). However, extending the *ansa* chain to 15 members led to the loss of planar chirality due to insufficient steric hindrance to restrict the benzene ring flipping (see **33c**). Notably, the use of a bulkier NHBn directing group allowed for the extension of the *ansa* chain to 15–19 members (see **33d**,**e**), while preserving planar chirality and functional group compatibility. Remarkably, the chiral paracyclophane product **33a** could be directly used as a planarly chiral primary amine catalyst in the asymmetric electrophilic amination reaction of aldehyde **34**, which yielded the α-amination product **35** with high enantioselectivity.

In 2022, our group disclosed an enantioselective macrocyclization protocol for the asymmetric synthesis of planarly chiral paracyclophanes [39]. Commenced with a macrocyclization precursor **36** featuring both a hydroxy group and an allenamide moiety, the CPA-catalyzed asymmetric intramolecular addition led to the successful construction of planarly chiral macrocycles **37** (Scheme 10). This method demonstrated broad substrate compatibility, accommodating sterically demanding dibromo and various dialkynyl substitutions on the phenyl ring. A series of planarly chiral macrocycles with *ansa* chains

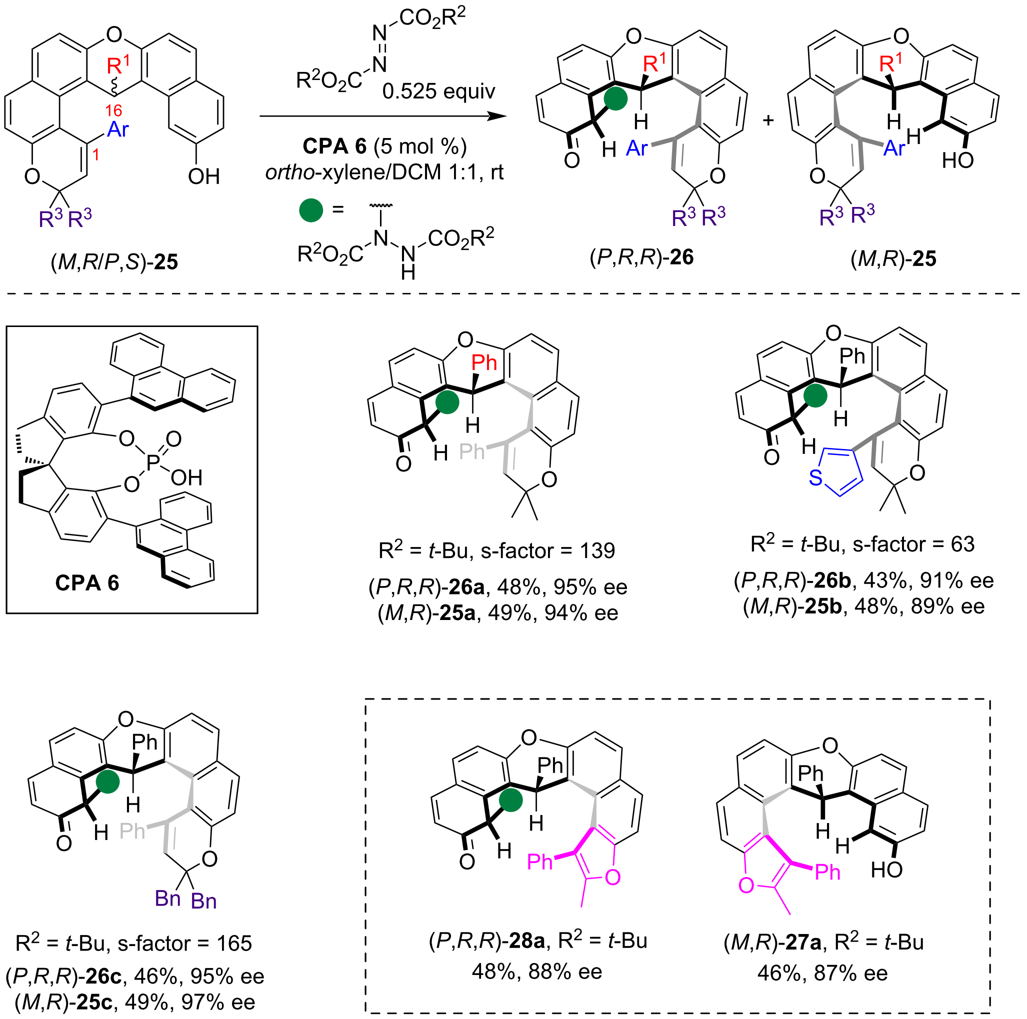

Scheme 7: Kinetic resolution of helical polycyclic phenols via CPA-catalyzed enantioselective aminative dearomatization reaction.

ranging from 15 to 18 members was synthesized with good to high enantioselectivity, albeit with moderate yield. Significantly, thermal stability studies demonstrated high configurational stability of these planarly chiral macrocycles, a critical feature that enhances their potential for future utility.

In 2023, Zhao and co-worker reported the asymmetric synthesis of planarly chiral paracyclophanes through either catalytic kinetic resolution or dynamic kinetic resolution [40]. The authors designed and synthesized a series of benzaldehyde-containing macrocyclic cyclophanes **38**. Therein, they achieved the construction of planar chirality through CPA-catalyzed asymmetric reductive amination with arylamines using Hantzsch ester **HEH-2** as the hydrogen transfer reagent (Scheme 11). Notably, when starting from macrocyclic substrates featuring relatively shorter *ansa* chains (11–14 members, see **38a–c**), highly efficient kinetic resolution was achieved, resulting in both recovered (R_p)-**38** and reductive amination products (S_p)-**39** with high enantioselectivity. Conversely, employing macrocyclic paracyclophane with longer *ansa* chains (≥15 members) enabled efficient dynamic kinetic resolution due to the instable planar chirality of the substrates, which produced the planarly chiral macrocycles with high yield and enantioselectivity (up to 98% yield and 99% ee).

In 2025, Li and co-workers utilized analogous racemic benzaldehyde-containing paracyclophanes as substrates and accomplished their efficient kinetic resolution through catalytic asymmetric allylation [41]. Employing CPA/$Bi(OAc)_3$ as a combined catalyst, the asymmetric allylation of racemic **40** with allylboronic acid pinacol ester (**41**) led to efficient kinetic resolution, yielding the recovery of (S_p)-**40** with high enantiopurity (Scheme 12). Notably, the allylation products **42**, possessing both planar chirality and central chirality, were produced with

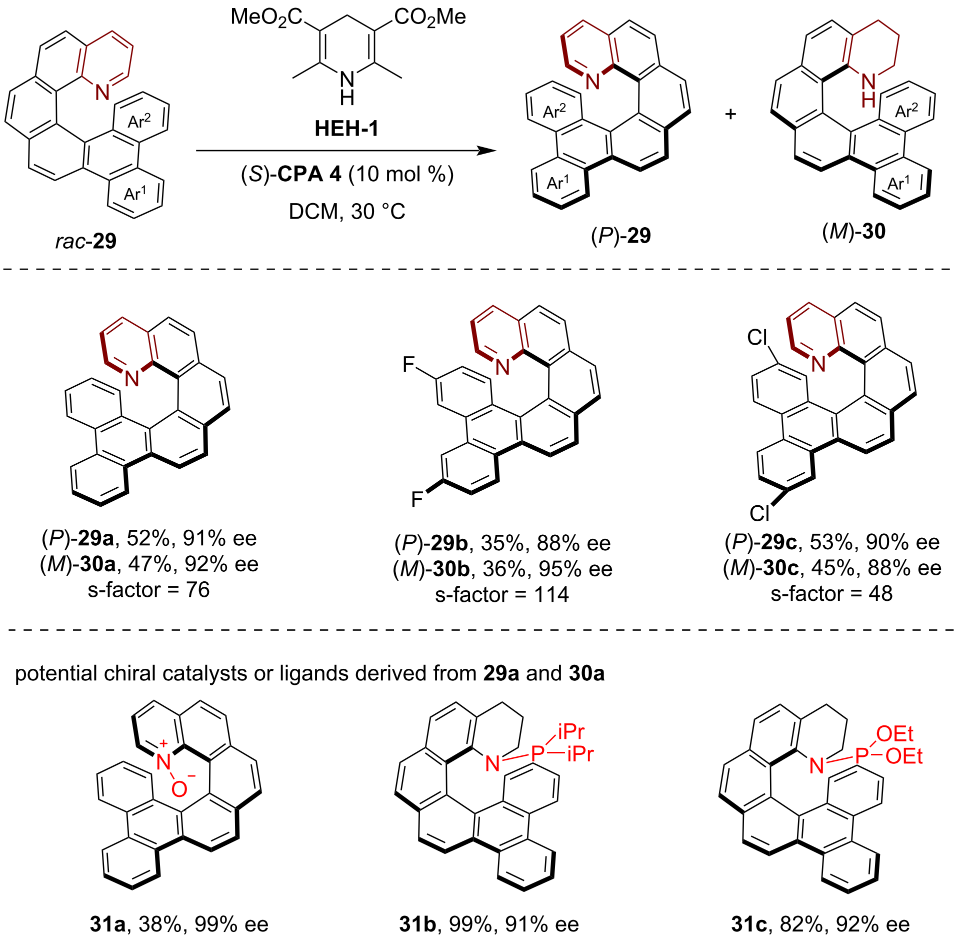

Scheme 8: Kinetic resolution of azahelicenes via CPA-catalyzed transfer hydrogenation.

high enantioselectivity and diastereoselectivity. Previously, they have been challenging to access in an asymmetric one-step reaction. A range of paracyclophanes with diverse substitutions, including aryl, heteroaryl, alkynyl and bromo substitutions, along with a varying length of the *ansa* chain, were found to be amenable to this method, resulting in kinetic resolution with an exceptional performance.

In 2025, Zhou and co-workers disclosed the asymmetric synthesis of planarly chiral macrocycles via CPA-catalyzed atroposelective macrocyclization [42]. The authors devised and prepared a series of indole-based hydroxy-substituted carboxylic acid substrates **43** which, upon treatment with ynamide **44**, yielded the vinyl acetate intermediate **INT-A** (Scheme 13). Subsequently, the one-pot CPA-catalyzed intramolecular esterification of this intermediate afforded the planarly chiral macrocycles **45** with good yield and high enantioselectivity. Investigations of the substrate scope revealed the compatibility of the method with various substitutions on the indole moiety and modifications to the length of the *ansa* chain, which produced planarly chiral macrocycles with up to 99% ee. In addition, this method was successfully employed for the catalytic asymmetric synthesis of planarly chiral macrocyclic paracyclophane **47** from the corresponding hydroxy-substituted carboxylic acid substrate **46**. Notably, the authors also demonstrated the application of this method in the enantioselective synthesis of axially chiral C–N and N–N atropisomers, highlighting the versatility of this method in the asymmetric synthesis of diverse chiral molecular structures.

Substituted [2.2]paracyclophanes represent another class of conformationally rigid, planarly chiral molecules, which have emerged as versatile scaffolds for developing chiral catalysts, ligands and functional materials. In 2023, our group reported the first catalytic kinetic resolution of racemic amido[2.2]paracyclophanes through a CPA-catalyzed asymmetric aromatic amination reaction [43]. Treating the racemic *N*-Boc-substituted [2.2]paracyclophane **48a** with dibenzyl azodicarboxylate

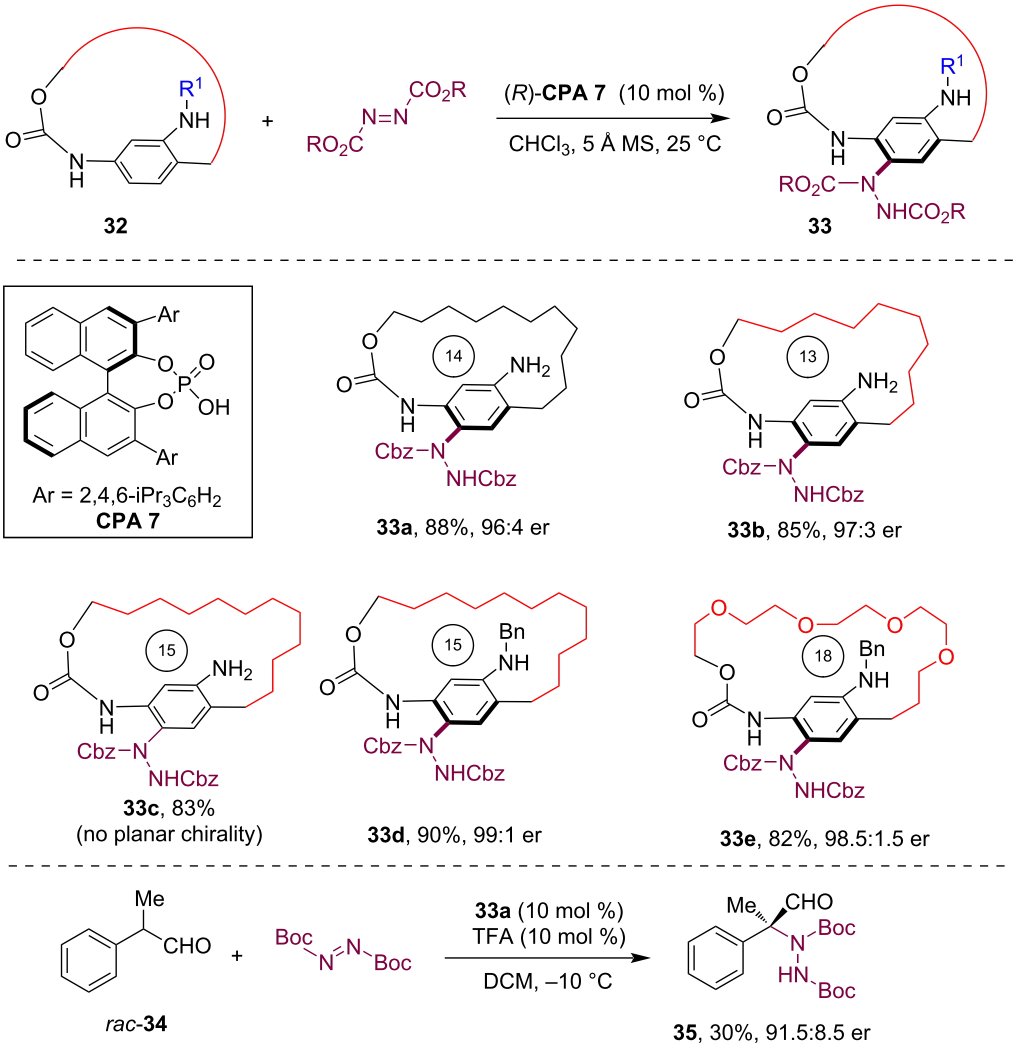

Scheme 9: Asymmetric synthesis of planarly chiral macrocycles via CPA-catalyzed electrophilic aromatic amination.

(0.7 equiv) in the presence of **CPA 6** (10 mol %) led to efficient kinetic resolution, yielding both the *para*-C–H amination product **49a** and the recovered starting material (R_p)-**48a** with high enantioselectivity (Scheme 14). Notably, subjecting **49a** to strongly basic conditions resulted in dehydrazidation to give (S_p)-**48a**, and thus enabling facile access to both amido[2.2]paracyclophane enantiomers. Moreover, this method demonstrated broad substrate generality, which enabled the efficient kinetic resolution of various disubstituted amido[2.2]paracyclophanes, including the pseudo-*geminal*- (see **48b**,**c**), pseudo-*ortho*- (see **48d**,**e**), pseudo-*meta*- (**48f**,**g**) and pseudo-*para*-substituted ones (see **48h**,**i**). Furthermore, this method could also be utilized for the enantioselective desymmetrization of achiral diamido-substituted [2.2]paracyclophane substrate **50**, delivering the C–H amination product **51** with excellent enantioselectivity (99% ee).

Inherent chirality

The concept of inherent chirality was first coined by Böhmer and co-workers in 1994 to describe the chirality originating from the asymmetric arrangement of achiral substituents within calixarene frameworks [44]. This term was later extended to encompass other conformationally rigid chiral molecules that do not fit into conventional categories of central, axial, planar or helical chirality, such as saddle-shaped, medium-sized cyclic compounds [45] and others [46]. These structurally distinct chiral molecules have received considerable research attention due to their broad range of potential applications in chiral recognition, sensing and asymmetric catalysis. However, achieving the catalytic asymmetric synthesis of these inherently chiral molecules remains highly challenging owing to their unique three-dimensional structures and relatively large size [47,48].

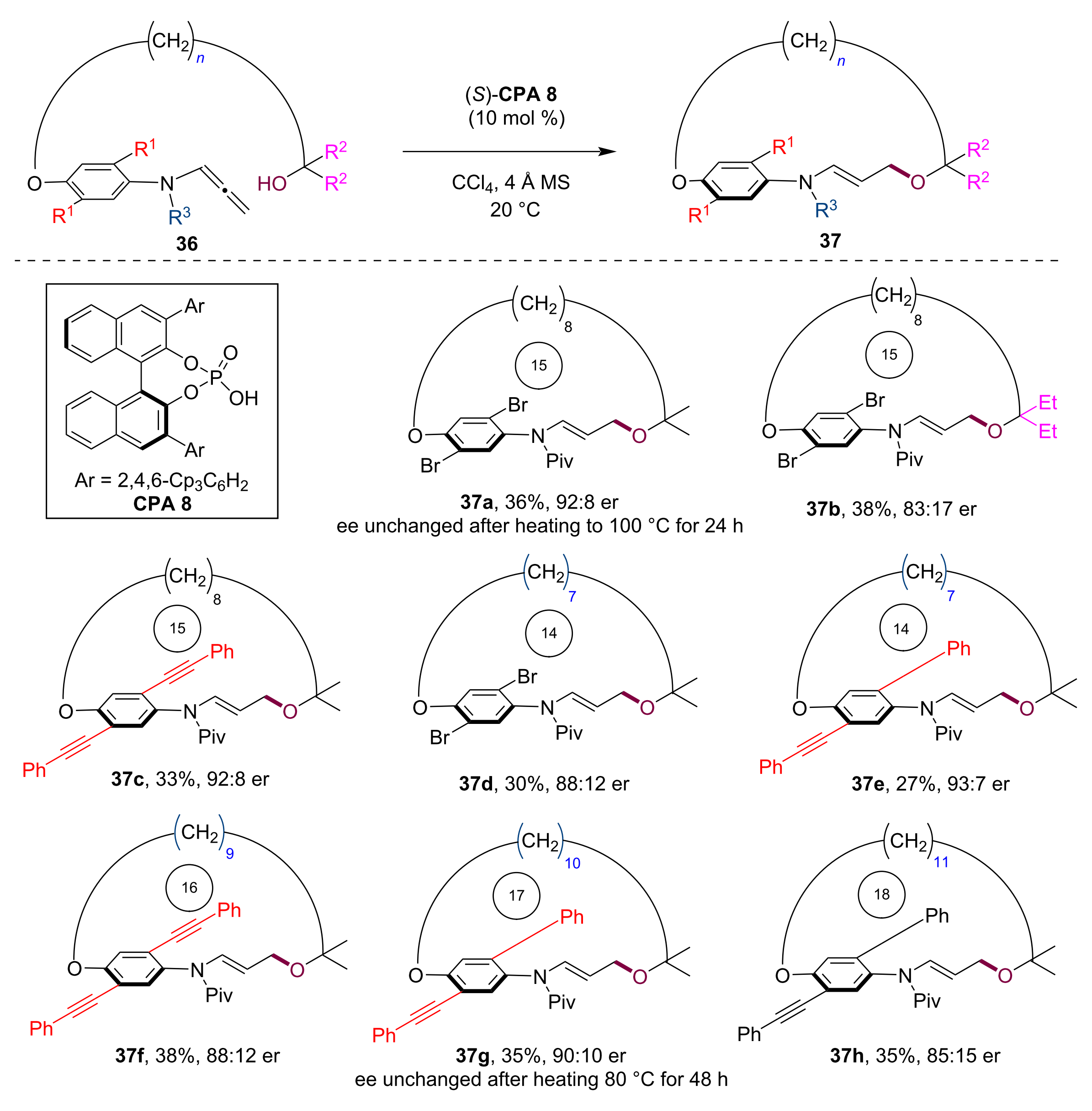

Scheme 10: Enantioselective synthesis of planarly chiral macrocycles via CPA-catalyzed macrocyclization.

In 2024, both our group [49] and the Liu group [50] independently reported the asymmetric synthesis of inherently chiral calix[4]arenes through an enantioselective desymmetrization strategy. Starting from the achiral aniline-containing calix[4]arenes **52**, we employed the **CPA 11**-catalyzed asymmetric Povarov reaction [51] with enamide **6a** and various aldehydes **7** to break the symmetry of substrates **52**, which was followed by a one-pot oxidative aromatization mediated by DDQ to yield the quinoline-containing inherently chiral calix[4]arenes **53** (Scheme 15). Notably, the prochiral calix[4]arenes bearing a disubstitution pattern on the 1,3-phenyl rings (see **53d**) or 1,3-diamino substitution (see **53e**) on the calix[4]arene scaffold were also amenable to this method, which yielded a series of structurally diverse novel quinoline-containing inherently chiral calix[4]arenes. Moreover, by using **CPA 4** as the optimal catalyst, the sequential asymmetric Povarov reaction of **52a** with dienamide **6b** and benzaldehyde **7a**, followed by oxidative aromatization, led to the formation of enamide-substituted, quinoline-containing inherently chiral calix[4]arene **54a**, whose enamide moiety could undergo diverse derivatizations. Analogously, the Liu group achieved the asymmetric synthesis of inherently chiral quinoline-containing calix[4]arenes **53** through the same approach, using (*S*)-**CPA 12** as the optimal catalyst.

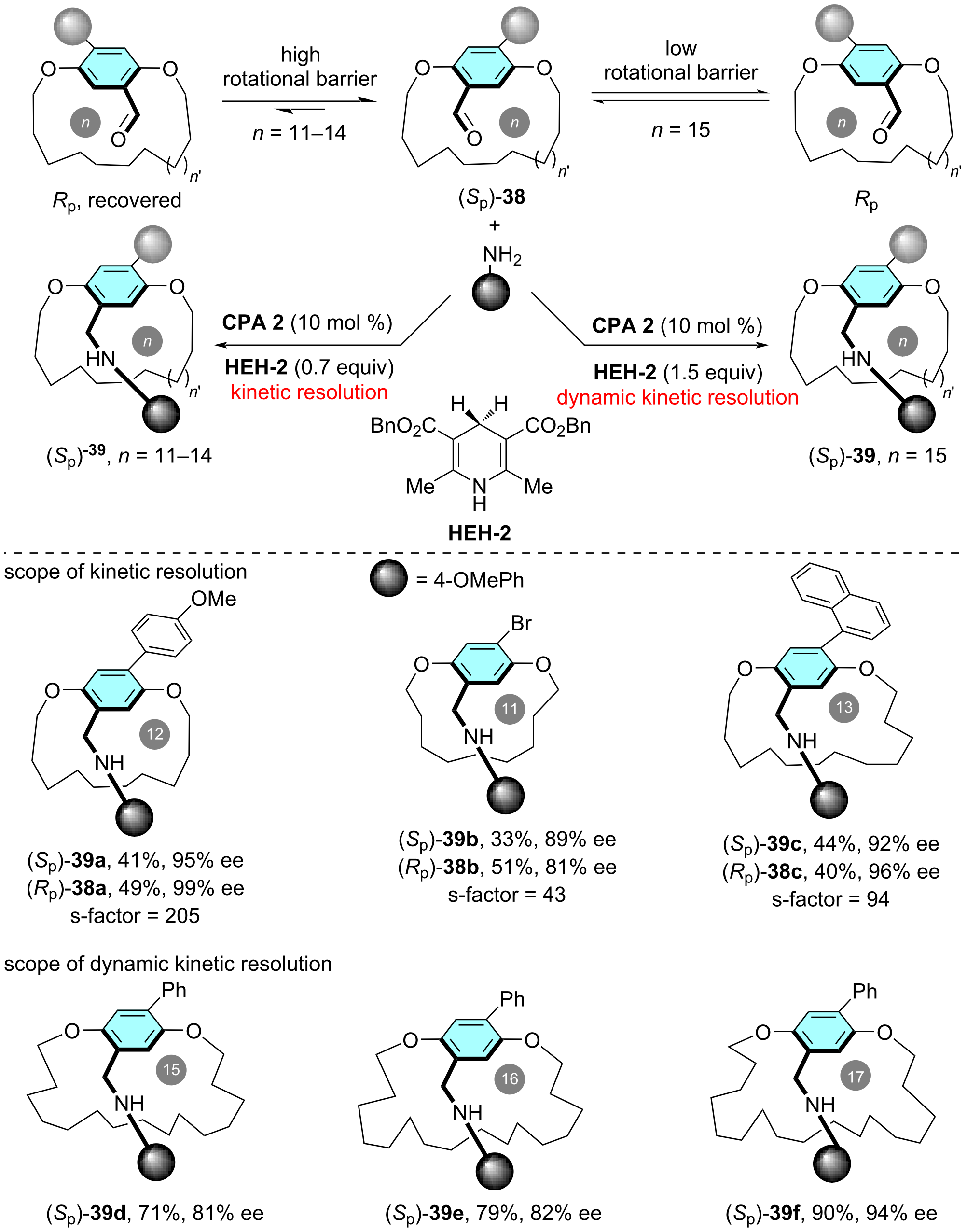

Scheme 11: (Dynamic) kinetic resolution of planarly chiral paracyclophanes via CPA-catalyzed asymmetric reductive amination.

In 2025, our group presented another example of an asymmetric synthesis of inherently chiral calix[4]arenes using a CPA-catalyzed enantioselective desymmetrization strategy [52]. Commencing with phenol-containing prochiral calix[4]arenes **55**, the **CPA 3**-catalyzed asymmetric *ortho*-C–H amination with electrophilic azo reagents **56** effectively broke the symmetry of the substrate, leading to the formation of inherently chiral calix[4]arenes **57** with high enantioselectivity (Scheme 16). Notably, with the use of acyclic azodicarboxylate as amination reagent, the products exhibited both inherent chirality and intriguing C–N axial chirality (see **57a**). This method demonstrates excellent substrate compatibility, accommodating various calix[4]arenes with 1,3-phenyl ring disubstitution patterns (see **57c**,**d**) and diphenol-containing calix[4]arenes (see **57e**,**f**). The aminated chiral calix[4]arene products underwent diverse derivatizations due to the abundance of functional groups present. Moreover, the potential applications of these unique inherently chiral calix[4]arenes have also been showcased. For instance, facile derivatizations of **57a** afforded the inherently chiral *meta*-amino-substituted calix[4]arene **58** and

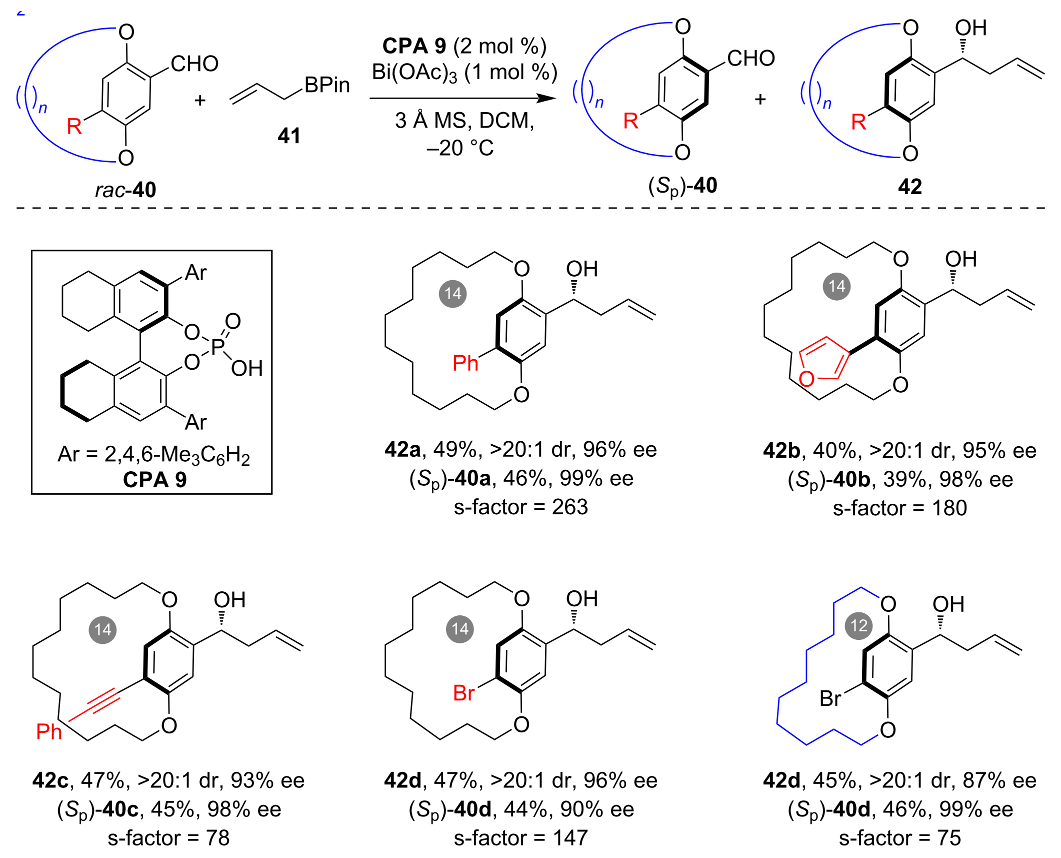

Scheme 12: Kinetic resolution of macrocyclic paracyclophanes through CPA/Bi-catalyzed asymmetric allylation.

the corresponding aniline *N*-oxide **59**. Our study suggested that inherently chiral calix[4]arene **58** could successfully be used as a chiral organocatalyst in the asymmetric amination of aldehyde **34**, whereas inherently chiral aniline *N*-oxide **59** showed promise in the chiral recognition of mandelic acid.

In 2024, Tong, Wang and co-workers disclosed an efficient method for synthesizing inherently chiral heterocalix[4]arenes through an asymmetric macrocyclization strategy [53]. Starting from the linear precursor **60** bearing two triazine moieties, the intramolecular S_NAr reaction catalyzed by **CPA 13** (30 mol %) led to macrocyclization, which produced the inherently chiral N_3,O-calix[2]arene[2]triazines **61** with high enantioselectivity, albeit in moderate yield (Scheme 17). The addition of K_2CO_3 after 12 hours improved the enantioselectivity of this reaction by scavenging the HCl produced during the S_NAr reaction, which was believed to potentially promote the nonenantioselective background macrocyclization reaction. Notably, these inherently chiral heterocalix[4]arenes displayed a distinctive 1,3-alternate conformation, notably differing from the typical cone conformation of the conventional calix[4]arenes. Moreover, unlike previously documented examples, the inherent chirality of these products arises from the difference of just one heteroatom (O and NH) in the linking positions of the heterocalix[4]arenes, which may pave new avenues for designing and synthesizing inherently chiral macrocycles.

Cyclic molecules smaller than calix[4]arenes that possess a rigid nonplanar conformation can also exhibit inherent chirality. In 2023, Luo, Zhu and co-workers reported the efficient asymmetric synthesis of inherently chiral eight-membered N-heterocycle 6,7-diphenyldibenzo[*e*,*g*][1,4]diazocines (DDDs), which displayed a rigid saddle-shaped configuration [16]. Starting from readily available [1,1'-biphenyl]-2,2'-diamines **62** and benzyl compounds **63**, the asymmetric cyclocondensation between these two components enabled by CPA catalysts yielded the inherently chiral DDDs **64** with good to high enantioselectivity (Scheme 18). While a number of reactions did not initially yield satisfactory enantioselectivity, facile phase separation during the workup process removed the less soluble racemic products, which resulted in the isolation of chiral products with exceptional enantiopurity. Moreover, this method accommodated [1,1'-biphenyl]-2,2'-diamines **62** with *ortho*-substitutions, which underwent either dynamic kinetic resolution or kinetic resolution to produce chiral substituted DDD products **64e**. Moreover, the authors showcased the facile derivatization of

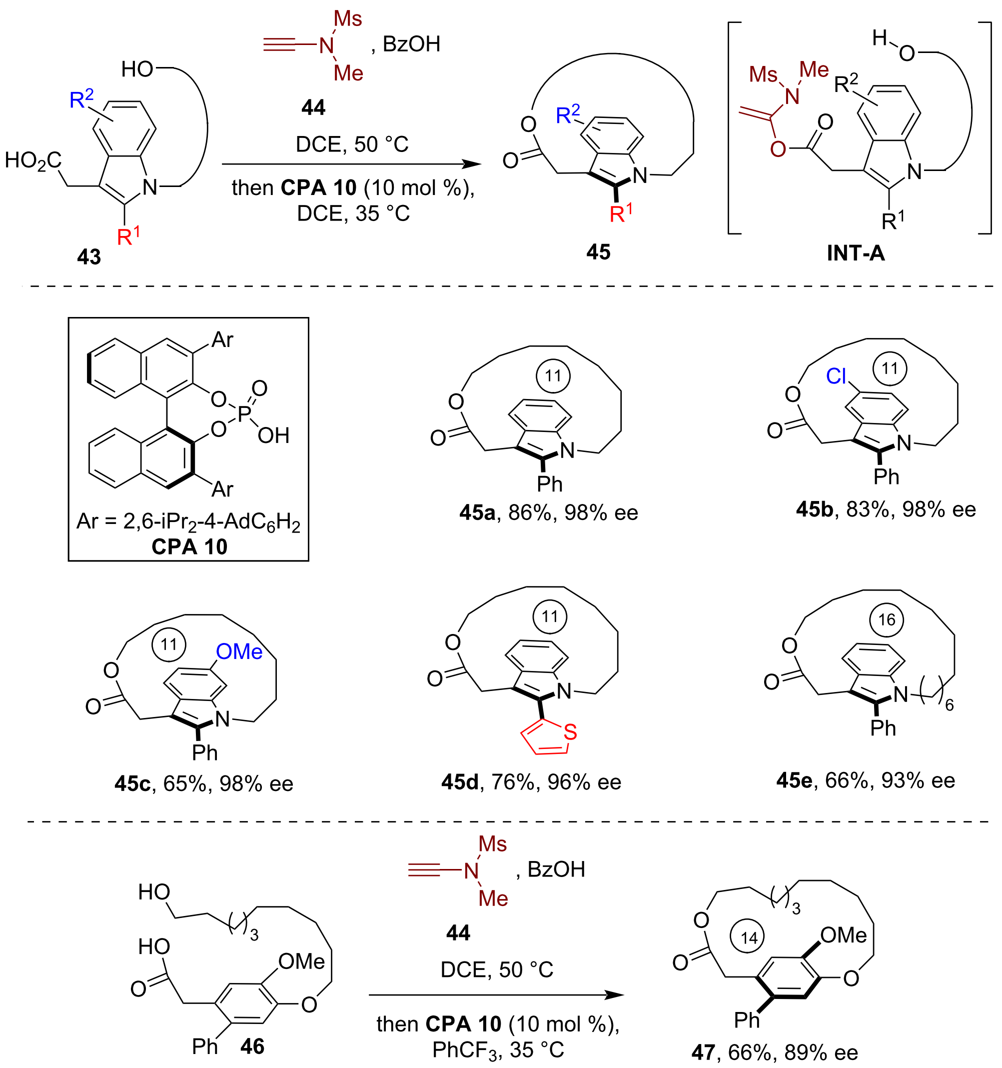

Scheme 13: Enantioselective synthesis of planarly chiral macrocycles via CPA-catalyzed coupling of carboxylic acids with alcohols via ynamide mediation.

dimethoxy-substituted chiral DDD **64f** into various DDD-based chiral ligands, such as the phosphoramidites **65**, phosphoric acid as well as monophosphine ligands and diphosphine ligands **66**. Notably, the applications of these novel inherently chiral ligands have been explored. For example, they demonstrated excellent enantioselectivity control in some asymmetric reactions, such as the Rh/diphosphine ligand **66**-catalyzed asymmetric addition reaction between cyclic enone and arylboronic acid.

In 2024, our group reported the catalytic asymmetric synthesis of saddle-shaped inherently chiral 9,10-dihydrotribenzoazocines via CPA-catalyzed kinetic resolution and dynamic kinetic resolution strategies [54]. By leveraging the reactivity of the aniline moiety in 9,10-dihydrotribenzoazocines **68**, the **CPA 16**-catalyzed enantioselective *para*-selective C–H amination reaction with dibenzyl azodicarboxylate (0.8 equiv) resulted in efficient kinetic resolution, which yielded both the C–H amination product **69** and recovered (+)-**68** with high enantioselectivity (see **68a–c**, Scheme 19). Moreover, this method was also applicable to the kinetic resolution of racemic 10-substituted 9,10-dihydrotribenzoazocines featuring both inherent and central chirality, delivering excellent kinetic resolution performance (see **68d–g**). During our studies, we serendipitously found that the imine-containing eight-membered azaheterocycles **70**, derived from the oxidative dehydrogenation of **68**, displayed unexpectedly low configurational stability. Consequently, we developed a more efficient dynamic kinetic resolution protocol for the asymmetric synthesis of inherently chiral **68**. This method involved the **CPA 17**-catalyzed asymmetric

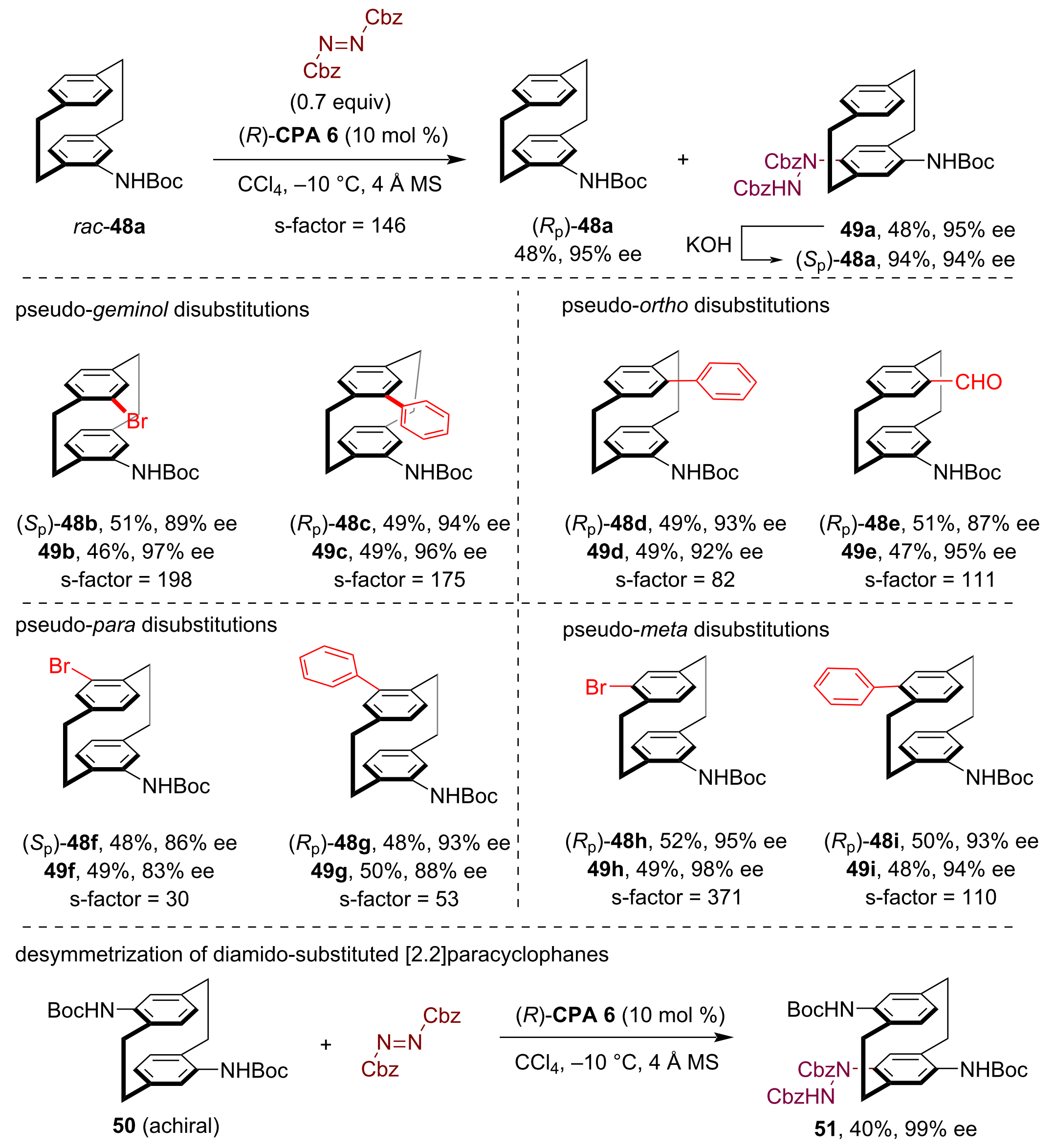

Scheme 14: Kinetic resolution of substituted amido[2.2]paracyclophanes via CPA-catalyzed asymmetric electrophilic amination.

hydrogen transfer reaction of racemic **70** using Hantzsch ester **HEH-3** as the reductant, which enabled the asymmetric synthesis of some inherently chiral substituted 9,10-dihydrotribenzoazocines that had been challenging to access through the aminative dearomatization method (see **68h**,**i**).

In 2024, our group reported a convenient method for the asymmetric synthesis of saddle-shaped inherently chiral dibenzo[*b*,*f*][1,5]diazocines **72** via CPA catalysis [55]. In the presence of **CPA 7** (10 mol %) and the corresponding 2-acylaniline **73** (20 mol %) as co-catalysts, the asymmetric dimerization of 2-acylbenzo isocyanates **71** allowed access to inherently chiral eight-membered azaheterocycles **72** with moderate to good enantioselectivity, along with the release of CO_2 (Scheme 20). While the enantioselectivity using certain substrates was initially unsatisfactory, simple phase separation significantly enhanced the enantiopurity of the products by removing the less soluble racemic products. Detailed studies were conducted to explore the reaction mechanism, focusing specifically on the role of the 2-acylanilines **73** as co-catalysts. Based on the experimental results and previous research, a plausible mechanism was proposed. Isomerization of substrates **71** yielded the cyclic intermediate **INT-B**, which then underwent addition with aniline co-catalyst **73** to form **INT-C**. The CPA-enabled release of CO_2 from **INT-C** yielded the imine-containing intermediate **INT-D**, which underwent iterative addition

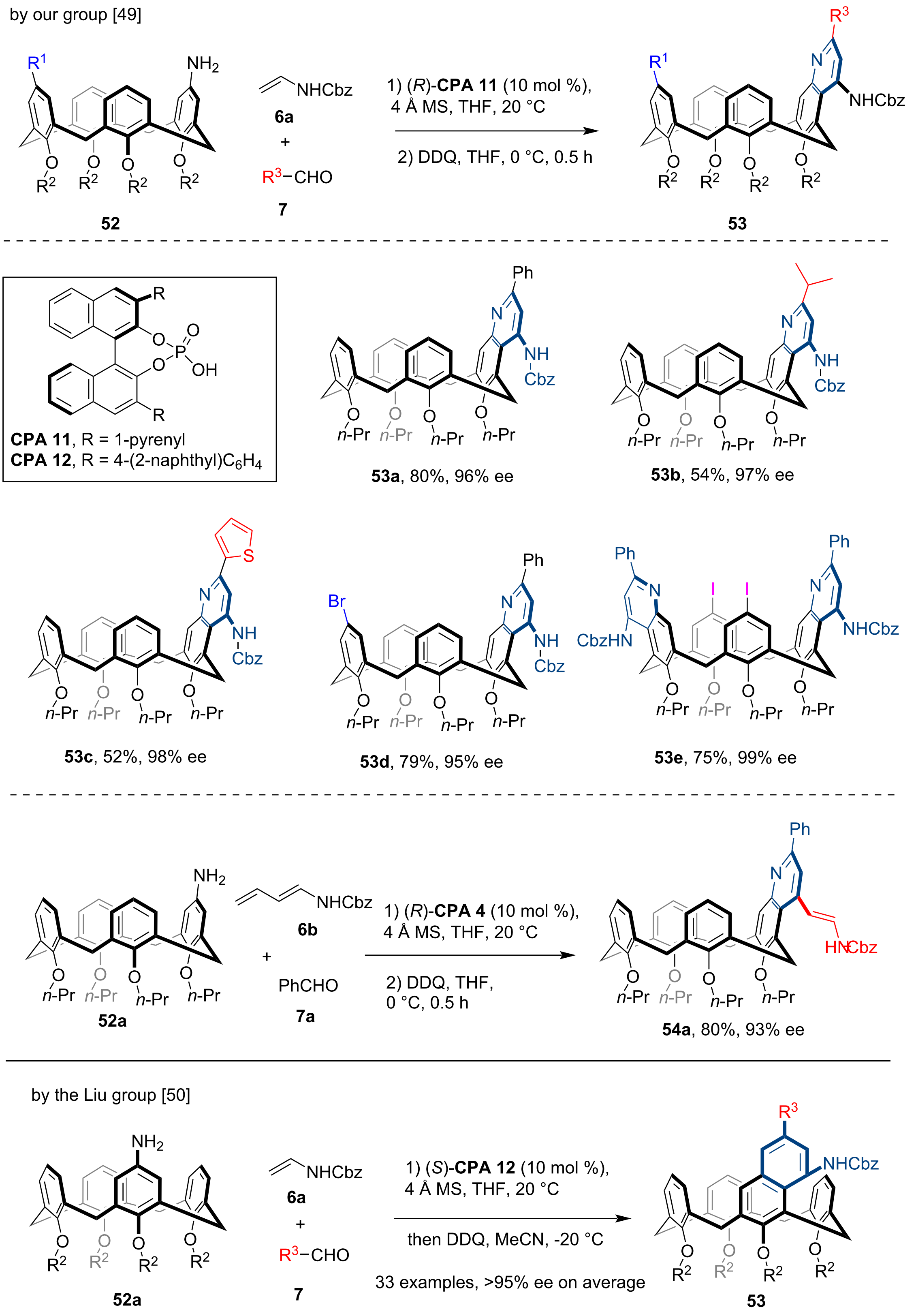

Scheme 15: Enantioselective synthesis of inherently chiral calix[4]arenes via sequential CPA-catalyzed Povarov reaction and aromatization.

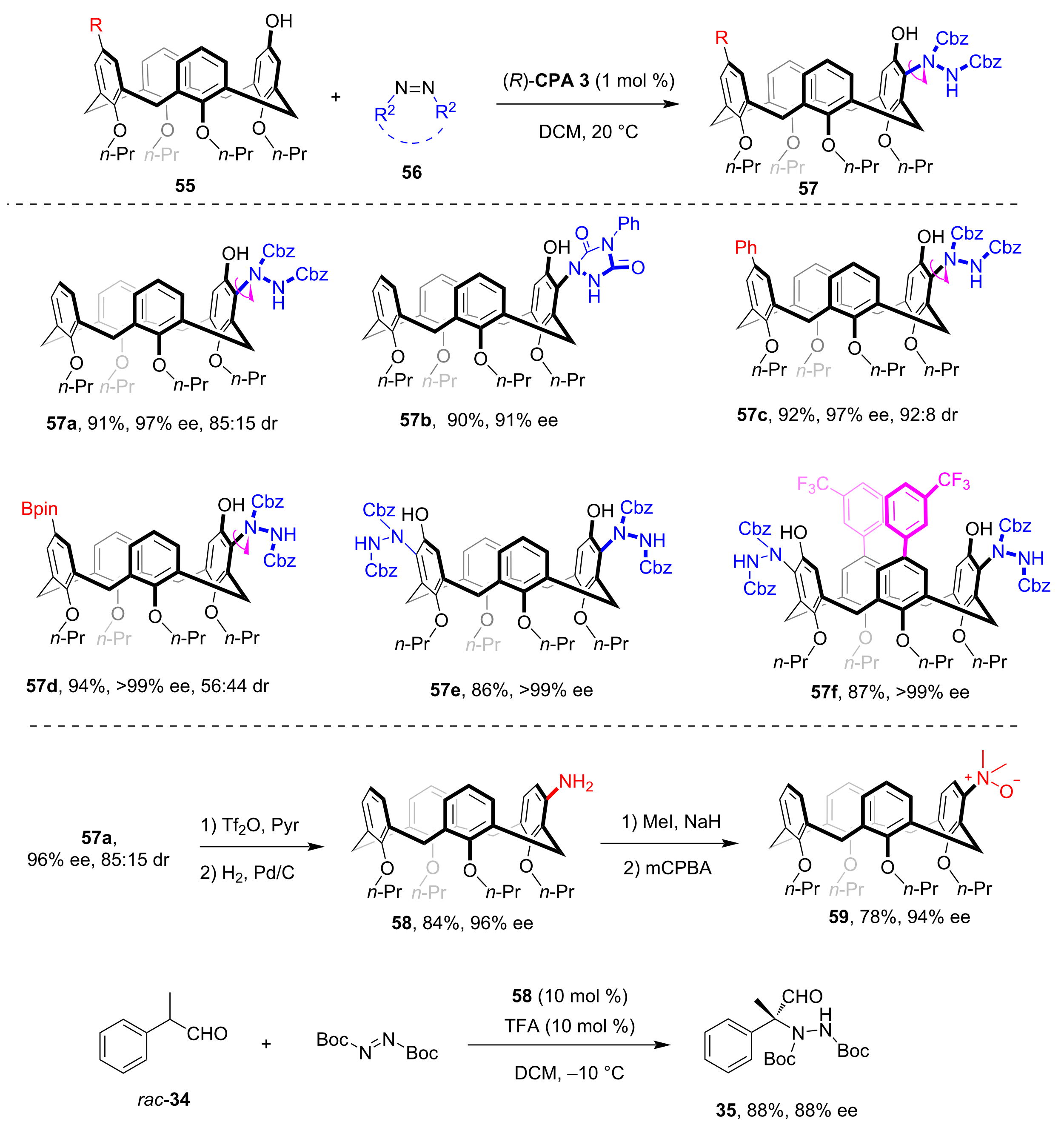

Scheme 16: Asymmetric synthesis of inherently chiral calix[4]arenes via CPA-catalyzed aminative desymmetrization.

with **INT-B**, followed by release of CO_2 to afford **INT-E**. The CPA-catalyzed cyclization of **INT-E** through the dual hydrogen bonding activation transition state **TS-1** afforded the eight-membered heterocycle **INT-F** with a stereogenic center. Through the elimination of aniline **73**, the saddle-shaped dibenzo[1,5]diazocine **72** was produced via a central-to-inherent chirality transfer process. Notably, while only the amino group of the co-catalysts was shown to engage in the catalytic cycle, the 2-acyl group of **73** was believed to participate in hydrogen bonding interactions with the substrate and the CPA catalyst, playing additional crucial roles.

In addition to various saddle-shaped eight-membered azaheterocycles, conformationally rigid seven-membered cyclic compounds can also exhibit inherent chirality. In 2017, Antilla et al. developed the CPA-catalyzed asymmetric condensation of 4-substituted cyclohexanones with *O*-arylhydroxylamines, which yielded axially chiral cyclohexylidene oxime ethers with

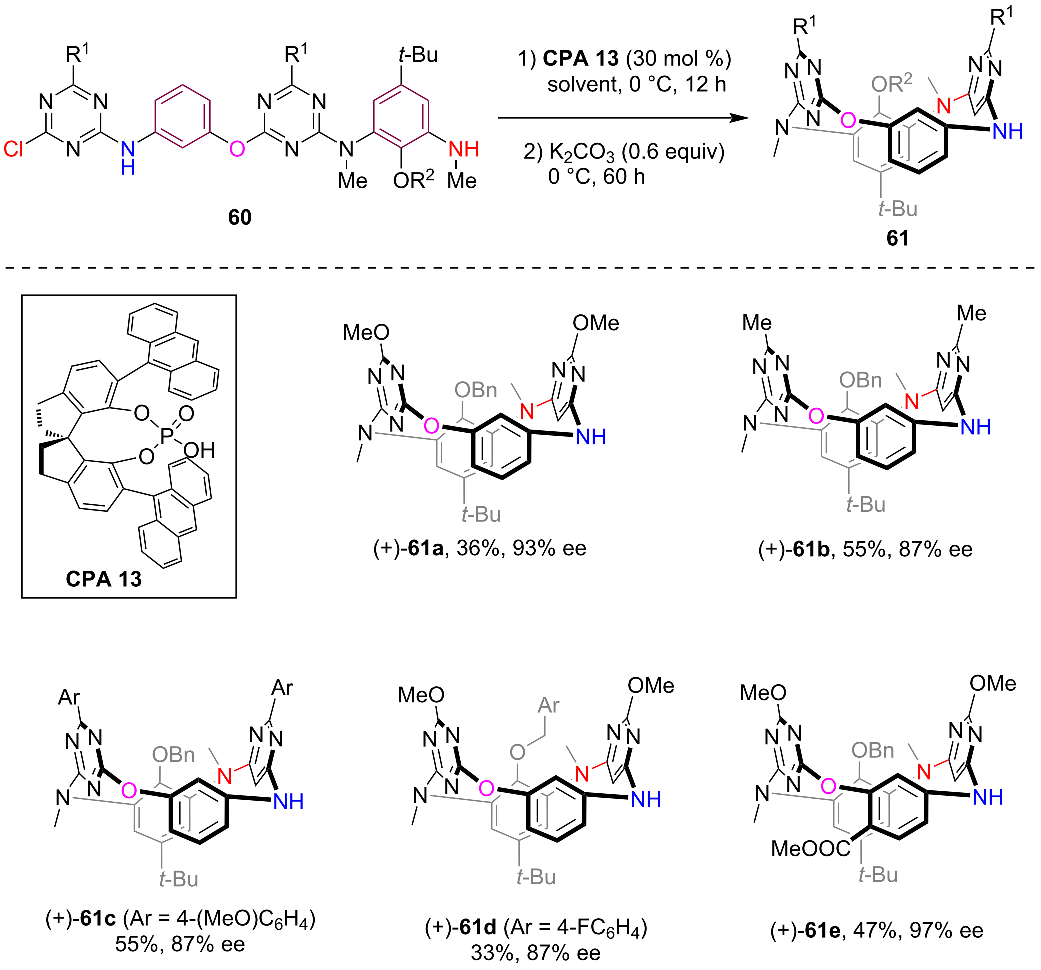

Scheme 17: Asymmetric synthesis of chiral heterocalix[4]arenes via CPA-catalyzed intramolecular S_NAr reaction.

high enantioselectivity [56]. In 2024, through the utilization of this method, Liu and co-workers disclosed the enantioselective synthesis of inherently chiral 7-membered tribenzocycloheptene oximes **76** through **CPA 18**-catalyzed asymmetric condensation between 7-membered cyclic ketones **74** and hydroxylamines **75** (Scheme 21) [57]. High to excellent yield and enantioselectivity were achieved for the inherently chiral products when using a range of substituted arylhydroxylamines (see **76a–c**). The racemization barrier of the product **76a** was determined to be 110.5 kJ/mol, which suggested the relative instability of the configuration of these structurally unique products compared to the eight-membered inherently chiral compounds. Moreover, unsymmetrical substituted cyclic ketones **74** were investigated under the standard conditions, which produced a pair of diastereomers with poor diastereoselectivity while maintaining high enantioselectivity for both diastereomers (see **76d–g**). Furthermore, the authors have investigated the asymmetric condensation using other seven-membered cyclic ketones (see **77a**) as well as the coupling with alkylhydroxylamine (see **77b**), tosylhydrazide (see **77c**) and *N*-aminoindole (see **77d**), which all produced the inherently chiral products with moderate to good enantioselectivity, albeit requiring the use of different CPA catalysts.

Conclusion

The increasing number of applications of non-centrally-chiral molecules, including helically chiral, planarly chiral and inherently chiral molecules across diverse research fields, has spurred considerable research focus toward the catalytic asymmetric synthesis of these unique chiral molecules. While methods for the asymmetric synthesis of these chiral molecules remain relatively underexplored compared to the enantioselective synthesis of centrally and axially chiral compounds, significant progress has been made in these fields in recent years. Among numerous chiral catalysts, CPAs have emerged as key players in the asymmetric synthesis of these structurally unique chiral molecules, owing to their diverse catalytic abilities, precise stereoselectivity control and mild reaction conditions. In

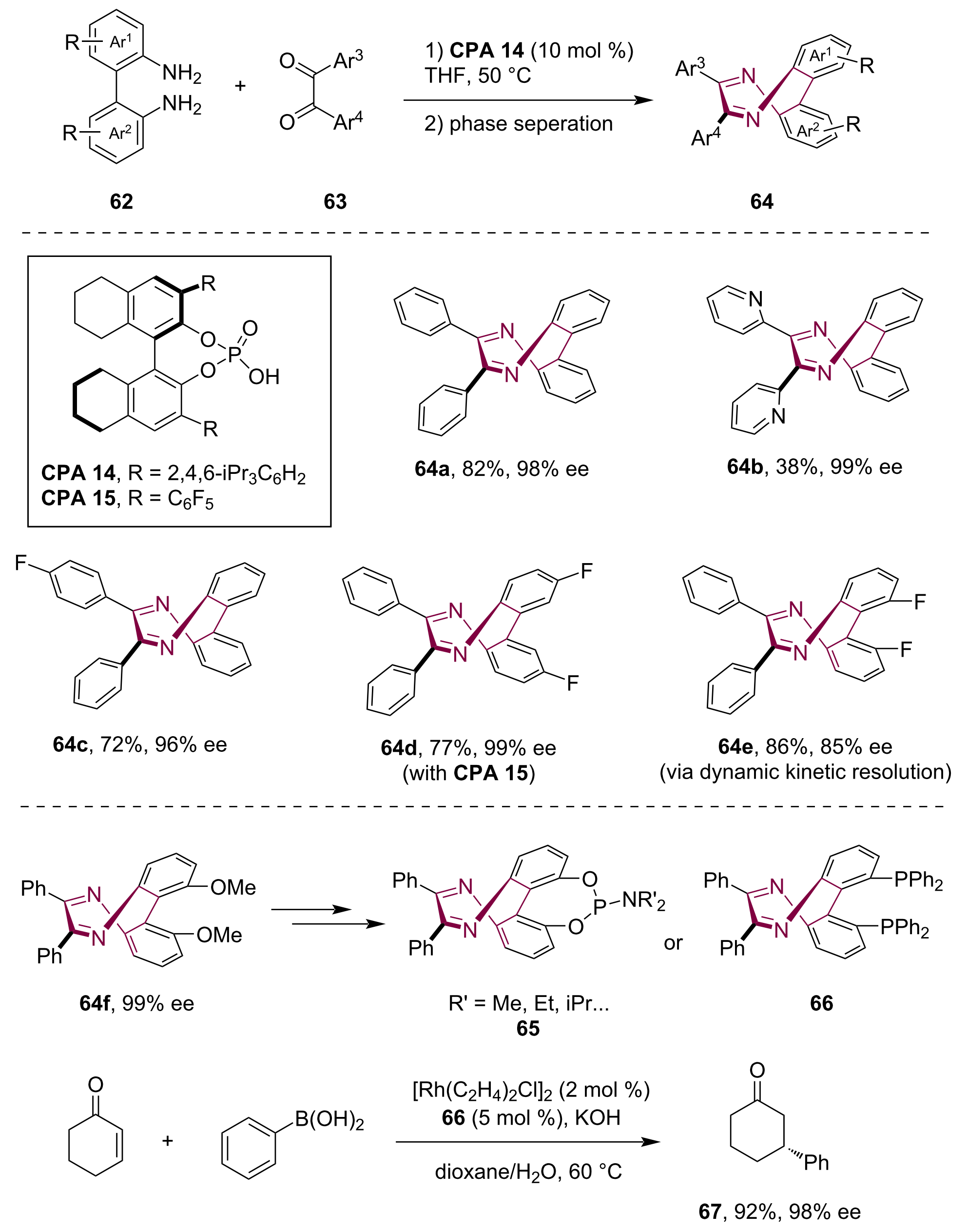

Scheme 18: Enantioselective synthesis of inherently chiral DDDs via CPA-catalyzed cyclocondensation.

this Review, we systematically summarized the advancements in the CPA-catalyzed asymmetric synthesis of helically chiral, planarly chiral and inherently chiral molecules. Various CPA-catalyzed reactions, such as cyclizations, aromatic substitutions and condensations, along with asymmetric synthesis strategies, such as enantioselective desymmetrization and (dynamic) kinetic resolution, have been employed for the asymmetric construction of these chiral elements.

Despite remarkable progress and significant potential in the CPA-catalyzed asymmetric synthesis of these unique chiral molecules, some current limitations and challenges still need to be addressed, particularly enhancing the efficiency of the methods and expanding the structural diversity of the products. Firstly, the chiral products generated through CPA-catalyzed methods are still relatively simple. For instance, in terms of helically chiral helicenes, typically, only the relatively shorter [5]helicenes have been produced, while the more complex, longer helicenes and multihelicenes have not yet been successfully synthesized through CPA-catalyzed asymmetric methods. Secondly, asymmetric synthetic strategies based on presynthesized three-dimensional molecular structures are commonly em-

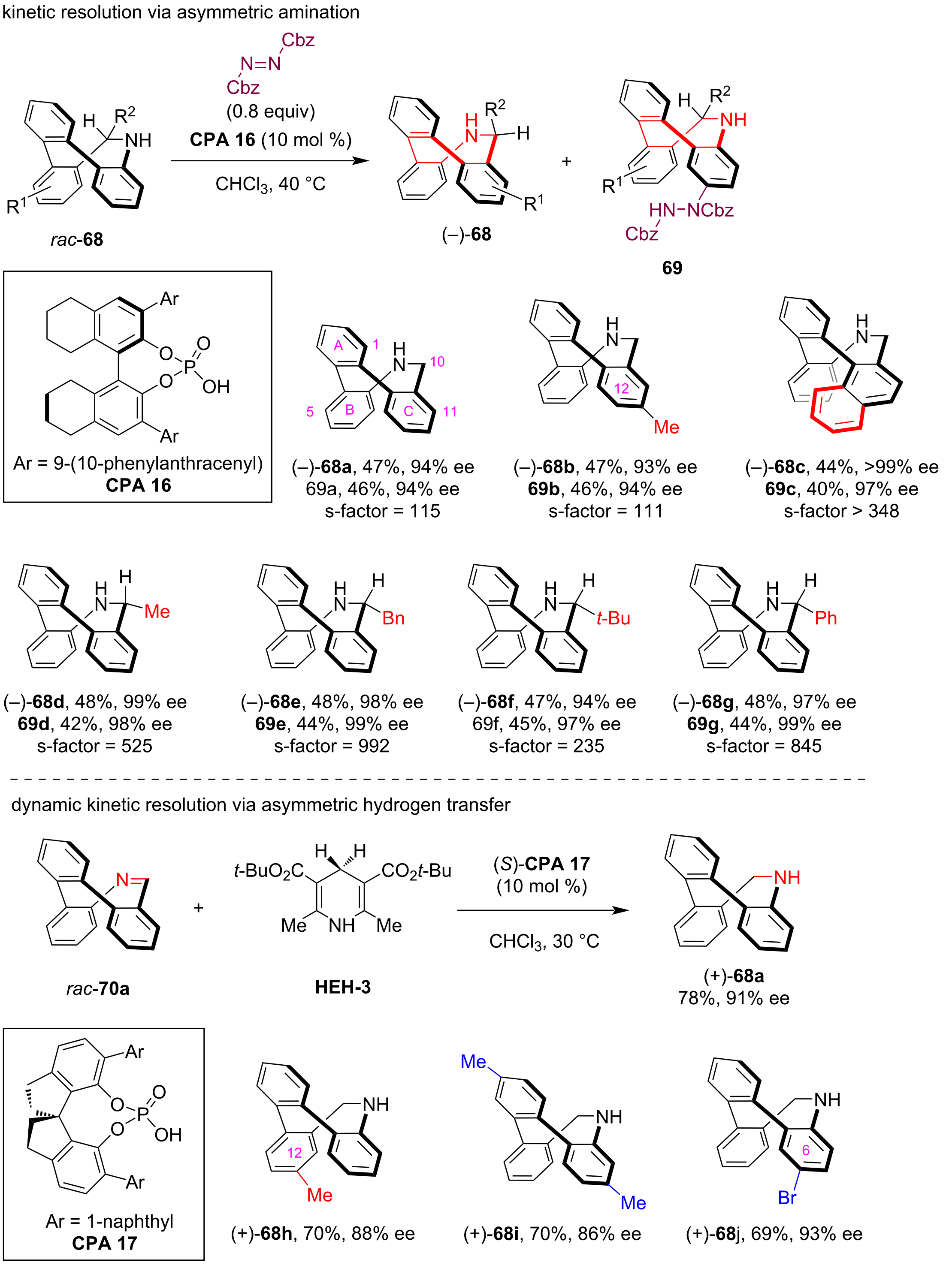

Scheme 19: Asymmetric synthesis of saddle-shaped inherently chiral 9,10-dihydrotribenzoazocines via CPA-catalyzed (dynamic) kinetic resolution.

ployed, such as enantioselective desymmetrization and (dynamic) kinetic resolution. While these strategies have proven effective, the efficiency of these methods may not be considered highly satisfactory due to the requirement to prepare relatively complex substrates. Therefore, there is a high demand for the development of more efficient asymmetric methods through which molecular structures can be directly constructed while achieving high enantioselectivity. Overall, with the recent rapid

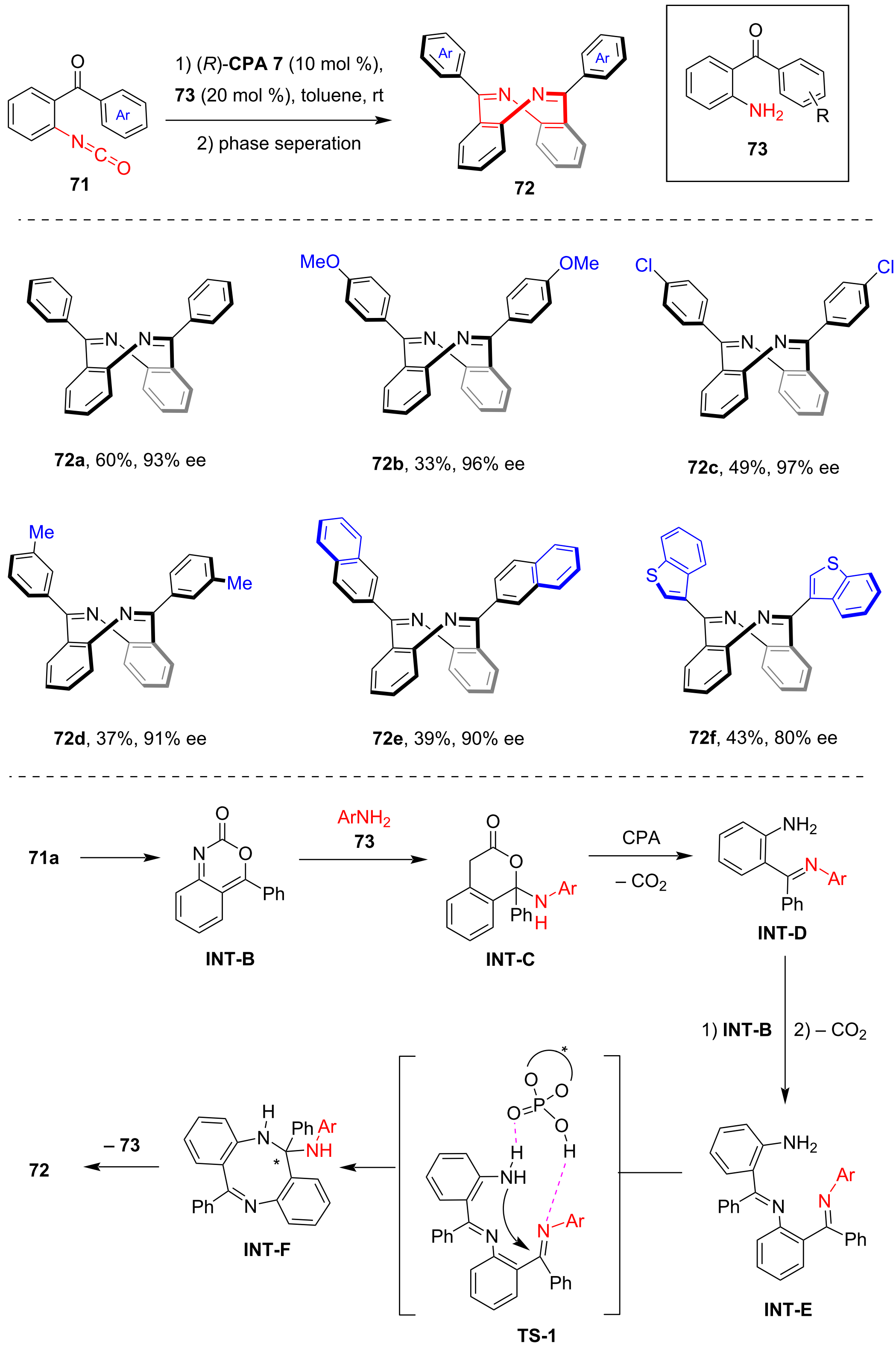

Scheme 20: Enantioselective synthesis of inherently chiral saddle-shaped dibenzo[*b*,*f*][1,5]diazocines via CPA-catalyzed dimerization of 2-acylbenzo isocyanates.

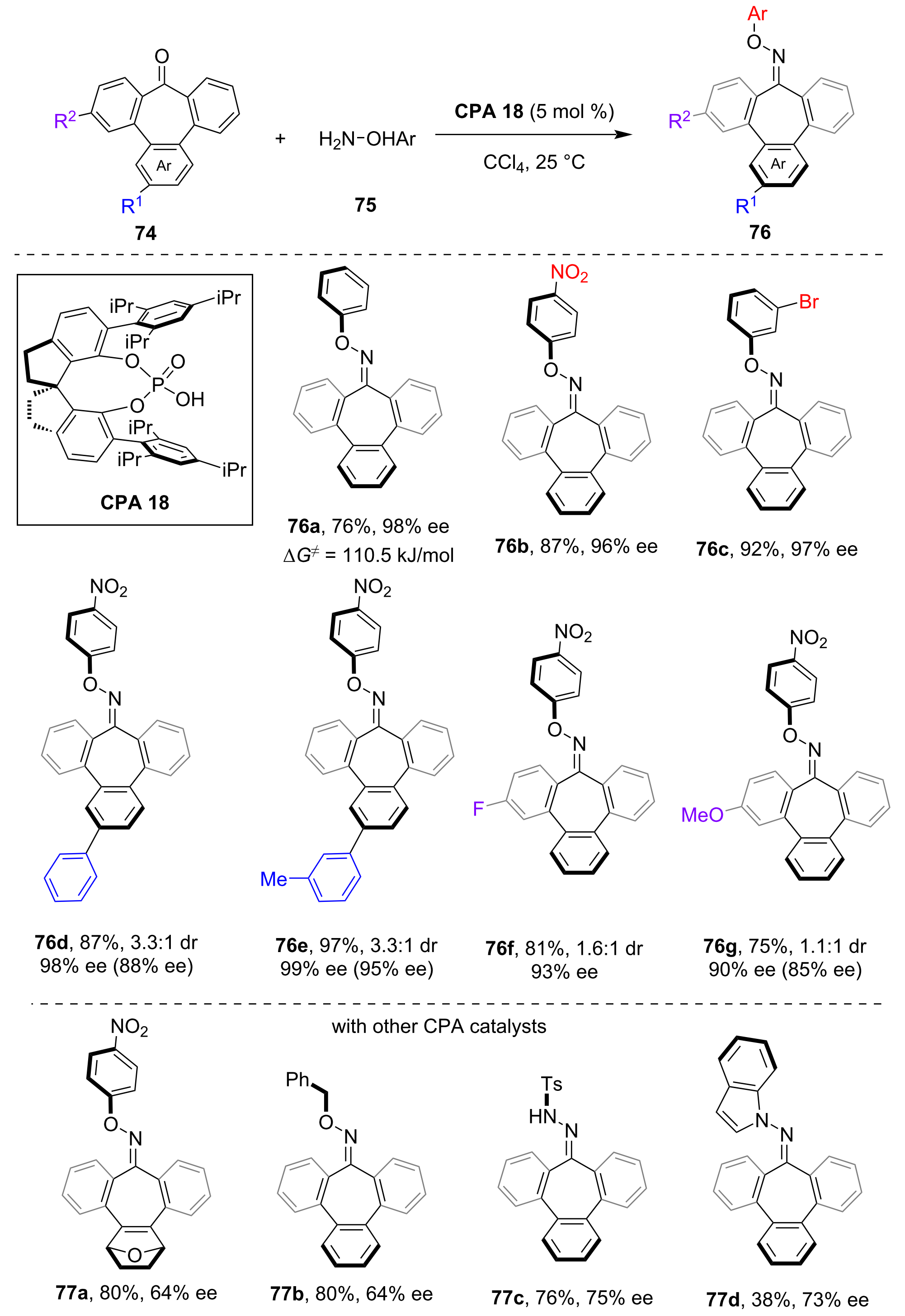

Scheme 21: Enantioselective synthesis of inherent chiral 7-membered tribenzocycloheptene oximes via CPA-catalyzed condensation.

advancements of CPA catalysis, along with the utilization of CPA catalysts in asymmetric radical chemistry, transition metal-catalyzed reactions and photoredox chemistry, we envision that CPA catalysts will continue to play a central role in the future asymmetric synthesis of helically chiral, planarly chiral and inherently chiral molecules.

Funding

We gratefully acknowledge financial support from the National Natural Science Foundation of China (grant nos. 22222107 and 22171186), the ShanghaiTech University Start-up funding and the Anyang Institute of Technology Doctoral Scientific Research Start-up funding (BSJ2025023).

Author Contributions

Wei Liu: conceptualization; writing – original draft. Xiaoyu Yang: conceptualization; funding acquisition; supervision; writing – review & editing.

ORCID® iDs

Xiaoyu Yang - https://orcid.org/0000-0002-0756-0671

Data Availability Statement

Data sharing is not applicable as no new data was generated or analyzed in this study.

References

1. Akiyama, T.; Itoh, J.; Yokota, K.; Fuchibe, K. *Angew. Chem., Int. Ed.* **2004,** *43,* 1566–1568. doi:10.1002/anie.200353240
2. Uraguchi, D.; Terada, M. *J. Am. Chem. Soc.* **2004,** *126,* 5356–5357. doi:10.1021/ja0491533
3. Akiyama, T. *Chem. Rev.* **2007,** *107,* 5744–5758. doi:10.1021/cr068374j
4. Terada, M. *Synthesis* **2010,** 1929–1982. doi:10.1055/s-0029-1218801
5. Parmar, D.; Sugiono, E.; Raja, S.; Rueping, M. *Chem. Rev.* **2014,** *114,* 9047–9153. doi:10.1021/cr5001496
6. Akiyama, T.; Mori, K. *Chem. Rev.* **2015,** *115,* 9277–9306. doi:10.1021/acs.chemrev.5b00041
7. Rahman, A.; Lin, X. *Org. Biomol. Chem.* **2018,** *16,* 4753–4777. doi:10.1039/c8ob00900g
8. Li, X.; Song, Q. *Chin. Chem. Lett.* **2018,** *29,* 1181–1192. doi:10.1016/j.cclet.2018.01.045
9. Cheng, J. K.; Xiang, S.-H.; Li, S.; Ye, L.; Tan, B. *Chem. Rev.* **2021,** *121,* 4805–4902. doi:10.1021/acs.chemrev.0c01306
10. Mori, K.; Ichikawa, Y.; Kobayashi, M.; Shibata, Y.; Yamanaka, M.; Akiyama, T. *J. Am. Chem. Soc.* **2013,** *135,* 3964–3970. doi:10.1021/ja311902f
11. Da, B.-C.; Xiang, S.-H.; Li, S.; Tan, B. *Chin. J. Chem.* **2021,** *39,* 1787–1796. doi:10.1002/cjoc.202000751
12. Kötzner, L.; Webber, M. J.; Martínez, A.; De Fusco, C.; List, B. *Angew. Chem., Int. Ed.* **2014,** *53,* 5202–5205. doi:10.1002/anie.201400474
13. Liu, W.; Qin, T.; Xie, W.; Zhou, J.; Ye, Z.; Yang, X. *Angew. Chem., Int. Ed.* **2023,** *62,* e202303430. doi:10.1002/anie.202303430
14. Li, C.; Shao, Y.-B.; Gao, X.; Ren, Z.; Guo, C.; Li, M.; Li, X. *Nat. Commun.* **2023,** *14,* 3380. doi:10.1038/s41467-023-39134-9
15. Wang, D.; Shao, Y.-B.; Chen, Y.; Xue, X.-S.; Yang, X. *Angew. Chem., Int. Ed.* **2022,** *61,* e202201064. doi:10.1002/anie.202201064
16. Luo, Y.; Wang, X.; Hu, W.; Peng, Y.; Wang, C.; Yu, T.; Cheng, S.; Li, J.; He, Y.; Gan, C.; Luo, S.; Zhu, Q. *CCS Chem.* **2023,** *5,* 982–993. doi:10.31635/ccschem.022.202201901
17. Shen, Y.; Chen, C.-F. *Chem. Rev.* **2012,** *112,* 1463–1535. doi:10.1021/cr200087r
18. Wang, Y.; Wu, Z.-G.; Shi, F. *Chem Catal.* **2022,** *2,* 3077–3111. doi:10.1016/j.checat.2022.10.011
19. Liu, W.; Qin, T.; Xie, W.; Yang, X. *Chem. – Eur. J.* **2022,** *28,* e202202369. doi:10.1002/chem.202202369
20. Huang, Q.; Tang, Y.-P.; Zhang, C.-G.; Wang, Z.; Dai, L. *ACS Catal.* **2024,** *14,* 16256–16265. doi:10.1021/acscatal.4c05345
21. Xie, W.; Zhou, J.; Liu, W.; Qin, T.; Yang, X. *Cell Rep. Phys. Sci.* **2024,** *5,* 101993. doi:10.1016/j.xcrp.2024.101993
22. Qin, T.; Xie, W.; Liu, W.; Yang, X. *Org. Chem. Front.* **2025,** *12,* 1417–1424. doi:10.1039/d4qo02188f
23. Xu, W.-L.; Zhang, R.-X.; Wang, H.; Chen, J.; Zhou, L. *Angew. Chem., Int. Ed.* **2024,** *63,* e202318021. doi:10.1002/anie.202318021
24. Vedejs, E.; Jure, M. *Angew. Chem., Int. Ed.* **2005,** *44,* 3974–4001. doi:10.1002/anie.200460842
25. Liu, W.; Yang, X. *Asian J. Org. Chem.* **2021,** *10,* 692–710. doi:10.1002/ajoc.202100091
26. Jiang, Q.; Zhang, D.; Tang, M.; Liu, H.; Yang, X. *Sci. China: Chem.* **2024,** *67,* 973–980. doi:10.1007/s11426-023-1810-9
27. Xie, J.; Guo, Z.; Liu, W.; Zhang, D.; He, Y.-P.; Yang, X. *Chin. J. Chem.* **2022,** *40,* 1674–1680. doi:10.1002/cjoc.202200125
28. Chen, Y.; Zhu, C.; Guo, Z.; Liu, W.; Yang, X. *Angew. Chem., Int. Ed.* **2021,** *60,* 5268–5272. doi:10.1002/anie.202015008
29. Liu, W.; Jiang, Q.; Yang, X. *Angew. Chem., Int. Ed.* **2020,** *59,* 23598–23602. doi:10.1002/anie.202009395
30. Chu, A.; Zhu, B.; Zhang, X.; Zhu, H.; Zhang, J.; Liu, X. *Sci. Adv.* **2024,** *10,* eadr1628. doi:10.1126/sciadv.adr1628
31. Liu, W.-M.; Hao, Y.-J.; Zhang, Y.; Li, X.-G.; Ji, S.-J.; Cai, Z.-J. *Org. Lett.* **2025,** *27,* 363–368. doi:10.1021/acs.orglett.4c04350
32. Hassan, Z.; Spuling, E.; Knoll, D. M.; Lahann, J.; Bräse, S. *Chem. Soc. Rev.* **2018,** *47,* 6947–6963. doi:10.1039/c7cs00803a
33. Zhu, K.; Yang, L.; Yang, Y.; Wu, Y.; Zhang, F. *Chin. Chem. Lett.* **2025,** *36,* 110678. doi:10.1016/j.cclet.2024.110678
34. Zhao, Y.-H.; Zhu, D.; Chen, Z.-M. *ChemCatChem* **2024,** *16,* e202401312. doi:10.1002/cctc.202401312
35. Yang, G.; Wang, J. *Angew. Chem., Int. Ed.* **2024,** *63,* e202412805. doi:10.1002/anie.202412805
36. Dong, Z.; Li, J.; Zhao, C. *Eur. J. Org. Chem.* **2024,** *27,* e202400841. doi:10.1002/ejoc.202400841
37. Zhang, D.; Chen, Y.; Lai, Y.; Yang, X. *Cell Rep. Phys. Sci.* **2021,** *2,* 100413. doi:10.1016/j.xcrp.2021.100413
38. Pan, Y.; Wang, D.; Chen, Y.; Zhang, D.; Liu, W.; Yang, X. *ACS Catal.* **2021,** *11,* 8443–8448. doi:10.1021/acscatal.1c02331
39. Yu, S.; Shen, G.; He, F.; Yang, X. *Chem. Commun.* **2022,** *58,* 7293–7296. doi:10.1039/d2cc01690g
40. Li, J.; Zhao, C. *ACS Catal.* **2023,** *13,* 14155–14162. doi:10.1021/acscatal.3c03718
41. Wang, Z.; Zhang, X.-X.; Sun, Y.; Zheng, H.; Li, X. *Chin. J. Chem.* **2025,** *43,* 1263–1270. doi:10.1002/cjoc.202500010
42. Chen, H.-H.; Jiang, J.-T.; Yang, Y.-N.; Ye, L.-W.; Zhou, B. *Angew. Chem., Int. Ed.* **2025,** *64,* e202505167. doi:10.1002/anie.202505167
43. Yu, S.; Bao, H.; Zhang, D.; Yang, X. *Nat. Commun.* **2023,** *14,* 5239. doi:10.1038/s41467-023-40718-8
44. Böhmer, V.; Kraft, D.; Tabatabai, M. *J. Inclusion Phenom. Mol. Recognit. Chem.* **1994,** *19,* 17–39. doi:10.1007/bf00708972
45. Han, J.-W.; Chen, J.-X.; Li, X.; Peng, X.-S.; Wong, H. N. C. *Synlett* **2013,** *24,* 2188–2198. doi:10.1055/s-0033-1339859
46. Liu, Y.; Wu, G.; Yang, Z.; Rouh, H.; Katakam, N.; Ahmed, S.; Unruh, D.; Cui, Z.; Lischka, H.; Li, G. *Sci. China: Chem.* **2020,** *63,* 692–698. doi:10.1007/s11426-019-9711-x
47. Luo, Y.; Luo, S.; Zhu, Q. *J. Org. Chem.* **2025,** *90,* 5307–5322. doi:10.1021/acs.joc.5c00479
48. Tang, M.; Yang, X. *Eur. J. Org. Chem.* **2023,** *26,* e202300738. doi:10.1002/ejoc.202300738

49. Yu, S.; Yuan, M.; Xie, W.; Ye, Z.; Qin, T.; Yu, N.; Yang, X. *Angew. Chem., Int. Ed.* **2024,** *63,* e202410628. doi:10.1002/anie.202410628
50. Jiang, Y.-K.; Tian, Y.-L.; Feng, J.; Zhang, H.; Wang, L.; Yang, W.-A.; Xu, X.-D.; Liu, R.-R. *Angew. Chem., Int. Ed.* **2024,** *63,* e202407752. doi:10.1002/anie.202407752
51. Ye, Z.; Xie, W.; Liu, W.; Zhou, C.; Yang, X. *Adv. Sci.* **2024,** *11,* 2403125. doi:10.1002/advs.202403125
52. Yuan, M.; Xie, W.; Yu, S.; Liu, T.; Yang, X. *Nat. Commun.* **2025,** *16,* 3943. doi:10.1038/s41467-025-59221-3
53. Li, X.-C.; Cheng, Y.; Wang, X.-D.; Tong, S.; Wang, M.-X. *Chem. Sci.* **2024,** *15,* 3610–3615. doi:10.1039/d3sc06436k
54. Zhang, D.; Zhou, J.; Qin, T.; Yang, X. *Chem Catal.* **2024,** *4,* 100827. doi:10.1016/j.checat.2023.100827
55. Zhou, J.; Tang, M.; Yang, X. *Chin. J. Chem.* **2024,** *42,* 1953–1959. doi:10.1002/cjoc.202400243
56. Nimmagadda, S. K.; Mallojjala, S. C.; Woztas, L.; Wheeler, S. E.; Antilla, J. C. *Angew. Chem., Int. Ed.* **2017,** *56,* 2454–2458. doi:10.1002/anie.201611602
57. Li, J.-H.; Li, X.-K.; Feng, J.; Yao, W.; Zhang, H.; Lu, C.-J.; Liu, R.-R. *Angew. Chem., Int. Ed.* **2024,** *63,* e202319289. doi:10.1002/anie.202319289

License and Terms

The definitive version of this article is the electronic one which can be found at:
https://doi.org/10.3762/bjoc.21.145

BEILSTEIN JOURNAL OF ORGANIC CHEMISTRY

Synthesis of N-doped chiral macrocycles by regioselective palladium-catalyzed arylation

Shuhai Qiu[1] and Junzhi Liu[*1,2,3]

Full Research Paper

Open Access

Address:
[1]Department of Chemistry, The University of Hong Kong, Pokfulam Road, Hong Kong, China, [2]State Key Laboratory of Synthetic Chemistry, HKU-CAS Joint Laboratory on New Materials and Shanghai-Hong Kong Joint Laboratory on Chemical Synthesis, The University of Hong Kong, Pokfulam Road, Hong Kong, China and [3]Materials Innovation Institute for Life Sciences and Energy (MILES), HKU-SIRI, Shenzhen, China

Email:
Junzhi Liu* - juliu@hku.hk

* Corresponding author

Keywords:
dihydroindolocarbazole; inherent chirality; N-doped macrocycle; nonplanarity; regioselective cyclization

Beilstein J. Org. Chem. **2025,** *21,* 1917–1923.
https://doi.org/10.3762/bjoc.21.149

Received: 01 June 2025
Accepted: 01 September 2025
Published: 15 September 2025

This article is part of the thematic issue "Non-central chirality in organic chemistry".

Associate Editor: N. Yoshikai

Abstract

A series of nitrogen (N)-doped macrocycles was successfully synthesized through palladium-catalyzed arylation. X-ray crystallographic characterization revealed the formation of isomeric products depending on the substituents on the N atoms. Notably, two intrinsically chiral macrocycles **MC1** and **MC3** with C_1 symmetry were successfully obtained. These macrocycles exhibit exceptional photophysical properties, particularly remarkable high fluorescence quantum yields (Φ_F up to 0.69). Furthermore, enantiomeric resolution of inherent chiral **MC1** was achieved using preparative chiral HPLC, enabling detailed investigation of its chiroptical behavior through circular dichroism and circularly polarized luminescence spectroscopy.

Introduction

Chiral macrocycles have attracted significant research interest owing to their diverse applications in enantioselective recognition [1,2], catalysis [3,4], and circularly polarized luminescence [5,6]. Generally, chirality in macrocycles arises from subunits featuring classical chiral elements [7], such as central, axis, planar and helical configurations. In contrast, inherent chirality represents a non-classical phenomenon where chirality emerges from the rigid and nonplanar architecture of macrocycles that inherently lacks symmetry [8,9]. One of the most typical representatives are calix[4]arenes (Figure 1a), first reported by Böhmer in 1994 [10], where asymmetric substitutions on the macrocyclic rim induce inherent chirality. Subsequent advancements have identified other inherent chiral systems, including molecular bowls [11-13] and medium-sized macrocycles containing a saddle-shaped eight-membered ring [14,15]. In the past decades, despite rapid progress in chiral macrocycles,

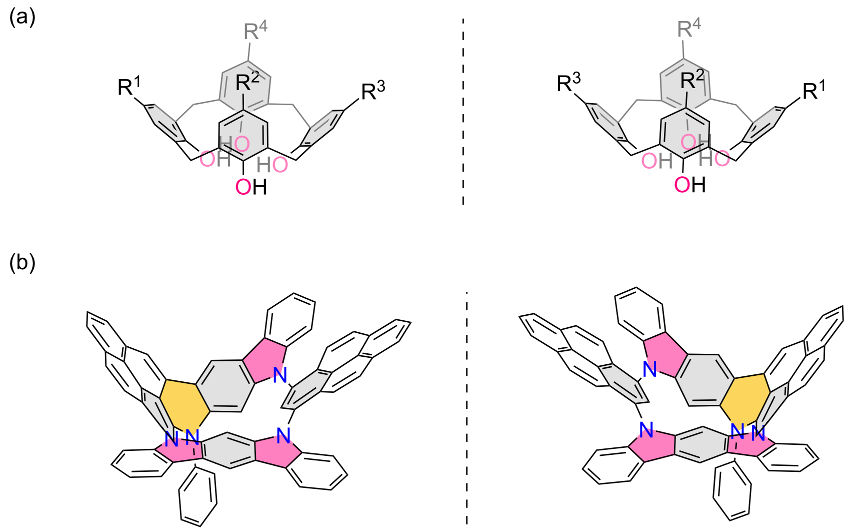

Figure 1: (a) Representatives of inherent chiral calix[4]arenes. (b) Molecular skeletons of inherent chiral N-doped macrocycles in this work.

inherent chirality is largely limited to calix[*n*]arene derivatives. This underscores a critical opportunity to design novel macrocyclic frameworks with intrinsic asymmetry.

Nitrogen (N)-doped macrocycles are of peculiar interest due to their unique optical, electronic and magnetic properties [16-19]. Among them, aza[1_n]metacyclophanes, in which *m*-phenylene units are linked via N atoms, serves as N-bridged structural analogs of [1_n]metacyclophanes. In comparison to all-carbon [1_n]metacyclophanes, the incorporation of N atoms endows them with unique features, such as enhanced molecular dynamics and tunable redox property, positioning them as key precursors to construct organic high-spin materials [20-23]. In addition to benzene-based systems, pyridine-embedded aza[1_n]metacyclophanes have been synthesized by Wang [24]. Despite these advances, N-doped chiral macrocycles incorporating extended π-conjugated moieties remain largely underexplored. To date, only a few examples, carbazole-based chiral macrocycles, have been reported [17,25], highlighting a critical gap in the design of chiral macrocycles with tailored electronic landscapes. Herein, we reported the synthesis, characterizations and photophysical properties of inherent chiral N-doped macrocycles (Figure 1b) via regioselective palladium (Pd)-catalyzed arylation of aza[1_4]metacyclophane derivatives. By modulating the substitutions on the N atoms, two isomeric macrocycles, a C_1-symmetric one as the minor fraction (**MC1**) and a C_{2v}-symmetric one as the major product (**MC2**), were successfully obtained when 4-*tert*-butylphenyl groups were introduced. In contrast, when bulky 3,5-bis(trifluoromethyl)phenyl groups were introduced, only inherent chiral macrocyclic products (**MC3**) were obtained in high yield. Their molecular structures are unambiguously characterized by NMR, mass spectra and X-ray crystallographic characterization. In addition, these macrocycles show blue to green emissions with high fluorescence quantum yields (Φ_F up to 0.69). Owing to the existence of inherent chirality, two enantiomers of N-doped macrocycle **MC1** were successfully isolated by chiral resolution, enabling detailed investigation of its chiroptical properties through circular dichroism (CD) and circularly polarized luminescence (CPL) spectroscopy.

Results and Discussion

The syntheses of N-doped macrocycles **MC1–3** are shown in Scheme 1. Diamines **1a** and **1b** were synthesized by double Pd-catalyzed C–N coupling reaction of 4,6-dichlorobenzene-1,3-diamine with phenyl bromide (see Supporting Information File 1). Subsequent Buchwald–Hartwig reaction with 1,3-dibromo-7-*tert*-butylpyrene (**2**) gave the [2 + 2] macrocyclic precursors **3a**,**b** as the major product in 16%/10% yields, and trace amounts of higher oligomers as detected by mass spectrometry. Notably, compounds **3a**,**b** could be viewed as the aza[1_4]metacyclophane derivatives, in which two benzene rings are replaced by two pyrenes. The Pd-catalyzed arylation of **3a** with $Pd(OAc)_2$, $PMe(t\text{-}Bu)_2 \cdot HBF_4$ and DBU under microwave conditions gave two isomeric macrocycles **MC1** and **MC2** with four newly formed C–C bonds in yields of 5% and 90%, respectively. For **MC2,** four C–C bonds are formed between the dichlorobenzene units and *tert*-butylphenyl groups, generating two dihydroindolo[2,3-*b*]carbazole subunits. In contrast, there is only one newly formed C–C bond between the dichlorobenzene unit and one pyrene moiety for **MC1**. Interestingly, for the cyclization of **3b**, only compound **MC3** was obtained in 85% yield, which is probably attributed to larger steric hindrance deriving from bis(trifluoromethyl)phenyl groups. These macro-

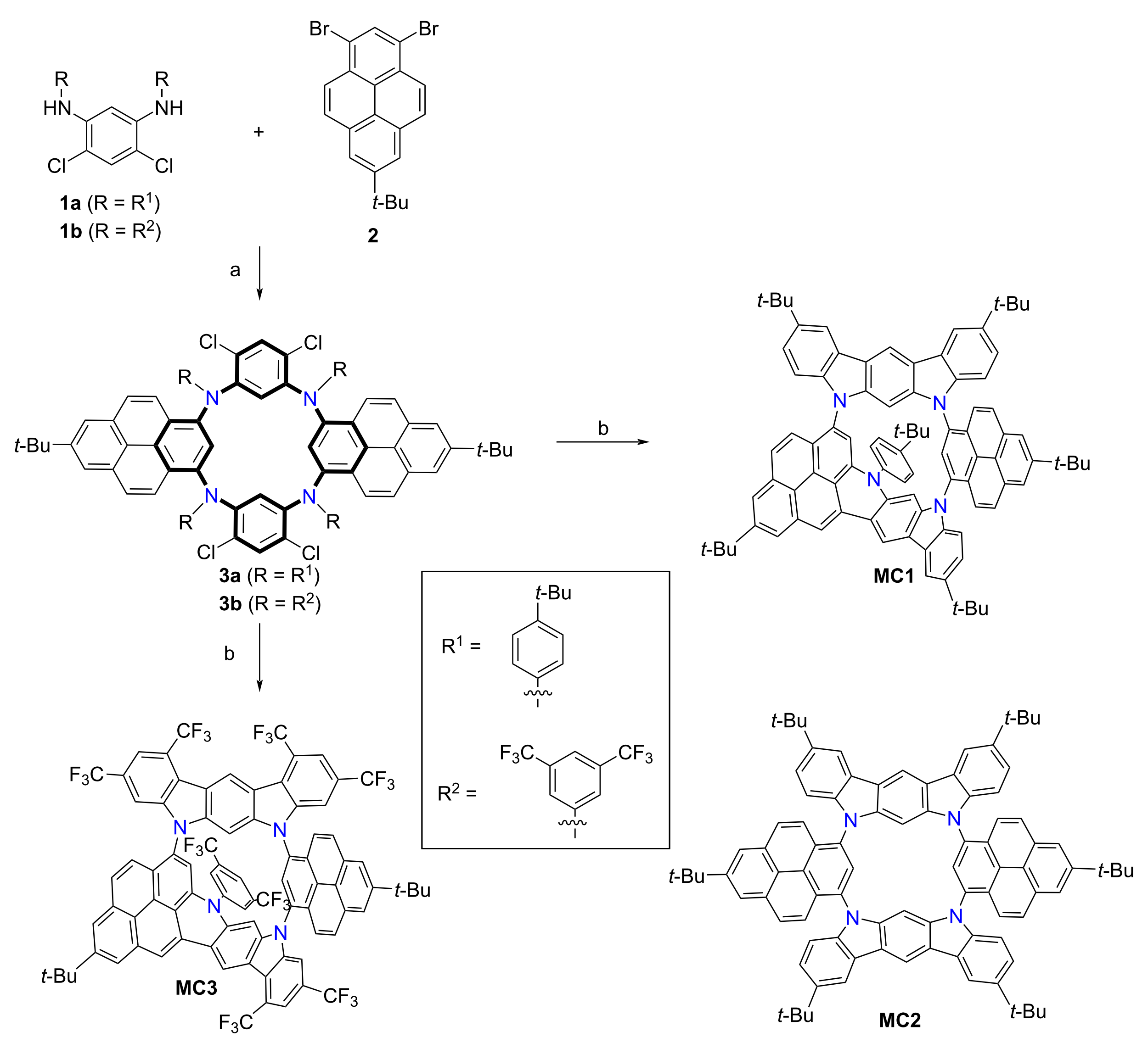

Scheme 1: Synthesis of N-doped macrocycles **MC1**, **MC2**, and **MC3**. Reaction conditions: a) $Pd_2(dba)_3$, P*t*-Bu_3·HBF_4, NaO*t*-Bu, toluene, 110 °C, 24 h. **3a**: 16%; **3b**: 10%. b) $Pd(OAc)_2$, PMe(*t*-Bu)$_2$·HBF_4, 1,8-diazabicyclo[5.4.0]undec-7-ene (DBU), DMAc, microwave, 170 °C, 5 h. **MC1**: 5%; **MC2**: 90%; **MC3**: 85%.

cycles show good solubility in common solvents, and their chemical structures have been unambiguously characterized by NMR spectroscopy, mass spectrometry, and X-ray crystallography.

Single crystals suitable for X-ray diffraction measurements of compounds **3a**, **MC2**, and **MC3** were successfully obtained to reveal their molecular structures. In the crystal structure of **3a** (Figure 2a), the two pyrene units are nearly coplanar with a dihedral angle of 170°. The two dichlorobenzene rings are parallel to each other and perpendicular to the pyrene plane, and the four *tert*-butylphenyl groups are directed on one side of the pyrene plane to minimize steric repulsion. **MC2** takes a C_{2v}-symmetric saddle-shaped geometry with two planar dihydroindolo[2,3-*b*]carbazole subunits orienting upwards with a dihedral angle of 75° and two pyrene units downwards (Figure 2b). Besides, the central cavity is highly symmetric, and the shortest diameters are determined to be 4.34 Å and 4.99 Å, respectively. In contrast to **MC2**, **MC3** shows an asymmetric geometry due to the fusion of the pyrene unit (Figure 2c). The two pyrene units are oriented antiparallel, which is distinctive from that observed in **3a** and **MC2**. Notably, the pyrene-fused moiety is highly curved with a bending angle of 85.3° as defined by the angle of the planes of the terminal rings. In the molecular arrangement, a pair of enantiomers exists in each cell for **MC3** (Figure 2d). Considering the C–C single bonds between the

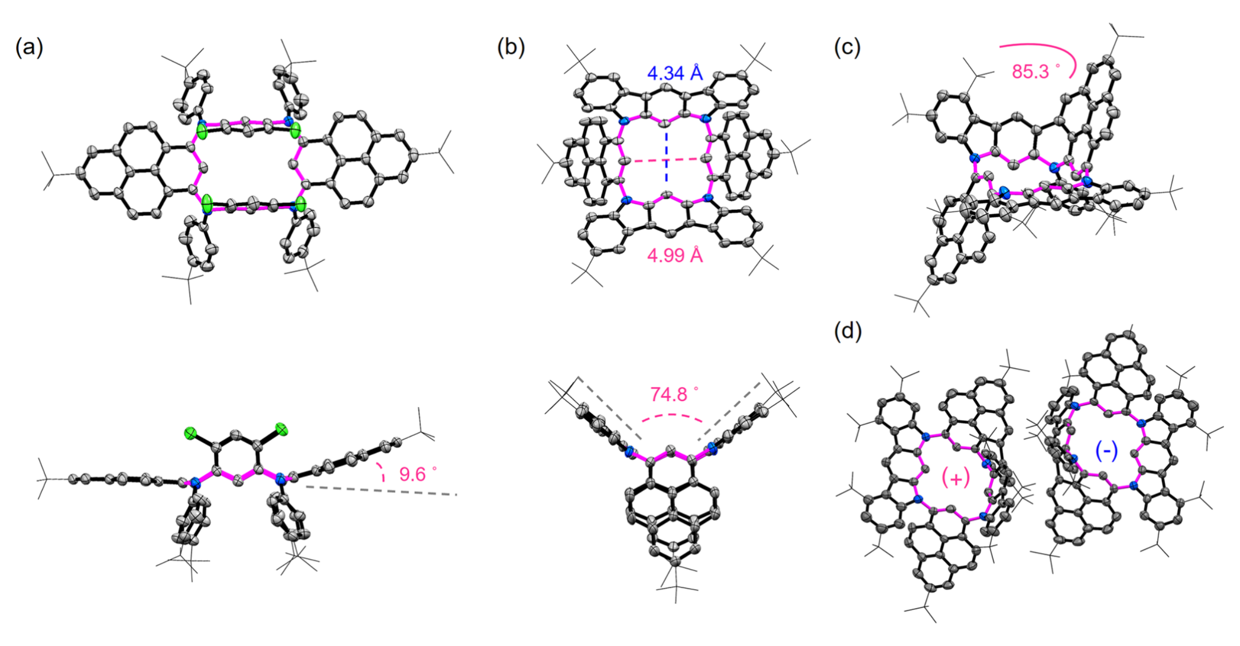

Figure 2: Crystal structures of compounds (a) **3a**, (b) **MC2**, and (c) **MC3**. (d) Molecular arrangements of **MC3**. Hydrogen atoms are omitted for clarity.

π-subunits, isomerization among different molecular configurations might occur via rotations. To further investigate the conformational stability of **MC3**, theoretical calculations were performed to evaluate the energy barriers of isomerization. As shown in Figure S3 (Supporting Information File 1), the configuration observed in the crystal structure has the lower energy by 24.0 kcal mol^{-1} than that of the isomeric structure with two pyrene units at the same side. The energy barrier was calculated to be 66.7 kcal mol^{-1}, indicating **MC3** is highly conformationally stable.

The optical properties of the synthesized macrocycles were investigated in dichloromethane (Figure 3). The precursors **3a**,**b** show intense absorptions with maxima at 425 nm and 395 nm, respectively. Correspondingly, **3a** exhibits a deep blue emission at 453 nm with a quantum yield (Φ_F) of 0.79, while a hypsochromic shift of the signal for **3b** to 424 nm is observed and the Φ_F value is decreased to 0.22 due to the electron-deficient character of the 3,5-bis(trifluoromethyl)phenyl groups. The absorption maximum of **MC1** is more redshifted by 42 nm compared to **MC2**, which is attributed to the extended conjugation after the fusion of one pyrene unit. Similarly, both **MC1** and **MC2** have higher Φ_F values of 0.45 and 0.69 than compound **MC3** ($\Phi_F = 0.13$). The optical energy bandgaps were determined to be 2.48 eV for **MC1**, 2.61 eV for **MC2**, and 2.68 eV for **MC3**, respectively, based on the onset absorptions. **MC2** and **MC3** display strong blue emissions at 487 nm and 458 nm, respectively, while **MC1** exhibits green photoluminescence at 516 nm.

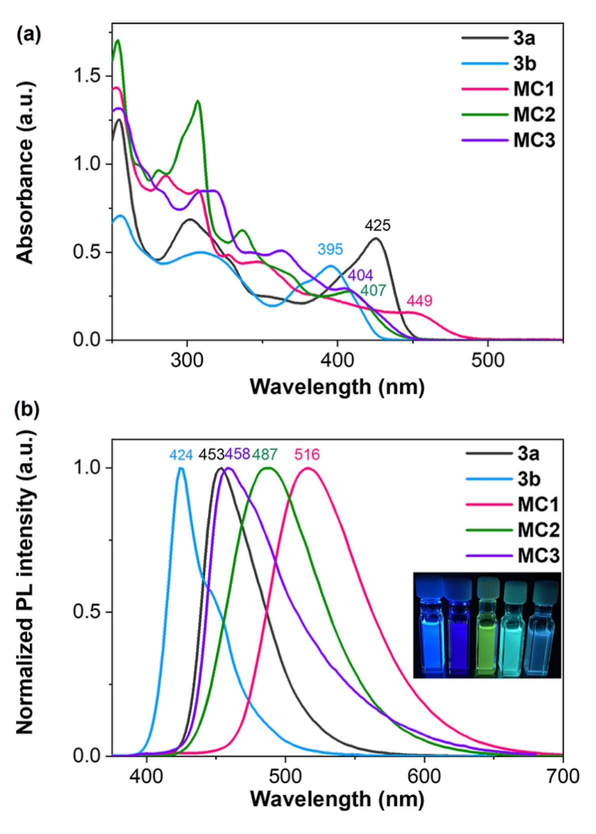

Figure 3: (a) Absorptions and (b) emissions of compounds **3a**, **3b**, **MC1**, **MC2**, and **MC3** measured in dichloromethane at room temperature. The inset shows the photographs under UV light at 365 nm. The concentration is 10 μM.

To better understand the electronic structures of these N-doped macrocycles, theoretical calculations on the frontier molecular orbitals were carried out based on the optimized structures. As shown in Figure 4, the distributions of the highest occupied molecular orbitals (HOMOs) are disjointed from that of the lowest unoccupied molecular orbitals (LUMOs). Specifically, the HOMOs of **MC1** and **MC3** mainly distribute on the fused pyrene moiety and the substituent on the N atom, while the LUMOs localize on the other pyrene unit. In contrast, the HOMOs of **MC2** are mainly located on two dihydroindolo[2,3-*b*]carbazole subunits, and the LUMOs localize on two pyrene units. Owing to electron-deficient character, both the HOMO and LUMO energy levels of **MC3** are obviously decreased in comparison to **MC1** and **MC2**. Accordingly, the calculated energy gaps are 2.81 eV for **MC1**, 3.01 for **MC2** and 3.08 for **MC3**, respectively, which are in line with the optical ones.

In view of the existence of inherent chirality for both **MC1** and **MC3**, chiral resolutions using chiral high-performance liquid chromatography (HPLC) were performed. Due to insufficient solubility, **MC3** failed in chiral separation via preparative chiral columns. Fortunately, two enantiomers of **MC1** were successfully isolated with a Daicel Chiralpak IF column (Figure S1, Supporting Information File 1). The absolute configuration of the separated enantiomers of **MC1** was determined based on the calculated CD spectra (Figure S4, Supporting Information File 1). The first fraction was defined as the (+)-enantiomer, and the second fraction was assigned as the (−)-enantiomer. As shown in Figure 5, the CD spectra displayed mirror images with positive and negative Cotton effects at wavelengths from 250 to 500 nm, indicating strong chiroptical responses. (+)-**MC1** shows five positive Cotton effects at 259, 305, 355, 392, and 453 nm, as well as four negative Cotton effects at 288, 317, 331, and 432 nm, respectively. (−)-**MC1** exhibits a mirror image with the opposite signals to that of (+)-**MC1**. The maximum absorption dissymmetry factor (g_{abs}) value of 1.1×10^{-3} at 453 nm is observed (Figure 5b), which is derived from the $S_0 \rightarrow S_1$ transition. Similar to the CD spectra, mirror images of the CPL spectra (Figure S2, Supporting Information File 1) and luminescence dissymmetry factor (g_{lum}) plots (Figure 5c) were observed for the enantiomers of **MC1**. However, both enantiomers show a low g_{lum} value below 1.0×10^{-3}.

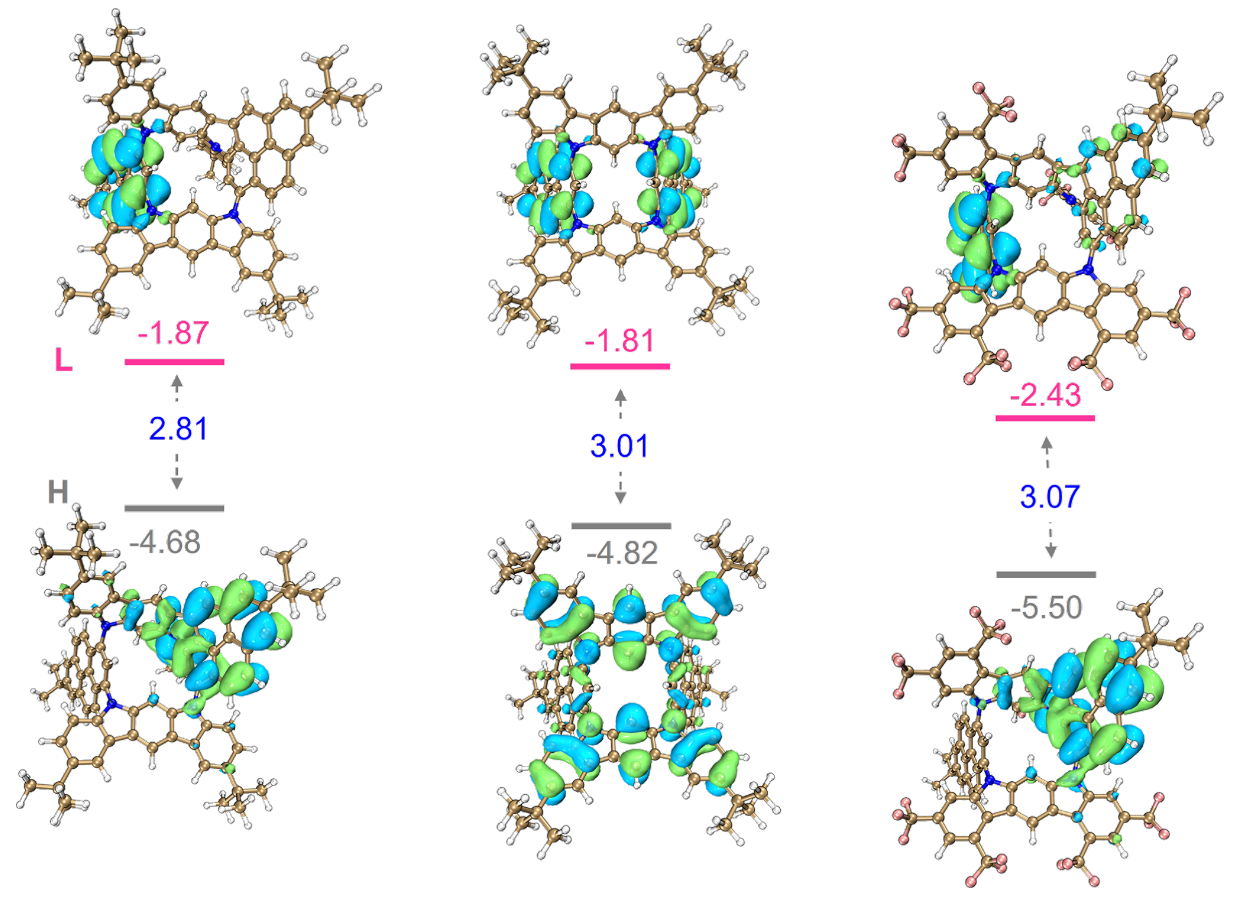

Figure 4: Calculated frontier molecular orbitals and relative energy levels of **MC1** (left), **MC2** (middle), and **MC3** (right) calculated at the B3LYP/6-31G(d) level of theory.

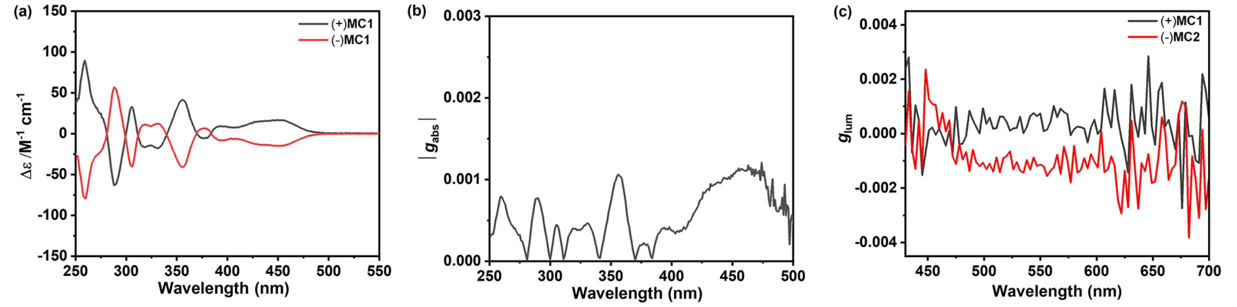

Figure 5: (a) CD spectra, (b) |g_{abs}|, and (c) g_{lum} values of enantiomers of **MC1** measured in dichloromethane at room temperature. The concentrations were 10 μM.

Conclusion

In summary, we demonstrated the synthesis and characterizations of N-doped macrocycles **MC1–3** by palladium-catalyzed arylations. The molecular structures of the macrocyclic precursors and targets were unambiguously revealed by X-ray crystallographic characterization. These macrocycles exhibit strong fluorescence with Φ_F values up to 0.69. Remarkably, **MC1** and **MC3** are inherent chiral owing to their C_1 symmetric structures. The enantiomers of **MC1** were successfully isolated by chiral resolution, which indicate a g_{abs} value of 1.1×10^{-3} and a g_{lum} value at the level of 10^{-4}. Our work represents one of the rare examples of non-classical chiral macrocycles, providing insights into molecular design of chiral macrocycles with high emissions.

Supporting Information

Supporting Information File 1

Experimental procedures, synthetic details, and X-ray crystallographic data.
[https://www.beilstein-journals.org/bjoc/content/supplementary/1860-5397-21-149-S1.pdf]

Supporting Information File 2

Crystallographic information files for compounds **3a**, **MC2**, and **MC3**.
[https://www.beilstein-journals.org/bjoc/content/supplementary/1860-5397-21-149-S2.zip]

Acknowledgements

We thank Dr. Faan-Fung Hung and Prof. Chi-Ming Che for the assistance in measurements of photophysical and chiroptical properties. Prof. Zhaohui Wang from Tsinghua University is acknowledged for helpful discussions. We thank the UGC funding administered by HKU for supporting the Time-of-Flight Mass Spectrometry Facilities under the Support for Interdisciplinary Research in Chemical Science. We acknowledge the computer cluster (HPC2021) of HKU for generous allocations of compute resources.

Funding

This work was supported by the Hong Kong Research Grants Council (27301720, 17304021), National Natural Science Foundation of China (22122114). J. L. is grateful for the funding from The University of Hong Kong (HKU) and ITC to the SKL. The work described in this paper was partially supported by a grant from the Co-funding Mechanism on Joint Laboratories with the Chinese Academy of Sciences (CAS) sponsored by the Research Grants Council of the Hong Kong Special Administrative Region, China and the CAS (Project No. JLFS/P-701/24 and Project No. JLFS/P-404/24).

Author Contributions

Shuhai Qiu: investigation; methodology; writing – original draft. Junzhi Liu: conceptualization; funding acquisition; project administration; writing – review & editing.

ORCID® iDs

Junzhi Liu - https://orcid.org/0000-0001-7146-0942

Data Availability Statement

All data that supports the findings of this study is available in the published article and/or the supporting information of this article.

References

1. Sun, G.; Zhang, X.; Zheng, Z.; Zhang, Z.-Y.; Dong, M.; Sessler, J. L.; Li, C. *J. Am. Chem. Soc.* **2024,** *146,* 26233–26242. doi:10.1021/jacs.4c07924
2. Zhang, X. X.; Bradshaw, J. S.; Izatt, R. M. *Chem. Rev.* **1997,** *97,* 3313–3362. doi:10.1021/cr960144p
3. Kellogg, R. M. *Angew. Chem., Int. Ed. Engl.* **1984,** *23,* 782–794. doi:10.1002/anie.198407821
4. Yamashita, K.; Tabata, Y.; Yamakawa, K.; Mochizuki, T.; Matsui, K.; Hatano, M.; Ishihara, K. *J. Am. Chem. Soc.* **2023,** *145,* 26238–26248. doi:10.1021/jacs.3c08905

5. Wang, J.-Q.; Han, X.-N.; Han, Y.; Chen, C.-F. *Chem. Commun.* **2023,** *59,* 13089–13106. doi:10.1039/d3cc04187e
6. Hasegawa, M.; Nojima, Y.; Mazaki, Y. *ChemPhotoChem* **2021,** *5,* 1042–1058. doi:10.1002/cptc.202100162
7. Sun, Z.; Tang, H.; Wang, L.; Cao, D. *Chem. – Eur. J.* **2025,** *31,* e202404217. doi:10.1002/chem.202404217
8. Szumna, A. *Chem. Soc. Rev.* **2010,** *39,* 4274–4285. doi:10.1039/b919527k
9. Dalla Cort, A.; Mandolini, L.; Pasquini, C.; Schiaffino, L. *New J. Chem.* **2004,** *28,* 1198–1199. doi:10.1039/b404388j
10. Böhmer, V.; Kraft, D.; Tabatabai, M. *J. Inclusion Phenom. Mol. Recognit. Chem.* **1994,** *19,* 17–39. doi:10.1007/bf00708972
11. Higashibayashi, S.; Sakurai, H. *J. Am. Chem. Soc.* **2008,** *130,* 8592–8593. doi:10.1021/ja802822k
12. Tan, Q.; Higashibayashi, S.; Karanjit, S.; Sakurai, H. *Nat. Commun.* **2012,** *3,* 891. doi:10.1038/ncomms1896
13. Wu, Y.-T.; Hayama, T.; Baldridge, K. K.; Linden, A.; Siegel, J. S. *J. Am. Chem. Soc.* **2006,** *128,* 6870–6884. doi:10.1021/ja058391a
14. Shi, S.-Q.; Cui, C.-C.; Xu, L.-L.; Zhang, J.-P.; Hao, W.-J.; Wang, J.; Jiang, B. *Nat. Commun.* **2024,** *15,* 8474. doi:10.1038/s41467-024-52823-3
15. Luo, Y.; Luo, S.; Zhu, Q. *J. Org. Chem.* **2025,** *90,* 5307–5322. doi:10.1021/acs.joc.5c00479
16. Zhang, F.; Du, X.-S.; Zhang, D.-W.; Wang, Y.-F.; Lu, H.-Y.; Chen, C.-F. *Angew. Chem., Int. Ed.* **2021,** *60,* 15291–15295. doi:10.1002/anie.202104259
17. Zhao, F.; Zhao, J.; Liu, H.; Wang, Y.; Duan, J.; Li, C.; Di, J.; Zhang, N.; Zheng, X.; Chen, P. *J. Am. Chem. Soc.* **2023,** *145,* 10092–10103. doi:10.1021/jacs.3c00306
18. Ma, Y.; Han, Y.; Hou, X.; Wu, S.; Chi, C. *Angew. Chem., Int. Ed.* **2024,** *63,* e202407990. doi:10.1002/anie.202407990
19. Qiu, S.; Zhao, Y.; Zhang, L.; Ni, Y.; Wu, Y.; Cong, H.; Qu, D.-H.; Jiang, W.; Wu, J.; Tian, H.; Wang, Z. *CCS Chem.* **2023,** *5,* 1763–1772. doi:10.31635/ccschem.023.202302830
20. Ito, A.; Ono, Y.; Tanaka, K. *J. Org. Chem.* **1999,** *64,* 8236–8241. doi:10.1021/jo990983m
21. Vale, M.; Pink, M.; Rajca, S.; Rajca, A. *J. Org. Chem.* **2008,** *73,* 27–35. doi:10.1021/jo702151n
22. Ito, A.; Inoue, S.; Hirao, Y.; Furukawa, K.; Kato, T.; Tanaka, K. *Chem. Commun.* **2008,** 3242–3244. doi:10.1039/b805333b
23. Ito, A. *J. Mater. Chem. C* **2016,** *4,* 4614–4625. doi:10.1039/c6tc00973e
24. Wang, M.-X. *Acc. Chem. Res.* **2012,** *45,* 182–195. doi:10.1021/ar200108c
25. Shi, Y.; Li, X.; Di, J.; Xue, Y.; Zhang, N.; Jin, T.; Chen, C.-F.; Chen, P. *CCS Chem.* **2025,** *7,* 2781–2797. doi:10.31635/ccschem.024.202404995

License and Terms

The definitive version of this article is the electronic one which can be found at:
https://doi.org/10.3762/bjoc.21.149

BEILSTEIN JOURNAL OF ORGANIC CHEMISTRY

Measuring the stereogenic remoteness in non-central chirality: a stereocontrol connectivity index for asymmetric reactions

Ivan Keng Wee On‡, Yu Kun Choo‡, Sambhav Baid and Ye Zhu*

Full Research Paper

Open Access

Address:
Department of Chemistry, Faculty of Science, National University of Singapore, 3 Science Drive 2, Singapore 117543

Email:
Ye Zhu* - chmzhu@nus.edu.sg

* Corresponding author ‡ Equal contributors

Keywords:
asymmetric reactions; axial chirality; catalysis; planar chirality; stereocontrol

Beilstein J. Org. Chem. **2025,** *21,* 1995–2006.
https://doi.org/10.3762/bjoc.21.155

Received: 14 July 2025
Accepted: 19 September 2025
Published: 30 September 2025

This article is part of the thematic issue "Non-central chirality in organic chemistry".

Associate Editor: N. Yoshikai

Abstract

Despite the rapid development of asymmetric synthesis, judging the remoteness of stereocontrol has remained an intuitive and empirical practice, particularly for reactions that create non-central chirality. We put forward a stereocontrol connectivity index to parameterize asymmetric reactions according to the bond connectivity relationships between the prochiral stereogenic elements, the reactive sites, and the stereochemical-defining substituents. The indices can be generated based on analysis of the chemical structures of the starting materials and products, without mechanistic insights of the transformation. Representative examples of reactions that establish point chirality, axial chirality, planar chirality, and “inherent chirality” are illustrated using the stereocontrol connectivity index produced following a unified 3-step process. Application of such stereochemical classification could facilitate the development of new synthetic methodologies and catalyst systems to construct diverse chiral molecules.

Introduction

Chirality is a ubiquitous and fundamental phenomenon in nature and thus holds an irreplaceable position in organic synthesis. At its most rudimental definition, chirality in a molecule is characterized by the absence of mirror planes and centers of inversion. Central chirality arises when four distinct substituents (a, b, c, and d) are arranged tetrahedrally around a central atom (Scheme 1A). Non-central chirality – such as axial and planar chirality – are becoming increasingly important in pharmaceuticals, catalysts, and advanced materials due to their unique stereogenic scaffolds and associated properties. Consequently, synthetic chemists have been pursuing molecules featuring these forms of non-central chirality, where the stereogenic elements are not localized on a single central atom (Scheme 1B).

While chemists often classify chirality (stereogenicity) into distinct types according to the stereogenic elements, such as

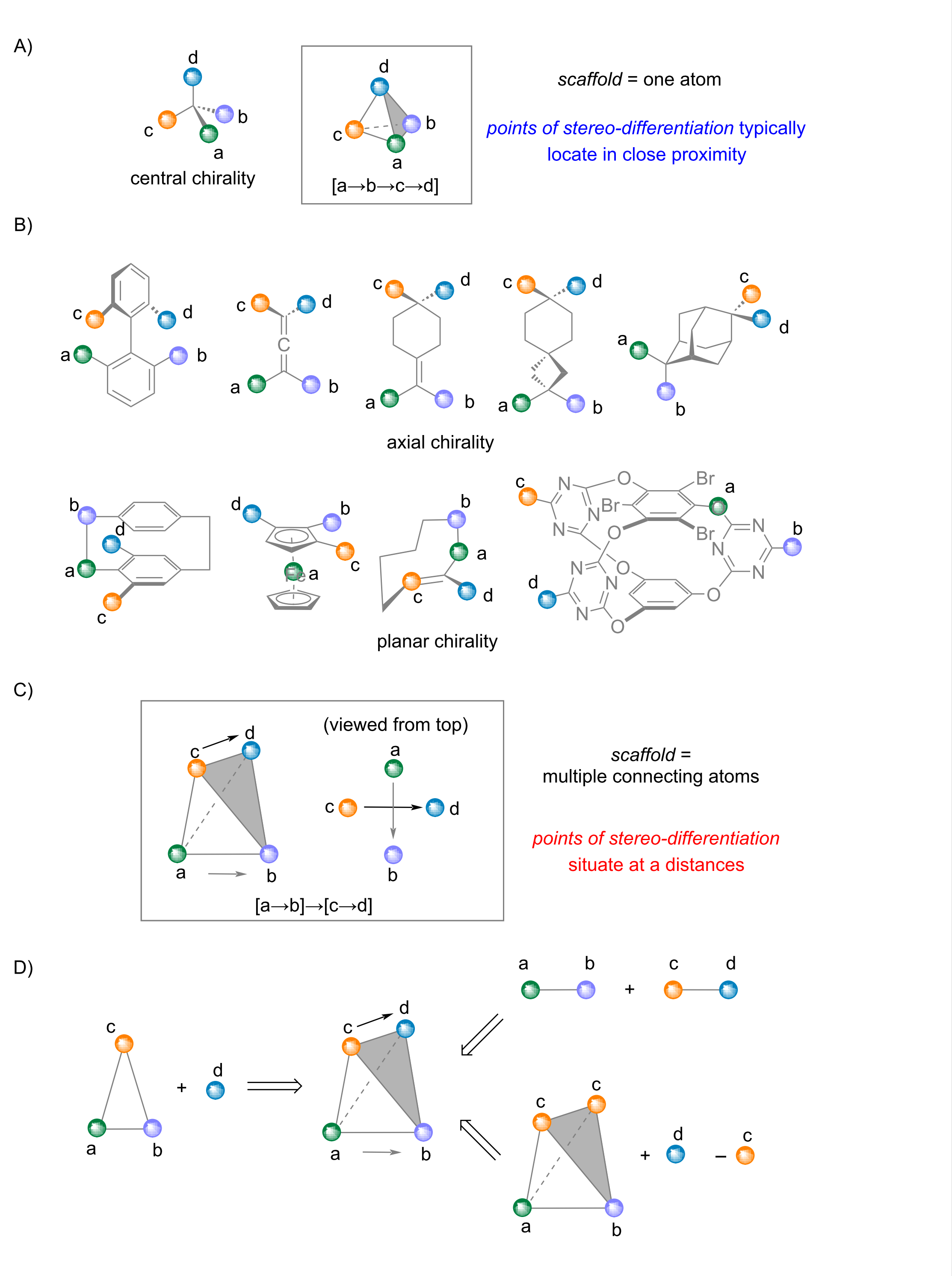

Scheme 1: Illustration of chirality and the intrinsic remoteness of stereogenic elements for axial chirality and planar chirality.

central (point) chirality, axial chirality, and planar chirality, these categories are inherently related. They can be viewed as arrangements of groups within three-dimensional molecular frameworks that restrict conformational freedom. The geometric scaffolds can be a central atom, an axis, or a plane, and the combination and spatial arrangement of chemically distinct substituents establish the stereogenicity. Therefore, despite the apparent differences among these scaffolds, the various types of chirality are permutations of substituents on diverse stereogenic elements (Scheme 1C).

Although this analysis offers a unified view of chirality, the realization of these chiral systems through asymmetric synthesis is far from trivial. Stereogenic compounds can be generated from achiral starting substrates by various means that assemble the four distinct substituents (a, b, c, and d) (Scheme 1D). In the case of central chirality, the differentiating substituents are often directly attached to the newly formed stereocenter. By contrast, for non-central chirality, the pairs of substituents (a and b, c and d) are separated in space because the stereogenic scaffolds span multiple atoms. Consequently, bond cleavage and formation occur at positions that are distant from the stereogenic elements and remote from the actual points of differentiation among the substituents.

Intuitively, the intrinsic spatial separation among prochiral stereogenic elements, the reactive sites, and the stereochemical-defining substituents makes stereoinduction for non-central chirality using a chiral catalyst or reagent particularly challenging. However, a quantitative parameterization of asymmetric reactions remains unavailable, and the remoteness of stereocontrol for reactions that establish non-central chirality is judged based on empirical chemical intuition. While developing catalytic methods to establish remote stereogenic elements, we became increasingly interested in parameterizing the relay of stereochemical information from the chiral catalysts to the prochiral substrates. In this study, we propose a stereocontrol connectivity index that quantitatively characterizes asymmetric reactions. The index could serve as a basis for classifying asymmetric reactions according to the positioning of stereochemically relevant elements, independent of the type of transformation. Additionally, the index enables the identification of the minimal set of structural features in a molecule that are recognized by chiral catalysts to achieve stereocontrol.

Results and Discussion

We envisaged that the stereocontrol connectivity index should reflect the bond connectivity of prochiral stereogenic elements, the reactive sites, and the stereochemical-defining substituents. These structural elements contribute to the transmission of chirality from the chiral catalysts and reagents to the prochiral substrates, thereby representing the minimal structural features recognized by chiral catalysts or reagents.

Furthermore, the index should be derived from straightforward analysis of the chemical structures of the substrates and the products without the need for conformational analysis and mechanistic understanding of the catalytic process. The chemical reaction is the movements of electrons that change the bond connections, which can be denoted by the bond break and bond formation. The stereochemical outcome is expressed as the chirality of the product, which can be designated following the Cahn–Ingold–Prelog rules.

We now put forward a stereocontrol connectivity index [i_j] for a transformation that encodes the bond-connecting relationship between the establishment of chirality and the site of reaction. The index [i_j] of asymmetric reactions can be assigned following a 3-step process:

Step 1: Identification of atoms involved in bond changes.

1.1 Determine which bonds are newly formed and which are cleaved in the transformation.

1.2 Label all atoms directly involved in these bond changes.

Step 2: Identification of atoms responsible for stereochemical outcome.

2.1 Identify the new stereogenic element formed in the product.

2.2 Determine, according to the Cahn–Ingold–Prelog (CIP) rules, the atoms that distinguish the newly created stereogenic element's configuration. These are the atoms whose identities represent the first point of difference between the set of substituents in assigning the configuration of the new stereogenic element. One or two sets of atoms could be identified.

a) These atoms labeled in step 1 are considered higher in priority than any other atoms.

b) If the comparison is down to between an atom already labeled in step 1 and one other atom, such comparison and this set of atoms are excluded. In other words, the number set of atoms will be reduced by one.

c) Consider "dummy" atoms from multiple bonds as lower priority than real atoms of the same type.

Step 3: Determination of stereocontrol pathways.

For each set of atoms identified in step 2:

3.1 Find the shortest path connecting the labeled atoms from step 1 to each atom identified in step 2.

3.2 Count the minimum number of connecting bonds (i).

3.3 Count the number of bonds shared (j) between the shortest paths.

The reaction is then assigned a stereocontrol connectivity index of $[i_j]$ or $[i_j,i'_{j'}]$, depending on the number of sets of atoms identified in step 2 (one or two sets).

Before discussing applications to non-central chirality, we analyze two examples of stereoselective reactions that establish central chirality to illustrate the concept of stereogenic remoteness measured using the stereocontrol connectivity index (Scheme 2). A detailed process for assigning the index is shown in Scheme 2A for asymmetric hydrogenation of 2-butanone [1]. The atoms involved in bond cleavage and bond formation are highlighted in orange color. The atoms responsible for assignment of the stereochemical configuration of the products are highlighted in grey color. The shortest connecting bonds between them are colored red. Accordingly, the asymmetric hydrogenation of 2-butanone is designated as $[2_0]$ process because there are two connecting bonds between the stereogenic carbon and the stereochemical differentiation atoms, and they do not share a common path.

Typically, in stereoselective reactions involving central chirality, the proximity between the site of reaction and the points of stereo-differentiation means that the indices $[i_j]$ are expected to have small values. In general, $j = 0$ in the index $[i_j]$ of an addition reaction to two prochiral faces of a planar substrate, where the prostereogenic carbon is part of the reaction site. However, this is not always the case, particularly in remote desymmetrization reactions [2-8]. For instance, the catalytic desymmetrization of phosphine oxides [9] will be defined as a $[9_4]$ process (Scheme 2B). As such, the index $[i_j]$ indicates the number of connecting bonds (i) between the reaction site and the points of stereochemical differentiation, and the number of connecting bonds (j) between the reaction site and the stereogenic center. The indices are not defined by the reaction types, the mode of catalysis, or the nature of the stereogenic centers.

Unlike central chirality, the stereogenic remoteness of non-central chirality could not be measured using a central stereogenic atom as the starting point. The stereocontrol connectivity index allows parameterization for reactions that establish axially chirality and planar chirality regardless of the absence of stereogenic centers. Applications to reactions that forge axial chirality follow the same 3-step procedure. The two substituents at each

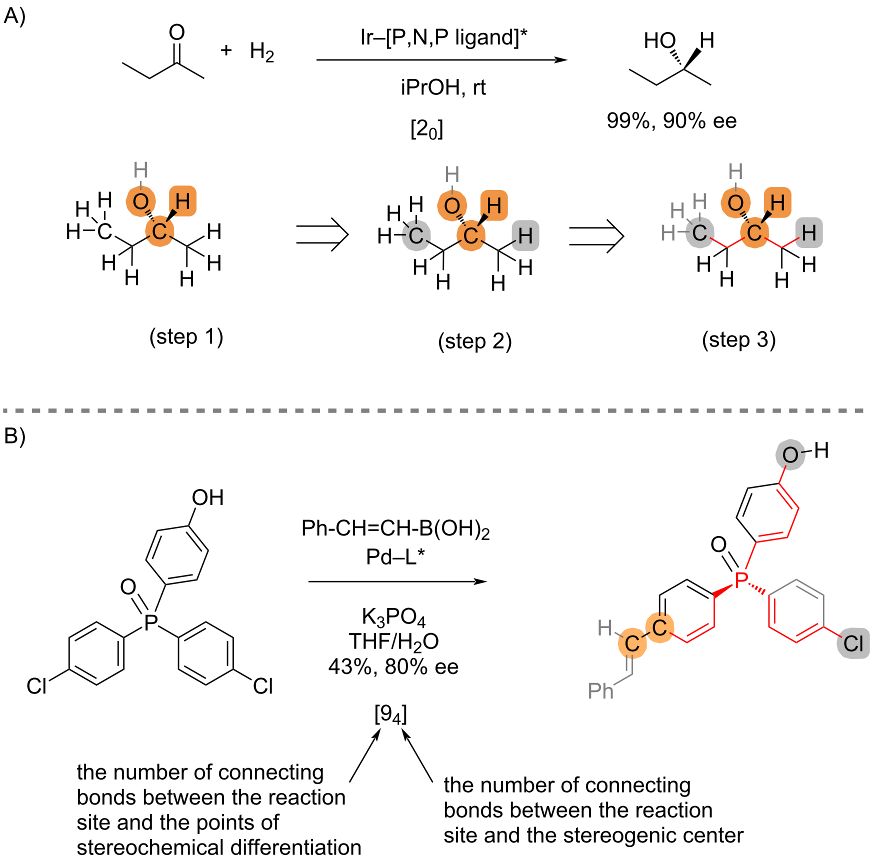

Scheme 2: Illustrations of assignment using point chirality.

end of the stereogenic axis are ranked based on the CIP priority rules, and the set(s) that do not involve bond formation and bond cleavage are used to identify the points of stereochemical differentiation.

Different stereocontrol strategies could be employed to achieve asymmetric synthesis of axially chiral biaryls (Scheme 3). The stereocontrol connectivity indices are assigned following the 3-step procedure for all types of strategies including cyclization,

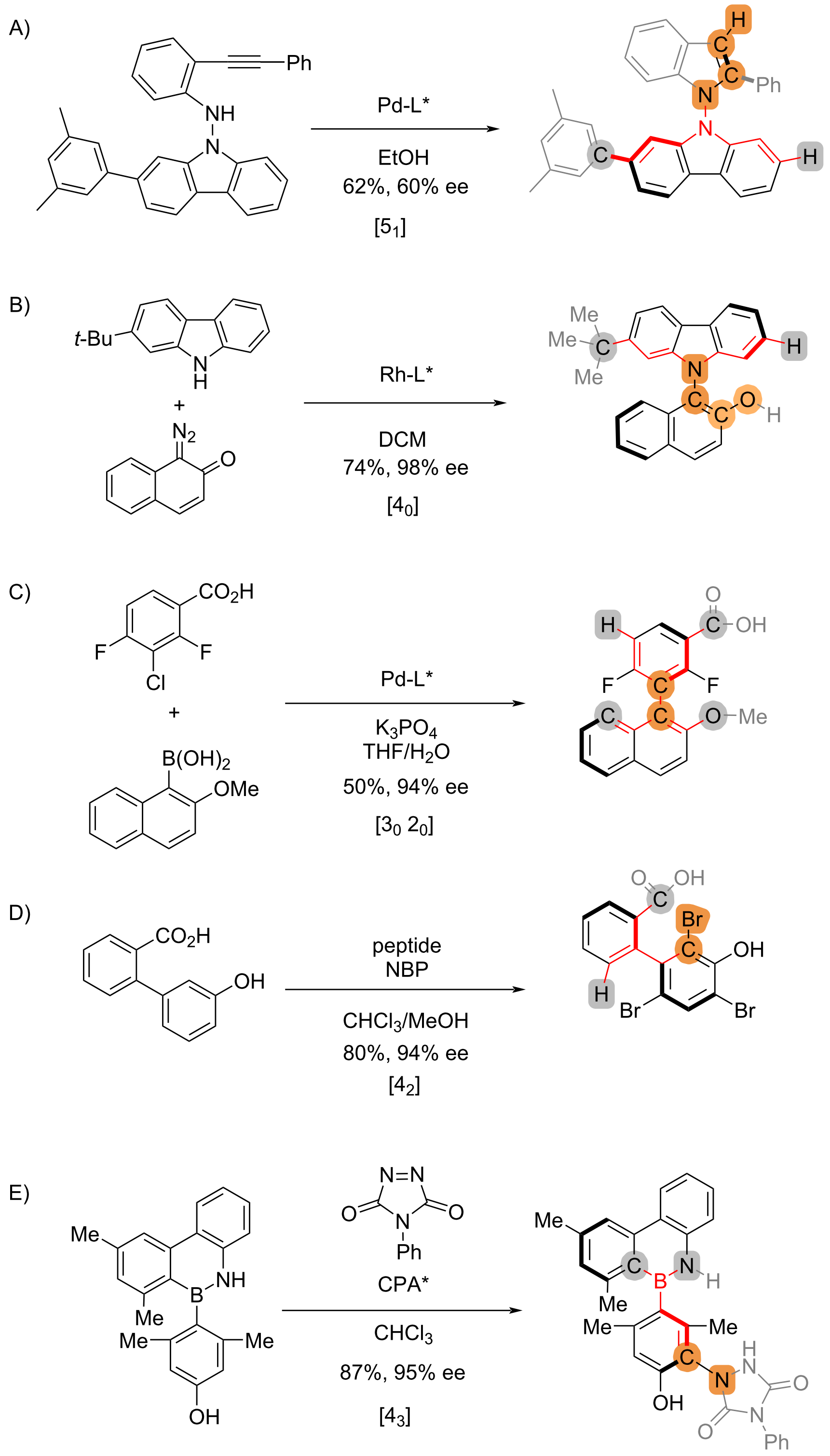

Scheme 3: Examples of reactions that establish axial chirality derived from biaryls.

biaryl coupling, and desymmetrization, irrespective of the chemical identity of the newly established chiral axis including C–C [10,11] (Scheme 3C and 3D), C–N [12] (Scheme 3B), N–N [13] (Scheme 3A), and C–B [14] (Scheme 3E) bonds. In the case of an asymmetric cross-coupling reaction (Scheme 3C) [10], both sets of the substituents on individual aryl groups are considered because neither is involved in the bond formation/cleavage. Accordingly, the catalyst-controlled atroposelective Suzuki–Miyaura coupling of biaryls is designated as [3_0 2_0].

In addition to biaryls, axially chiral allenes are popular targets for asymmetric synthesis. Three examples of asymmetric reactions that form axially chiral allenes are shown in Scheme 4. For example, the enantioselective nucleophilic substitution to yield chiral allenes [15] is defined as [6_0] (Scheme 4A), while the desymmetrizing reactions of allenes [16] (Scheme 4B) and anthracenylidene [17] (Scheme 4C) are both classified as [5_4]. In the cases of Scheme 3A and 3C, the reaction intermediates (i.e., the *p*-quinone methide and the carbopalladation intermediate, respectively) are neglected to simplify the assignment, considering such information is inexplicit based on the chemical transformations alone and is not available in commonly used chemical databases. Therefore, the index is a denotation of the overall transformation, which is not always representative of the stereochemical-determining elementary step.

The stereocontrol connectivity indices can be extended to reactions that establish planar chirality (Scheme 5). In the case of metallocenes, the metal is considered to be σ-bonded to the arene ring for convenience. In other words, the centroid atom is treated as a pseudo-tetrahedral center, with the metal regarded as one of the substituents. Accordingly, a C–H activation reaction that forms planar chiral ferrocenes [18] is assigned as [3_0] (Scheme 5A). For cyclophanes, if the bond formation or cleavage is on the stereogenic arene, the stereochemical differentiation should at least be traced to the two pilot atoms that are directly attached, but not within the stereogenic plane – similar to the assignment of stereochemistry for cyclophanes. This way, the asymmetric Pd-catalyzed coupling [19,20] would be assigned as [3_0] (Scheme 5B and 5C). On the other hand, if the bond formation/cleavage is within the macrocycle, the stereochemical differentiation atoms are traced to the stereogenic

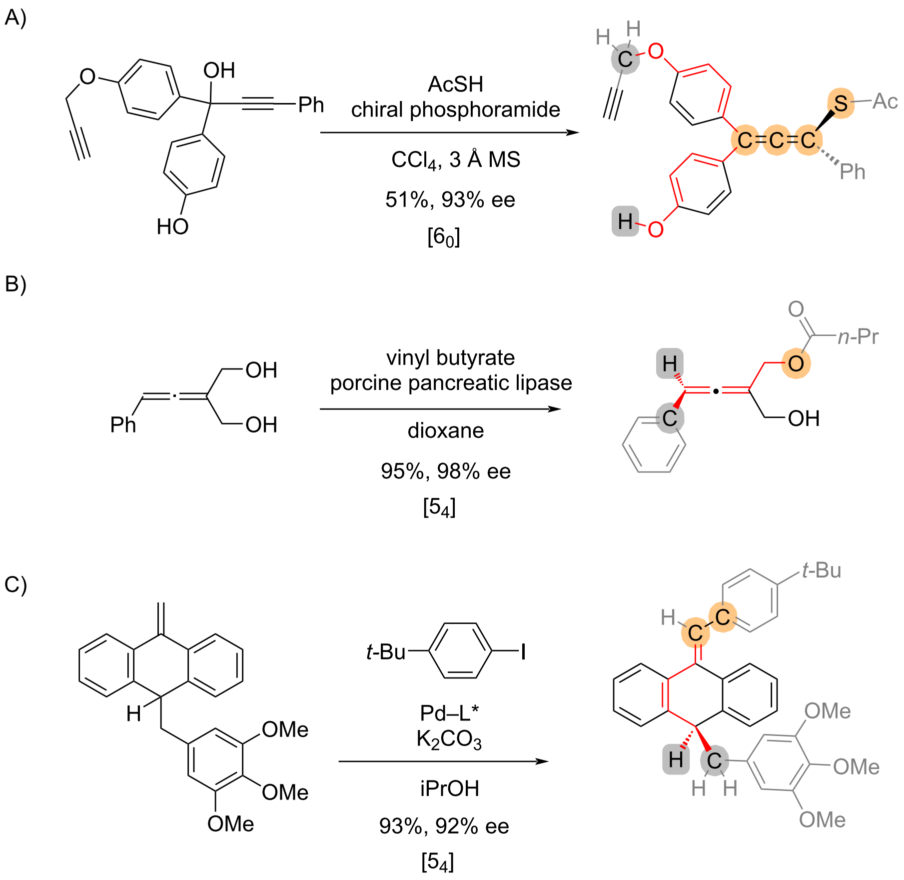

Scheme 4: Examples of reactions that establish axial chirality derived from C=C bonds.

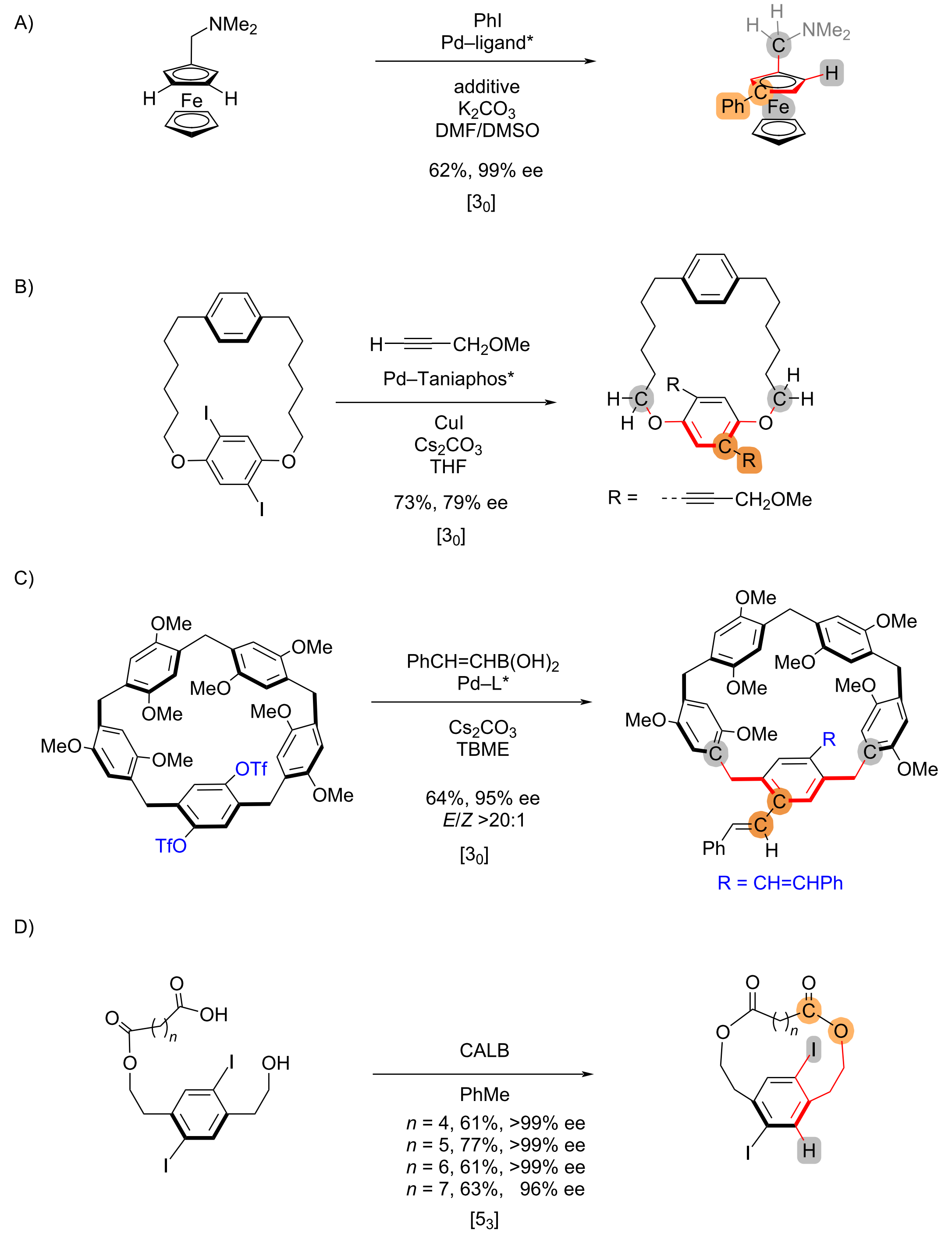

Scheme 5: Examples of reactions that establish planar chirality.

arene. Therefore, the CALB-mediated esterification to cyclophenes [21] is [5_3], regardless of the length of the linkage $(CH_2)_n$ (Scheme 5D).

In recent years, asymmetric synthesis of "inherently chiral" macrocycles have gained growing attention [22]. Practically, such reactions that yield "inherently chiral" macrocycles can be treated similarly as planar chirality (Scheme 6). The synthesis of calix[4]arenes via C–H arylation [23] is [3_1] (Scheme 6A), following the same procedure as in Scheme 5C. In analogy to Scheme 5B, the direct cyclization forging the planar chirality [24] in Scheme 6B is regarded as [3_1 1_0], in which two stereo-

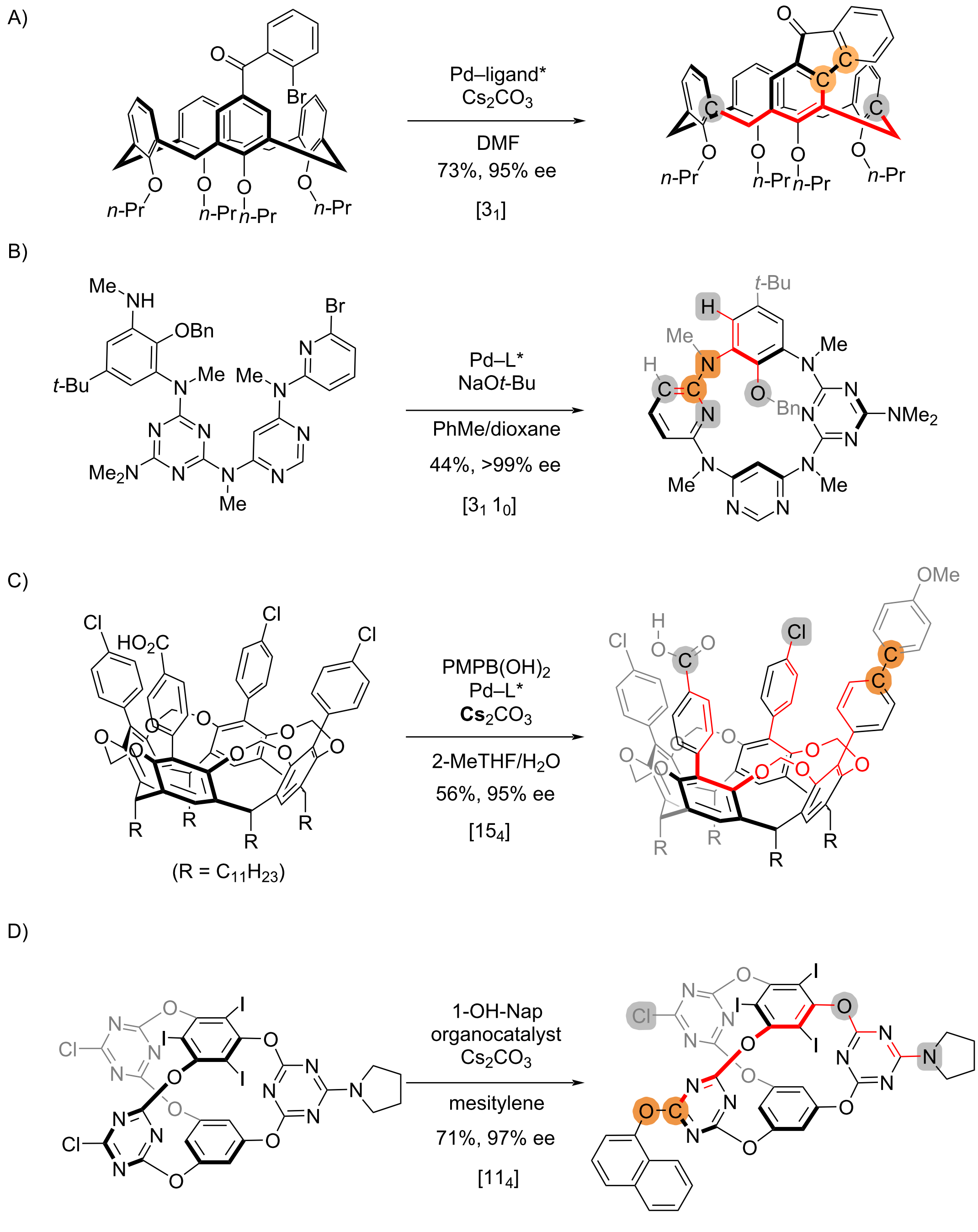

Scheme 6: Examples of reactions that establish “inherent” chirality.

genic arenes are proximate and the two distal arenes are considered diastereomeric. The desymmetrization cross-coupling of cavitands [25] in Scheme 6C is designated as [15_4]. In this case, the stereochemical differentiation viewed from the reaction sites can only be made beyond the two pilot atoms; the bond connectivity remains the same till the chloro group and the carboxyl group. Recently, Wang has reported an organocatalytic protocol to access inherently chiral cages via desymmetrization promoted by a chiral phase-transfer catalyst [26], which is designated as a [11_4] process (Scheme 6D).

Asymmetric reactions can be categorized based on the stereocontrol connectivity index. For example, the remote desymmetrization reactions to axial chiralities [27-30] in Scheme 7A to 7D are all [5_3] processes irrespective of the reaction types, the catalysts, and the scaffolds. The index corre-

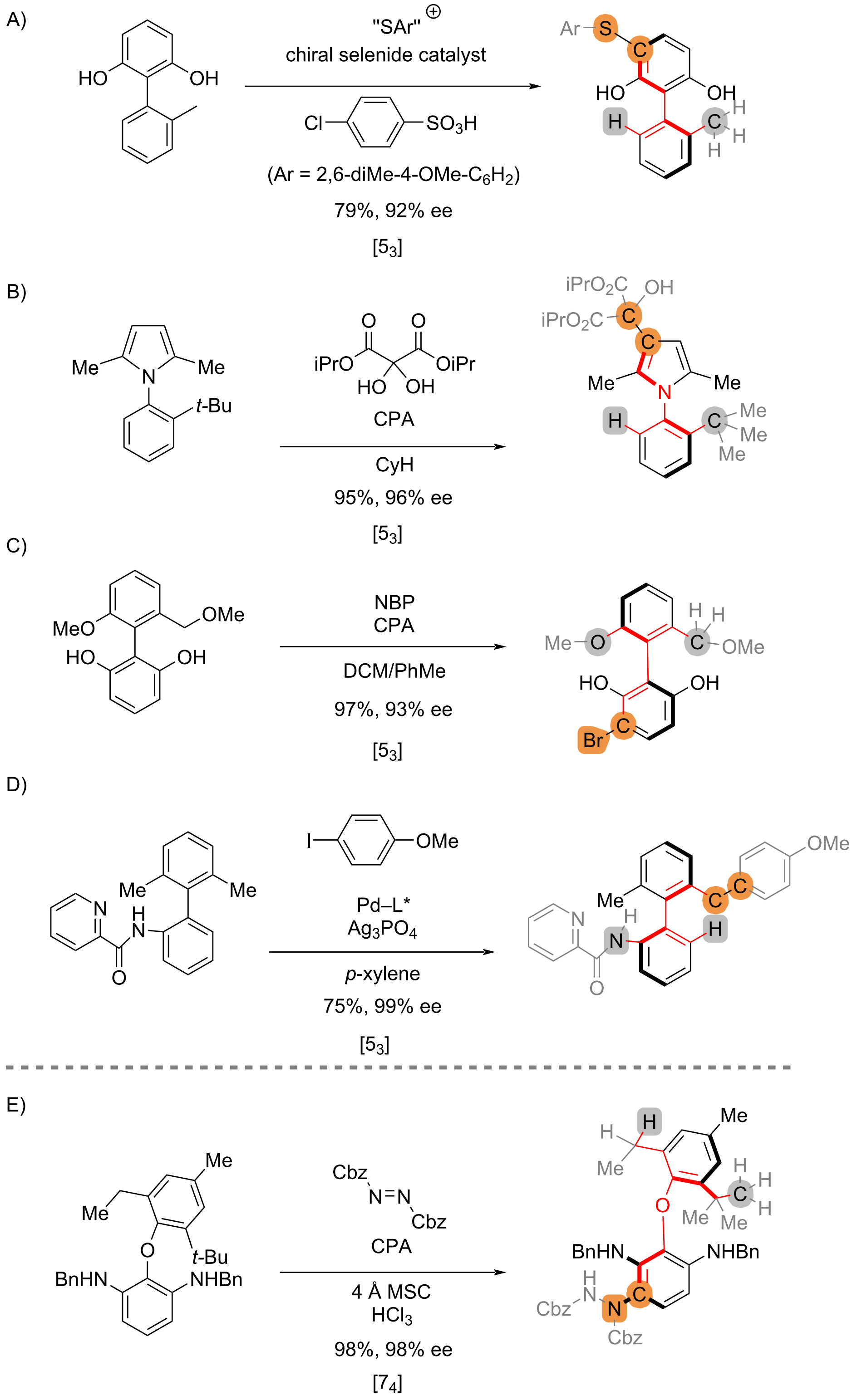

Scheme 7: Parameterization of asymmetric reactions that establish axial chirality.

sponds to the minimal substructure of the prochiral substrates that a chiral catalyst needs to recognize, if the bond connectivity is the only factor considered, without taking into account the electronic, steric and conformational properties. For example, the stereocontrol of the desymmetrization reaction in Scheme 7E [31] would require the catalyst to discern between the two non-reactive *ortho*-substituents at distant points across the biphenyl ether backbone (H vs Me, highlighted in grey), which is reflected by the relatively large values of the index $[7_4]$.

Although we intend to avoid reaction intermediates in the assignment of the stereocontrol connectivity index, we recognize the limitations in cases that chemical bonds are cleaved and restored in the course of the transformations (e.g., Scheme 4A and 4C). Such limitations become obvious in the cases of multi-step, multi-intermediate reactions [32,33], particularly in the case of helical chirality where chirality transfer of intermediates is common [34-39]. In addition, the 3-step procedure is not applicable to asymmetric synthesis of interlocked molecules including mechanically planar chiral rotaxanes and catenanes, where the bond connectivity between stereogenic components is absent [40-43].

Finally, we explored the automated process for the generation of indices following the 3-step procedure using a prototypic program coded using Python or through coaching GPT-4.1. Stereoselective reactions were input as SMILES (for Python) or InChI (for GPT-4.1) of the starting materials and products, and the corresponding indices were generated automatically. It is possible that functions could be expanded in the future so that the automated designation is applicable to various types of chirality and chemical structures.

The stereocontrol connectivity index is related to the minimum path across the prochiral substrate for effective transmission of chirality from the chiral catalyst to the product. In other words, the chiral catalyst needs to recognize, through electronic and steric effects, at least the structural features reflected by the stereocontrol connectivity index to induce enantioselectivity. Therefore, the stereocontrol connectivity index is relevant to the minimal dimension of an effective chiral catalyst for a given asymmetric transformation. We surveyed the relationship between the numbers of non-hydrogen atoms (N) in the chiral catalysts and the value of i (or sum of i) in $[i_j]$ for the 21 non-enzymatic transformations analyzed above (Figure 1). These transformations scattered across a broad area: 10 showed $20 \times i > N > 10 \times i$, and 9 showed $10 \times i > N > 5 \times i$. Although neither $N_{\text{non-H}}$ of the catalyst nor the index $[i_j]$ is related to the mechanism of stereocontrol, a low N-to-i ratio could occur when attractive secondary interactions between the catalyst and the substrates were involved in stereoinduction. In contrast, if this strategy is not applicable as a result of the non-polar nature of the substituents in the prochiral substrate, a high N-to-i ratio is expected to provide the necessary structural basis of the catalyst for stereoinduction by steric biasing.

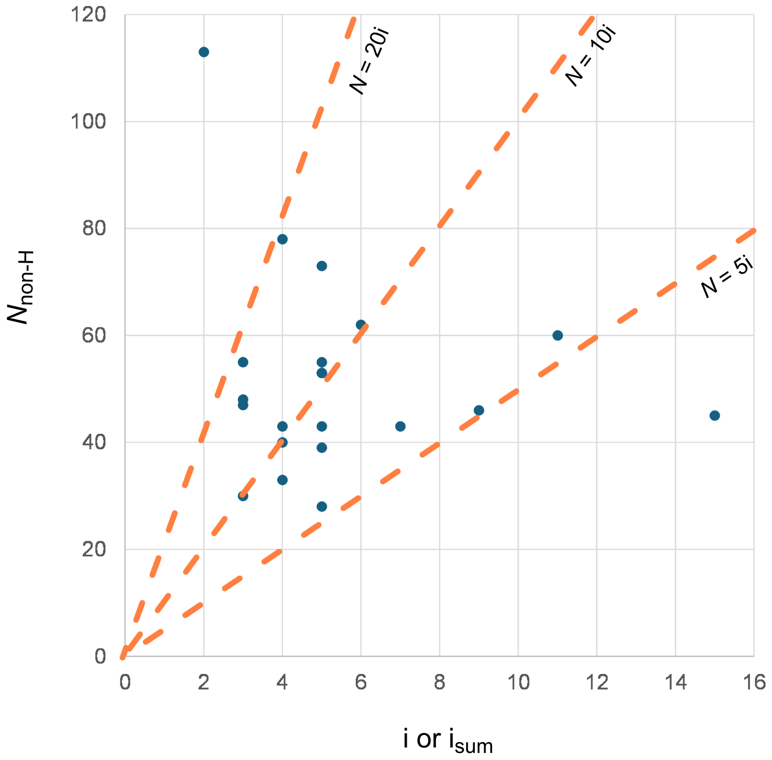

Figure 1: The relationship between the numbers of non-hydrogen atoms (N) in the chiral catalysts and the value of i in $[i_j]$.

The stereocontrol connectivity index does not reflect the difficulty of inducing stereoselectivity, which can be subjective. In particular, the actual spatial distances between critical structural elements cannot be measured simply by using bond connectivity. Nonetheless, the stereocontrol connectivity index can provide information on the stereochemical properties of reactions, beyond the existing binary (yes/no) stereochemistry classifications in widely used chemical databases such as CAS SciFinder and Reaxys. This exercise applies not only to existing asymmetric reactions but also to chemical transformations without effective stereocontrol, thus presenting new avenues for research.

Conclusion

In summary, we have developed a stereocontrol connectivity index that parameterizes the stereogenic remoteness of asymmetric reactions. The index is applicable to chemical transformations that establish central chirality, axial chirality, planar chirality, and "inherent chirality". The 3-step procedure for the designation of the stereocontrol connectivity index is derived from the chemical structures of the starting materials and the products, and it does not rely on knowledge in reaction mechanisms. Particularly, the application to reactions that establish non-central chirality allows a numeric measurement of the stereogenic remoteness – an intrinsic property of non-central chirality reflected by the large values of the indices ($i \geq 3$). We anticipate that application of the stereocontrol connectivity index will facilitate the classification of stereoselective reactions and promote the development of challenging asymmetric transformations that establish non-central chirality.

Supporting Information

Supporting Information File 1

The set of code (Python) and sample inputs and outputs, as well as the sample inputs and outputs using GPT-4.1 for the designation of stereocontrol connectivity indices are illustrated. The data used in Figure 1 is listed in Table S1.
[https://www.beilstein-journals.org/bjoc/content/supplementary/1860-5397-21-155-S1.pdf]

Acknowledgements

We thank Singapore Ministry of Education and The National University of Singapore for support.

Funding

This research was supported by Singapore Ministry of Education (Academic research fund MOET2EP10222-0004). I.K.W.O. and Y.K.C. thanks NUS for scholarships.

Author Contributions

Ivan Keng Wee On: investigation. Yu Kun Choo: investigation; writing – original draft. Sambhav Baid: software. Ye Zhu: conceptualization; investigation; methodology; writing – original draft.

ORCID® iDs

Ye Zhu - https://orcid.org/0000-0002-8566-576X

Data Availability Statement

All data that supports the findings of this study is available in the published article and/or the supporting information of this article.

References

1. Zhang, F.-H.; Zhang, F.-J.; Li, M.-L.; Xie, J.-H.; Zhou, Q.-L. *Nat. Catal.* **2020,** *3,* 621–627. doi:10.1038/s41929-020-0474-5
2. Kim, B.; Chinn, A. J.; Fandrick, D. R.; Senanayake, C. H.; Singer, R. A.; Miller, S. J. *J. Am. Chem. Soc.* **2016,** *138,* 7939–7945. doi:10.1021/jacs.6b03444
3. Shi, H.; Herron, A. N.; Shao, Y.; Shao, Q.; Yu, J.-Q. *Nature* **2018,** *558,* 581–585. doi:10.1038/s41586-018-0220-1
4. Genov, G. R.; Douthwaite, J. L.; Lahdenperä, A. S. K.; Gibson, D. C.; Phipps, R. J. *Science* **2020,** *367,* 1246–1251. doi:10.1126/science.aba1120
5. Tang, Y.; Miller, S. J. *J. Am. Chem. Soc.* **2021,** *143,* 9230–9235. doi:10.1021/jacs.1c04431
6. Lou, Y.; Wei, J.; Li, M.; Zhu, Y. *J. Am. Chem. Soc.* **2022,** *144,* 123–129. doi:10.1021/jacs.1c12345
7. Morack, T.; Myers, T. E.; Karas, L. J.; Hardy, M. A.; Mercado, B. Q.; Sigman, M. S.; Miller, S. J. *J. Am. Chem. Soc.* **2023,** *145,* 22322–22328. doi:10.1021/jacs.3c08727
8. Wei, J.; Gandon, V.; Zhu, Y. *J. Am. Chem. Soc.* **2023,** *145,* 16796–16811. doi:10.1021/jacs.3c04877
9. Liu, C.; Yang, Y.; Hong, W.; Ma, J.-A.; Zhu, Y. *Angew. Chem., Int. Ed.* **2025,** *64,* e202417827. doi:10.1002/anie.202417827
10. On, I. K. W.; Hong, W.; Zhu, Y. *Chem Catal.* **2023,** *3,* 100523. doi:10.1016/j.checat.2023.100523
11. Gustafson, J. L.; Lim, D.; Miller, S. J. *Science* **2010,** *328,* 1251–1255. doi:10.1126/science.1188403
12. Niu, C.; Zhou, Y.; Chen, Q.; Zhu, Y.; Tang, S.; Yu, Z.-X.; Sun, J. *Org. Lett.* **2022,** *24,* 7428–7433. doi:10.1021/acs.orglett.2c03003
13. Hutskalova, V.; Sparr, C. *Synthesis* **2023,** *55,* 1770–1782. doi:10.1055/a-1993-6899
14. Yang, J.; Zhang, J.-W.; Bao, W.; Qiu, S.-Q.; Li, S.; Xiang, S.-H.; Song, J.; Zhang, J.; Tan, B. *J. Am. Chem. Soc.* **2021,** *143,* 12924–12929. doi:10.1021/jacs.1c05079
15. Qian, D.; Wu, L.; Lin, Z.; Sun, J. *Nat. Commun.* **2017,** *8,* 567. doi:10.1038/s41467-017-00251-x
16. Manzuna Sapu, C.; Bäckvall, J.-E.; Deska, J. *Angew. Chem., Int. Ed.* **2011,** *50,* 9731–9734. doi:10.1002/anie.201103227
17. He, S.-J.; Shen, B.; Zuo, L.-Z.; Xiang, S.-H.; Liu, H.-H.; Yu, P.; Tan, B. *J. Am. Chem. Soc.* **2024,** *146,* 19137–19145. doi:10.1021/jacs.4c04024
18. Zhou, L.; Cheng, H.-G.; Li, L.; Wu, K.; Hou, J.; Jiao, C.; Deng, S.; Liu, Z.; Yu, J.-Q.; Zhou, Q. *Nat. Chem.* **2023,** *15,* 815–823. doi:10.1038/s41557-023-01176-3

19. Luan, T.-R.; Sun, C.; Tian, Y.-L.; Jiang, Y.-K.; Xi, L.-L.; Liu, R.-R. *Nat. Commun.* **2025,** *16,* 2370. doi:10.1038/s41467-025-57461-x
20. Kanda, K.; Koike, T.; Endo, K.; Shibata, T. *Chem. Commun.* **2009,** 1870–1872. doi:10.1039/b818904h
21. Gagnon, C.; Godin, É.; Minozzi, C.; Sosoe, J.; Pochet, C.; Collins, S. K. *Science* **2020,** *367,* 917–921. doi:10.1126/science.aaz7381
22. Tang, M.; Yang, X. *Eur. J. Org. Chem.* **2023,** *26,* e202300738. doi:10.1002/ejoc.202300738
23. Zhang, Y.-Z.; Xu, M.-M.; Si, X.-G.; Hou, J.-L.; Cai, Q. *J. Am. Chem. Soc.* **2022,** *144,* 22858–22864. doi:10.1021/jacs.2c10606
24. Tong, S.; Li, J.-T.; Liang, D.-D.; Zhang, Y.-E.; Feng, Q.-Y.; Zhang, X.; Zhu, J.; Wang, M.-X. *J. Am. Chem. Soc.* **2020,** *142,* 14432–14436. doi:10.1021/jacs.0c05369
25. Li, M.; Ho, C. K. S.; On, I. K. W.; Gandon, V.; Zhu, Y. *Chem* **2024,** *10,* 3323–3341. doi:10.1016/j.chempr.2024.06.012
26. Fang, S.; Bao, Z.; Liu, Z.; Wu, Z.; Tan, J.-P.; Wei, X.; Li, B.; Wang, T. *Angew. Chem., Int. Ed.* **2024,** *63,* e202411889. doi:10.1002/anie.202411889
27. Luo, H.-Y.; Li, Z.-H.; Zhu, D.; Yang, Q.; Cao, R.-F.; Ding, T.-M.; Chen, Z.-M. *J. Am. Chem. Soc.* **2022,** *144,* 2943–2952. doi:10.1021/jacs.1c09635
28. Zhang, L.; Xiang, S.-H.; Wang, J.; Xiao, J.; Wang, J.-Q.; Tan, B. *Nat. Commun.* **2019,** *10,* 566. doi:10.1038/s41467-019-08447-z
29. Mori, K.; Ichikawa, Y.; Kobayashi, M.; Shibata, Y.; Yamanaka, M.; Akiyama, T. *J. Am. Chem. Soc.* **2013,** *135,* 3964–3970. doi:10.1021/ja311902f
30. Uchikura, T.; Kato, S.; Makino, Y.; Fujikawa, M. J.; Yamanaka, M.; Akiyama, T. *J. Am. Chem. Soc.* **2023,** *145,* 15906–15911. doi:10.1021/jacs.3c03552
31. Bao, H.; Chen, Y.; Yang, X. *Angew. Chem., Int. Ed.* **2023,** *62,* e202300481. doi:10.1002/anie.202300481
32. Ye, Z.; Xie, W.; Liu, W.; Zhou, C.; Yang, X. *Adv. Sci.* **2024,** *11,* 2403125. doi:10.1002/advs.202403125
33. Yu, S.; Yuan, M.; Xie, W.; Ye, Z.; Qin, T.; Yu, N.; Yang, X. *Angew. Chem., Int. Ed.* **2024,** *63,* e202410628. doi:10.1002/anie.202410628
34. Wang, Y.; Wu, Z.-G.; Shi, F. *Chem Catal.* **2022,** *2,* 3077–3111. doi:10.1016/j.checat.2022.10.011
35. Kimura, Y.; Shibata, Y.; Noguchi, K.; Tanaka, K. *Eur. J. Org. Chem.* **2019,** 1390–1396. doi:10.1002/ejoc.201801694
36. Kinoshita, S.; Yamano, R.; Shibata, Y.; Tanaka, Y.; Hanada, K.; Matsumoto, T.; Miyamoto, K.; Muranaka, A.; Uchiyama, M.; Tanaka, K. *Angew. Chem., Int. Ed.* **2020,** *59,* 11020–11027. doi:10.1002/anie.202001794
37. Wang, L.-H.; Hayase, N.; Sugiyama, H.; Nogami, J.; Uekusa, H.; Tanaka, K. *Angew. Chem., Int. Ed.* **2020,** *59,* 17951–17957. doi:10.1002/anie.202006959
38. Nogami, J.; Nagashima, Y.; Miyamoto, K.; Muranaka, A.; Uchiyama, M.; Tanaka, K. *Chem. Sci.* **2021,** *12,* 7858–7865. doi:10.1039/d1sc00861g
39. Liu, W.; Qin, T.; Xie, W.; Yang, X. *Chem. – Eur. J.* **2022,** *28,* e202202369. doi:10.1002/chem.202202369
40. Imayoshi, A.; Lakshmi, B. V.; Ueda, Y.; Yoshimura, T.; Matayoshi, A.; Furuta, T.; Kawabata, T. *Nat. Commun.* **2021,** *12,* 404. doi:10.1038/s41467-020-20372-0
41. Li, M.; Chia, X. L.; Tian, C.; Zhu, Y. *Chem* **2022,** *8,* 2843–2855. doi:10.1016/j.chempr.2022.08.009
42. Goldup, S. M. *Acc. Chem. Res.* **2024,** *57,* 1696–1708. doi:10.1021/acs.accounts.4c00195
43. Tang, M.; Zhou, J.; Xie, W.; Ren, J.; Ye, Z.; Gu, H.; Yang, X. *Chem* **2025,** 102694. doi:10.1016/j.chempr.2025.102694

License and Terms

The definitive version of this article is the electronic one which can be found at:
https://doi.org/10.3762/bjoc.21.155

BEILSTEIN JOURNAL OF ORGANIC CHEMISTRY

A *m*-quaterphenyl probe for absolute configurational assignments of primary and secondary amines

Yuka Takeuchi[1], Mutsumi Kobayashi[1], Yuuka Gotoh[1], Mari Ikeda[2], Yoichi Habata[1,3], Tomohiko Shirai[1,3] and Shunsuke Kuwahara[*1,3]

Full Research Paper

Open Access

Address:
[1]Department of Chemistry, Faculty of Science Toho University, 2-2-1 Miyama, Funabashi, Chiba 274-8510, Japan, [2]Education Center, Faculty of Engineering, Chiba Institute of Technology, 2-1-1 Shibazono, Narashino, Chiba 275-0023, Japan and [3]Research Center for Materials with Integrated Properties, Toho University, 2-2-1 Miyama, Funabashi, Chiba 274-8510, Japan

Email:
Shunsuke Kuwahara[*] - kuwahara@chem.sci.toho-u.ac.jp

* Corresponding author

Keywords:
absolute configuration; chiral amine; chiral quaternary ammonium salt; circular dichroism; DFT calculation

Beilstein J. Org. Chem. **2025,** *21,* 2211–2219.
https://doi.org/10.3762/bjoc.21.168

Received: 31 May 2025
Accepted: 27 August 2025
Published: 20 October 2025

This article is part of the thematic issue "Non-central chirality in organic chemistry".

Associate Editor: N. Yoshikai

Abstract

We report a method for determining the absolute configurations of chiral amino alcohols, amino acid esters, and secondary amines through the combined use of a *m*-quaterphenyl probe **1** and theoretical calculations. The probe **1** is covalently attached to chiral amines to form conjugates that exhibit exciton-coupled circular dichroism (ECCD) in the *m*-quaterphenyl chromophores. The calculated ratios of the *P* and *M* conformers, obtained via DFT calculations, show a correlation with both the sign and intensity of the experimentally observed CD spectra.

Introduction

Determining the absolute configurations of both natural and synthetic compounds continues to pose a considerable challenge in the life and materials sciences [1]. While X-ray crystallography remains a reliable method for this purpose, the requirement for high-quality single crystals often limits its applicability. In recent years, empirical approaches based on ^{1}H NMR anisotropy method have gained attention as alternative strategies for stereochemical assignment of chiral molecules. Among these, the modified Mosher method, which utilizes the ring current effects of aryl substituents, has been extensively applied to chiral alcohols [2]. However, its use in the analysis of chiral amines has been restricted, largely due to the complexity arising from their conformational flexibility [3].

Circular dichroism (CD) spectroscopy offers a highly sensitive technique for stereochemical analysis at the microgram scale [4-6]. In particular, exciton-coupled CD has emerged as a powerful chiroptical method, providing a non-empirical correlation between the sign of the Cotton effect and the spatial arrangement of the electric transition dipole moments of interacting chromophores [7]. More recently, CD-based chiroptical probes have been developed for determining the absolute configurations of chiral alcohols [8-14], primary amines [14-32], secondary amines [33-35], carboxylic acids [36-38], sulfoxides [39], and cyanohydrins [40].

We have reported a *m*-quaterphenyl probe **1** to determine the absolute configurations of primary amines [41]. When compound **1** is linked to the amines, the information on the absolute configurations were transcribed into a twist of two biphenyl chromophores in the *m*-quarterphenyl group. From the sign of the Cotton effect in CD, the direction of twist can be estimated. The absolute configuration of amines can be determined by comparing the direction of the twist determined by CD with that obtained by conformational analysis using theoretical calculations. However, this method has only been applied to simple primary amines. In this work, we report that the method was applied to chiral amino alcohols and amino acid esters. We also applied the method to chiral secondary amines, for which it is generally difficult to determine the absolute configuration due to the conformational complexity of their derivatives [33]. By comparing the observed and calculated sign of the CD Cotton effect, their absolute configurations were determined.

Results and Discussion

The probe **1** was prepared as described previously [41]. Probe **1**–primary amine conjugates **2a**–**e** were prepared by the reaction of **1** with chiral amino alcohols and amino acid esters in the presence of K_2CO_3 in CH_3CN (Scheme 1). The quaternary ammonium salt conjugates **2f**–**h** were also prepared by reacting **1**

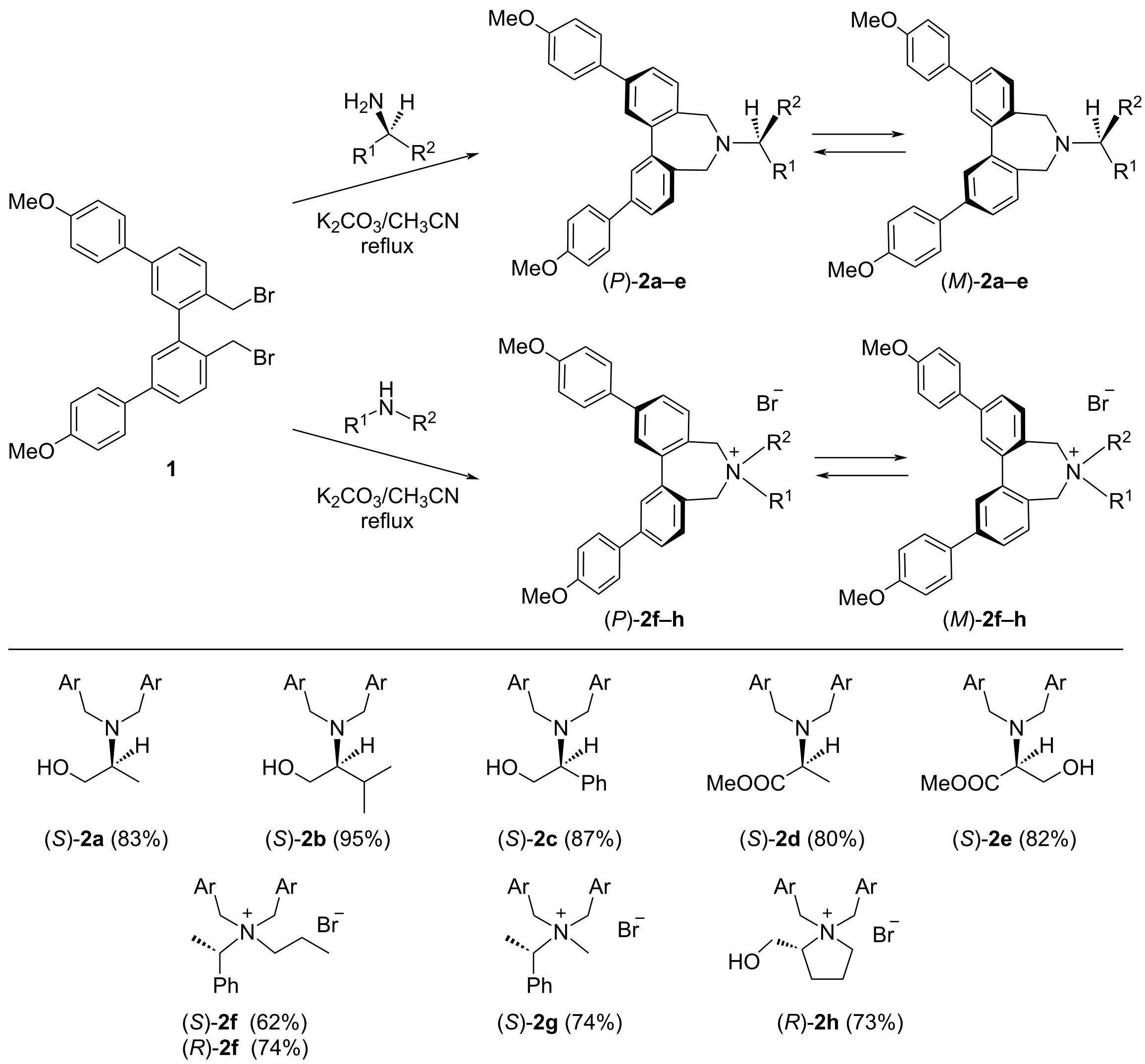

Scheme 1: Coupling reaction of **1** and chiral primary and secondary amines. The central biphenyl moiety rotates freely, forming an equilibrium mixture of *P* and *M* conformers.

with chiral secondary amines under similar conditions. It is reported that the central biphenyl moiety of amines and ammonium salts with seven-membered rings freely rotates at room temperature [41-43]. The central biphenyl moiety of conjugates **2a**–**h** also rotates freely, forming an equilibrium mixture of *P* and *M* conformers. The relative amounts of *P* and *M* conformers depend on the chirality of the linked amine moieties.

Figure 1a shows the UV and CD spectra of the conjugates (*S*)-**2a**–**e** in CH_3CN. The UV and CD spectra of the previously reported conjugates were measured in various polar and non-polar solvents, but the intensities and shapes were almost unchanged [41]. The conjugates (*S*)-**2a**–**e** are composed of two methoxybiphenyl chromophores connected with a C–C single bond. Therefore, the π-electron conjugation is widespread almost over the chromophores. However, the UV spectrum of **1**–L-alaninol conjugate (*S*)-**2a** shows an intense absorption, maintaining the nature of methoxybiphenyl chromophore. The absorption band at 259 nm is attributed to the π–π* transition polarized along the long axes of the methoxybiphenyl chromophores. The CD spectrum of (*S*)-**2a** shows Cotton effects arising from exciton-coupling between the two methoxybiphenyl chromophores; λ_{ext} = 278 nm ($\Delta\varepsilon_1$ = −0.6 dm^3 mol^{-1} cm^{-1}) and λ_{ext} = 258 nm ($\Delta\varepsilon_2$ = +1.7 dm^3 mol^{-1} cm^{-1}). The amplitude of exciton-coupled CD (A_{CD} value) [7], defined as A_{CD} = $\Delta\varepsilon_1$ (first Cotton effect) − $\Delta\varepsilon_2$ (second Cotton effect), is measured to be −2.3 dm^3 mol^{-1} cm^{-1}.

The direction of the twist of the two chromophores in biaryl compounds can be determined by the sign of the Cotton effect of the exciton-coupled CD. Maison [44], Hanazaki [45], and Salvadori [46] have used chiral 1,1-binaphthyl derivatives to clarify the relationship between the direction of the twist of the two naphthyl chromophores and the sign of the exciton-coupled CD. In this case, the information on the dihedral angle between the two naphthyl chromophores is required [7]. When the angle is between 0 and 110 degrees, the direction of twist of the chromophores can be determined by the CD exciton method.

From the conformational analyses of the previously reported conjugates, the dihedral angle in the two methoxybiphenyl chromophores of (*S*)-**2a** is predicted to be approximately 42 degree. The negative first and positive second Cotton effects in CD spectrum of (*S*)-**2a** indicates that the two long axes in the methoxybiphenyl chromophores constitute an *M* twist. The CD spectra of **1**–L-valinol conjugate (*S*)-**2b** exhibited the opposite sign for the Cotton effects compared with (*S*)-**2a**. This inversion of Cotton effects is due to the difference in steric features between the two substituents of amines: methyl and hydroxymethyl group in (*S*)-**2a**, and isopropyl and hydroxymethyl group in (*S*)-**2b**. The CD spectra of **1**–(*S*)-2-phenylglycinol conjugate (*S*)-**2c** showed the same sign for the Cotton effects compared with (*S*)-**2a**. We consider that the hydroxymethyl group is sterically more hindered than the planar phenyl groups in the conjugates. This tendency is the same as that of the previously re-

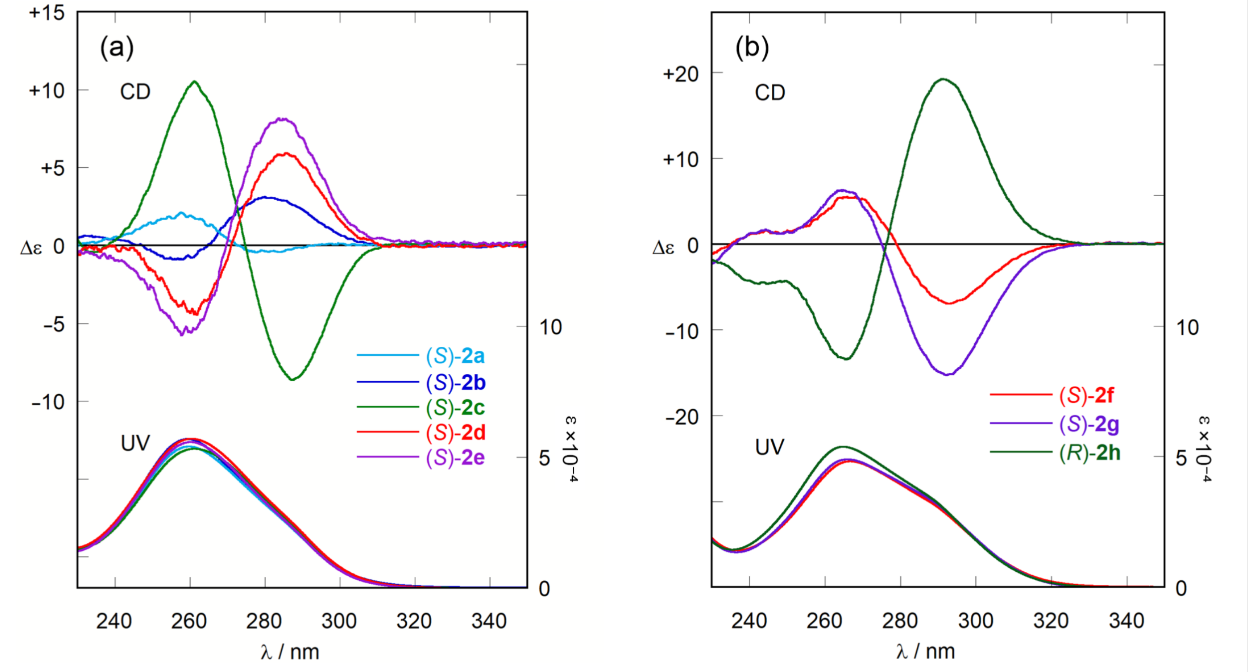

Figure 1: CD and UV spectra of (a) tertiary amines (*S*)-**2a**–**e** and (b) quaternary ammonium salts (*S*)-**2f**,**g** and (*R*)-**2h** (2.0×10^{-4} M in CH_3CN, 293 K).

ported **1**–(*S*)-2-phenylethylamine conjugates [41]. The CD spectra of **1**-L-amino acid ester conjugates (*S*)-**2d**,**e** exhibited positive first and negative second Cotton effects indicating that the two long axes in the methoxybiphenyl chromophores constitute a *P* twist. The methyl ester group is estimated to be sterically more hindered than the planar ester carbonyl group in (*S*)-**2d**,**e**.

The CD spectra of the quaternary ammonium salts (*S*)-**2f**,**g** and (*R*)-**2h** exhibit CD Cotton effects due to the exciton-coupling between the two methoxy-biphenyl chromophores (Figure 1b). Compound (*R*)-**2f** exhibited the mirror image of the CD spectrum of (*S*)-**2f** (Figure S19 in Supporting Information File 1). The direction of twist of the two chromophores of quaternary ammonium salts (*S*)-**2f**,**g** and (*R*)-**2h** can be determined from the sign of the Cotton effect in CD. However, it is more difficult to predict the direction of twist from the structure of the quaternary ammonium salts than in the case of the **1**–primary amine conjugates.

Since the CD spectra revealed the twist between the two methoxybiphenyl chromophores, we next examined the relationship between the absolute configuration of the amine and the observed twist. Based on the previously reported stable conformations obtained from theoretical calculations of related derivatives [41] the preferred conformation of (*S*)-**2a** can be proposed (Figure 2). In the case of the *P* conformer, a Newman projection along the C–N bond reveals that the bulkier substituent, the hydroxymethyl group (denoted as L), is close to a seven-membered ring, and is destabilized by steric repulsion with the methylene protons. In contrast, in the *M* conformer, the medium-sized methyl group (denoted as M) is located near the seven-membered ring, reducing the steric repulsion involving the hydroxymethyl group with the methylene protons. Moreover, considering that the phenyl ring and the ester carbonyl group are planar, while the methyl group is more sterically demanding in three-dimensional space, this conformational model is supported (Table S1 in Supporting Information File 1). Although intramolecular electronic interactions should also be considered, the twist of the phenyl chromophores can be reasonably predicted by simply evaluating the relative steric bulkiness of substituents near the amine moiety. The relative substituents' priority is determined not by the CIP rule, but by the steric bulkiness of substituents. On the other hand, for quaternary amines, it was difficult to assess the relative sizes of the substituents and to predict the direction of the twist. Therefore, we next employed conformational analysis using theoretical calculations to determine the twist of the methoxybiphenyl chromophores.

To determine the direction of twist of the two methoxybiphenyl chromophores of the conjugates (*S*)-**2a**–**g** and (*R*)-**2h**, theoretical calculations were carried out using a methoxy-omitted model (*S*)-**3a**–**g** and (*R*)-**3h**. To estimate the relative populations of the *P* and *M* conformers of (*S*)-**3a**, an initial conformational search was performed using the MMFF force field, followed by geometry optimizations of all local minima employing DFT at the B3LYP/6-31G* level of theory [47]. Four

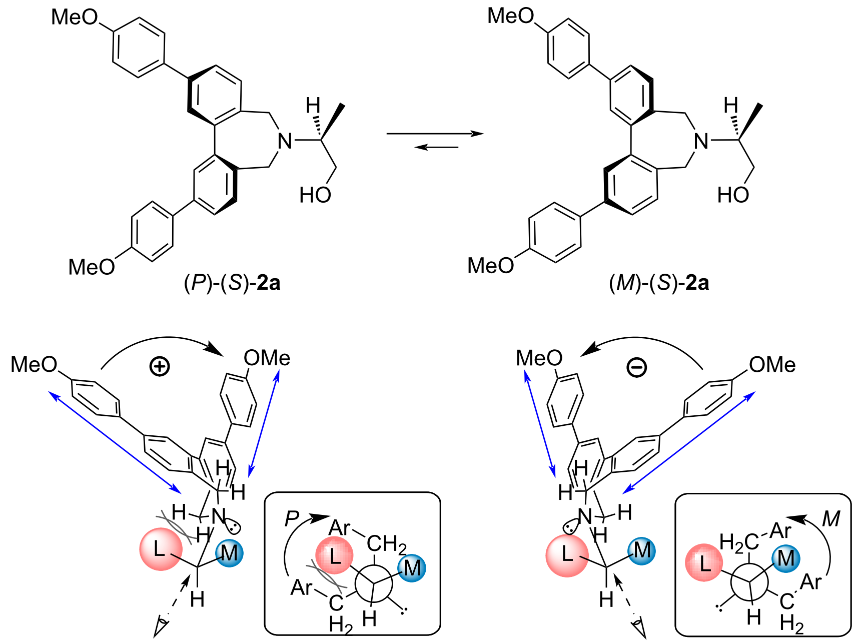

(*P*)-(*S*)-**2a**

(*M*)-(*S*)-**2a**

Figure 2: Schematic representation of the preferred conformation of (*S*)-**2a**.

low-energy conformers of (*S*)-**3a** were identified within 10.0 kJ/mol (Figure 3). Among them, conformers A and D exhibited an *M* twist between the long axes of the biphenyl chromophores, whereas conformers B and C displayed a *P* twist. Based on a Boltzmann distribution analysis (T = 298 K), the relative populations of the *P* and *M* conformers in (*S*)-**3a** were determined to be 48:52. (Table S3 in Supporting Information File 1). In contrast, the *P* conformers were found to predominate in (*S*)-**3b** (Figure S21 and Table S4 in Supporting Information File 1). In the quaternary ammonium salts (*S*)-**3f**, the populations of the *M* conformers were greater than those of the *P* conformers (Figure 4). These computational results were consistent with the signs of the experimentally observed CD Cotton effects.

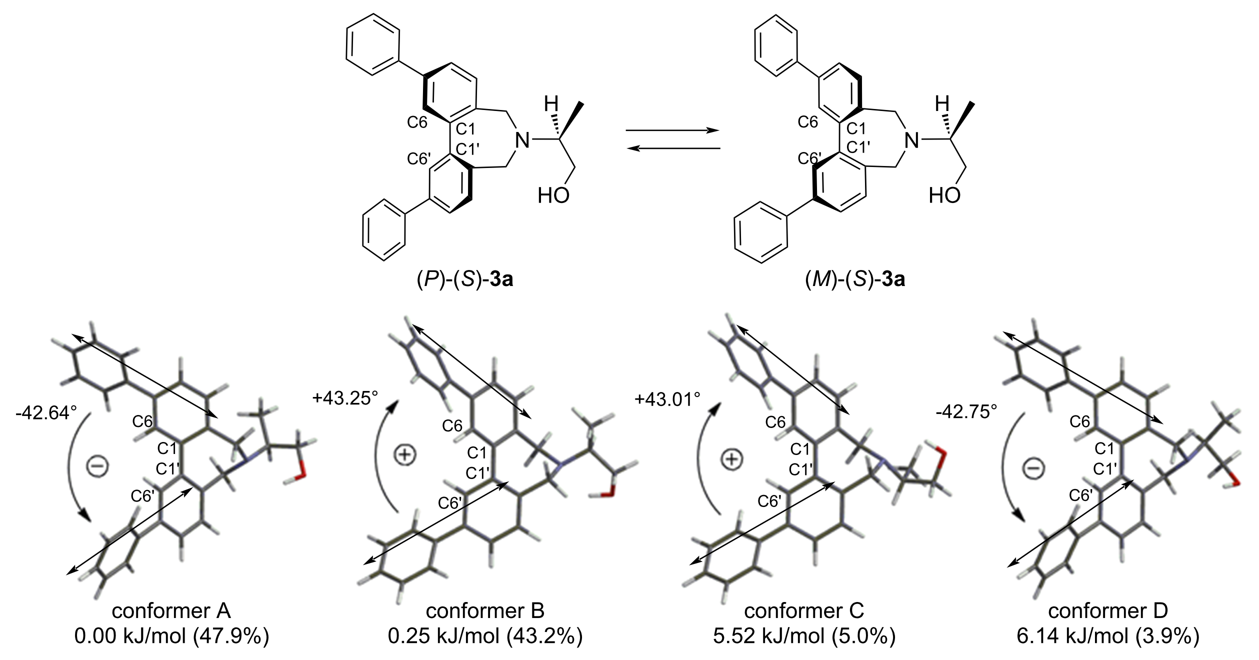

Figure 3: Four major conformers of (*S*)-**3a** based on B3LYP/6-31G* level.

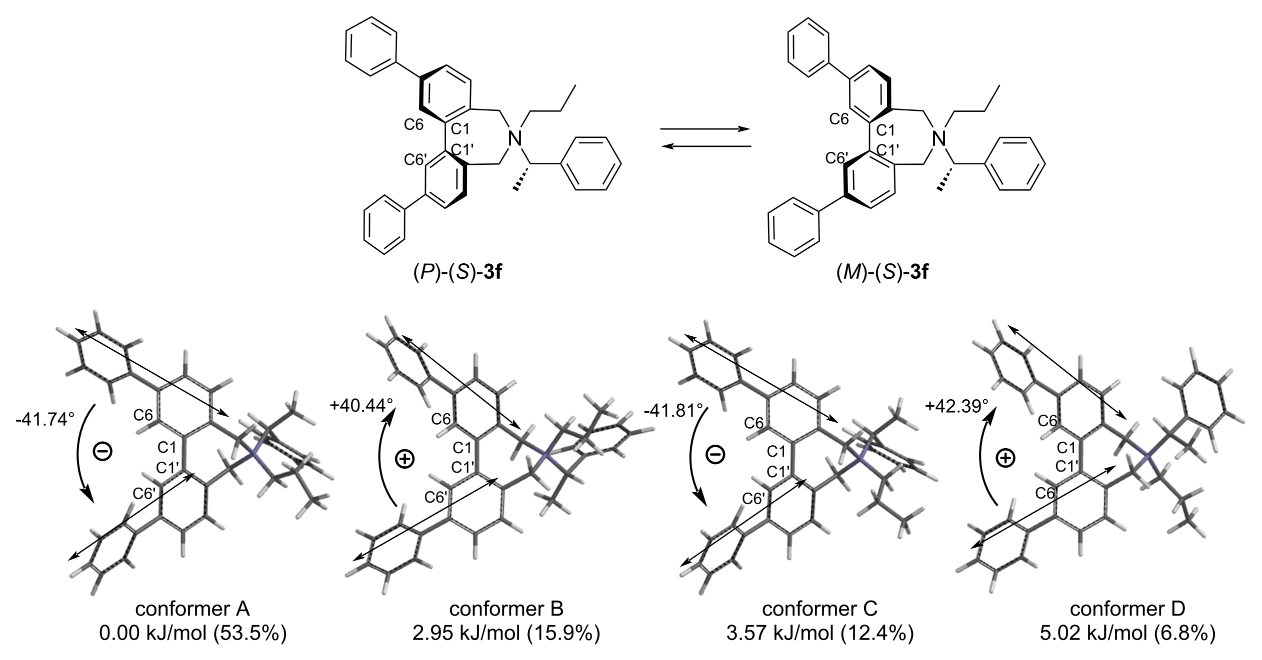

Figure 4: Four major conformers of (*S*)-**3f** based on B3LYP/6-31G* level.

From the conformational analyses described above, the C6–C1–C1'–C6' dihedral angles in all conformers of (*S*)-**3a**–**g** and (*R*)-**3h** were approximately constant (plus or minus ca. 42 degree). The range of distribution of the angles was also small, ranging from +39.8 to +43.9 degrees, or −40.2 to −45.8 degrees (Figure 5). In the solid state of (*S*)-**2b**, the C6–C1–C1'–C6' dihedral angles in the conformers were approximately constant. There are four conformers of (*S*)-**2b** in the unit cell, two of which are *P* and the other two are *M* conformers, with C6–C1–C1'–C6' dihedral angles of +39.2, +43.5, −39.5 and −46.6 degrees, respectively (Figure 6) [48].

The intensity of the exciton-coupled CD depends on the torsion angle of the two chromophores [7]. Therefore, the CD intensity of (*S*)-**2a**–**g** and (*R*)-**2h**, directly reflects the abundance ratio of the *P* and *M* conformers. A linear relationship between the A_{CD} values and the calculated excess of *P* conformers, $([P] - [M])/([P] + [M]) \times 100$, was obtained with $R^2 = 0.963$ (Figure 7). A similar linear correlation was observed when previously reported conjugates were applied (Figure S28 in Supporting Information File 1). By comparing the observed and calculated sign of the CD Cotton effect, the absolute configurations of chiral amines were determined. Reported chiroptical probes for determining the absolute configuration of chiral compounds only used the sign of the Cotton effect in CD. This method uses not only the sign but also the intensity of the Cotton effect in CD to determine the absolute configuration of chiral primary and secondary amines. In other words, by comparing the sign and the intensity of the CD using the relationship in Figure 7, the determination of the absolute configuration can be guaranteed.

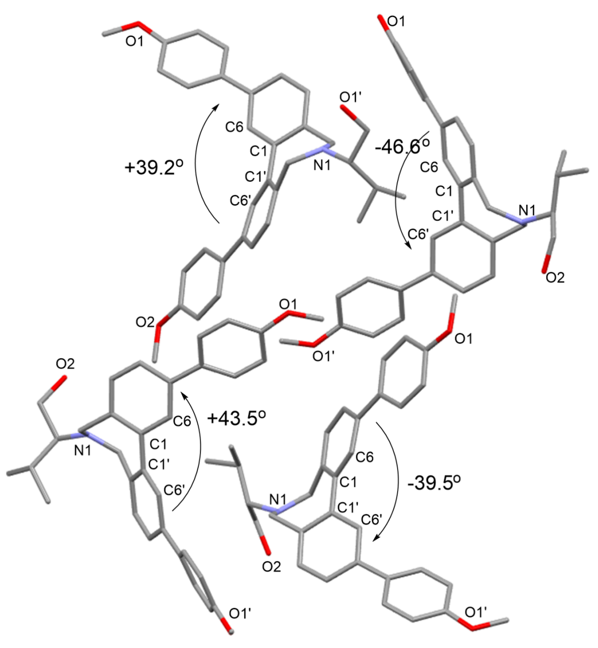

Figure 6: Crystal structure of (*S*)-**2b**. Four conformers exist in the unit cell. Hydrogen atoms are omitted for clarity.

Conclusion

The combination of the CD spectra and conformational analysis by theoretical calculations using *m*-quaterphenyl probe **1**

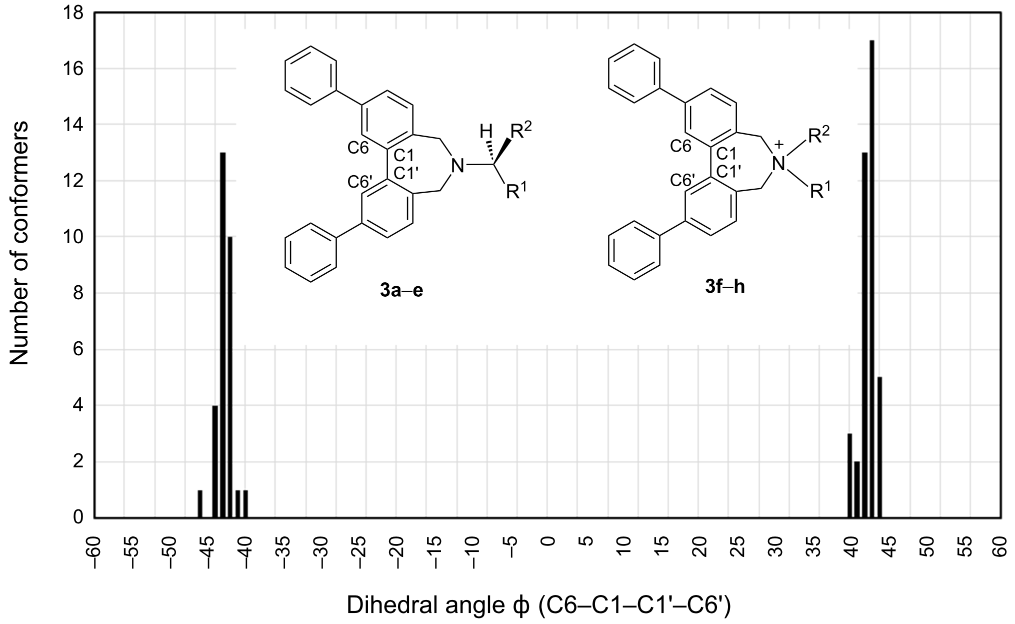

Figure 5: The distribution of conformers of (*S*)-**3a–h** against dihedral angles ϕ (C6–C1–C1'–C6') calculated by B3LYP/6-31G*.

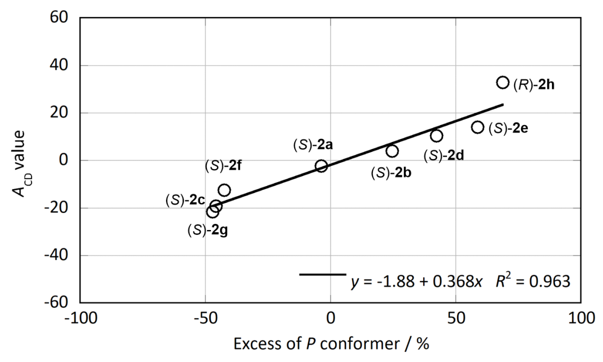

Figure 7: The relationship between the A_{CD} values and excess of *P* conformer. Excess of *P* conformer (%) = ([*P*] − [*M*])/([*P*] + [*M*]) × 100, where [*P*] and [*M*] are the amounts of *P* and *M* conformers calculated by B3LYP/6-31G*, respectively.

represents an effective method to determine both the absolute configuration of chiral primary amino alcohols and amino acid esters. This method is also useful for chiral secondary amines, for which it is generally difficult to determine the absolute configuration. By comparing the intensities of the A_{CD} values, the reliability of determining the absolute configurations can be guaranteed. Further application of the method to amines with more complex structures is currently in progress.

Experimental

General methods

All reagents and solvents were commercially available and used without further purification. Melting points were obtained with a Mel-Temp capillary apparatus and were not corrected. IR spectra were obtained as KBr disks on a JASCO FT/IR-410 spectrophotometer. The FAB mass spectra were recorded using a JEOL 600H mass spectrometer. ^{1}H and ^{13}C{^{1}H} NMR spectra were recorded on a Jeol ECP400 spectrometer (400 MHz) and a Bruker AVANCE II spectrometer (400 MHz). All NMR spectroscopic data of $CDCl_3$ solutions are reported in ppm (δ) downfield from TMS. UV and CD spectra were recorded on JASCO V-650 and JASCO J-820 spectrometers, respectively. X-ray single-crystal structure analysis was performed on a Bruker SMART diffractometer equipped with a CCD area detector at 120 K. Silica gel 60 F_{254} precoated plates on glass from Merck Ltd. were used for thin-layer chromatography (TLC).

General procedure for the synthesis of conjugates **2a–h**

(*S*)-2-[2,10-Bis(4-methoxyphenyl)-5,7-dihydro-6*H*-dibenzo[*c,e*]azepin-6-yl]propan-1-ol ((*S*)-2a). A mixture of *m*-quaterphenyl probe **1** (290 mg, 0.526 mmol), L-alaninol (48.3 mg, 0.643 mmol) and K_2CO_3 (294 mg, 2.12 mmol) in CH_3CN (12 mL) was stirred at 85 °C for 3 h. After cooling to room temperature, the mixture was filtered through a pad of Celite, and then evaporated to dryness. The crude product was purified by column chromatography on silica gel (EtOAc) to yield amine (*S*)-**2a** (203 mg, 83% yield) as colorless solid: mp 164.2–165.5 °C; ^{1}H NMR (400 MHz, $CDCl_3$) δ 7.73 (d, *J* = 1.8 Hz, 2H), 7.62–7.56 (m, 6H), 7.44 (d, *J* = 7.8 Hz, 2H), 7.00 (dt, J_1 = 8.7 Hz, J_2 = 3.6 Hz, 4H), 3.86 (s, 6H), 3.68–3.46 (m, 6H), 3.20–3.12 (m, 2H), 1.12 (d, *J* = 6.6 Hz); ^{13}C NMR (100 MHz, $CDCl_3$) δ 159.3, 141.4, 140.7, 134.0, 133.2, 130.3, 128.2, 126.3, 126.0, 114.3, 63.4, 60.7, 55.4, 51.3, 13.3; IR (KBr) ν_{max}: 3407, 2959, 1732, 1607, 1517, 1489, 1249, 1178, 1038, 822 cm^{-1}; FABMS (matrix DTT/TG = 1:1) *m/z*: 465 [M]$^+$ (100%); Anal. calcd for $C_{31}H_{31}NO_3$: C, 79.97; H, 6.71; N, 3.01; found: C, 79.73; H, 6.75; N, 2.98.

Theoretical calculations

To obtain the population between *M* and *P* conformers, preliminary conformational searches were run on the structures of (*S*)-**3a–g** and (*R*)-**3h** using MMFF. All local minimum conformers were then optimized with DFT using the B3LYP/6-31G* model [47]. The lower energy conformers with relative energies ranging from 0.0 to 10.0 kJ/mol were selected. By the Bolzmann distribution based on the energy difference of the conformers at 293 K, the population of the *P* and *M* conformers were determined.

Supporting Information

Supporting Information File 1

Experimental procedures, characterization data including copies of NMR spectra (^{1}H NMR, ^{13}C NMR), CD spectra of (*S*)-**2f** and (*R*)-**2f**, theoretical calculations, and X-ray structure of (*S*)-**2b**.
[https://www.beilstein-journals.org/bjoc/content/supplementary/1860-5397-21-168-S1.pdf]

Supporting Information File 2

Crystallographic information file for compound **2b**.
[https://www.beilstein-journals.org/bjoc/content/supplementary/1860-5397-21-168-S2.cif]

Funding

This work was partly supported by JSPS KAKENHI (Grant No. 17K05845, 24K08368).

Author Contributions

Yuka Takeuchi: data curation; formal analysis; investigation; methodology; validation. Mutsumi Kobayashi: data curation; formal analysis; investigation; methodology; validation. Yuuka

Gotoh: data curation; formal analysis; investigation; methodology; validation. Mari Ikeda: data curation; formal analysis; investigation; methodology; validation. Yoichi Habata: conceptualization; investigation; methodology; validation. Tomohiko Shirai: investigation; methodology; validation; visualization; writing – review & editing. Shunsuke Kuwahara: conceptualization; funding acquisition; investigation; methodology; project administration; resources; supervision; validation; visualization; writing – original draft; writing – review & editing.

ORCID® iDs

Mari Ikeda - https://orcid.org/0000-0003-4037-689X
Yoichi Habata - https://orcid.org/0000-0003-0712-6231
Tomohiko Shirai - https://orcid.org/0000-0001-7669-0288
Shunsuke Kuwahara - https://orcid.org/0000-0002-9673-4580

Data Availability Statement

All data that supports the findings of this study is available in the published article and/or the supporting information of this article.

References

1. Polavarapu, P. L., Ed. *Chiral Analysis: Advances in Spectroscopy, Chromatography and Emerging Methods,* 2nd ed.; Elsevier: Amsterdam, Netherlands, 2018. doi:10.1016/c2017-0-00050-2
2. Seco, J. M.; Quiñoá, E.; Riguera, R. *Chem. Rev.* **2012,** *112,* 4603–4641. doi:10.1021/cr2003344
3. Seco, J. M.; Quiñoá, E.; Riguera, R. *Chem. Rev.* **2004,** *104,* 17–118. doi:10.1021/cr000665j
4. Berova, N.; Nakanishi, K.; Woody, R. W., Eds. *Circular Dichroism: Principles and Applications;* John Wiley & Sons: Hoboken, NJ, USA, 2000.
5. Berova, N.; Polavarapu, P. L.; Nakanishi, K.; Woody, R. W., Eds. *Comprehensive Chiroptical Spectroscopy, Instrumentation, Methodologies, and Theoretical Simulations;* John Wiley & Sons: Hoboken, NJ, USA, 2011. doi:10.1002/9781118120187
6. Berova, N.; Polavarapu, P. L.; Nakanishi, K.; Woody, R. W., Eds. *Comprehensive Chiroptical Spectroscopy, Applications in Stereochemical Analysis of Synthetic Compounds, Natural Products, and Biomolecules;* John Wiley & Sons: Hoboken, NJ, USA, 2012. doi:10.1002/9781118120392
7. Harada, N.; Nakanishi, K. *Circular dichroic spectroscopy: exciton coupling in organic stereochemistry;* University Science Books: Mill Valley, CA, USA, 1983.
8. Lintuluoto, J. M.; Borovkov, V. V.; Inoue, Y. *J. Am. Chem. Soc.* **2002,** *124,* 13676–13677. doi:10.1021/ja0267270
9. Gawroński, J.; Kwit, M.; Gawrońska, K. *Org. Lett.* **2002,** *4,* 4185–4188. doi:10.1021/ol0268079
10. Li, X.; Tanasova, M.; Vasileiou, C.; Borhan, B. *J. Am. Chem. Soc.* **2008,** *130,* 1885–1893. doi:10.1021/ja0752639
11. Li, X.; Burrell, C. E.; Staples, R. J.; Borhan, B. *J. Am. Chem. Soc.* **2012,** *134,* 9026–9029. doi:10.1021/ja2119767
12. Ikbal, S. A.; Dhamija, A.; Brahma, S.; Rath, S. P. *J. Org. Chem.* **2016,** *81,* 5440–5449. doi:10.1021/acs.joc.6b00724
13. Mądry, T.; Czapik, A.; Kwit, M. *ACS Omega* **2019,** *4,* 3244–3256. doi:10.1021/acsomega.8b03337
14. Santoro, E.; Vergura, S.; Scafato, P.; Belviso, S.; Masi, M.; Evidente, A.; Superchi, S. *J. Nat. Prod.* **2020,** *83,* 1061–1068. doi:10.1021/acs.jnatprod.9b01068
15. Huang, X.; Rickman, B. H.; Borhan, B.; Berova, N.; Nakanishi, K. *J. Am. Chem. Soc.* **1998,** *120,* 6185–6186. doi:10.1021/ja973539e
16. Kurtán, T.; Nesnas, N.; Li, Y.-Q.; Huang, X.; Nakanishi, K.; Berova, N. *J. Am. Chem. Soc.* **2001,** *123,* 5962–5973. doi:10.1021/ja010249w
17. Borovkov, V. V.; Lintuluoto, J. M.; Inoue, Y. *J. Am. Chem. Soc.* **2001,** *123,* 2979–2989. doi:10.1021/ja0032982
18. Gawroński, J.; Grajewski, J. *Tetrahedron: Asymmetry* **2004,** *15,* 1527–1530. doi:10.1016/j.tetasy.2004.04.003
19. Mazaleyrat, J.-P.; Wright, K.; Gaucher, A.; Toulemonde, N.; Wakselman, M.; Oancea, S.; Peggion, C.; Formaggio, F.; Setnička, V.; Keiderling, T. A.; Toniolo, C. *J. Am. Chem. Soc.* **2004,** *126,* 12874–12879. doi:10.1021/ja040100v
20. Borovkov, V. V.; Hembury, G. A.; Inoue, Y. *Acc. Chem. Res.* **2004,** *37,* 449–459. doi:10.1021/ar0302437
21. Dutot, L.; Wright, K.; Gaucher, A.; Wakselman, M.; Mazaleyrat, J.-P.; De Zotti, M.; Peggion, C.; Formaggio, F.; Toniolo, C. *J. Am. Chem. Soc.* **2008,** *130,* 5986–5992. doi:10.1021/ja800059d
22. Ghosn, M. W.; Wolf, C. *J. Am. Chem. Soc.* **2009,** *131,* 16360–16361. doi:10.1021/ja907741v
23. Nieto, S.; Dragna, J. M.; Anslyn, E. V. *Chem. – Eur. J.* **2010,** *16,* 227–232. doi:10.1002/chem.200902650
24. Anyika, M.; Gholami, H.; Ashtekar, K. D.; Acho, R.; Borhan, B. *J. Am. Chem. Soc.* **2014,** *136,* 550–553. doi:10.1021/ja408317b
25. Thanzeel, F. Y.; Wolf, C. *Angew. Chem., Int. Ed.* **2017,** *56,* 7276–7281. doi:10.1002/anie.201701188
26. Scaramuzzo, F. A.; Badetti, E.; Licini, G.; Zonta, C. *Eur. J. Org. Chem.* **2017,** 1438–1442. doi:10.1002/ejoc.201601381
27. Vergura, S.; Pisani, L.; Scafato, P.; Casarini, D.; Superchi, S. *Org. Biomol. Chem.* **2018,** *16,* 555–565. doi:10.1039/c7ob02730c
28. Pilicer, S. L.; Mancinelli, M.; Mazzanti, A.; Wolf, C. *Org. Biomol. Chem.* **2019,** *17,* 6699–6705. doi:10.1039/c9ob01265f
29. Mądry, T.; Czapik, A.; Kwit, M. *J. Org. Chem.* **2020,** *85,* 10413–10431. doi:10.1021/acs.joc.0c00734
30. Hassan, D. S.; Thanzeel, F. Y.; Wolf, C. *Chirality* **2020,** *32,* 457–463. doi:10.1002/chir.23185
31. Mądry, T.; Czapik, A.; Kwit, M. *Symmetry* **2021,** *13,* 325. doi:10.3390/sym13020325
32. Penasa, R.; Pandey, A. K.; Wurst, K.; Rancan, M.; Armelao, L.; Licini, G.; Zonta, C. *Inorg. Chem.* **2024,** *63,* 17701–17705. doi:10.1021/acs.inorgchem.4c02531
33. Huang, X.; Fujioka, N.; Pescitelli, G.; Koehn, F. E.; Williamson, R. T.; Nakanishi, K.; Berova, N. *J. Am. Chem. Soc.* **2002,** *124,* 10320–10335. doi:10.1021/ja020520p
34. Kuwahara, S.; Chamura, R.; Tsuchiya, S.; Ikeda, M.; Habata, Y. *Chem. Commun.* **2013,** *49,* 2186–2188. doi:10.1039/c2cc38758a
35. Ni, C.; Zha, D.; Ye, H.; Hai, Y.; Zhou, Y.; Anslyn, E. V.; You, L. *Angew. Chem., Int. Ed.* **2018,** *57,* 1300–1305. doi:10.1002/anie.201711602
36. Proni, G.; Pescitelli, G.; Huang, X.; Nakanishi, K.; Berova, N. *J. Am. Chem. Soc.* **2003,** *125,* 12914–12927. doi:10.1021/ja036294g
37. Superchi, S.; Bisaccia, R.; Casarini, D.; Laurita, A.; Rosini, C. *J. Am. Chem. Soc.* **2006,** *128,* 6893–6902. doi:10.1021/ja058552a
38. Tanasova, M.; Anyika, M.; Borhan, B. *Angew. Chem., Int. Ed.* **2015,** *54,* 4274–4278. doi:10.1002/anie.201410371
39. Gholami, H.; Zhang, J.; Anyika, M.; Borhan, B. *Org. Lett.* **2017,** *19,* 1722–1725. doi:10.1021/acs.orglett.7b00495

40. Gholami, H.; Anyika, M.; Zhang, J.; Vasileiou, C.; Borhan, B. *Chem. – Eur. J.* **2016,** *22,* 9235–9239. doi:10.1002/chem.201601064
41. Kuwahara, S.; Nakamura, M.; Yamaguchi, A.; Ikeda, M.; Habata, Y. *Org. Lett.* **2013,** *15,* 5738–5741. doi:10.1021/ol402767a
42. Dutot, L.; Wright, K.; Wakselman, M.; Mazaleyrat, J.-P.; Peggion, C.; De Zotti, M.; Formaggio, F.; Toniolo, C. *Tetrahedron Lett.* **2008,** *49,* 3475–3479. doi:10.1016/j.tetlet.2008.03.087
43. Ooi, T.; Uematsu, Y.; Kameda, M.; Maruoka, K. *Angew. Chem., Int. Ed.* **2002,** *41,* 1551–1554. doi:10.1002/1521-3773(20020503)41:9<1551::aid-anie1551>3.0.co;2-l
44. Mason, S. F.; Seal, R. H.; Roberts, D. R. *Tetrahedron* **1974,** *30,* 1671–1682. doi:10.1016/s0040-4020(01)90689-1
45. Hanazaki, I.; Akimoto, H. *J. Am. Chem. Soc.* **1972,** *94,* 4102–4106. doi:10.1021/ja00767a007
46. Di Bari, L.; Pescitelli, G.; Salvadori, P. *J. Am. Chem. Soc.* **1999,** *121,* 7998–8004. doi:10.1021/ja990326b
47. *Spartan'18;* Wavefunction: Irvine, CA, USA, 2018.
48. CCDC 2455547 ((*S*)-**2b**) contains the supplementary crystallographic data for this paper. These data can be obtained free of charge from The Cambridge Crystallographic Data Centre via https://www.ccdc.cam.ac.uk/structures.

License and Terms

The definitive version of this article is the electronic one which can be found at:
https://doi.org/10.3762/bjoc.21.168

BEILSTEIN JOURNAL OF ORGANIC CHEMISTRY

Catalytic enantioselective synthesis of selenium-containing atropisomers via C–Se bond formations

Qi-Sen Gao‡, Zheng-Wei Wei‡ and Zhi-Min Chen*

Review

Address:
State Key Laboratory of Synergistic Chem-Bio Synthesis, School of Chemistry and Chemical Engineering, Shanghai Key Laboratory for Molecular Engineering of Chiral Drugs, Shanghai Jiao Tong University, Shanghai 200240, P. R. China

Email:
Zhi-Min Chen* - chenzhimin221@sjtu.edu.cn

* Corresponding author ‡ Equal contributors

Keywords:
asymmetric catalysis; atropisomer; chiral selenium-containing compound; C–Se bond formation

Beilstein J. Org. Chem. **2025,** *21,* 2447–2455.
https://doi.org/10.3762/bjoc.21.186

Received: 21 August 2025
Accepted: 29 October 2025
Published: 06 November 2025

This article is part of the thematic issue "Non-central chirality in organic chemistry".

Associate Editor: N. Yoshikai

Abstract

Atropisomers are not only prevalent in biologically active natural products and pharmaceuticals, but they have also garnered increasing attention for their effectiveness as ligands and catalysts in the field of catalytic asymmetric synthesis. Asymmetric catalysis serves as a key strategy for the enantioselective synthesis of atropisomers, and significant progress has been made in recent years. However, selenium-containing atropisomers have long remained underexplored as synthetic targets, and only in recent years have they begun to attract increasing attention from the community. Recently, several synthetic approaches for constructing selenium-containing atropisomers have been reported, such as C–H selenylation of arenes, selenosulfonylation of vinylidene *o*-quinone methides (VQM), and hydroselenation of alkynes. Nevertheless, a comprehensive review that systematically summarizes these advances is currently lacking. This review aims to provide an overview of recent developments in the catalytic enantioselective synthesis of selenium-containing atropisomers via C–Se bond formation. We hope this review will serve as a valuable reference for researchers interested in further exploring this area.

Introduction

Selenium is an essential trace element for human body [1]. It plays an important role in metabolism. In 1817, the Swedish chemist Berzelius found that red residual mud was attached to the wall and bottom of the lead chamber when roasting pyrite to produce sulfuric acid. After analysis, it was confirmed that there was a new element in it. Referring to the name of tellurium (originally meaning earth), he named it selenium according to the word "Selene" in ancient Greek mythology [2]. Selenium is a non-metallic element, but compared with sulfur of the same main group, selenium has a larger atomic radius, smaller electronegativity, and exhibits certain metallic properties. Due to the special physical and chemical properties of selenium between metal and nonmetal, selenium not only has many applications in industry, but also plays an important role in many fields, such as electronics [3], agriculture [4], environmental protection [5] and cosmetics [6]. Chiral organic selenium-containing compounds also have important applications in organic synthesis and biomedicine [7,8]. These compounds can participate in asymmetric synthesis reactions and construct chiral molecules with specific stereoconfiguration, which is particularly critical for drug synthesis [9]. In the field of organic catalysis, chiral organic selenium-containing compounds can be used as chiral ligands or catalysts to participate in various types of asymmetric reactions, significantly improving the selectivity of reactions (Figure 1) [10-14].

Catalytic asymmetric synthesis is the main method to construct chiral organic selenium-containing compounds. Centrally chiral selenium-containing compounds can be efficiently constructed by catalytic asymmetric hydroselenation, catalytic asymmetric allyl substitution, catalytic asymmetric electrophilic selenylation/cyclization, etc. The research content of this part has already been covered by relevant reviews [15-17], so it is not within the scope of discussion in this review. Axially chiral selenium-containing compounds also play an irreplaceable role in asymmetric catalysis, functional materials, pharmaceutical chemistry and other fields. However, little attention has been paid to these compounds, which led to slow development and a relative lack of catalytic asymmetric synthesis methods. Only recently, methods for the formation of C–Se bonds have been established for the construction of selenium-containing atropisomers. However, there is no comprehensive review to summarize this great progress. In this paper, the catalytic asymmetric synthesis of axially chiral selenium-containing compounds by the formation of C–Se bonds is reviewed from three aspects.

Review

1. Catalytic atroposelective synthesis of selenium-containing atropisomers by transition-metal-catalyzed C–H selenylation reactions

Transition-metal-catalyzed enantioselective C–H activation has emerged as a powerful strategy for the rapid synthesis of functionally enriched axially chiral diaryl compounds. However, due to the potential strong coordination between organoselenium compounds and transition metals, the direct construction of C–Se bonds via metal-catalyzed C–H bond functionalization remains a significant challenge. In 2024, You and co-workers reported a breakthrough in the enantioselective direct C–H selenylation of 1-arylisoquinolines and 2-(phenylselenyl)isoindoline-1,3-diones under rhodium catalysis to afford axially chiral diaryl selenides [18]. In this protocol, $AgPF_6$ was employed as an additive and mesitylene served as the solvent. The reaction was conducted at 60 °C under an argon atmosphere. When 1-(naphthalen-1-yl)benzo[*h*]isoquinoline derivatives bearing various substituents were used as substrates, the reaction proceeded efficiently, yielding the products with excellent conversion rates (up to 95% yield) and high enantioselectivity (up to 96% ee). Notably, isoquinoline derivatives containing polycyclic naphthalene moieties or *ortho*-substituted phenyl

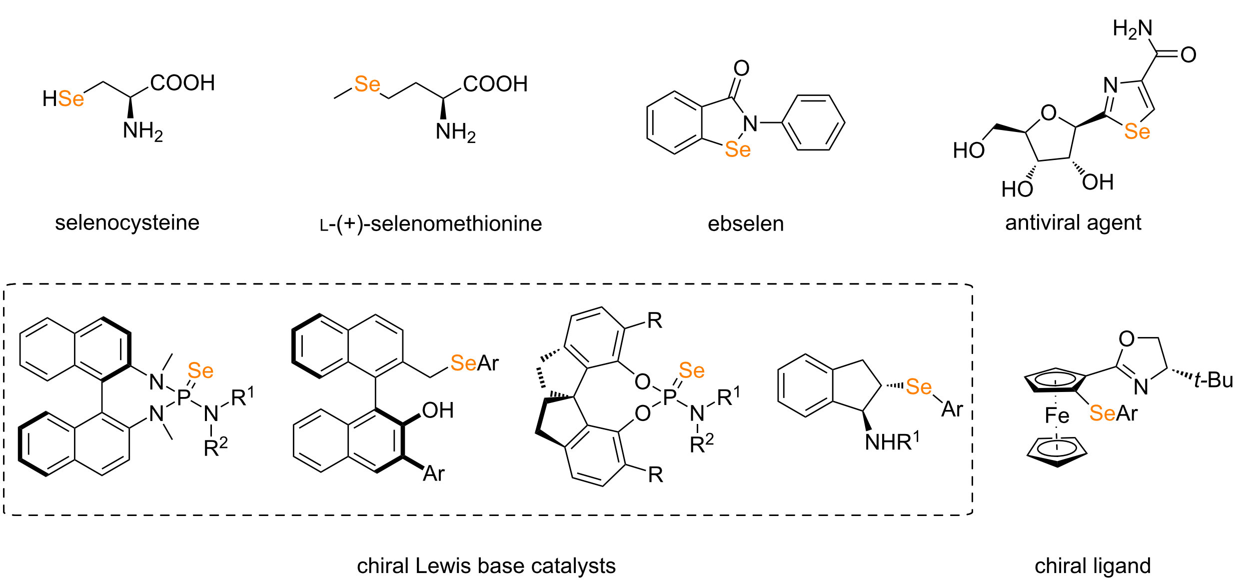

Figure 1: Representative examples of chiral selenium-containing compounds.

groups also demonstrated good reactivity and compatibility. DFT calculations indicated that the C–Se bond formation proceeded through an S_N2-type nucleophilic substitution mechanism (Scheme 1).

In 2025, Li and co-workers reported a highly efficient rhodium-catalyzed enantioselective C–H selenylation reaction of 1-arylisoquinolines with diselenides, employing 3,5-$(CF_3)_2C_6H_3CO_2Ag$ and $AgSbF_6$ as additives [19]. When a *para*-fluorine substituent is present on the naphthalene ring of the substrate, the reaction proceeds with a yield of up to 90% and an enantioselectivity reaching 92% ee. The methodology demonstrates a broad substrate scope, accommodating various polycyclic naphthalene isoquinolines as well as phenyl-substituted benzoisoquinoline derivatives. Two plausible reaction mechanisms were proposed in the study: one involving oxidative addition of **Int 4**, a five-membered rhodium cyclic intermediate, followed by reductive elimination and the other proceeding via a bimolecular nucleophilic substitution pathway. In both pathways, the active chiral rhodium catalyst is regenerated through a silver salt-mediated recycling, with Ag–SePh being formed as a byproduct (Scheme 2).

2. Catalytic atroposelective synthesis of selenium-containing atropisomers by spontaneous selenosulfonylation of alkynes

Vinyl selenides, recognized as valuable synthetic intermediates and biologically active compounds, have been demonstrated to exhibit a broad spectrum of biological activities. Among them, the synthesis of β-(selenium)vinyl sulfones can be accomplished via selenosulfonylation reactions initiated by free radicals or cationic species. In 2019, Qin and co-workers reported a methodology enabling the difunctionalization of alkynes through selenosulfonylation of a VQM intermediate under mild reaction conditions [20]. This racemic transformation proceeds without the need for any catalyst or additive, and the reaction yielded the desired product at room temperature with high regioselectivity and stereoselectivity (*E*/*Z* ratio >99:1). Notably, when chiral catalyst (**cat.1**) was used, the reaction afforded the axially chiral product **9** in 43% yield with 84% ee. The proposed mechanism proceeds as follows. Catalyst **cat.1** initially engages substrate **7** through hydrogen bonding, forming intermediate **Int 7**. Subsequently, deprotonation of the naphthol group by quinuclidine yields intermediate **Int 8**. This intermediate then undergoes nucleophilic attack on the selenium atom in substrate **8**, leading to the formation of the VQM intermediate **Int 9** and benzenesulfonic acid. Finally, benzenesulfonic acid further reacts with the VQM intermediate to afford product **9**, concomitant with regeneration of the catalyst. This protocol provides a promising approach for the enantioselective synthesis of axially chiral styrenes containing both selenium and sulfone functionalities, highlighting the potential for further exploration of expanded catalyst and substrate scopes (Scheme 3).

3. Catalytic atroposelective synthesis of selenium-containing atropisomers by hydroselenation reactions of alkynes

The catalytic enantioselective hydroselenation of alkynes can provide an efficient and direct method for the synthesis of chiral vinyl selenides. However, to date, the enantioselective hydroselenation of alkynes remains underexplored. Building upon recent advances in rhodium-catalyzed asymmetric hydroselenation of olefins, in 2024, Li and co-workers reported an asymmetric hydroselenation reaction of 1-alkynylindoles using a catalytic system based on $[Rh(cod)OAc]_2$ and $Mg(NTf_2)_2$ [21]. The Mg(II) salt not only activates the rhodium catalyst but also supplies the necessary NTf_2^- anion for the reaction system, thereby significantly enhancing the catalytic performance. The developed catalytic system demonstrated high activity, excellent yields (mostly exceeding 85%), mild reaction conditions, broad functional group tolerance, as well as high regioselectivity, (*E*)-selectivity, and enantioselectivity (up to 99% ee). According to the kinetic study, the alkyne insertion step may be rate-limiting, as it involves the participation of selenol, alkyne, and the rhodium catalyst. The Rh(III) mechanism appears to be more plausible than route B, which can be attributed to the enhanced ion-pairing effect resulting from the higher oxidation state of rhodium (Scheme 4).

In 2025, Yang, Lu, and co-workers employed bifunctional catalysts, including chiral thiourea derivatives or chiral phosphoric acid, to activate alkynes and selenols through multiple hydrogen-bonding interactions, thereby achieving an enantioselective hydroselenation of alkynes [22]. All products demonstrated complete *E*-stereoselectivity (*E*/*Z* ratio >20:1). Notably, under the same reaction conditions, aliphatic selenols remained unreactive. Density functional theory (DFT) calculations revealed that the rate-determining step involves the nucleophilic attack of the selenium anion in intermediate **Int 16** on VQM to form intermediate **Int 17**. As bifunctional organic catalysts, chiral ureas can synergistically activate both alkynes and selenols, thereby addressing the challenge of overcoming the increased difficulty of racemization caused by the presence of bulky SeR groups (Scheme 5).

Summary and Outlook

Overall, organic chemists have increasingly focused on the catalytic asymmetric synthesis of selenium-containing atropisomers, and significant progress has been made in recent years. Nevertheless, several limitations and challenges remain. For example, catalytic asymmetric electrophilic selenylation reactions

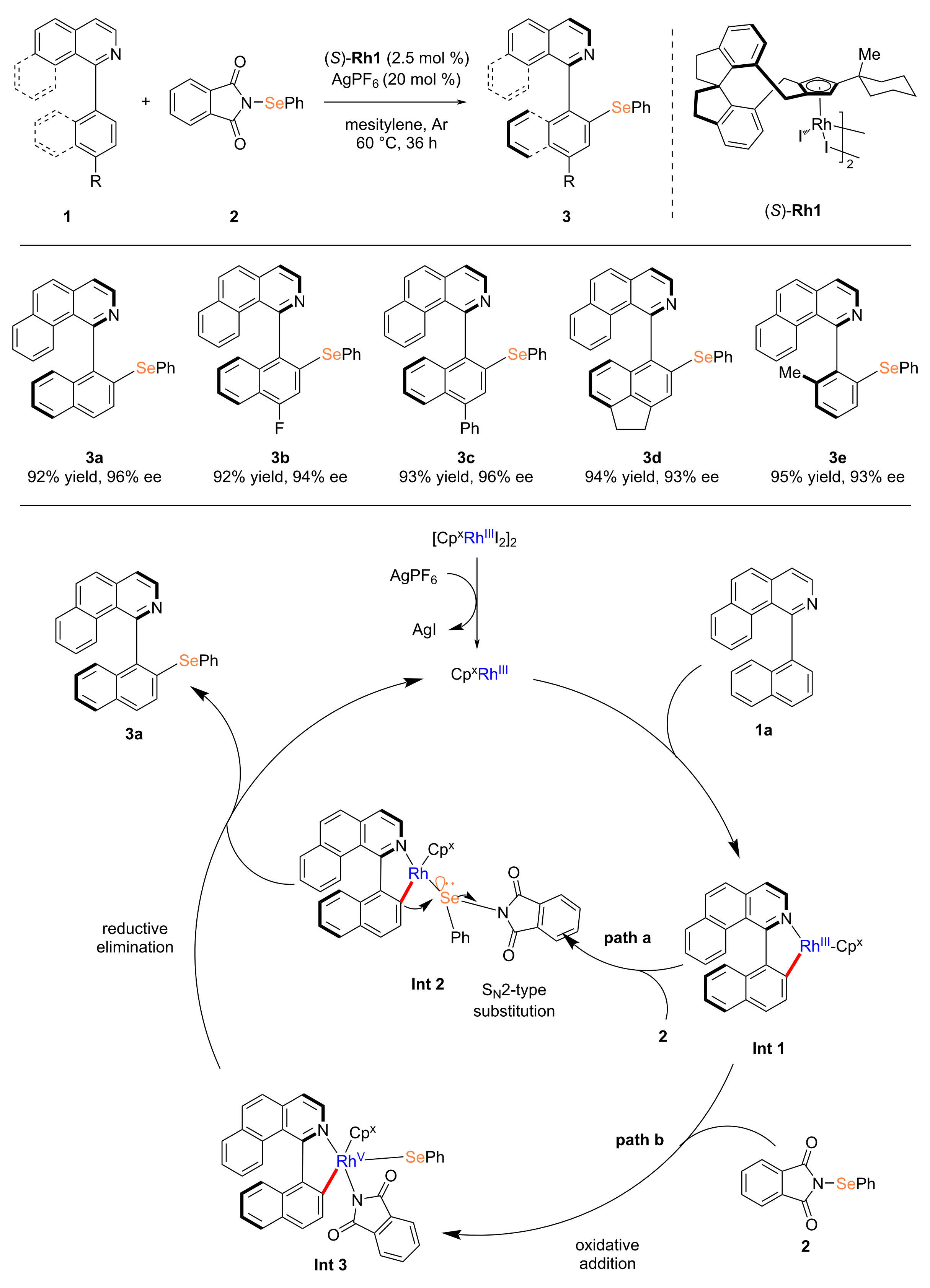

Scheme 1: Rhodium-catalyzed atroposelective C–H selenylation reported by You's group [18].

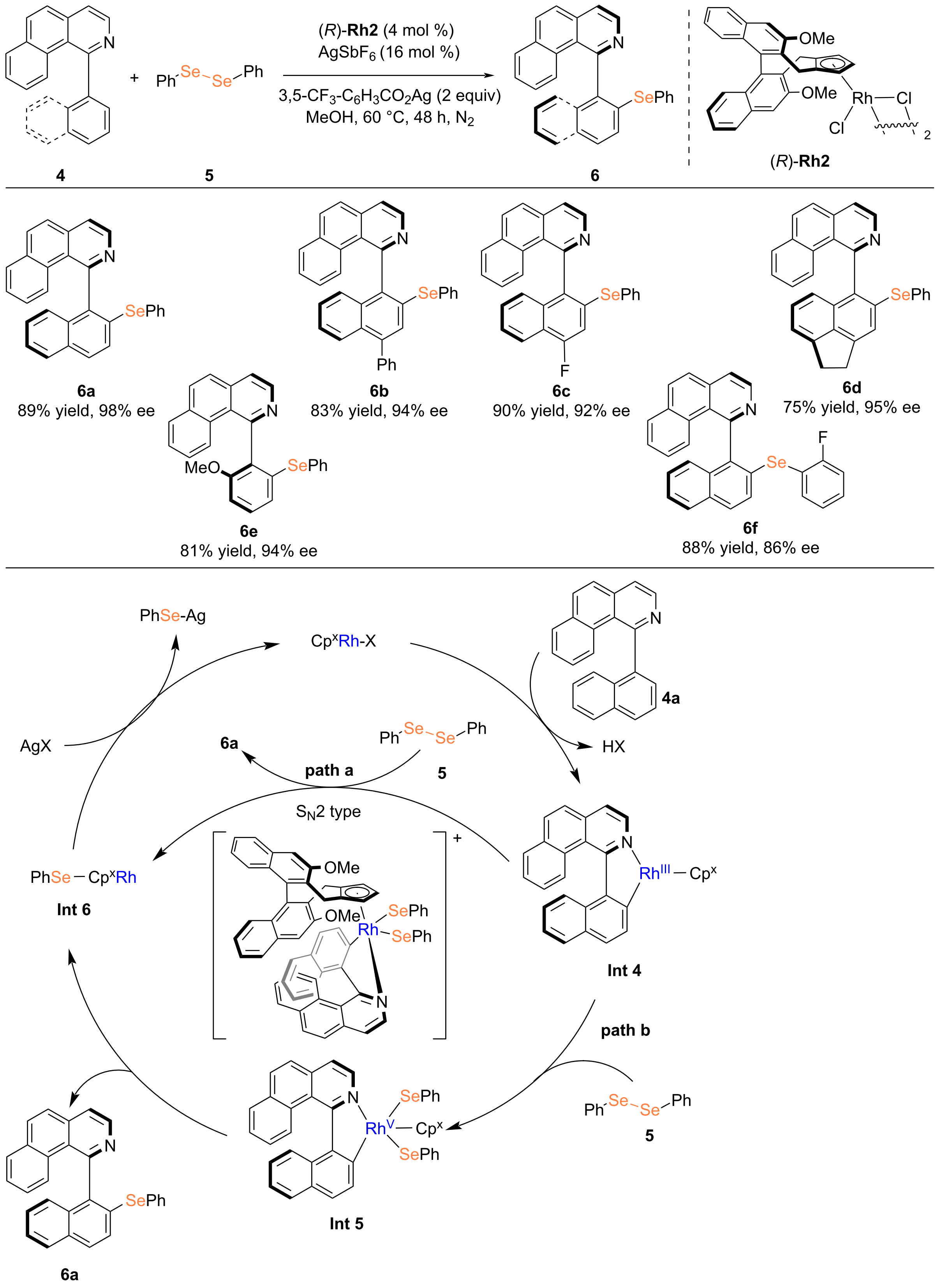

Scheme 2: Rhodium-catalyzed atroposelective C–H selenylation reported by Li et al. [19].

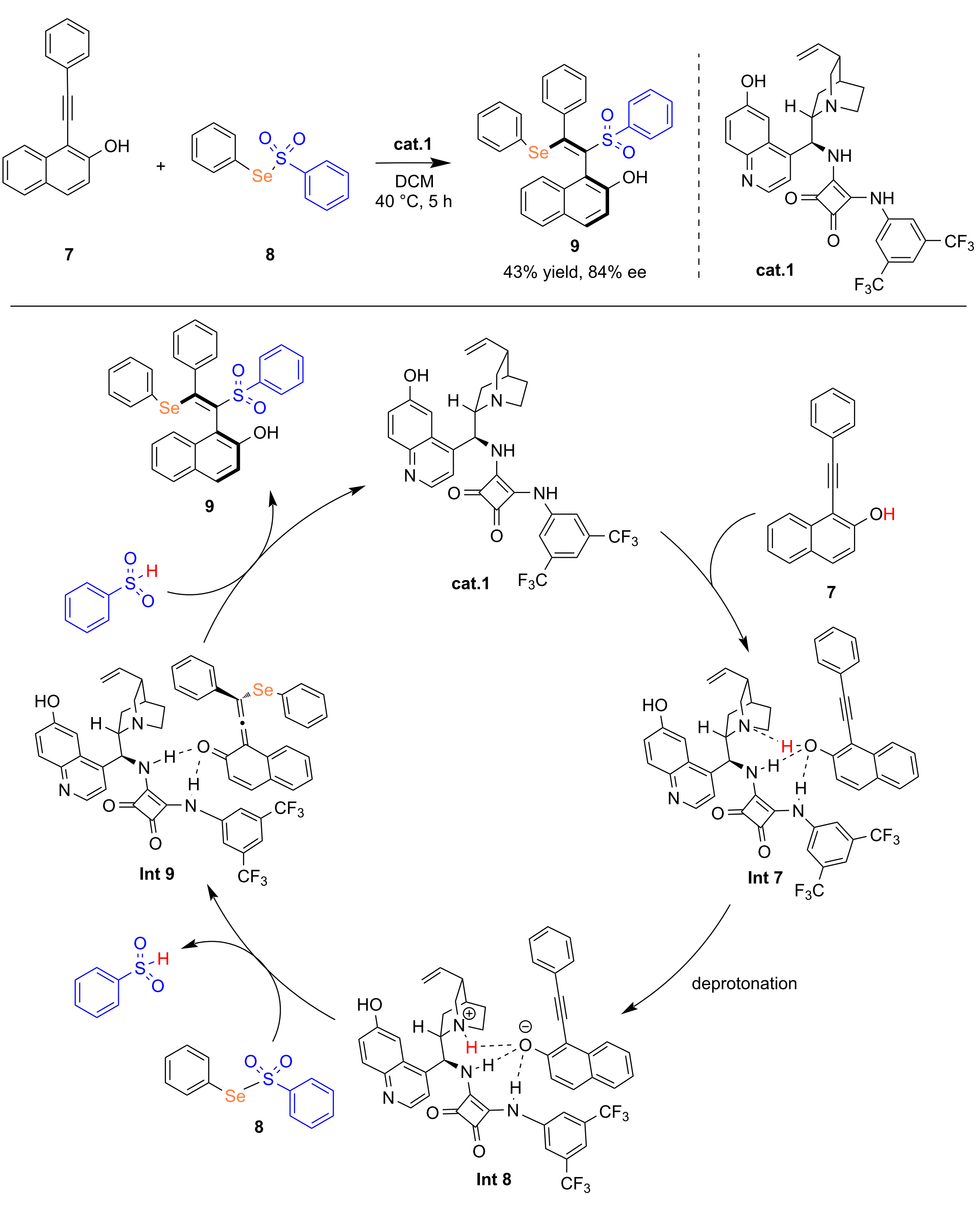

Scheme 3: Organocatalytic asymmetric selenosulfonylation of alkynes.

have not yet enabled the effective synthesis of selenium-containing atropisomers. Moreover, the current methodologies are largely restricted to the use of selenium aryl groups. It is our intention to draw the attention of emerging researchers to this field and to promote its continued growth and development.

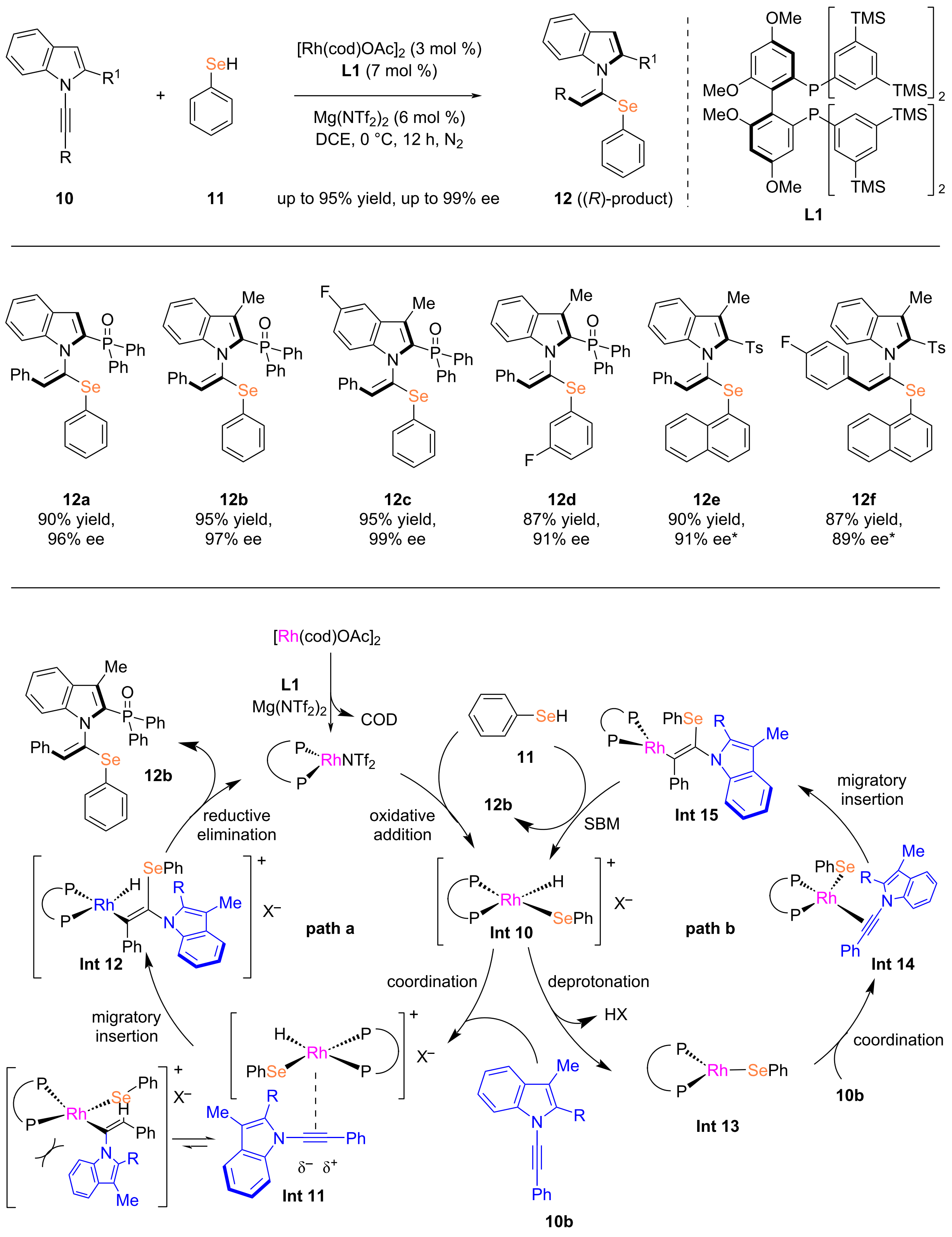

Scheme 4: Rhodium-catalyzed asymmetric hydroselenation of 1-alkynylindoles. *DCE/DCM 2:1 (v/v), −50 °C.

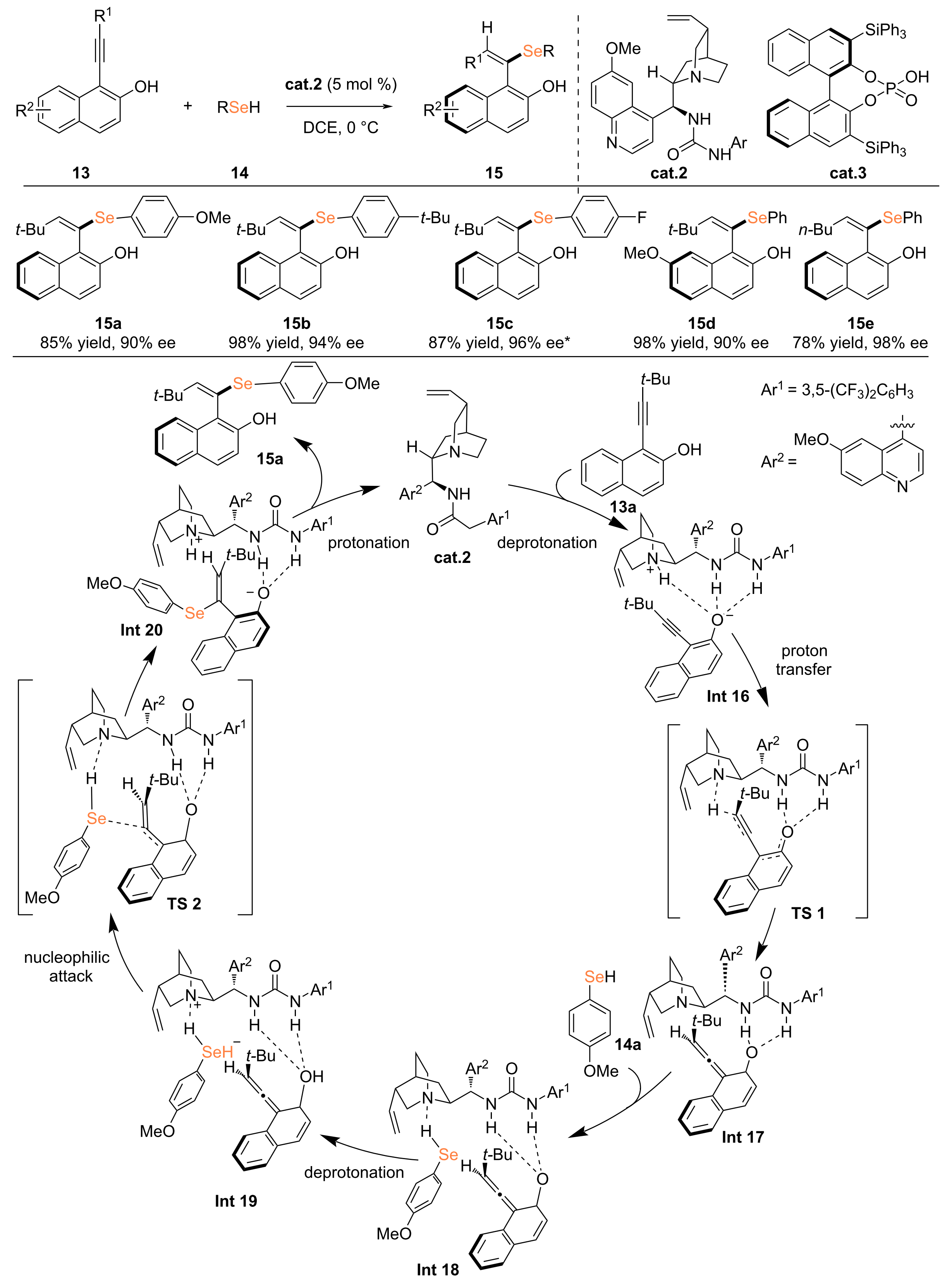

Scheme 5: Organocatalytic atroposelective hydroselenation of alkynes. *Using **cat.3**, 4 h.

Funding

We thank National Natural Science Foundation of China (22471158, 22071149), Natural Science Foundation of Shanghai (23ZR1428200) and the Fundamental Research Funds for the Central Universities (YG2024QNB27) for financial support.

ORCID® iDs

Zhi-Min Chen - https://orcid.org/0000-0002-6988-8955

Data Availability Statement

Data sharing is not applicable as no new data was generated or analyzed in this study.

References

1. Genchi, G.; Lauria, G.; Catalano, A.; Sinicropi, M. S.; Carocci, A. *Int. J. Mol. Sci.* **2023,** *24,* 2633. doi:10.3390/ijms24032633
2. Berzelius, J. J. *Afh. Fys., Kemi Mineral.* **1818,** *6,* 42.
3. Kamat, P. V. *J. Phys. Chem. C* **2008,** *112,* 18737–18753. doi:10.1021/jp806791s
4. Wang, M.; Li, B.; Li, S.; Song, Z.; Kong, F.; Zhang, X. *J. Agric. Food Chem.* **2021,** *69,* 15458–15467. doi:10.1021/acs.jafc.1c04992
5. Chang, C.; Chen, C.; Yin, R.; Shen, Y.; Mao, K.; Yang, Z.; Feng, X.; Zhang, H. *Environ. Sci. Technol.* **2020,** *54,* 3228–3236. doi:10.1021/acs.est.9b06486
6. Lv, J.; Ai, P.; Lei, S.; Zhou, F.; Chen, S.; Zhang, Y. *J. Trace Elem. Med. Biol.* **2020,** *62,* 126548. doi:10.1016/j.jtemb.2020.126548
7. Hou, W.; Dong, H.; Zhang, X.; Wang, Y.; Su, L.; Xu, H. *Drug Discovery Today* **2022,** *27,* 2268–2277. doi:10.1016/j.drudis.2022.03.020
8. Franchetti, P.; Cappellacci, L.; Sheikha, G. A.; Jayaram, H. N.; Gurudutt, V. V.; Sint, T.; Schneider, B. P.; Jones, W. D.; Goldstein, B. M.; Perra, G.; De Montis, A.; Loi, A. G.; La Colla, P.; Grifantini, M. *J. Med. Chem.* **1997,** *40,* 1731–1737. doi:10.1021/jm960864o
9. Wirth, T. *Angew. Chem., Int. Ed.* **2000,** *39,* 3740–3749. doi:10.1002/1521-3773(20001103)39:21<3740::aid-anie3740>3.0.co;2-n
10. Denmark, S. E.; Ryabchuk, P.; Chi, H. M.; Matviitsuk, A. *Org. Synth.* **2019,** *96,* 400–417. doi:10.15227/orgsyn.096.0400
11. Nishiyori, R.; Mori, T.; Okuno, K.; Shirakawa, S. *Org. Biomol. Chem.* **2023,** *21,* 3263–3275. doi:10.1039/d3ob00292f
12. Zhang, X.-Y.; Zhu, D.; Huo, Y.-X.; Chen, L.-L.; Chen, Z.-M. *Org. Lett.* **2023,** *25,* 3445–3450. doi:10.1021/acs.orglett.3c01002
13. You, S.-L.; Hou, X.-L.; Dai, L.-X. *Tetrahedron: Asymmetry* **2000,** *11,* 1495–1500. doi:10.1016/s0957-4166(00)00078-1
14. Liao, L.; Zhao, X. *Acc. Chem. Res.* **2022,** *55,* 2439–2453. doi:10.1021/acs.accounts.2c00201
15. Lai, S.; Liang, X.; Zeng, Q. *Chem. – Eur. J.* **2024,** *30,* e202304067. doi:10.1002/chem.202304067
16. Stadel, J. T.; Back, T. G. *Chem. – Eur. J.* **2024,** *30,* e202304074. doi:10.1002/chem.202304074
17. Jian, Y.; Singh, T.; Andersson, P. G.; Zhou, T. *Molecules* **2024,** *29,* 3685. doi:10.3390/molecules29153685
18. Zheng, D.-S.; Xie, P.-P.; Zhao, F.; Zheng, C.; Gu, Q.; You, S.-L. *ACS Catal.* **2024,** *14,* 6009–6015. doi:10.1021/acscatal.4c01082
19. Wang, Y.; Yu, S.; Li, X. *Org. Chem. Front.* **2025,** *12,* 816–823. doi:10.1039/d4qo01905a
20. Huang, S.; Chen, Z.; Mao, H.; Hu, F.; Li, D.; Tan, Y.; Yang, F.; Qin, W. *Org. Biomol. Chem.* **2019,** *17,* 1121–1129. doi:10.1039/c8ob02967a
21. Kang, Y.; Wang, F.; Li, X. *ACS Catal.* **2024,** *14,* 13055–13064. doi:10.1021/acscatal.4c03710
22. Wang, Y.-X.; Wang, J.-R.; Cui, C.; Wang, Z.; Lu, Y.; Yang, X.-H. *ACS Catal.* **2025,** *15,* 4051–4060. doi:10.1021/acscatal.4c07281

License and Terms

The definitive version of this article is the electronic one which can be found at:
https://doi.org/10.3762/bjoc.21.186

BEILSTEIN JOURNAL OF ORGANIC CHEMISTRY

Design and synthesis of an axially chiral platinum(II) complex and its CPL properties in PMMA matrix

Daiki Tauchi*[1], Sota Ogura[1], Misa Sakura[2], Kazunori Tsubaki[2] and Masashi Hasegawa*[1]

Full Research Paper

Open Access

Address:
[1]Department of chemistry, Kitasato University, Kanagawa 252-0373, Japan and [2]Graduate School of Life and Environmental Science, Kyoto Prefectural University, Kyoto 606-8522, Japan

Email:
Daiki Tauchi* - tauchi.daiki@kitasato-u.ac.jp; Masashi Hasegawa* - masasi.h@kitasato-u.ac.jp

* Corresponding author

Keywords:
axial chirality; chiral chemistry; circularly polarized luminescence (CPL); phosphorescence; platinum(II) complex

Beilstein J. Org. Chem. **2026,** *22,* 143–150.
https://doi.org/10.3762/bjoc.22.7

Received: 31 August 2025
Accepted: 30 December 2025
Published: 15 January 2026

This article is part of the thematic issue "Non-central chirality in organic chemistry".

Associate Editor: N. Yoshikai

Abstract

A pair of an axially chiral platinum(II) complex was synthesized via Sonogashira coupling and subsequent coordination of a pincer ligand to a precursor. The complex exhibited a broad absorption band ranging from 250 to 550 nm in the UV–vis spectrum, with TD-DFT calculations indicating mixed ligand-to-ligand charge transfer (LL’CT) and metal-to-ligand charge transfer (MLCT) character. Photoluminescence measurements in CH_2Cl_2 solution revealed dual emission peaks at 427 nm and 596 nm, with a quantum yield of 3%. In PMMA matrix, the emission peaks were blue-shifted to 408 nm and 558 nm, and the quantum yield slightly increased to 4%. CD spectra showed distinct Cotton effects in the MLCT region, and CPL signals were observed only in the PMMA matrices, with a dissymmetry factor $|g_{\text{lum}}| = 0.4 \times 10^{-3}$. These results demonstrate that axial chirality of the binaphthyl moiety governs the three-dimensional chiral arrangement of two platinum(II) chromophore units, leading to the chiroptical properties in the MLCT region through exciton coupling under restricted molecular motion.

Introduction

Luminescent materials based on metal complexes have been extensively studied due to their high phosphorescence efficiency, making them promising candidates for applications in organic light-emitting diodes (OLEDs) [1-5], sensors [6-9], and bioimaging materials [10,11]. Among these materials, pincer-type platinum(II) complexes have attracted particular attention, owing to the structural robustness imparted by tridentate chelating ligands and their excellent luminescent properties [12-17]. These complexes have been widely investigated, not only for practical application but also from the perspective of fundamental chemistry.

In recent years, the design and synthesis of luminescent pincer-type platinum(II) metal complexes incorporating chirality, as well as the study of their physicochemical properties, have gained significant interest [18-22]. Such efforts aim to explore the development of materials exhibiting circularly polarized luminescence (CPL). However, most reported chiral pincer-type platinum(II) complexes utilize point chirality as the chiral element. For instance, Zhong and co-workers reported a chiral platinum(II) complex bearing a leucine-derived pendant group, which exhibited aggregation-enhanced red phosphorescence and CPL properties in the solid states [20], while Yam and co-workers also reported pincer-type platinum(II) complexes containing chiral amine moieties, and investigated their aggregation behavior and chiroptical properties [22]. In both cases, significant CPL signals were observed only in the aggregated state, because the introduction of chirality through point chirality does not induce a significant electronic effect in the monomeric state; instead, the observed chiroptical activity originates from the chiral spatial arrangement of several molecules in the aggregated state. To expand the scope of chirality in metal complex chemistry with pincer ligands and to facilitate the design of next-generation CPL-active materials, alternative chiral motifs beyond point chirality are highly desirable.

Herein, we report the design and synthesis of a chiral ligand featuring an axially chiral binaphthyl backbone and its employment in the construction of novel types of a chiral platinum(II) complex with pincer ligand (Figure 1). We investigated the spectroscopic properties of the resulting complex, including its chiroptical behavior, through a combination of experimental measurements and density functional theory (DFT) calculations. The experimental UV–vis spectrum was in good agreement with the DFT calculations, revealing that the electronic transitions originate from both ligand-to-ligand charge transfer (LL’CT) and metal-to-ligand charge transfer (MLCT). Furthermore, chiroptical measurements by circular dichroism (CD) and CPL spectroscopy indicated that the axial chirality of the binaphthyl moiety governs the relative orientation of the Pt(II)-based chromophore pair, generating MLCT-band CD and CPL signals through exciton coupling in both the ground and excited states. While no CPL was observed in solution, distinct CPL properties observed in the PMMA matrices. This behavior is attributed to the effect of the axial chirality, which becomes more effective upon suppression of molecular motion within the polymer environment.

Results and Discussion

Synthesis

Each enantiomer of the target platinum(II) complex was synthesized separately. The synthesis of the chiral backbone ***S*****/*****R*****-3** was prepared in two steps starting from a chiral binaphthyl derivative [23]. Compound ***S*****/*****R*****-2** was obtained by using a Sonogashira coupling reaction of ***S*****/*****R*****-1** with trimethtylsilylacetylene in toluene (Scheme 1). Subsequent deprotection of the trimethylsilyl (TMS) groups with tetrabutylammonium fluoride (TBAF) afforded the desired ligand ***S*****/*****R*****-3**. The preparation of the target platinum(II) complex was performed by using a similar procedure of other platinum(II) complexes with pincer ligand moieties [12]. Thus, the reaction of ***S*****/*****R*****-3** with platinum(II) precursor **4** in the presence of CuI and diisopropylamine afforded the target platinum(II) complex ***S*****/*****R*****-Pt** in moderate yield. The identification of the complex ***S*****/*****R*****-Pt** were carried out with ^{1}H and ^{13}C NMR spectroscopy, as well as high-resolution mass spectrometry (HRMS). Due to its low solubility, single crystals suitable for X-ray crystallographic analysis could not be obtained.

Spectroscopic analysis and DFT calculations

To elucidate the electronic structure of the platinum(II) complex, UV–vis absorption spectroscopy was performed in dilute solution of dichloromethane (1.0×10^{-5} M) (Figure 2a). The absorption spectrum displayed wide range absorption character

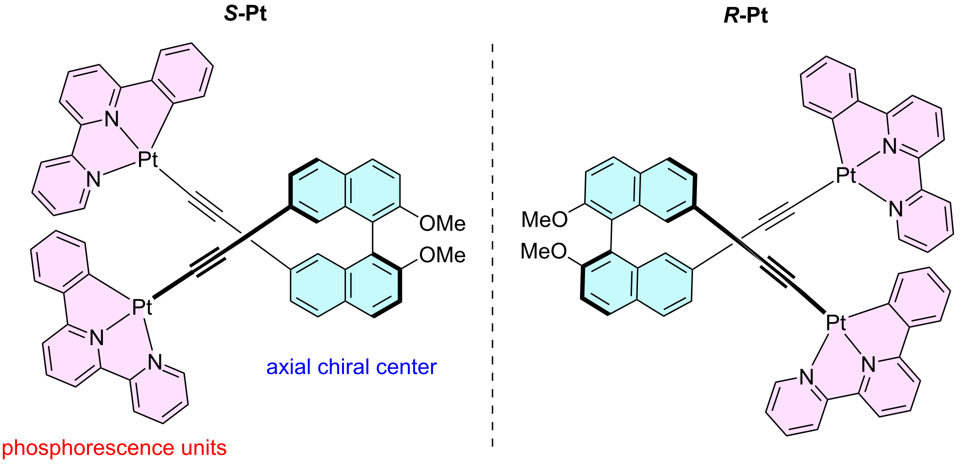

Figure 1: Molecular design for axially chiral platinum(II) complex ***S*****/*****R*****-Pt** based on a pincer ligand.

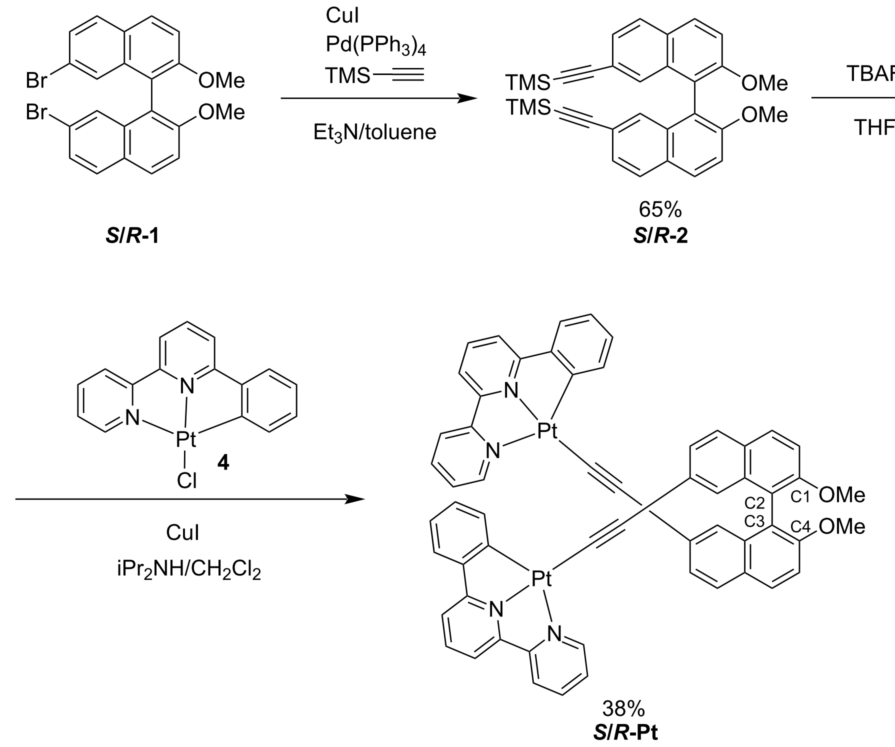

Scheme 1: Synthesis of the binaphthyl-based ligand and the platinum(II) complex. Yields indicated correspond to the *S*-isomer.

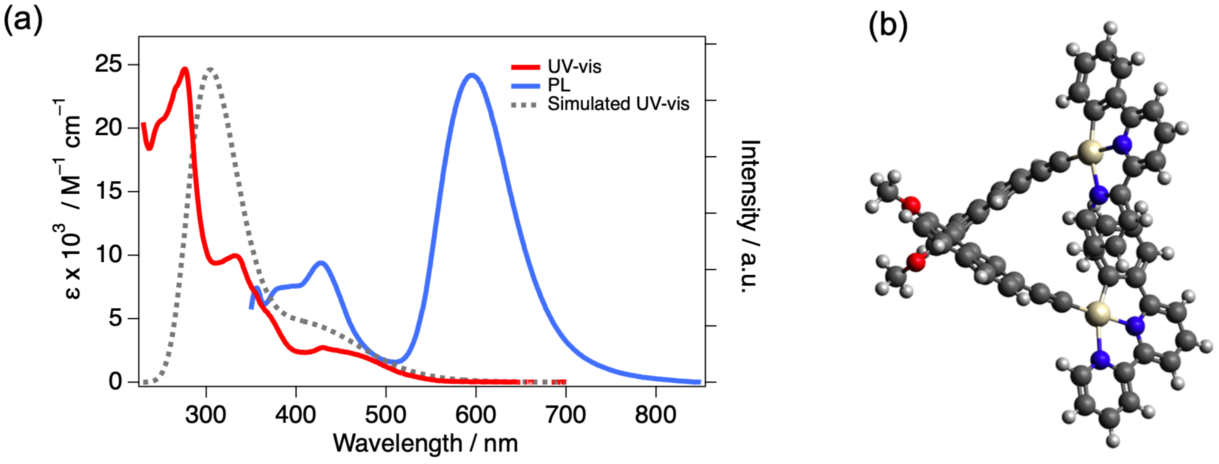

Figure 2: (a) UV–vis and PL spectra (λ_{ex} = 300 nm) in 1.0 × 10^{-5} M dichloromethane solution, the gray dotted line shows a simulated UV–vis spectrum by TD-DFT calculation. (b) Optimized structure of ***R*-Pt** by DFT calculation.

from 250 to 700 nm with maxima at 430, 331, and 276 nm. To gain deeper insight into the nature of these electronic transitions, density functional theory (DFT) calculations were carried out. The calculations were performed at the CAM-B3LYP/6-31G+(d,p) level, with the LANL2DZ basis set applied to the Pt atoms. The optimized structure of ***R*-Pt** is shown in Figure 2b. The dihedral angle of the binaphthyl moiety (∠C1–C2–C3–C4) was 71°, which is smaller than the 80–100° range typically reported for the most stable conformation of binaphthyl groups [24]. In contrast, the dihedral angles between the binaphthyl unit and the coordination plane were 54° and 52°, respectively. The UV–vis spectral simulation based on electronic transition obtained from time-dependent (TD)-DFT qualitatively reproduced the observed spectra. The details of the electronic transition were attached in Supporting Information File 1. The broad absorption band in the long-wavelength region was assigned to a MLCT transition, while the absorption bands in the shorter wavelength region were attributed to a mixture of LL'CT and MLCT transitions. These electronic characteristics are similar to those reported for other chiral platinum(II) complexes [25-27].

The photoluminescence (PL) spectrum of the platinum(II) complex was measured in dichloromethane solution (1.0×10^{-5} M), revealing two emission bands centered at approximately 427 nm and 596 nm (Figure 2). The corresponding emission decays were well fitted by a three-exponential function, yielding fluorescence components of 3.6 ns (62%), 8.0 ns (20%), and 0.39 ns (18%) at 427 nm, and phosphorescence components of 0.11 µs (64%), 69 ns (35%), and 6.3 ns (1%) at 596 nm, respectively. The photoluminescence quantum yield (PLQY) in dichloromethane was measured to be 3%. The relatively low PLQY is likely attributed to non-radiative deactivation pathways associated with rotational motions of the axially chiral moiety and the ethynyl-linked coordination sites. Therefore, we prepared a PMMA polymer matrix containing 1 wt % of ***S*/*R*-Pt** to investigate the emission behavior under conditions where molecular motion was suppressed.

The PMMA matrix was obtained by dissolving ***S*/*R*-Pt** and PMMA in chloroform under heating at 40 °C, casting the solution onto a glass substrate, and allowing it to dry slowly under ambient conditions. The emission spectrum of the PMMA matrix exhibited two emission components, similar to those observed in solution (Figure 3). Compared to the solution phase, the longer-wavelength emission peak (558 nm) was blue-shifted by 38 nm, and the shorter-wavelength emission peak (408 nm) was blue-shifted by 19 nm. These blue shifts are attributed to the hydrophobic environment in the PMMA matrix. In such low-polarity surroundings, the excited state is less stabilized, resulting in a higher excited-state energy and thus a blue-shifted emission. The PLQY in the PMMA matrix was 4%, comparable to that observed in solution. In the film, the emission lifetimes could be fitted with double- or triple-exponential functions, resulting in fluorescence components of 0.49 ns (50%) and 0.48 ns (50%) at 408 nm, and phosphorescence components of 0.25 µs (76%), 0.024 µs (11%), and 2.8 ns (10%) at 558 nm, consistent with similar excited-state dynamics in both environments.

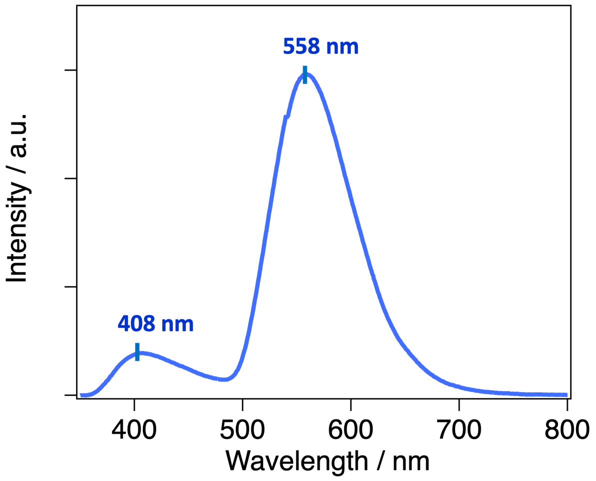

Figure 3: Emission spectrum of 1 wt % PMMA matrix (***R*-Pt**) (λ_{ex} = 300 nm).

To investigate the chiroptical properties of the complex, CD spectra were recorded in 1.0×10^{-5} M dichloromethane solution (Figure 4a). The CD spectra of both enantiomers showed clear mirror-image signals, and the experimental results were in good agreement with the simulated spectra obtained from DFT calculations (see Supporting Information File 1). The first Cotton effect attributed by MLCT transition was observed

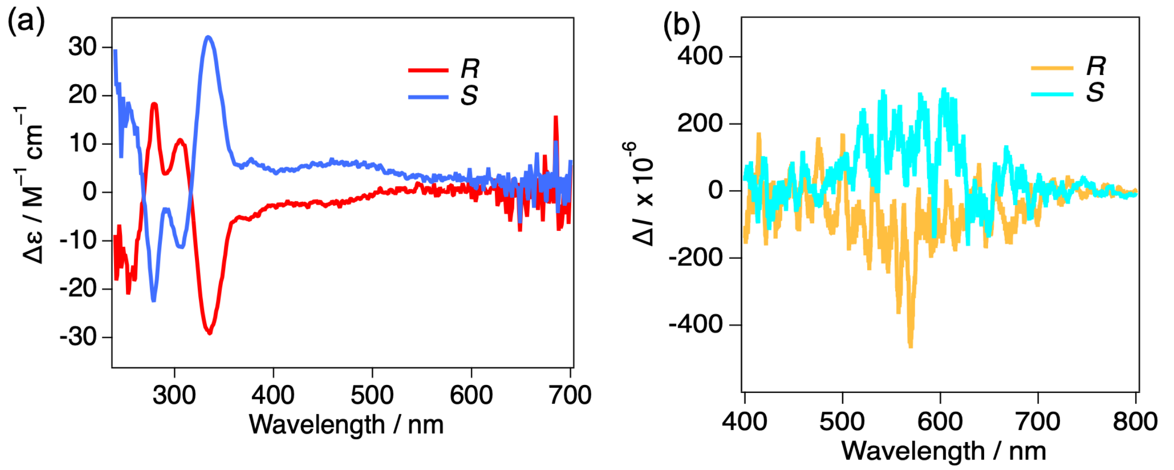

Figure 4: (a) CD spectra of ***S*/*R*-Pt** in 1.0×10^{-5} M dichloromethane solution. (b) CPL spectra of 1 wt % PMMA film (λ_{ex} = 300 nm).

around 400 to 500 nm, indicating the axial chirality of the binaphthyl groups reflect the CD signals. It assumes circularly polarized phosphorescence (CPP) properties by platinum(II) centered emission. The TD-DFT calculation also reproduces the CD spectrum, showing the same sign in the first Cotton effect ($g_{\mathrm{abs}} = 1.1 \times 10^{-3}$ at 404 nm). The corresponding g_{abs} chart is included in Supporting Information File 1. The CPL measurements were conducted to further elucidate the chiral emissive properties of the platinum(II) complex. The dichloromethane solution of the complex showed no detectable CPL signal, this is likely due to averaging of the transition dipole moments caused by intramolecular motions, leading to a cancellation of dipole moment or potentially weak magnetic dipole moment. In contrast, 1 wt % PMMA matrices exhibited distinct CPL activity, with the CPL signal showing the same sign as the first Cotton effect in the CD spectrum (Figure 4b). The dissymmetry factor is defined as follows: $g_{\mathrm{lum}} = 2\Delta I/I = 2(I_{\mathrm{L}} - I_{\mathrm{R}})/(I_{\mathrm{L}} + I_{\mathrm{R}})$, where I_{L} and I_{R} denote the luminescence intensities of left- and right-handed circularly polarized luminescence, respectively. The measured dissymmetry factor $|g_{\mathrm{lum}}|$ was 0.4×10^{-3} (at 558 nm), which is within the typical range for organic small-molecule systems [28-30], indicating the restriction of molecular motions in PMMA matrices induced CPL properties. The g_{lum} value was significantly smaller than the g_{abs} value in solution, which is considered to originate from structural flexibility in the excited state [28].

Conclusion

In conclusion, we synthesized a novel pincer-type platinum(II) complex by incorporating an axially chiral binaphthyl ligand through an acetylene linker. Spectroscopic and theoretical analyses revealed that the axial chirality of the binaphthyl moiety imposes a chiral arrangement on the pair of platinum(II)-based chromophores, giving rise to MLCT-band CD and CPL through exciton coupling rather than through chirality induction at the platinum(II) center. The complex exhibited dual emission and distinct CPL activity in PMMA matrices, with a dissymmetry factor $|g_{\mathrm{lum}}|$ of 0.4×10^{-3}, highlighting the role of restricted molecular motion in enhancing chiroptical properties. These findings underscore the potential of axial chirality as a design principle for developing chiral phosphorescent materials and open avenues for further exploration of chiral metal complexes in optoelectronic applications.

Experimental

General information

All reagents and solvents were of commercial reagent grade and used without further purification. Dichloromethane for spectroscopy was purchased from FUJIFILM Wako Pure Chemical Corporation. All compounds were identified by ^{1}H , ^{13}C NMR and ESI-MS. ^{1}H and ^{13}C NMR spectra were recorded on a Bruker Avance III 400 or JEOL JNM-ECZ600R spectrometer at 25 °C in chloroform-d_1 or DMSO-d_6. ^{1}H NMR chemical shifts are expressed in parts per million (δ) relative to trimethylsilane (TMS) as a reference. Mass spectra were obtained with a Thermo Scientific, Exactive Plus Orbitrap mass spectrometer for electrospray ionization (ESI). IR spectra were measured using a FT/IR-4600 spectrometer with KBr pellets. UV–vis absorption spectra of CH_2Cl_2 solutions (1.0×10^{-5} M) were recorded with a JASCO V-560 UV–vis spectrometer. Photoluminescence spectra of CH_2Cl_2 solutions (1.0×10^{-5} M) and 1 wt % PMMA matrices were acquired using a JASCO FP-8550 spectrometer at room temperature, at excitation wavelength of 300 nm (both solution and PMMA matrix). CPL spectra of CH_2Cl_2 solutions (1.0×10^{-5} M) and 1 wt % PMMA matrices were measured with a JASCO CPL-300 spectrofluoropolarimeter at room temperature, at a scattering angle of 0° upon excitation with unpolarized, monochromated incident light. Absolute PLQYs of solutions and powder samples were determined using a JASCO FP-8550 spectrometer with an integrating sphere (JASCO ILF-533, diameter 96 mm) at an excitation wavelength of 300 nm. Fluorescence lifetimes were measured for solutions and powder samples with a HORIBA DeltaFlex spectrometer with a 370 nm LED light source for excitation. For the lifetime measurements of solution, a conventional 1 cm quartz cell was used. Optical rotation values were measured with a JASCO P-1030 polarimeter using the sodium D line (λ = 589 nm). All calculations were performed by using the Gaussian 16 rev C.02 program package. Density functional theory (DFT) calculations were performed at the level of CAM-B3LYP/LANL2DZ for Pt atoms. The optimized equilibrium structures were confirmed by normal coordinate analyses, with no imaginary frequency found.

Synthesis of axially chiral ligand and Pt(II) complex

Synthesis of ***S*/*R*-2**

The following describes the procedure for the *S*-enantiomer. Under an argon atmosphere, a mixture of ***S*-1** (282 mg, 0.597 mmol), CuI (32 mg, 0.17 mmol), $Pd(PPh_3)_4$ (112 mg, 0.0962 mmol) and trimethylsilylacetylene (0.40 mL, 2.9 mmol) was added degassed solution of Et_3N (2.6 mL, 19 mmol) and toluene (5.2 mL) by argon bubbling. The reaction mixture was refluxed at 90 °C for 21 hours. After cooling to room temperature, the reaction mixture was filtered through Celite. The Celite was thoroughly washed with dichloromethane, and the combined filtrate was washed three times with saturated aqueous NH_4Cl and brine. The organic layer was dried over anhydrous sodium sulfate. The crude product was purified by silica gel column chromatography using a 1:1 mixture of dichloromethane and hexane as the eluent. The eluent was evaporated to give the off-white solid ***S*-2** (197 mg, 65%).

Data for ***S*-2**: Off white solid; mp 103 °C (dec); HRMS (orbitrap) *m*/*z*: $[M + H]^+$ calcd. for $C_{32}H_{34}O_2Si_2$, 529.1990; found, 529.1990; ^1H NMR (400 MHz, $CDCl_3$) δ 7.94 (d, *J* = 9.2 Hz, 2H), 7.79 (d, *J* = 8.4 Hz, 2H), 7.45 (d, *J* = 8.8 Hz, 2H), 7.36 (dd, *J* = 1.6, 8.4 Hz, 2H), 7.202–7.198 (m, 2H), 3.74 (s, 6H), 0.17 (s, 18H); ^{13}C NMR (100 MHz, $CDCl_3$) δ 155.5, 133.7, 129.4, 128.9, 128.7, 128, 126.7, 121, 119.1, 114.7, 106.1, 94.2, 56.6, 0.05; IR (KBr) ν_{max}: 3058, 1774, 1409, 1191, 1152, 969, 698, 553, 431 cm^{-1}. The *R*-isomer was synthesized using a similar procedure to that of the *S*-isomer, except that compound ***R*-1** (300 mg, 0.52 mmol), trimethylsilylacetylene (0.30 mL, 2.2 mmol), CuI (32 mg, 0.17 mmol), $Pd(PPh_3)_4$ (112 mg, 0.096 mmol), Et_3N (2.3 mL) in toluene (4.5 mL) were used. The yield was 78%.

Synthesis of *S*/*R*-3

Under an argon atmosphere. ***S*-2** (197 mg, 0.389 mmol) in tetrahydrofuran (1.7 mL) was treated with a dropwise addition of 1 M TBAF solution (16.7 mL, 16.7mmol), and the resulting solution was stirred at room temperature for 2 hours. After the addition of water, the mixture was extracted with dichloromethane three times, and the combined organic layer was washed with saturated brine. The organic layer was dried over anhydrous sodium sulfate, after drying, the solvent was removed under reduced pressure. The crude product was purified by silica gel column chromatography using a 1:1 mixture of dichloromethane and hexane as the eluent. The eluent was evaporated to give the white crystalline solid ***S*-3** (121 mg, 86%).

Data for ***S*-3**: White crystal; mp 160 °C (dec); HRMS (orbitrap) *m*/*z*: $[M]^+$ calcd. for $C_{26}H_{18}O_2$, 362.1301; found, 362.1299; ^1H NMR (400 MHz, $CDCl_3$) δ 7.96 (d, *J* = 8.8 Hz, 2H), 7.81 (d, *J* = 8.4 Hz, 2H), 7.47 (d, *J* = 8.8 Hz, 2H), 7.37 (dd, *J* = 1.6, 8.4 Hz, 2H), 7.26 (s, 2H), 3.76 (s, 6H), 2.95 (s, 2H); ^{13}C NMR (100 MHz, $CDCl_3$) δ 155.5, 133.5, 129.5, 129.4, 128.8, 128.2, 126.4, 119.9, 118.9, 114.9, 84.6, 77.1 56.7; IR(KBr) ν_{max}: 3238, 2938, 2839, 2457, 1352, 1320, 1171, 1152, 961, 882, 597, 530, 432 cm^{-1}.

The *R*-isomer was synthesized using a similar procedure to that of the *S*-isomer, except that compound ***R*-2** (208 mg, 0.41 mmol) and TBAF (1.7 mL) in THF (17 mL) were used. The yield was 81%.

Synthesis of *S*/*R*-Pt

The synthesis of platinum(II) complex describe the *R*-enantiomer. Under an argon atmosphere, a mixture of ***R*-3** (16 mg, 0.043 mmol), **4** (39 mg, 0.084 mmol), and CuI (2.4 mg, 0.013 mmol) were dissolved in degassed dichloromethane (10 mL) and diisopropylamine (10 mL). The reaction mixture was refluxed for 28 hours. After cooling to room temperature, water was added, and the mixture was extracted three times with dichloromethane and saturated aqueous NH_4Cl. The organic layers were washed with saturated brine, then dried over anhydrous sodium sulfate. After drying the solvent was removed under reduced pressure. The crude product was then purified by silica gel column chromatography using a 9:1 mixture of dichloromethane and methanol as the eluent. The eluate was evaporated, and the resulting solid was washed with methanol and dried under vacuum to afford the orange solid of ***R*-Pt** (24 mg, 47%).

Data for ***R*-Pt**: Orange solid; mp 280 °C (dec); HRMS (orbitrap) *m*/*z*: $[M + H]^+$ calcd. for $C_{58}H_{38}N_4O_2Pt_2$, 1212.2343; found, 1212.2342; ^1H NMR (400 MHz, DMSO-d_6) δ 8.81 (d, *J* = 5.2 Hz, 2H), 8.41 (d, *J* = 8.0 Hz, 2H), 8.25 (t, *J* = 8.0 Hz, 2H), 8.14 (d, *J* = 8.0 Hz, 2H), 8.00–8.07 (m, 4H), 7.93 (d, *J* = 8.0 Hz, 2H), 7.85 (d, *J* = 8.4 Hz, 2H), 7.67–7.75 (m, 2H), 7.50–7.57 (m, 6H), 7.32 (dd, *J* = 1.2 and 8.4 Hz, 2H), 7.20–6.95 (m, 6H), 3.77 (s, 6H); ^{13}C NMR (100 MHz, DMSO-d_6) δ 164.1, 157.6, 155.0, 154.0, 150.8, 147.1, 142.2, 140.1, 137.6, 133.7, 130.7, 129.1, 128.5, 127.8, 127.2, 126.8, 126.7, 126.1, 125.0, 124.1, 123.6, 119.3, 119.2, 117.9, 113.4, 110.1, 109.5, 106.2, 56.3; IR(KBr) ν_{max}: 3448, 3061, 2923, 2846, 2371, 2345, 2091, 1610, 1499, 1458, 1255, 1092, 880, 835, 757, 477 cm^{-1}. $[\alpha]_D^{25}$ = −409 (*c* 0.0123, CH_2Cl_2).

The ***S*-Pt** complex was synthesized using a similar procedure to that of the ***R*-Pt** complex, except that compound ***S*-3** (20 mg, 0.055 mmol), **4** (51 mg, 0.11 mmol), diisopropylamine (10 mL) in CH_2Cl_2 (10 mL) were used. The yield was 25 mg, 38%.

Supporting Information

Supporting Information File 1

Spectroscopic details and theoretical calculations.
[https://www.beilstein-journals.org/bjoc/content/supplementary/1860-5397-22-7-S1.pdf]

Acknowledgements

The authors are grateful to Prof. Dr. Takahiro Tsuchiya and Dr. Masafumi Ueda (Kitasato University) for their helpful discussions. We would also like to thank Ms. Chika Hasegawa (Kitasato University) for her assistance in the synthesis of a part of the axially chiral binaphthyl units.

Funding

This work was supported by a Grant-in-Aid for Research Activity Start-up (D.T., Grant number 25K23609) and CREST from Japan Science and Technology Agency (M.H., Grant Number

JP-MJCR2001). This work was also partly supported by a Kitasato University Research Grant for Young Researchers.

Author Contributions

Daiki Tauchi: conceptualization; formal analysis; investigation; supervision; writing – original draft. Sota Ogura: investigation. Misa Sakura: investigation. Kazunori Tsubaki: investigation; supervision. Masashi Hasegawa: supervision.

ORCID® iDs

Daiki Tauchi - https://orcid.org/0009-0007-5434-2590

Data Availability Statement

Data generated and analyzed during this study is available from the corresponding author upon reasonable request.

Preprint

A non-peer-reviewed version of this article has been previously published as a preprint: https://doi.org/10.3762/bxiv.2025.53.v1

References

1. Rashamuse, T. J.; Mohlala, R. L.; Coyanis, E. M.; Magwa, N. P. *Molecules* **2023,** *28,* 5272. doi:10.3390/molecules28135272
2. Li, X.; Xie, Y.; Li, Z. *Chem. – Asian J.* **2021,** *16,* 2817–2829. doi:10.1002/asia.202100784
3. Li, S.; Zhou, L.; Zhang, H. *Light: Sci. Appl.* **2022,** *11,* 177. doi:10.1038/s41377-022-00866-w
4. Kourkoulos, D.; Karakus, C.; Hertel, D.; Alle, R.; Schmeding, S.; Hummel, J.; Risch, N.; Holder, E.; Meerholz, K. *Dalton Trans.* **2013,** *42,* 13612. doi:10.1039/c3dt50364j
5. Li, G.; Zhao, X.; Fleetham, T.; Chen, Q.; Zhan, F.; Zheng, J.; Yang, Y.-F.; Lou, W.; Yang, Y.; Fang, K.; Shao, Z.; Zhang, Q.; She, Y. *Chem. Mater.* **2020,** *32,* 537–548. doi:10.1021/acs.chemmater.9b04263
6. Demas, J. N.; DeGraff, B. A. *J. Chem. Educ.* **1997,** *74,* 690. doi:10.1021/ed074p690
7. Higgins, B.; DeGraff, B. A.; Demas, J. N. *Inorg. Chem.* **2005,** *44,* 6662–6669. doi:10.1021/ic050044e
8. Dey, N.; Biswakarma, D.; Bhattacharya, S. *ACS Sustainable Chem. Eng.* **2019,** *7,* 569–577. doi:10.1021/acssuschemeng.8b04107
9. Singh, J.; Yadav, M.; Singh, A.; Singh, N. *Dalton Trans.* **2015,** *44,* 12589–12597. doi:10.1039/c5dt01063b
10. Zhao, Q.; Huang, C.; Li, F. *Chem. Soc. Rev.* **2011,** *40,* 2508. doi:10.1039/c0cs00114g
11. Lee, L. C.-C.; Lo, K. K.-W. *Chem. Rev.* **2024,** *124,* 8825–9014. doi:10.1021/acs.chemrev.3c00629
12. Wong, K. M.-C.; Tang, W.-S.; Lu, X.-X.; Zhu, N.; Yam, V. W.-W. *Inorg. Chem.* **2005,** *44,* 1492–1498. doi:10.1021/ic049079p
13. Lu, W.; Mi, B.-X.; Chan, M. C. W.; Hui, Z.; Che, C.-M.; Zhu, N.; Lee, S.-T. *J. Am. Chem. Soc.* **2004,** *126,* 4958–4971. doi:10.1021/ja0317776
14. Chow, P.-K.; Cheng, G.; Tong, G. S. M.; To, W.-P.; Kwong, W.-L.; Low, K.-H.; Kwok, C.-C.; Ma, C.; Che, C.-M. *Angew. Chem., Int. Ed.* **2015,** *54,* 2084–2089. doi:10.1002/anie.201408940
15. Li, K.; Zou, T.; Chen, Y.; Guan, X.; Che, C.-M. *Chem. – Eur. J.* **2015,** *21,* 7441–7453. doi:10.1002/chem.201406453
16. Albrecht, M.; van Koten, G. *Angew. Chem., Int. Ed.* **2001,** *40,* 3750–3781. doi:10.1002/1521-3773(20011015)40:20<3750::aid-anie3750>3.0.co;2-6
17. Dikova, Y. M.; Yufit, D. S.; Williams, J. A. G. *Inorg. Chem.* **2023,** *62,* 1306–1322. doi:10.1021/acs.inorgchem.2c04116
18. Gong, Z.-L.; Zhong, Y.-W. *Sci. China: Chem.* **2021,** *64,* 788–799. doi:10.1007/s11426-020-9911-4
19. Ikeda, T.; Takayama, M.; Kumar, J.; Kawai, T.; Haino, T. *Dalton Trans.* **2015,** *44,* 13156–13162. doi:10.1039/c5dt01284h
20. Gong, Z.-L.; Dan, T.-X.; Yao, J.; Zhong, Y.-W. *ChemPhotoChem* **2022,** *6,* e202100239. doi:10.1002/cptc.202100239
21. Zhang, X.-P.; Chang, V. Y.; Liu, J.; Yang, X.-L.; Huang, W.; Li, Y.; Li, C.-H.; Muller, G.; You, X.-Z. *Inorg. Chem.* **2015,** *54,* 143–152. doi:10.1021/ic5019136
22. Li, B.; Li, Y.; Chan, M. H.-Y.; Yam, V. W.-W. *J. Am. Chem. Soc.* **2021,** *143,* 21676–21684. doi:10.1021/jacs.1c10943
23. Nojima, Y.; Hasegawa, M.; Hara, N.; Imai, Y.; Mazaki, Y. *Chem. Commun.* **2019,** *55,* 2749–2752. doi:10.1039/c8cc08929a
24. Nishizaka, M.; Mori, T.; Inoue, Y. *J. Phys. Chem. A* **2011,** *115,* 5488–5495. doi:10.1021/jp202776g
25. Biet, T.; Cauchy, T.; Sun, Q.; Ding, J.; Hauser, A.; Oulevey, P.; Bürgi, T.; Jacquemin, D.; Vanthuyne, N.; Crassous, J.; Avarvari, N. *Chem. Commun.* **2017,** *53,* 9210–9213. doi:10.1039/c7cc05198k
26. Inoue, R.; Kondo, R.; Morisaki, Y. *Chem. Commun.* **2020,** *56,* 15438–15441. doi:10.1039/d0cc06205g
27. Ikeshita, M.; Shimizu, I.; Watanabe, S.; Yamada, T.; Suzuki, S.; Tanaka, S.; Hattori, S.; Shinozaki, K.; Imai, Y.; Tsuno, T. *Inorg. Chem.* **2024,** *63,* 23642–23650. doi:10.1021/acs.inorgchem.4c03675
28. Tanaka, H.; Inoue, Y.; Mori, T. *ChemPhotoChem* **2018,** *2,* 386–402. doi:10.1002/cptc.201800015
29. Wang, X.; Ma, S.; Zhao, B.; Deng, J. *Adv. Funct. Mater.* **2023,** *33,* 2214364. doi:10.1002/adfm.202214364
30. Ikeshita, M.; Imai, Y.; Tsuno, T. *Chem. Lett.* **2025,** *54,* upaf066. doi:10.1093/chemle/upaf066

License and Terms

The definitive version of this article is the electronic one which can be found at:
https://doi.org/10.3762/bjoc.22.7

BEILSTEIN JOURNAL OF ORGANIC CHEMISTRY

Screwing the helical chirality through terminal *peri*-functionalization

Devesh Chandra[1], Sachin[1,2] and Upendra Sharma[*1,2]

Perspective

Address:
[1]Chemical Technology Division, CSIR-IHBT, Palampur, HP 176 061, India and [2]Academy of Scientific and Innovative Research (AcSIR), Ghaziabad-201002, India

Email:
Upendra Sharma* - upendra@ihbt.res.in

* Corresponding author

Keywords:
catalysis; C–H functionalization; helical chirality

Beilstein J. Org. Chem. **2026,** *22,* 205–212.
https://doi.org/10.3762/bjoc.22.14

Received: 27 September 2025
Accepted: 16 January 2026
Published: 28 January 2026

This article is part of the thematic issue "Non-central chirality in organic chemistry".

Associate Editor: N. Yoshikai

Abstract

Helical chirality is an important, but underrated form of chirality than other types of chirality. Molecules with helical chirality impart a crucial role in several biological phenomena as well as in modern materials applications. Classically, the generation of chiral helicity in organic molecules relies on a ring extension by means of cycloaddition and related reactions. Recently, the *peri*-functionalization approach paved a new pathway for the generation of chiral helical molecules. In this article, we highlight the key advancements in these parallel approaches for the generation of helical chiral architectures.

Introduction

Nature utilizes helical chirality for the inception of life. The double-helical structure of DNA and the helical conformations of proteins are key examples of the helical chirality. Inspired by these natural systems, chemists have developed methods to construct and control helicity in synthetic systems. These methods aim to achieve precise enantioselectivity, enabling the synthesis of helical molecules with specific handedness. In modern day science, helical chirality is gaining more and more importance in various fields such as drug design, optoelectronics, spintronics, diagnosis tool, biosensors and other forms of the materials sciences continuing its relevance to cutting edge research [1,2]. However, precise control and manipulation of helical chirality in synthetic systems remain technically challenging. This complexity may have led to underestimation of its potential, as research frequently focused toward other types of chirality, like point chirality [3], axial chirality [4], and planar chirality [5-7], often overshadowing the potential of helical chirality. Point chirality has major applications in medicinal chemistry and several drug molecules contain point chirality centers in their core structure [8]. Point chirality is the simplest form of chirality, and it is relatively easy to control and characterize during the synthesis of organic molecules. Due to these facts point chirality holds a central position among the different types of chirality. Axial chirality is another important type of chirality, where the chirality is controlled by restricted rotation among an axis. These types of molecules play an important role as chiral ligands in organic synthesis, i.e., BINOL, BINAP, etc. [9-11]. Another form of chirality, where chirality depends on a constrained substitution pattern along the plane of symmetry, is known as planar chirality, as seen in metallocene and cyclophanes. Molecules containing planar chirality have greater relevance in materials science and stereoselective transformations [12,13].

The fourth branch of the chiral tree is helical chirality. A helical system can undergo molecular to macroscopic systems due to its three-dimensional nature. Thus, helical systems, require more precise control of chirality compared to other forms of chirality. Helical chiral molecules have recently been found to display functional advantages, i.e., chirality-induced spin selectivity. These functionalities have great potential to transform in key areas such as drug discovery and modern diagnostic tools, as well as in distinct emerging fields like spintronics and optoelectronics [14].

Helicenes have found applications in chiral optoelectronics, i.e., as circularly polarized organic light emitting diodes (OLEDs), circularly polarized luminescence (CPL), and photonic devices, etc., due to their strong circular dichroism and circularly polarized luminescence [15,16]. Their well-defined three-dimensional chiral environment also makes helicenes useful in asymmetric synthesis, where they serve as chiral ligands and organocatalysts, delivering high enantioselectivities [17,18]. Their tunable HOMO–LUMO gaps and controlled π–π interactions, is key to the use of helicenes in molecular electronics and organic semiconductors as well. Helicenes function as active components in organic field effect transistors (OFETs), molecular wires, and chiral conductive materials [19-21]. Furthermore, helicenes are widely explored in chiroptical sensing, molecular recognition, and supramolecular self-assembly, enabling the construction of next generation responsive materials [22,23]. A very recent study also highlighted their potential application in biological interfaces [1], thus highlighting the versatility of helicenes in medicine along with next-generation materials and catalytic systems.

Due to the above-mentioned applications of chiral helicenes various synthetic approaches have been developed for the synthesis of chiral helical molecules and the most prevalent approaches include cycloaddition reactions [24], ring extensions [25], and related approaches [26,27]. However, some parallel and more sustainable approaches have emerged in recent years and C–H functionalizations are one of these approaches.

In the following section, we discuss the parallel approaches, i.e., *peri*-C–H functionalization, over the prevalent approach for the generation of helical chirality, which generally considers π extension. The *peri*-C–H functionalization approach provides direct access to a functional group installed in the terminal core of helicened with high level of stereocontrol, rather than merely increasing the number of fused rings in a helical system. The direct introduction of suitable functional groups at strategic positions can expand the structure diversity and enhance the utility of the parent helicene in diverse areas, thereby offering a more versatile alternative to classical helicene extension strategies.

Discussion

Only a handful attempts have been made for the asymmetric synthesis of helical molecules using π conjugation extension [28-30]. This prevalent method for the generation of helical chirality primarily involves cycloaddition and central/axial to helical chirality transfer reactions [31] (Figure 1A and B). In addition to this, a parallel strategy also offers a promising approach to achieving configurationally stable helicenes via terminal *peri*-functionalization, where a bulkier handle provides the required enantiomerization barrier to screw helical chirality (Figure 1C and D).

A straight forward preparation of various carbohelicenes via an organocatalytic enantioselective hydroamination reaction of polyaromatic phenols with diazodicarboxamide derivatives through a catalytic kinetic resolution (KR) process was developed by Liu and co-workers [32]. The authors screened a range of organocatalysts, i.e., Takemoto’s thiourea catalyst, (*S*,*S*)-1,2-cyclohexanediamine-derived thioureas, cinchona alkaloid-derived thiourea, and squaramides to achieve the desired outcome of the reaction. After rigorous testing, (*S*,*S*)-1,2-cyclohexanediamine-derived catalyst **L1** was found to be the most effective organocatalyst to induce both the helical chirality and remote axial chirality during the functionalization of the [4]- and [5]helicenes **3a**–**k** with good yield and excellent enantioselectivity. Notably, [6]helicene **3k** was also readily produced, via kinetic resolution (Scheme 1).

Computational studies suggested that hydrogen bonding and π interactions between the reactants and catalyst **L1** controlled the stereochemical output of the products **3**. The catalyst proximate both reactants to each other via hydrogen-bonding interaction, locking the relative orientation of the substrates producing the chiral [4]carbohelicene via *peri*-terminal functionalization (Figure 2).

To examine the utility of the developed protocol, the reaction was scaled up to a 2 mmol scale and the product was further

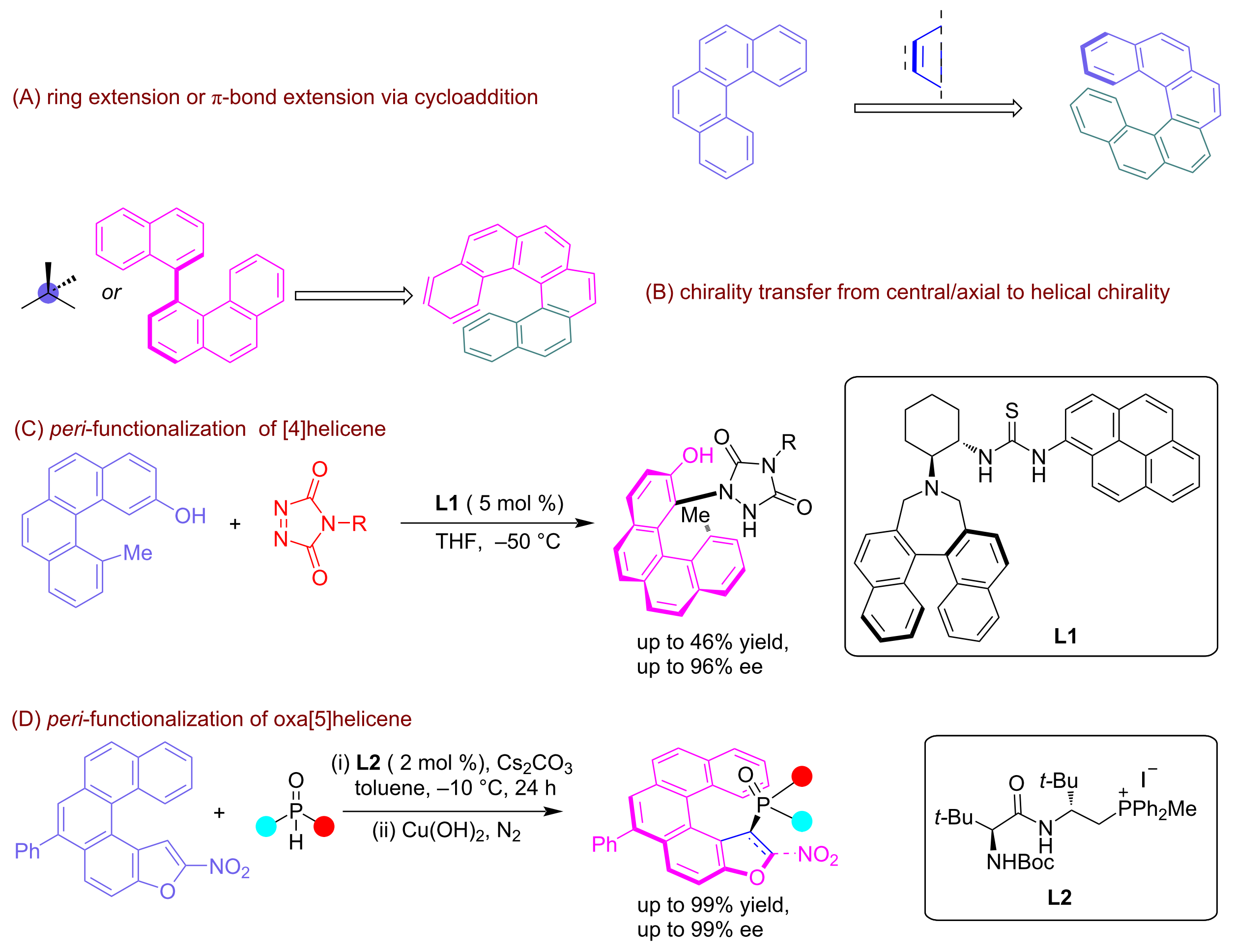
(A) ring extension or π-bond extension via cycloaddition

(B) chirality transfer from central/axial to helical chirality

(C) *peri*-functionalization of [4]helicene

(D) *peri*-functionalization of oxa[5]helicene

Figure 1: Representation of the general practices for the induction of helical chirality in organic scaffolds. A) Prelevant approach for the induction of helical chirality which majorly relies on the π extension of organic scaffolds via annulation/cycloaddition and B) central/axial to helical chirality conversion. C) Induction of helical chirality in [4]helicene via terminal *peri*-functionalization. D) Induction of helical chirality in [5]helicene via terminal *peri*-functionalization where a bulkier handle provides the required enantiomerization barrier to screw helicity.

transformed into representative derivatives. Notably, the reaction performed well in the scale-up demonstration and the post-synthetic transformations proceeded smoothly without hampering the enantiomeric excess (Scheme 2).

Another report applying *peri*-C–H functionalization for the synthesis of helical chiral entities was reported by Wang and co-workers. They reported an organocatalyzed asymmetric synthesis of phosphorus-containing chiral helicenes enabled by dynamic kinetic resolution using copper and peptide-mimetic phosphonium salts, i.e. amino acid-derived phosphonium iodide and bromide as catalysts [33]. A domino reaction was developed, beginning with a PPS **L2**-catalyzed Michael addition of phosphine oxides **7** to nitro-substituted oxa[5]helicenes **6**, followed by a copper-promoted aromatization. This sequence efficiently produced phosphorus-containing oxa[5]helicene derivatives **8** in high yields and with excellent enantioselectivities. The catalytic system operated under mild conditions within a practical timeframe and demonstrated broad substrate tolerance, providing a range of chiral helicenes. Notably, unsymmetrical phosphine oxides also underwent smooth Michael addition, with excellent enantiomeric excess and diastereomeric ratio (Scheme 3).

The developed protocol was also tested for up-scale synthesis and post-synthetic transformations. Notably, the reaction worked well at a 4.0 mmol scale providing product **8g** in quantitative yield and >99% ee. This product was further reduced to the corresponding amine followed by *N*-tosylation, providing product **10** in 63% yield without altering the enantiomeric excess (Scheme 4).

Additionally, product **8g** was converted into the chiral phosphine ligand **12** while fully preserving its helical chirality and successfully applied in palladium-catalyzed nucleophilic substitution reactions (Scheme 5).

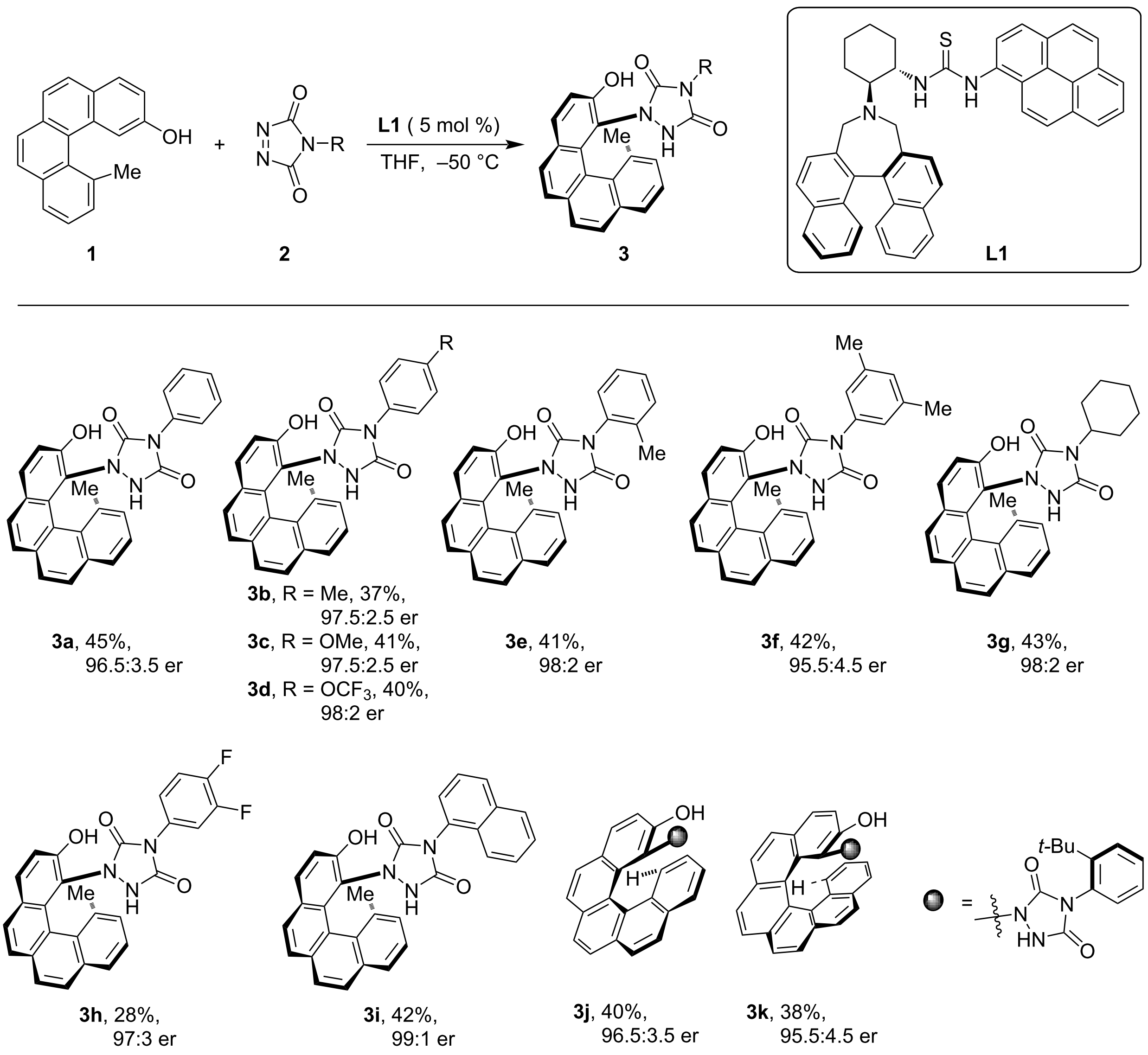

Scheme 1: Asymmetric synthesis of carbohelicenes via *peri*-C–H functionalization.

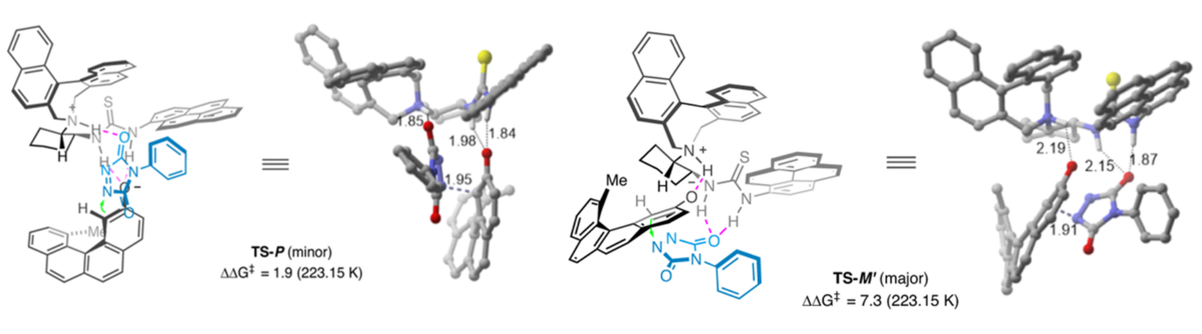

Figure 2: Stereomodel for *peri*-terminal functionalization of carbohelicene. (Figure 2 was reproduced from [32] (© 2024 X. Liu et al., published by Springer Nature, distributed under the terms of the Creative Commons Attribution 4.0 International License, https://creativecommons.org/licenses/by/4.0).

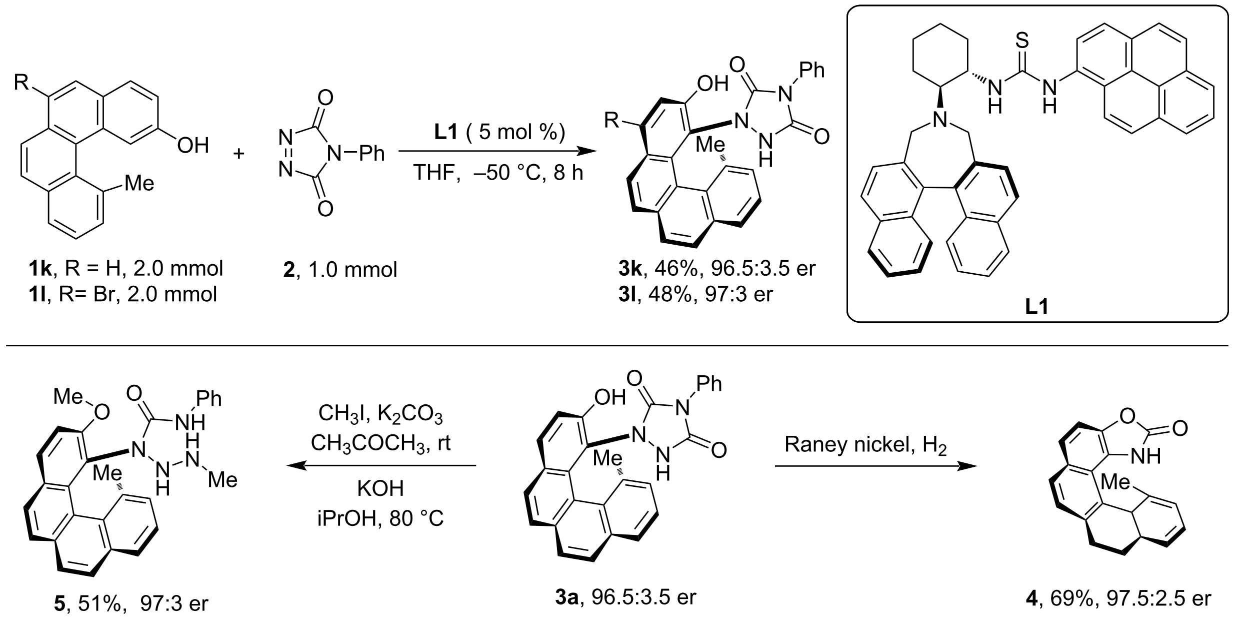

Scheme 2: Scale-up synthesis and post-synthetic application of chiral helical product **3**.

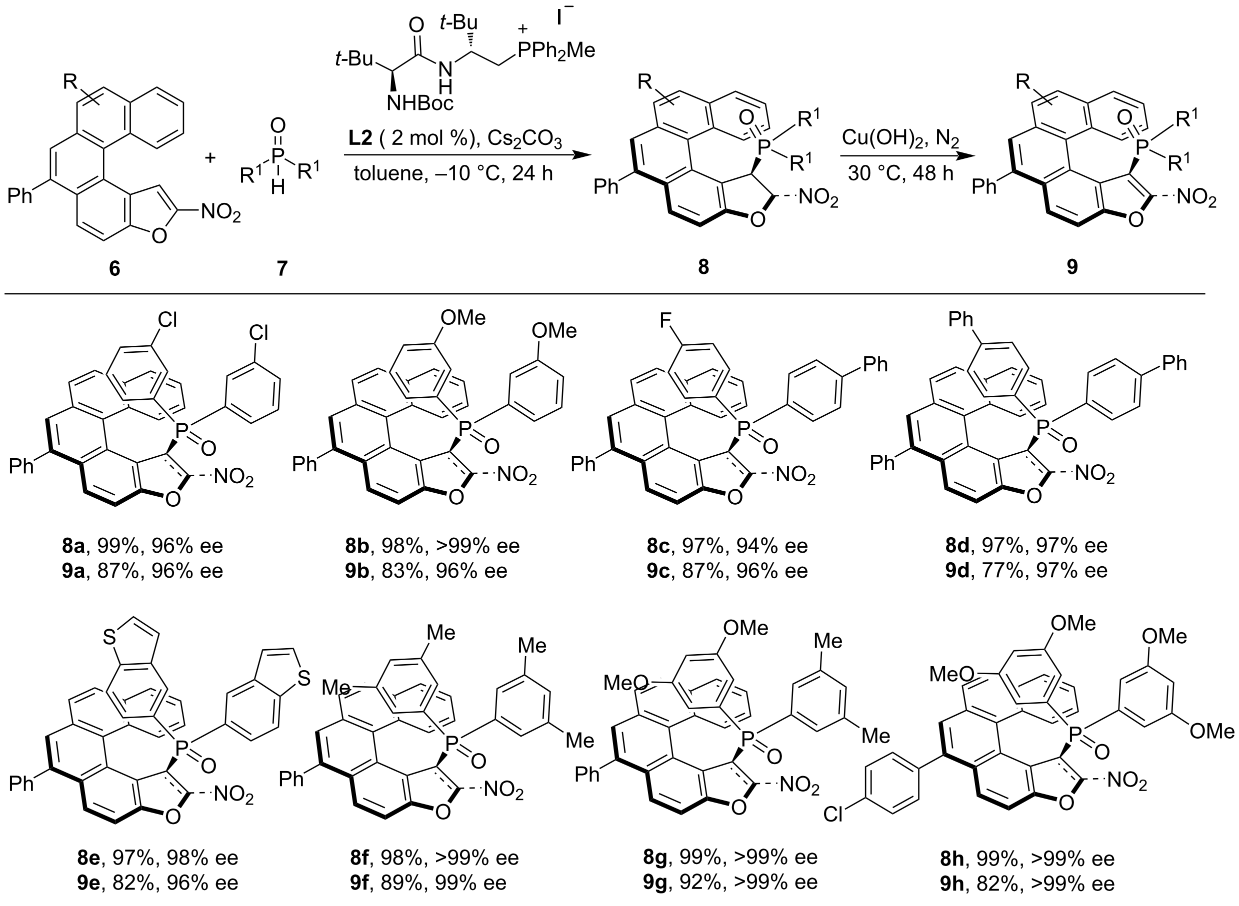

Scheme 3: Asymmetric peri-C–H functionalization of nitro-substituted oxa[5]helicenes.

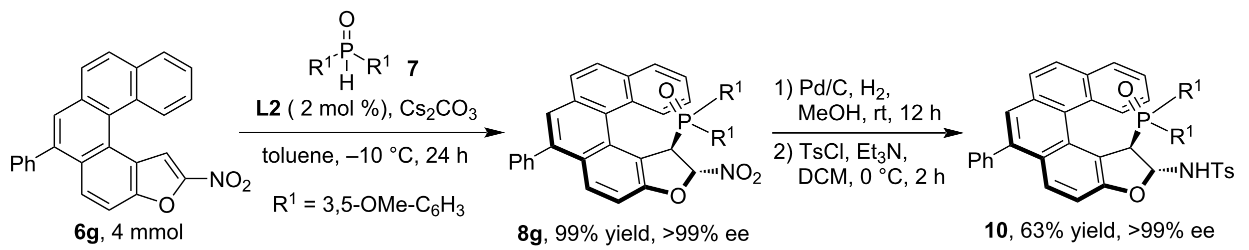

Scheme 4: Scale-up synthesis and post-synthetic application of chiral helical product **8g**.

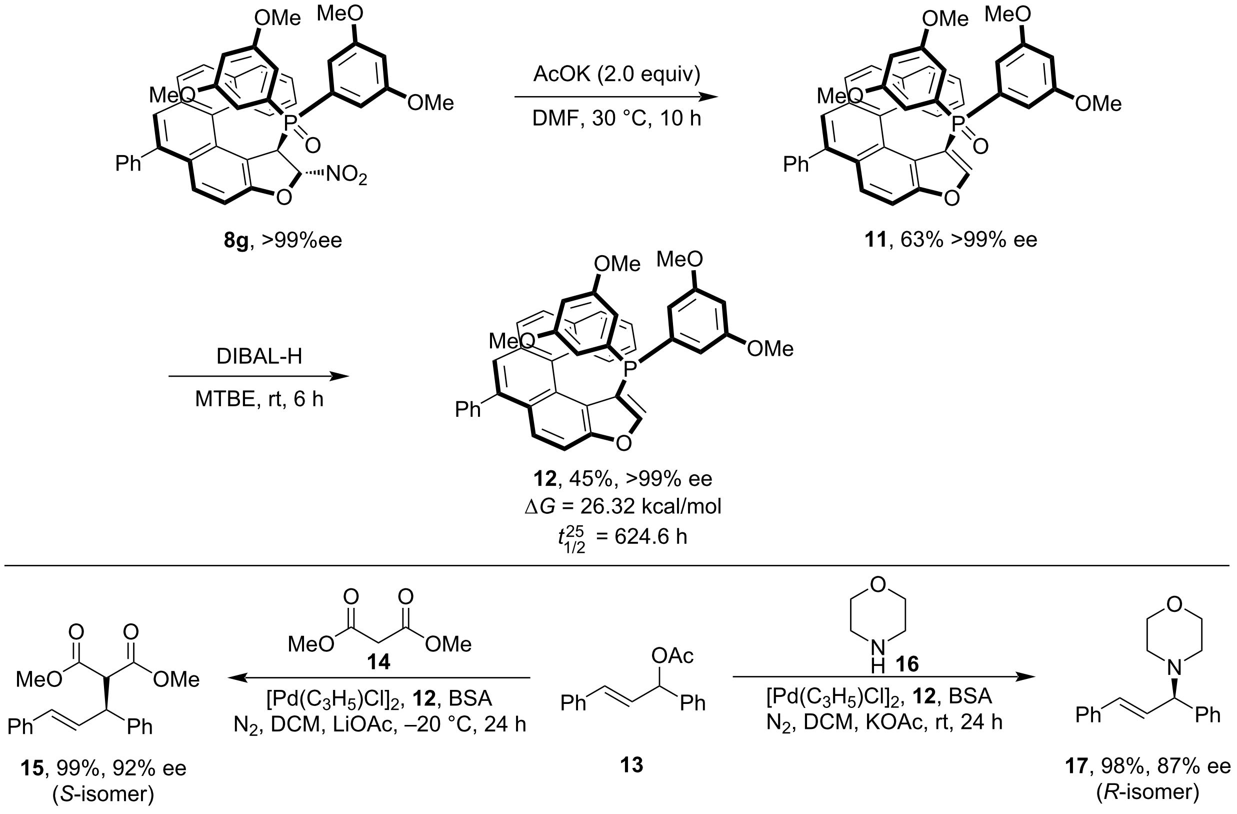

Scheme 5: Post-synthetic transformation of product **8g** to chiral phosphine ligand **12** and its application in Pd-catalyzed reactions.

A stereochemical model was proposed for the phospha-Michael addition, indicating that enantioselectivity was primarily influenced by steric effects arising from hydrogen bonding and ion pairing between the peptide mimetic phosphonium salt (PPS)-activated phosphine oxide and the nitro-functionalized oxa[5]helicene. This ion-pairing interaction was also studied using NMR titration and Job's plot analysis. The transition state depicted in Figure 3 was found to be most favorable providing the product with *M*-configuration.

Looking ahead, these strategies may also be applicable to other polyaromatic frameworks beyond specific helicenes for the construction of helically chiral structures.

Outlook

Despite its potential, this strategy has faced significant challenges in the context of catalytic enantioselective synthesis of functionalized helicenes and their heteroanalogues. These challenges include: (1) the limited availability of suitable substrates, (2) substantial steric hindrance from the terminal ring, making it difficult to introduce substituents at the required positions onto helical precursors, and (3) the complex nature of controlling helical chirality, a nanoscale phenomenon that requires the design of advanced catalysts to achieve high enantioselectivity. Although the parallel approach is still in its infancy, it holds immense promise. With the continued and widespread efforts of synthetic chemists, we anticipate that the existing challenges

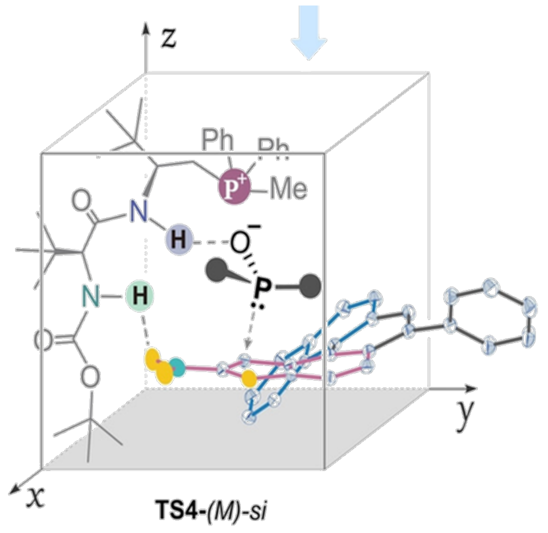

Figure 3: Stereomodel for the asymmetric *peri*-C–H functionalization of oxa[5]helicene. (Figure 3 was reproduced from [33], J.-H. Wu et al., *Angew. Chem., Int. Ed.*, with permission from John Wiley and Sons. Copyright © 2023 Wiley-VCH GmbH. This content is not subject to CC BY 4.0)

will be surmounted, paving the way for the development of innovative approaches and new materials. Such advancements are expected to unlock the full potential of chiral helicenes.

Acknowledgements

The authors acknowledge the CSIR-IHBT, Palampur for providing necessary resources. CSIR-IHBT Communication no. for this article is 5849.

Author Contributions

Devesh Chandra: data curation; formal analysis; investigation; methodology; software; writing – original draft. Sachin: data curation; methodology. Upendra Sharma: conceptualization; funding acquisition; project administration; resources; supervision; writing – review & editing.

ORCID® iDs

Devesh Chandra - https://orcid.org/0000-0003-1640-5865
Sachin - https://orcid.org/0000-0002-1808-114X
Upendra Sharma - https://orcid.org/0000-0002-7693-8690

Data Availability Statement

Data sharing is not applicable as no new data was generated or analyzed in this study.

References

1. Bouz, G.; Žádný, J.; Storch, J.; Vacek, J. *Biotechnol. Adv.* **2025,** *79,* 108513. doi:10.1016/j.biotechadv.2024.108513
2. Lee, H.; Kim, D.; Cho, J. H.; Lim, J. A. *Acc. Mater. Res.* **2025,** *6,* 434–446. doi:10.1021/accountsmr.4c00374
3. Kagan, H. B. Chiral Ligands for Asymmtric Catalysis. In *Asymmetric Synthesis;* Morrison, J. D., Ed.; Academic Press: San Diego, CA, USA, 1985. doi:10.1016/b978-0-08-092493-9.50006-2
4. Kozlowski, M. C.; Miller, S. J.; Perreault, S. *Acc. Chem. Res.* **2023,** *56,* 187–188. doi:10.1021/acs.accounts.2c00765
5. Colacot, T. J. *Chem. Rev.* **2003,** *103,* 3101–3118. doi:10.1021/cr000427o
6. López, R.; Palomo, C. *Angew. Chem., Int. Ed.* **2022,** *61,* e202113504. doi:10.1002/anie.202113504
7. Chandra, D.; Sharma, T.; Sarthi; Sachin; Sharma, U. *J. Catal.* **2024,** *439,* 115756. doi:10.1016/j.jcat.2024.115756
8. Brooks, H.; Guida, W. C.; Daniel, K. G. *Curr. Top. Med. Chem.* **2011,** *11,* 760–770. doi:10.2174/156802611795165098
9. Trost, B. M. *Proc. Natl. Acad. Sci. U. S. A.* **2004,** *101,* 5348–5355. doi:10.1073/pnas.0306715101
10. Sumit; Chandra, D.; Sharma, U. *Org. Biomol. Chem.* **2021,** *19,* 4014–4026. doi:10.1039/d1ob00232e
11. Sumit; Chandra, D.; Sharma, U. *Chem. Commun.* **2023,** *59,* 9288–9300. doi:10.1039/d3cc02293e
12. Patra, M.; Gasser, G. *Nat. Rev. Chem.* **2017,** *1,* 0066. doi:10.1038/s41570-017-0066
13. Dai, L.-X.; Hou, X.-L., Eds. *Chiral Ferrocenes in Asymmetric Catalysis;* Wiley-VCH: Weinheim, Germany, 2010. doi:10.1002/9783527628841
14. Bloom, B. P.; Paltiel, Y.; Naaman, R.; Waldeck, D. H. *Chem. Rev.* **2024,** *124,* 1950–1991. doi:10.1021/acs.chemrev.3c00661
15. Qiu, M.; Du, J.; Yao, N.-T.; Wang, X.-Y.; Gong, H.-Y. *Beilstein J. Org. Chem.* **2025,** *21,* 1422–1453. doi:10.3762/bjoc.21.106
16. Meng, D.; Fu, H.; Xiao, C.; Meng, X.; Winands, T.; Ma, W.; Wei, W.; Fan, B.; Huo, L.; Doltsinis, N. L.; Li, Y.; Sun, Y.; Wang, Z. *J. Am. Chem. Soc.* **2016,** *138,* 10184–10190. doi:10.1021/jacs.6b04368
17. Peng, Z.; Takenaka, N. *Chem. Rec.* **2013,** *13,* 28–42. doi:10.1002/tcr.201200010
18. Chen, C.-F.; Shen, Y. Helicenes in Catalysis. *Helicene Chemistry;* Springer: Berlin, Heidelberg, Germany, 2017; pp 187–199. doi:10.1007/978-3-662-53168-6_9
19. de Ara, T.; Hsu, C.; Martinez-Garcia, A.; Baciu, B. C.; Bronk, P. J.; Ornago, L.; van der Poel, S.; Lombardi, E. B.; Guijarro, A.; Sabater, C.; Untiedt, C.; van der Zant, H. S. J. *J. Phys. Chem. Lett.* **2024,** *15,* 8343–8350. doi:10.1021/acs.jpclett.4c01425
20. He, P.; Ye, J.; Zhang, J.; Lu, T.; Cui, W.; Liu, J.; Shen, C.; Hong, W.; Liu, X. *Angew. Chem., Int. Ed.* **2025,** *64,* e202416319. doi:10.1002/anie.202416319
21. Yang, Y.; da Costa, R. C.; Fuchter, M. J.; Campbell, A. J. *Nat. Photonics* **2013,** *7,* 634–638. doi:10.1038/nphoton.2013.176
22. Kanao, E.; Murata, Y.; Miwa, S.; Takikawa, H.; Takasu, K.; Ishihama, Y.; Kubo, T. *Anal. Chem. (Washington, DC, U. S.)* **2025,** *97,* 12690–12698. doi:10.1021/acs.analchem.5c01385
23. Yang, D.-C.; Li, M.; Chen, C.-F. *Chem. Commun.* **2017,** *53,* 9336–9339. doi:10.1039/c7cc03519e
24. Stará, I. G.; Starý, I. *Acc. Chem. Res.* **2020,** *53,* 144–158. doi:10.1021/acs.accounts.9b00364
25. Kötzner, L.; Webber, M. J.; Martínez, A.; De Fusco, C.; List, B. *Angew. Chem., Int. Ed.* **2014,** *53,* 5202–5205. doi:10.1002/anie.201400474

26. Liu, P.; Bao, X.; Naubron, J.-V.; Chentouf, S.; Humbel, S.; Vanthuyne, N.; Jean, M.; Giordano, L.; Rodriguez, J.; Bonne, D. *J. Am. Chem. Soc.* **2020,** *142,* 16199–16204. doi:10.1021/jacs.0c07995
27. Sako, M.; Takeuchi, Y.; Tsujihara, T.; Kodera, J.; Kawano, T.; Takizawa, S.; Sasai, H. *J. Am. Chem. Soc.* **2016,** *138,* 11481–11484. doi:10.1021/jacs.6b07424
28. Wang, Y.; Wu, Z.-G.; Shi, F. *Chem Catal.* **2022,** *2,* 3077–3111. doi:10.1016/j.checat.2022.10.011
29. Liu, P.; Bao, X.; Naubron, J.-V.; Chentouf, S.; Humbel, S.; Vanthuyne, N.; Jean, M.; Giordano, L.; Rodriguez, J.; Bonne, D. *J. Am. Chem. Soc.* **2020,** *142,* 16199–16204. doi:10.1021/jacs.0c07995
30. Gaucherand, A.; Yen-Pon, E.; García-López, D.; Naubron, J.-V.; Chentouf, S.; Giorgi, M.; Humbel, S.; Jean, M.; Rodriguez, J.; Bonne, D. *Chem. Sci.* **2024,** *15,* 7300–7307. doi:10.1039/d4sc00745j
31. Huang, Q.; Tang, Y.-P.; Zhang, C.-G.; Wang, Z.; Dai, L. *ACS Catal.* **2024,** *14,* 16256–16265. doi:10.1021/acscatal.4c05345
32. Liu, X.; Zhu, B.; Zhang, X.; Zhu, H.; Zhang, J.; Chu, A.; Wang, F.; Wang, R. *Nat. Commun.* **2024,** *15,* 732. doi:10.1038/s41467-024-45049-w
33. Wu, J.-H.; Fang, S.; Zheng, X.; He, J.; Ma, Y.; Su, Z.; Wang, T. *Angew. Chem., Int. Ed.* **2023,** *62,* e202309515. doi:10.1002/anie.202309515

License and Terms

The definitive version of this article is the electronic one which can be found at:
https://doi.org/10.3762/bjoc.22.14